2021

Characterising Stream Interaction Regions using 3D magnetohydrodynamic simulations

BOSTON UNIVERSITY

GRADUATE SCHOOL OF ARTS AND SCIENCES

Dissertation

CHARACTERISING STREAM INTERACTION REGIONS USING 3D MAGNETOHYDRODYNAMIC SIMULATIONS

by

DANIELLE M. PAHUD

M.A., Boston University, Boston, MA, 2010
B.Sc., University of Alberta, Edmonton, AB, 2007

Submitted in partial fulfillment of the

requirements for the degree of

Doctor of Philosophy

2021

Approved by

First Reader

W. Jeffrey Hughes, PhD
Professor of Astronomy

Second Reader

Merav Opher, PhD
Professor of Astronomy

Acknowledgments

In reflecting upon the time, effort, and experiences that have led up to the completion of my dissertation,I am overwhelmed with gratitude for all of the people who have helped me get here.

First, I would like to thank my advisor, Prof. Jeffrey Hughes. In addition to his expertise in the field, his wisdom, patient guidance, and willingness to allow me to begin again have been essential throughout the completion of this goal. I wold also like to thank my committee members for their encouragement and helpful feedback. Finally, I would like to thank the Astronomy Department at Boston University, and the people within it, for providing a jovial, collegial, and intellectually stimulating environment. I will always cherish memories of my time there.

I would further like to express my deep gratitude for my friends at BU, who made the work easier and the successes sweeter. I am grateful for my academic sisters, Sarah and Katie, who were compassionate cheerleaders throughout. I want to thank my dear friends, Patricio and Nick, amongst many others, whose confidence in me and general optimism was deeply reassuring.

Beyond BU, I am deeply indebted to my dearest nemesis, Rona, who has always made time to encourage and guide me through the most harrowing stages. Her insights, advice, and friendship has been invaluable. Thank you to my dear friends, Rachel and Emily, that took the time to sit and write with me, regularly making my life and my work richer. Thank you to Dana for her fierce faith and unfailing encouragement, and to the ladies of the Core for their enduring friendship and sup-

port. I am heartily grateful to Sandra and Truc, who provided a joyful and fruitful home-base for many years.

The completion of this degree would not have been possible without the support of my current department, colleagues, and friends. A special thank you to Bob, Ruth, and Johan for your mentorship, perspectives, and encouragement. Words fail to express how grateful I am to Brad and Kyla, whose unconditional encouragement, support and presence have made all the difference.

Finally, I would like to thank my parent, Robert and Solange, for their love and support that transcends distance and time, as I pursued this goal. Thank you to my siblings *et al*, Monique and Brandon, Nicolas and Jackie, for your encouragement and companionship. You have brought so much joy and laughter into this process. I could not have asked for better.

What a journey this has been. I am filled with gratitude.

CHARACTERISING STREAM INTERACTION REGIONS USING 3D MAGNETOHYDRODYNAMIC SIMULATIONS

DANIELLE M PAHUD

Boston University, Graduate School of Arts and Sciences, 2021

Major Professor: W. Jeffrey Hughes, Professor of Astronomy

ABSTRACT

Throughout the solar cycle and predominantly during the declining phase, Stream Interaction Regions (SIRs) drive space weather on Earth. SIRs occur when the Sun's rotation aligns a fast solar wind stream behind a slow solar wind stream. Both fast wind and slow wind are compressed and heated, forming a pressure ridge driven by the dynamic pressure of the fast wind. In the frame advecting with the SIR, the high pressure region is bound by a forward wave, which propagates away from the Sun, and reverse wave which propagates sunwards. The pressure waves steepen into shocks with increasing heliospheric distance, the shocks usually form beyond Earth's orbit. Located between the waves, the stream interface is a tangential discontinuity separating streams that were originally fast from slow. While the general mechanism for the formation and evolution of SIRs is relatively well known, the implications of the 3D structure in the inner heliosphere have not been well understood, in part due to the sparsity of *in situ* observations outside of the ecliptic plane.

In this dissertation, I have used the heliospheric adaptation of the Lyon-Fedder-Mobarry (LFM-helio) MHD model to simulate both idealized and realistic SIR struc-

tures in order to validate the model against *in situ* measurements and to elucidate which characteristics of the solar wind influence the evolution of SIRs. The LFM-helio is shown to accurately reproduce the solar wind conditions at various heliospheric distances. The simulations produced SIRs which agree with *in situ* observations. The simulations were used to show that the large scale shape of high speed streams driving SIRs affect the amount of heating, compression, and flow deflection. Further, for even small latitudinal separations, SIR evolution depends on the latitudinal structure of the High Speed Stream driving the SIR. Increasing the temperature at the inner boundary of the LFM-helio results in a solar wind that is globally faster and that produces SIRs exhibiting less compressive heating. Increasing the magnetic field strength uniformly at the inner boundary has an effect on the dynamical evolution SIRs whereas increasing the magnetic field strength in proportion to the solar wind speed latitudinally compresses the extent of the band of slow wind, modifying the global structure of the heliosphere.

Contents

List of Tables

List of Figures

List of Abbreviations

3D	3 Dimensional
AU	Astronomical Unit
CH	Coronal Hole
CHBL	Coronal Hole Boundary Layer
CIR	Corotating Interaction Region
CME	Coronal Mass Ejection
CR	Carrington Rotation
EUV	Extreme Ultraviolet
FIP	First Ionization Potential
GCR	Galactic Cosmic Rays
HCS	Heliospheric Current Sheet
HSS	High Speed Stream
IBC	Inner Boundary Conditions
ICME	Interplanetary Coronal Mass Ejection
LFM	Lyon Fedder Mobarry
LHS	Left Hand Side
MHD	Magnetohydrodynamic
RH	Rankine-Hugoniot
RHS	Right Hand Side
SI	Stream Interface
SIR	Stream Interaction Region
TVD	Total Variation Diminishing

Chapter 1

Introduction: The Solar Wind and MHD Solar wind modeling

The aurora, curtains of glowing, dancing light, have dazzled and intrigued humanity for thousands of years. Throughout most of human history however, there had been little understanding of what they are or of what causes them. While Earth's magnetic properties had long been known and used for navigation, their relation to the luminous displays have been established on in the last few hundred years.

Also observed since antiquity, visible during total solar eclipses, is the Sun's hot and tenuous atmosphere - the petal-shaped corona (*Wang and Siscoe*, 1980). Although the corona hints at the solar atmosphere extending great distances from the Sun, the presence of a continuous outflow was not suspected. The presence of the solar wind and the injection of matter, momentum, and energy into the Earth's space environment was deduced relatively recently, within the last 160 years.

The Cold War ushered in an era of launching spacecraft through the atmosphere and into Earth orbit. The Space Race allowed, for the first time, *in situ* measurements of Earth's plasma environment. Sputnik was the first artificial low earth orbit satellite, launched by the former USSR in 1957. The radio signals emitted by Sputnik allowed for the calculation of the density of the upper atmosphere and of the ionosphere. Explorer 1, the first satellite launched by the US in 1958, armed with a cosmic ray detector was used to deduce the radiation environment of Earth orbit. These and subsequent spacecraft measurements allowed the characterization of the

magnetosphere and its response to the Sun's own plasma environment. While the solar wind continuously buffets the magnetosphere, there are two types of occasional and transient solar wind structures that can drive large scale reconfiguration of the magnetosphere.

The first type of driver is interplanetary coronal mass ejections (ICMEs). ICMEs result from sudden reorganization of the magnetic field in the solar corona and the subsequent rapid propagation of a magnetic flux rope filled with hot plasma through the ambient solar wind. ICMEs occur frequently throughout the solar cycle but are most energetic and prevalent during solar maximum.

The second type of driver is stream interaction regions (SIRs), extents of high pressure solar wind. SIRs are caused by fast solar wind becoming radially aligned behind slow solar wind by solar rotation. As the fast wind catches up to the preceding slow wind, the fast wind compresses, heats and accelerates the plasma ahead of it and intensifies the magnetic field. SIRS are present throughout the solar cycle (*Richardson*, 2004) but are prevalent during the declining and minimum phases of the solar cycle. These structures are often well approximated as being relatively steady-state phenomenon. If the pattern of fast and slow solar wind persists for over a solar rotation period, the SIR will reccur from the perspective of Earth and these structures are called Corotating Interaction Regions (CIRs).

Both of these driver-structures evolve during their transit from the solar corona to 1 AU, compressing and accelerating solar wind preceding them and sometimes driving shocks. The characteristics of both are dependent on solar cycle, the phase therein, and on their own geometry. The evolution of SIRs as a function of latitude, distance, shape, and solar cycle will be the subject of this dissertation. This dissertation characterizes the evolution of SIRs, under steady state conditions using the Lyon Fedder Mobarry heliospheric model (LFM-helio).

To put the results of this dissertation in context, it begins with a description of the solar wind (Section 1.1) and of observations of SIRs (Section 1.1.1). Details of the MHD paradigm in which the solar wind is described, as well as the details of the LFM-helio model used are included.

1.1 Solar Wind

It took an extremely energetic event on the Sun, an explosive release of plasma and magnetic field, followed shortly by not only aurora but sparking telegraph lines, on September 1st 1859, for Richard Carrington to posit the connection between occurrences on the Sun and subsequent events on Earth (*Carrington*, 1859). Carrington doubted the ubiquity and omnipresence of the Sun's influence however, warning in his paper "One swallow does not make a summer".

Support for a more continuous solar wind came from the Norwegian scientist, Kristian Birkeland. The first experimental demonstrations of the aurora were made with Birkeland's terella (*Egeland and Burke*, 2010). He directed cathode rays toward a magnetized sphere in a vacuum and found that luminous ovals surrounded the magnetic poles. He had replicated the aurora. From his laboratory experiments along with observations made in the Arctic, he hypothesized as early as 1908 that the Sun was continuously emitting "electric corpuscular radiation", establishing the first persistent causal link between material leaving the Sun and that interacting with Earth's protective magnetosphere. *Chapman and Ferraro* (1931) posited the existence of an electrically neutral solar wind based on observations from magnetospheric storms.

This link was solidified in the 1950's when Biermann observed that comets' tails always pointed away from the Sun. In order to explain the speed at which gases flew away from the comet nuclei, the presence of an ionized gas outflow emanating

from the Sun was needed. Also in the 1950's, Chapmann used emission spectra measurements from the early 1900's which placed the temperature of the corona on the order of a million Kelvin. Given the high coronal temperature, Chapman and Alfvèn showed that a static hot corona would result in a finite pressure at infinity, larger than any pressure expected in the interstellar medium (*Kivelson and Russell*, 1995). To resolve this pressure inequality, they concluded that a *static* corona was impossible and that there must be a constant outflow from the corona.

Building on this, Eugene Parker famously laid the foundation for solar wind theory by solving the hydrodynamic equations for a spherically symmetric, isothermal, single fluid (*Parker*, 1958). He predicted that the plasma in the solar corona must accelerate, pass through a critical point, and expand supersonically throughout the heliosphere.

By including the magnetic properties of the Sun, Parker found that the corona's magnetic field would rotate as a solid body up to the critical distance at which the flow speed in the corona matched the Alfén speed, the Alfvén point. Beyond this distance, the plasma flow is purely radially outward. The Sun's rotation combined with the radial outflow of the solar wind, forms a spiral pattern in the magnetic field lines. Parker's prediction of a supersonic solar wind and a spiral-shaped heliospheric magnetic field were first confirmed by Mariner II spacecraft observations in 1962 (*Neugebauer and Snyder*, 1962). See 1.2 (left) for a schematic of the characteristic spiral pattern that now bears Parker's name. *in situ* observations revealed that while these models were astoundingly good first approximations, the actual solar wind is much more complex.

Some of the complexity arises from the solar wind's source; from the corona. At its simplest, the structure of the corona's magnetic field is roughly a dipole. The competition between the lowest energy configuration of the solar magnetic field, a

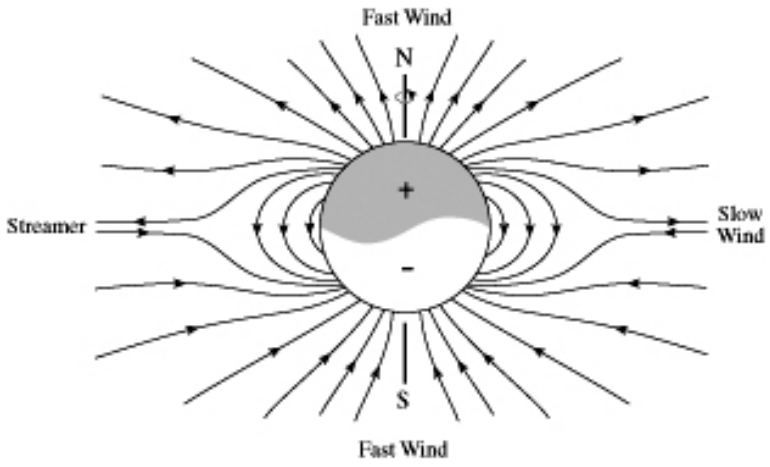

Fig. 1.1: Schematic of the Sun's dipolar magnetic field at solar minimum. The magnetic and rotation axes are aligned with open field lines at the poles and closed field lines at low latitudes.The field lines are stretched by the expansion of the coronal plasma. The open magnetic field lines produce fast solar wind while the closed magnetic field lines resist the flow of plasma and are sources of slow solar wind. The closed field lines are stretched out into streamers, which encompass the polarity reversal of the magnetic field lines, the Heliospheric Current Sheet (HCS). The diagram is from NASA's Cosmos (Copyright 2010, Professor Kenneth R. Lang, Tufts University)

dipole, and the expansion of the hot coronal plasma results in a stretched dipole configuration, as shown in Figure 1.1. The Sun's magnetic axis is roughly aligned with the Sun's rotation axis. In this configuration, open magnetic field lines, having only one footpoint tied to the Sun, are located at high latitudes while "closed" magnetic field lines, that have both footpoints tied to the solar surface, create a band around the heliographic equator.

The hot coronal plasma escapes unimpeded along the open magnetic field lines, resulting in fast solar wind at high heliographic latitudes. The outflow leaves the coronal region less dense than neighbouring regions of closed field lines. These underdense regions appear dark in Extreme Ultraviolet (EUV) images of the corona and have been called coronal holes (CH) (*Neugebauer et al.*, 1998; *Neugebauer et al.*,

2002). The open magnetic field lines, and the fast solar wind along with it, spread out to fill all latitudes of the heliosphere.

Conversely, the plasma expansion at low heliographic latitudes is perpendicular to closed field lines and stretches the latter into pointed structures called Helmet streamers - streamers for short. Streamers are thought to be the source region of slow solar wind. This formulation predicts two distinct populations of solar wind plasma; a fast wind and a slow wind. *in situ* observations show the solar wind indeed has a bimodal distribution, consisting of uniform fast solar wind ($\approx$ 800 km/s) and slow solar wind ($\approx 300\ km/s$) (*Neugebauer and Snyder*, 1966). Studies that kinematically trace back solar wind parcels to their coronal sources confirm that the fast solar wind originates from the open magnetic field lines which expand to fill the heliosphere and define coronal holes (*Neugebauer et al.*, 1998). While the mechanisms that generate the slow solar wind are still debated, there is consensus that the source region is along the boundary separating open magnetic field lines from closed (*Neugebauer et al.*, 1998; *Einaudi et al.*, 1999; *Neugebauer et al.*, 2002; *Schwadron and McComas*, 2003; *Lapenta and Knoll*, 2005; *Antiochos et al.*, 2011; *Abbo et al.*, 2016; *Bale et al.*, 2019).

Competing theories for the source mechanism of the slow solar wind involve either rapid expansion of flux tubes or dynamical processes involving opening of closed magnetic field lines. The coronal hole boundary layer (CHBL) is the region separating open field lines from closed. The CHBL is characterised by rapidly expanding magnetic flux tubes, which decreases the pressure accelerating plasma and reduces the asymptotic velocity attained. The CHBL, jostled by the convective motions of the photosphere, may bring a closed magnetic loop in contact with an open field line of opposite polarity and drive interchange reconnection (*Crooker et al.*, 2010),

releasing new plasma into the solar wind. Interchange reconnection may explain the variability of the properties of the slow wind.

The heliospheric extension of the streamers delineate the polarity reversal of the open magnetic field lines; the Heliospheric Current Sheet (HCS). Globally, the idealized configuration results in high speed solar wind at mid and high heliographic latitudes and a band of slow solar wind tracing the heliomagnetic equator. If there is an offset between the rotation and magnetic axes, the heliomagnetic equator will be tilted with respect to the heliographic equator. Over the course of a solar rotation, an observer near the heliographic equatorial plane was predicted to observe two sectors of high speed streams and two sectors of slow wind, each of the later containing a crossings of the HCS.

Consistent with the tilted dipole solar minimum description, observations from the Wind spacecraft within the ecliptic plane, the plane of Earth's orbit around the Sun, suggested a two sector, four stream pattern (*Crooker et al.* (1996), see Figure 1.2). This pattern entails two crossings of the HCS per Carrington rotation. The four streams are composed of two encounters with the slow wind that encompasses the HCS and two encounters with low-latitude extensions of polar coronal holes. Each high speed steam was observed to have opposite magnetic polarity. The observed pattern repeated over several Carrington rotations, with minimal evolution, supports the slow evolution of coronal fields during solar minimum.

The solar minimum, dipolar configuration of the global coronal magnetic field is stable, typically long-lived, and evolves slowly as the Sun's differential rotation and convection winds up the interior magnetic field. The magnetic field twists and kinks, building complexity which become visible as sunspots on the photosphere. The complexity increases as the solar cycle winds up to solar maximum and then slowly dissipates with the episodic release of build-up magnetic energy and a reversal

of magnetic polarity at the geographic poles. A full cycle, simply called a solar cycle, has a period of roughly 11 years although there is much variability therein.

While the configuration of the corona is relatively simple at solar minimum, at solar maximum, the global magnetic field is frequently dominated by higher order magnetic moments. The open and closed field lines are distributed across all latitudes, such that source regions of both fast and slow solar wind are present at all heliographic latitudes. The complex and tangled magnetic configuration at solar maximum also evolves more quickly in time than at solar minimum, is susceptible to rapid reconfigurations, causing transient and abrupt releases of energy, such as CMEs. CMEs propagate through the heliosphere at high speeds, drive shocks, and are particularly effective at driving geomagnetic storms.

The focus of this dissertation is Stream Interaction Regions (SIRs), the second type of geoeffectvie structure in the solar wind. SIRs are present throughout the solar cycle and are the dominant drivers of geomagnetic activity during the declining and minimum phases of the solar cycle. SIRs are typically long-lived, large-scale structures. They are also important when considering the background solar wind through which CMEs propagate. Section 1.1.1 will discuss the general properties of SIRs and highlight some observational trends.

1.1.1 Stream Interaction Regions

SIRs are regions of increased dynamic pressure in the solar wind which occur when fast solar wind is radially aligned behind slow solar wind by solar rotation. Momentum is transferred from the fast wind, which decelerates, is compressed and heated. The slow wind ahead of the high speed stream (HSS) is accelerated and also compressed and heated. Hence, both solar wind that was originally slow and wind that was originally fast propagate at intermediate speeds, are compressed and heated, creating a region of high thermal pressure relative to the surrounding solar

wind plasma. The magnetic field is frozen-in to the plasma on MHD-appropriate scales and is swept up into the interaction region and is also compressed. Thus the region of high thermal pressure is also a region of high magnetic pressure.

in situ observations of SIRs in the ecliptic plane at 1.0 AU reveal common signatures in the large scale structure. The driver of the SIR is a rapid and significant increase in solar wind speed. Observed solar wind speed increases are usually on the order of a few hundred km/s (*Badruddin and Falak*, 2016; *Jian et al.*, 2006). Concurrent with the speed increase, an increases in solar wind density, temperature, and magnetic field strength are observed. A shear in the non-radial components of the solar wind velocity is also frequently observed (*Siscoe et al.*, 1969; *Gosling et al.*, 1978; *Richardson*, 2018)

In terms of large scale structure of SIRs, the initial conditions are set in the corona, where a source of fast wind is located near a source of slower solar wind. To zeroth order, the solar wind propagates radially outward. Solar rotation continuously aligns fast solar wind behind slow solar wind, such that the SIR forms a spiral pattern. The frozen-in magnetic field lines, each with one footpoint anchored on the Sun, trace a similar spiral pattern, the Parker spiral. SIRs begin forming as soon as fast wind catches up to the slow solar wind and since the field lines can't cross, the compression of plasma and increase in pressure becomes significant at heliospheric distances as small as 0.3 AU (*Richter and Luttrell*, 1986). With increasing distance from the Sun, the HSS continue to accelerate, compress, and heat the plasma, causing a pressure ridge that grows in amplitude. The SIR pressure ridge is aligned with the Parker spiral for a speed intermediate to the fast and slow solar winds.

Sources of fast solar wind are distributed over a range of latitude and longitude, and the resulting SIRs necessarily have 3D structure which reflect the rough shape of the source (*Pizzo*, 1982). A SIRs latitudinal extent will depend on that of the

HSS driving it. The degree to which the extent and shape of the source affects the resulting SIR is not fully understood since most observations are made in the ecliptic plane. Observations made by the Ulysses spacecraft (*Gosling et al.*, 1993; *Gosling and Pizzo*, 1999; *Riley et al.*, 1997) and a number of simulations (*Pizzo*, 1978, 1980; *Pizzo*, 1982; *Gosling and Pizzo*, 1999; *Riley et al.*, 2001) have allowed some insight. The shape of the latitudinal extensions of SIRs are understood in an idealized sense.

If, for example, the coronal configuration causes an idealized two-sector, four stream-type pattern (*Crooker et al.*, 1996), then the interface between the slow and fast solar wind is an inclined plane on a spherical surface which extends into a roughly planar SIR structure. This is shown schematically in Figure 1.2. SIRs driven by HSSs having more complex shapes are not well understood, particularly at high latitudes and will be addressed in Chapter 4. However the effects of more complex high speed streams on the evolution of SIRs in the ecliptic plane will be discussed qualitatively in Section 3.2.

SIRs are localized high pressure regions bound by a forward and reverse wave at all latitudes. The forward waves are characterized by an increase in solar wind speed concurrent with an increase in pressure while reverse waves are characterized by an increase in solar wind speed but concurrent with a decrease in pressure. If the gradient in speed occurs on size scales that are of order less than the gyro-radii of the particles, the waves are said to have developed into shocks (*Gedalin et al.*, 2016). The distance at which shocks form varies from SIR to SIR and the parameters which control the shock development are still poorly understood (*Jian et al.*, 2006, 2011; *Simunac et al.*, 2009).

The forward wave, assumed to be locally planar and aligned with the Parker spiral, propagates outwards through the advecting solar wind plasma. In the frame moving with the forward wave, the slow wind upstream is flowing supersonically

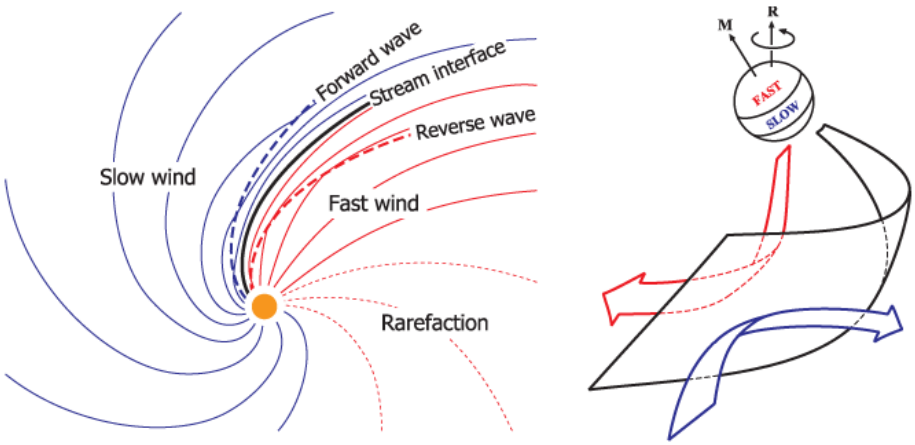

Fig. 1.2: Schematic of a canonical stream interaction region in the solar equatorial plane (left) and in 3D (right). On the left, the solar wind streams radially outward but the solar rotation, coupled with the frozen-in magnetic field, create the Parker spiral. Magnetic field polarity is shown in red or blue. The SIR develops where fast wind catches up to slow wind. It is bound by a forward wave on its leading edge and a reverse wave on it's trailing edge. The stream interface separates wind that was originally fast from wind that was originally slow. On the right, the difference between the rotation (R) and magnetic (M) axes are shown. The latitudinal tilt of the band of slow wind causes a SIR that is an inclined plane, shown in black as the tilted spiral surface. The red and blue arrows depict solar wind flow deflection in the plane of the SI.

sunward at an angle of $90° - \theta_{Parker}$ relative to the surface normal, where θ_{Parker} is the Parker spiral angle. The pressure gradient encountered by the slow wind decelerates and deflects the flow. If the forward wave has shocked, then the flow becomes subsonic across the shock. The angle between the upstream slow wind and the normal to the pressure gradient induces flow deflection in the direction of solar rotation in the azimuthal direction. Figure 1.3 shows the deflection of solar wind flow in a frame comoving with the forward wave.

The reverse wave also propagates through the plasma but moves sunward. In the frame moving with the reverse wave, the unperturbed fast solar wind flows supersonically into the reverse wave and is decelerated, deflected, heated, and compressed

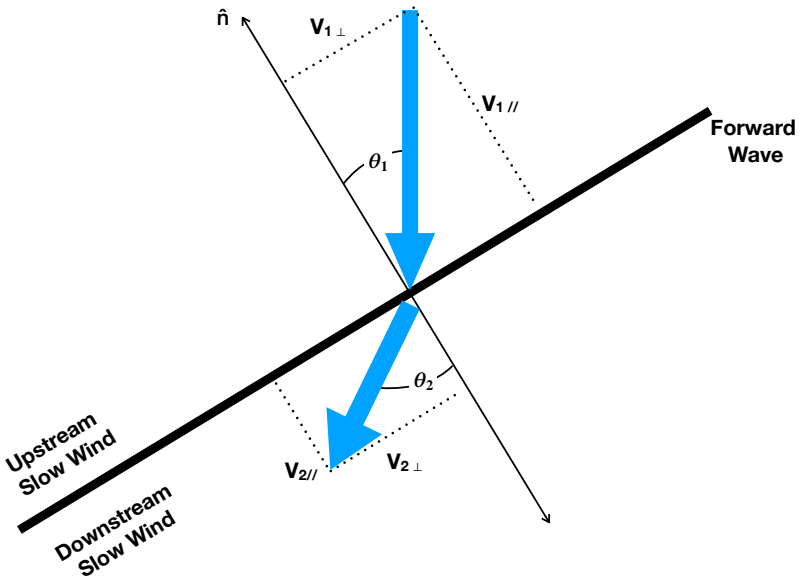

Fig. 1.3: Diagram of solar wind flow in a frame comoving with the forward wave. In an inertial frame, the upstream wind is the slow solar wind which is propagating radially outward. However, in the frame comoving with the forward wave, the upstream solar wind speed V_1 is supersonic and flows into the forward wave at an angle θ_1. The pressure gradient which defines the forward wave slows component of the flow parallel to the normal of the forward wave, $V_{1\|}$ but leaves the perpendicular component unaltered, resulting in a deflection of the flow direction downstream. The downstream flow, V_2 is subsonic and flows at angle θ_2 from the wave normal.

by the pressure gradient it encounters. The fast solar wind is deflected azimuthally in the direction counter to solar rotation. The deflections in the polar direction for both the forward and reverse waves depend on the latitudinal inclination of the high speed stream but are opposite each other for any particular high speed stream.

With increasing distance from the Sun, the forward and reverse waves propagate away from the SI, broadening the region of compressed plasma between them. In terms of the evolution of density and temperature with distance, the unperturbed solar wind expands adiabatically into the heliosphere such that the density scales

as r^{-2} and the temperature scales as $r^{-4/3}$ if the γ=5/3. When scaled by these factors, the heightened density and temperature within a SIR increase with increasing distance from the Sun, as the SIR is continually driven by the dynamic pressure of the HSS. This increase in pressure exerts a larger force and drives faster flow deflection. Hence, the SIR becomes increasingly pronounced as it propagates away from the Sun and the forward and reverse waves may evolve into shocks.

Located between the forward and reverse waves is the Stream Interface (SI), which separates solar wind that was originally slow from wind that which was originally fast. The wind on either side of the SI has intermediate speeds, having been either accelerated or decelerated. The configuration of the forward wave, SI, and reverse wave is shown schematically in Figure 1.4, obtained from an idealized simulation. The flow amplitude and direction in a frame comoving with the SI are also shown. Observationally, the SI is identified a few different ways (*Lazarus et al.*, 2003). Early observations by the IMP 6–8 spacecraft near 1 AU defined SIs as a discontinuous drop in density and a discontinuous rise in temperature occurring on the rising speed portions of high speed streams (*Gosling et al.*, 1978) but less than a third of SIRs contained SIs that satisfied these requirements. Another popular method of identifying the SI relies on the composition signatures of the solar wind on either side of the SI (*Wimmer-Schweingruber et al.*, 1997; *Crooker and McPherron*, 2012; *Zhao et al.*, 2009). The third method involves locating a sharp increase in specific entropy (*Siscoe and Intriligator*, 1993; *Lazarus et al.*, 2003; *Xu and Borovsky*, 2015). A fourth method for locating the SI is the location of the pressure maximum inside the SIR. *Crooker et al.* (2010) used the peak in magnetic pressure while *Jian et al.* (2006) used the peak in total pressure. One of most common methods to locate the SI is to identify the location of the null in azimuthal flow ($V_\phi = 0$) (*Gosling et al.*, 1978; *Crooker and McPherron*, 2012; *McPherron and Weygand*, 2006), separating

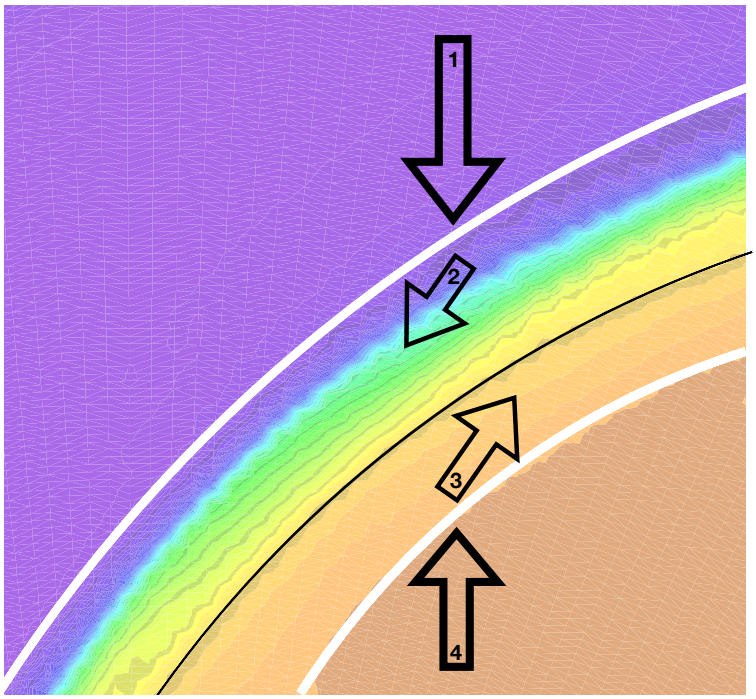

Fig. 1.4: Diagram of canonical stream interaction region in the solar equatorial plane (left). The colors represent v_r from the Slow Sine simulation in an inertial frame. Violet background represents slow solar wind (300 km/s), while orange represents fast wind (600 km/s). The stream interface is shown as a thin black line within intermediate solar wind speeds. The forward and reverse waves are shown as thicker lines, in the slow and fast wind respectively. The arrows show the flow speeds and directions in a frame comoving with the stream interface. The arrows are numbered in the order that a spacecraft would encounter the streams. Arrow 1 is upstream slow wind, Arrow 2 is compressed and deflected slow wind, Arrow 3 is compressed and deflected fast wind, and Arrow 4 is undisturbed fast wind. Bold type arrows, 1 and 4, are locally supersonic whereas arrows 2 and 3 are locally subsonic. If the Stream Interface is a true tangential discontinuity, there is is no flow across it.

regions of anti-parallel flow deflection in the azimuthal plane. A more stringent criterion is to find the maximum in vorticity along the spacecraft trajectory (*Borovsky and Denton*, 2010). Since the SI is theoretically present in all SIRs, other methods have been developed to identify the structure.

In addition to being used to identify the SI, the amplitude of flow deflection is frequently used to calculate the normal of the SIR, which is assumed to be roughly

plane parallel. The normal to the surface of the SIR has a predominantly azimuthal direction within 1.0 AU, following the winding of the Parker spiral. At 1.0 AU, the normal is oriented roughly 45° from the radial direction. At larger heliospheric distances, the normal becomes more and more aligned to the radial direction and SIRs become more tightly wound. The evolution of the SIR becomes more rapid as the expansion of the structure becomes aligned with solar wind flow. The forward and reverse waves typically develop into shocks beyond 1.0 AU (*Richter and Luttrell*, 1986). The steepening of SIRs continues to about 5.0 AU (*Siscoe and Intriligator*, 1993), much beyond which SIRs merge into each other and interactions between shock fronts cause destructive interference (*Provornikova et al.*, 2012). This thesis is predominantly concerned with the evolution of SIRs within 2.0 AU and the processes responsible for the steepening of SIRs.

While the general features of SIRs are known to consist of a region of compressed, heated plasma with intermediate speeds and exhibiting significant non-radial flow bound by forward and reverse waves, the particular characteristics of any given SIR vary. The amount of plasma compression, for example, typically increases with increasing heliospheric distance and is thought to depend on the magnitude of jump in speed (*Jian et al.*, 2011) but varies from SIR to SIR as observed at 1.0 AU.

Even for recurrences of the same high speed stream, which presumably would drive similar SIRs, characteristics such as the maximum density attained, timing of arrival, and orientation of the SIR normal differ (*Simunac et al.*, 2009; *Simunac et al.*, 2012). This is incongruent with the simplistic model of SIR evolution.

1.2 Magnetohydrodynamic Description

There exist multiple approaches with which we can learn about processes in heliophysical plasmas; from analytical theory to laboratory experiments, from *in situ*

measurements to computational modeling. The choice of approach is dictated by the problem being considered. The methods are motivated by the size and time scales of the phenomenon that is sought to be understood. SIRs and their evolution, the subject this dissertation, are large scale structures in the solar wind which contain physical processes on many scales, from bulk fluid flow to kinetic processes. The former scales are investigated in this dissertation, using magnetohydrodynamics. The magnetohydrodynamic (MHD) approach is used to characterise the structure of SIRs and their evolution. Section 1.2.1 presents the conditions in which it is appropriate to use MHD. Section 1.3 presents the specific MHD model used, namely the heliospheric adaptation of the Lyon Fedder Mobarry (LFM) MHD model, and details the way in which the LFM-helio is used throughout this dissertation.

1.2.1 Magnetohydrodynamics

Much of the matter in space exists in the plasma fundamental state of matter and the solar wind is no exception. A plasma is ionized gas in which ions and electrons, present in roughly equal quantities in a given volume, behave independently. The term *large scale* is relative in a plasma but generally refers to scales larger than the sphere of influence of any single charge. The radius of this sphere is the Debye length, defined as $\lambda_D = (\epsilon_o k_B T/ne^2)^{\frac{1}{2}}$, where ϵ_o is the permittivity of free space, k_B is the Boltzmann constant, T is the temperature of the particle, n is the number density and e is the electron charge. The plasma parameter, the number of particles within this sphere $N_D = (4\pi n {\lambda_D}^3)/3$, must be greater than one for the quasi-neutral, ionized gas to be an ideal plasma (*Kivelson and Russell*, 1995). In the solar wind, $N_D = 10^{10}$, which clearly satisfies the ideal plasma condition.

A second criterion for ideal plasma behavior is that the density of neutrals must be low enough that the collision frequency between charged particles and neutrals is small compared to the characteristic plasma frequency $\omega_s = (n_s e^2/\epsilon_o m_s)^{1/2}$ for

particle species s. For the solar wind, which is almost completely ionized and made up predominantly of protons and electrons, the plasma frequency depends on heliospheric distance since the unperturbed number density scales as the inverse square law. At Earth's orbit, during typical conditions, ω_e is $\approx \omega_e$=126 $krad/s$. Since the solar wind is primarily composed of protons and electrons, collisions with neutrals are rare. Collisions between charged particles will therefore be more frequent. Since the electron-electron collision time is 3×10^5 s, approximately 3.5 days, collisions between electrons are relatively infrequent and collisions with neutrals will be so infrequent as to be nearly negligible (*Kivelson and Russell*, 1995). The solar wind may hence be reasonably modeled as a collisionless ideal plasma.

The Sun's magnetic field dominates in the solar corona, and is pulled into the solar wind by the plasma outflow and permeates the heliosphere. Hence, the heliospheric plasma is threaded by a global magnetic field. Subject to external magnetic fields, charged particles undergo helical motion due to the Lorentz force. The presence of a magnetic field thus introduces two additional characteristic scales. The first is the time it takes a charged particle to orbit a magnetic field, the gyrofrequency, $\Omega = qB/m$, where q and m correspond to the particle's charge and mass respectively and B is the external magnetic field. The second is the gyroradius, or Larmor radius, of the charged particle's orbit around the magnetic field, $r_L = v_\perp/\Omega$. Typical gyroradii for protons in the solar wind near 1 AU is 80 km (*Kivelson and Russell*, 1995).

The solar wind is primarily composed of protons and electrons, a small fraction of helium nuclei called alpha particles, and trace amounts of highly ionized metals, such as oxygen, carbon, silicon, and iron (*Kivelson and Russell*, 1995; *Bochsler and Geiss*, 2013). As delineated in the previous paragraphs, the solar wind satisfies the criterion for an ideal plasma. The collision frequency criterion, when applied

to a magnetized plasma, implies that particles continuously orbit about a field line. Conversely, the field line is carried along by the particles that orbit it, essentially 'freezing-in' the magnetic field. Hence, on scales larger than Larmor radii, the magnetic field lines and particles move together.

When considering time and size scales much larger than those characteristic for individual particles, called kinetic scales, in an ideal magnetized plasma, it becomes impractical to consider each particle. A more appropriate description involves taking moments of particle distributions in order to describe the bulk properties of the plasma: namely the fluid description. Magnetohydrodynamics (MHD) include the bulk properties of the particle distributions and the effects of a large scale magnetic field. MHD is appropriate for size scales larger than particle gyroradii, for plasmas with a large enough N_D, and for time scales longer than the gyroperiod and plasma period. On large scales, particularly those used when characterising SIRs, MHD is indeed an appropriate approach and a powerful investigative tool.

The governing equations of MHD include the classical fluid formulations for the conservation of mass, momentum, and energy. Since the plasma is magnetized, versions of Maxwell's equations are incorporated. The following equations govern ideal MHD at the scales and processes considered in this dissertation. It is worth noting that the following equations assume that the plasma is a fluid composed of a single elemental species of particles, namely protons and electrons and that n_p=n_e. In the following equations, and throughout this dissertation, vector quantities are denoted in bold font.

The conservation of mass is stated in the continuity equation (Equation 1.1) which describes the density of the plasma as it flows. Here, ρ is the mass density, $\mathbf{u}$ is the center of mass velocity. The change in density in a given volume is the net result of the density flux flowing in or out of the bounding surface. Setting the right

hand side (RHS) of equation 1.1 to zero, as done here, implies that there are no sources or sinks of particles, thus mass is conserved. With its low collision frequency, this assumption holds in the inner heliosphere.

$$\frac{\partial \rho}{\partial t} + \nabla \cdot \rho \mathbf{u} = 0 \tag{1.1}$$

The momentum equation (Equation 1.2) shows the change in momentum density on the left hand side (LHS) and the force densities acting on the plasma on the right; here we include the gradient in thermal pressure, the Lorentz force, and contributions from external forces such as gravity. The Lorentz force depends on the magnetic field and the current density, j.

$$\rho \left(\frac{\partial \mathbf{u}}{\partial t} + \mathbf{u} \cdot \nabla \mathbf{u} \right) = \nabla P + \mathbf{j} \times \mathbf{B} + \rho \mathbf{F_g} / m_p \tag{1.2}$$

The thermal pressure is described using the ideal gas law, summed over the plasma's constituent species, as shown in Equation 1.3. Note we have included only protons and electrons in this formulation since the plasma is quasineutral. If the protons and electrons have the same temperature, then the constituent terms may be added to give the RHS of equation 1.3.

$$P = n_p k T_p + n_e k T_e = 2nkT \tag{1.3}$$

The conservation of energy in a fluid is given by Equation 1.4, where $\mathbf{E}$ is the electric field, $\mathbf{q}$ is the heat flux, and the internal energy of a mono-atomic plasma is $U = nNkT/2$, N is the number of degrees of freedom. Of these, only the heat flux is an independent parameter; it cannot be described with with previously defined variables.

$$\frac{\partial}{\partial t}\left(\frac{1}{2}\rho u^2 + U\right) + \nabla\cdot\left[\left(\frac{1}{2}\rho u^2 + U\right)\mathbf{u} + P\mathbf{u} + \mathbf{q}\right] = \mathbf{j}\cdot\mathbf{E} + \rho\mathbf{u} + \rho\mathbf{u}\cdot\mathbf{F_g}/m \quad (1.4)$$

In order to avoid introducing a governing equation for $\mathbf{q}$ explicitly, it is assumed that the entropy of a fluid element is constant. The system of equations is closed with the polytropic equation $P\rho^{-\gamma} = constant$, where γ is the polytropic index and is $\gamma = 5/3$ in three dimensional systems (*Kivelson and Russell*, 1995).

The divergencelessness of the magnetic field (Equation 1.5) states that the magnetic flux flowing into a closed surface must be equal to the flux flowing out of it or conversely, that magnetic field lines must eventually be closed.

$$\nabla\cdot\mathbf{B} = 0 \quad (1.5)$$

We next consider electric and magnetic field variations in time, using Ampere's Law (Equation 1.6) and Faraday's law (Equation 1.7).

$$\frac{1}{c^2}\frac{\partial\mathbf{E}}{\partial t} = \nabla\times\mathbf{B} - \mu_o\mathbf{j} \quad (1.6)$$

Since the solar wind is 3 orders of magnitude slower than the speed of light, the $1/c^2$ factor ensures that the LHS of the equation vanishes except in nearly relativistic phenomenon. Ampere's law in ideal MHD may then be restated as $\nabla\times\mathbf{B} = \mu_o\mathbf{j}$.

Faraday's law states that a changing magnetic field induces an electric field.

$$\frac{\partial\mathbf{B}}{\partial t} = -\nabla\times\mathbf{E} \quad (1.7)$$

This system of equations is closed by Ohm's Law (Equation 1.8) which relates the current to the fields via the conductivity constant σ.

$$\mathbf{j} = \sigma \left(\mathbf{E} - \mathbf{u} \times \mathbf{B} \right) \tag{1.8}$$

In ideal MHD, the conductivity may be so large it can be considered infinite. In this case, Equation 1.8 may be reorganized into $\mathbf{E}$=$\mathbf{u} \times \mathbf{B}$. A consequence of this reformulation, is that in the frame moving with the bulk plasma, $\mathbf{E} = 0$.

This set of ideal MHD equations describes the bulk motion of a quasi-neutral, mono-atomic species of plasma on large size and time scales. Though complete, this set of equations, for even a steady state solar wind, has proven difficult to solve analytically. As a result, several attempts at progressively more complex approximations of the solar wind have been put forth. Solving this system of equations analytically is only possible in highly idealized cases, often with reduced spatial dimensions, 1 or 2D for example, and for static systems. Even numerical approaches, though powerful, have had to use simplified systems to investigate the properties of the solar wind and the evolution of SIRs. Despite the simplifying approximations, important physical processes have been gleaned from these studies.

Hundhausen (1973) began with 1D hydrodynamic (HD) simulations of SIRs. Additional complexity was incorporated in Pizzo's three consecutive papers. *Pizzo* (1978) set the theoretical foundations for approaching the simulation of SIR evolution in the inner heliosphere while *Pizzo* (1980) and *Pizzo* (1982) dealt with the HD and MHD treatments respectively, for simple geometries of high speed solar wind sources. Since the 1980's, numerous simulation codes have been developed to model the solar wind and the inner heliosphere (eg *Odstrcil et al.*, 2004; *Riley et al.*, 2001; *Roussev et al.*, 2003; *Feng et al.*, 2010; *Odstrcil*, 1994; *van der Holst et al.*, 2010). Each takes different approaches and solves the system of equations with different numerical and computational tools.

This dissertation uses a particular model, the Lyon Fedder Mobarry heliospheric model (LFM-helio), to characterise the evolution of SIRs in 3D MHD with both highly idealized and realistic inputs at the inner boundary. The LFM-helio distinguishes itself from other models by being less numerically diffusive than other heliospheric models and as such, is a tool particularly well suited to addressing problems involving sharp boundaries and steep gradients, such as those found in SIRs. Indeed, the LFM was originally developed to study the terrestrial magnetosphere and designed to capture the physics of the bow shock (*Lyon et al.*, 2004). The LFM has successfully shed light on magnetospheric phenomena involving a range of types of discontinuities. The LFM-helio has been adapted to apply this powerful investigative tool to structures in the solar wind such as SIRs and the discontinuities therein. The nature of the discontinuities studied are described in Section 1.2.2. Details on the LFM-helio model are discussed in Section 1.3.

1.2.2 MHD Discontinuities and Shocks

Observations show that the solar wind is full of abrupt changes in plasma density, temperature, and speed as well as in magnetic field strength and orientation (*Belcher and Davis Jr.*, 1971; *Crooker et al.*, 1999; *Borovsky*, 2008; *Tsurutani et al.*, 2018). A change in one parameter may or may not be concurrent with others, may vary in magnitude, and duration. Such structures are classified as shocks and discontinuities; the specific classification depends on the conditions of the change. The word *abrupt* is relative and depends to some extent on the description of the plasma used. Theoretically, an abrupt transition is infinitely thin while in nature, an abrupt transition depends on the kinetic properties of the particles, such as mean free paths or gyroradii. In MHD models, abrupt refers to changes constrained within a simulation grid cell, which by condition of being MHD, will be much larger than kinetic scales. It is this last definition which is used throughout this dissertation.

Shocks are non-linear waves that have abrupt changes in parameters. They can be caused by obstacles in the solar wind flow, such as planetary magnetospheres, or large scale disruptions to the ambient plasma as is the case for ICMEs or HSSs. Shocks are non-reversible, entropy-increasing, dissipative waves propagating through the plasma at speeds faster than the critical speed at which information propagates. The critical speeds considered in MHD are the plasma sound speed, c_s, and the Alfvén speed, c_A. We define $c_s = \sqrt{\gamma P/\rho}$, where γ is the adiabatic invariant, and $c_A = \sqrt{B^2/\mu_0\rho}$.

There are a variety of MHD waves in an ideal plasma, driven by perturbations in plasma pressure, magnetic pressure, magnetic tension, or a combination of any of the above. Waves may be longitudinal, transverse, or both, and may propagate in any direction relative to the magnetic field. If the perturbations in plasma and magnetic pressures are coupled, the waves are said to be magnetosonic; fast-mode waves occur when the perturbations are in phase whereas the slow mode waves occur when the perturbations are in anti-phase. Waves will develop into shocks when the source of the pressure pile up accumulates faster than the waves can propagate the information away.

In the case of SIRs, the convergence of the fast and slow winds, both traveling at supersonic and super-Alfvénic speeds, create a pressure ridge, which may generate shocks which attempt to decrease the pressure gradient. The SIR compresses both the solar wind plasma and the magnetic field; the co-location of the high pressures causes a fast-mode wave or shock to develop. The forward shock expands into the preceding slow wind, and the reverse shock propagates Sunwards into the fast wind. In the frame of reference moving with the shock, shocks convert supercritical flow to subcritical flow.

Conversely, discontinuities, abrupt transitions in magnetic field or plasma properties, are non-compressive. Some discontinuities advect through the plasma, such as rotational discontinuities allowing for flow across the discontinuity, whereas contact and tangential discontinuities do not. The latter discontinuities often separate plasmas from distinct origins. On large scales, the SI in SIRs separates plasma that was originally fast from solar wind that was originally slow. On smaller scales, these discontinuities may separate individual flux tubes, which may map to granules or supergranules on the solar surface (*Borovsky*, 2008).

I have stated that there are several types of shocks and discontinuities in plasmas. The classification depends on the presence of flow across the boundary, whether plasma pressure is correlated or anticorrelated to changes in flow speed, and the orientation of the magnetic field relative to the interstitial surface. All types of discontinuities, however must satisfy the conservation of mass, momentum, and energy across the boundary in question. The conservation requirements puts constraints on how paramaters may change across the boundary. These constraints are expressed algebraically via the Rankine-Hugoniot (RH) relations.

In order to derive these, consider a steady-state, planar shock that is infinitely thin, with a normal in the $-\hat{\mathbf{x}}$ direction, as shown in Figure 1.5. In the frame of reference moving with the shock, the upstream plasma in region 1 flows into the shock with supercritcal velocity $\mathbf{v_1}$, and has density ρ_1, thermal pressure P_1, and magnetic field $\mathbf{B_1}$. The shock slows, compresses, and heats the plasma such that $\mathbf{v_2}$ is subcritical, $\rho_2 > \rho_1$, and $P_2 > P_1$.

The RH conditions are listed below; I clarify here some notation conventions. The square brackets indicate the difference between the upstream and downstream values. The subscripts n and t refer to vector components normal and tangential to the surface of the shock, respectively. Equation 1.9 is a consequence of the continuity

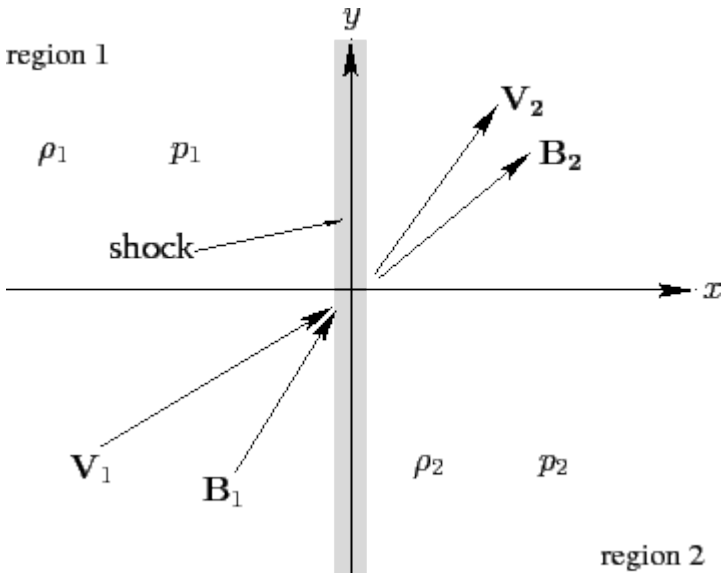

Fig. 1.5: Diagram of a planar shock, in the reference frame of the shock. The shock is infinitely thin in the y-z plane, with the shock normal oriented along $-\hat{\mathbf{x}}$. The upstream (region 1) plasma flows supercritically into the shock, $\mathbf{v_1} > c_{critical}$, with some density and pressure ρ_1 and p_1 and magnetic field $\mathbf{B_1}$. The flow on the downstream side (region 2) of the shock, $\mathbf{v_2}$, is subsonic and the $\rho_2 > \rho_1$ and $P_2 > P_1$.

equation (Eq 1.1). Since *in situ* observations are not made in either the rest frame of the solar wind or of the shock, this condition is frequently used to determine the speed of the shock.

$$[\rho u_n] = 0 \tag{1.9}$$

Equation 1.10 and Equation 1.11 are derived from the conservation of the momentum equation broken down into components normal and tangential to the shock surface.

$$\left[\rho {u_n}^2 + P + \frac{B^2}{2\mu_o}\right] = 0 \tag{1.10}$$

$$\left[\rho u_n u_t - \frac{B_n}{\mu_o}\mathbf{B_t}\right] = 0 \tag{1.11}$$

Equation 1.12 is derived from the conservation of energy and assumes an adiabatic equation of state.

$$\left[\rho u_n \left(\frac{1}{2}u^2 + \frac{\gamma}{\gamma - 1}\frac{P}{\rho}\right) + u_n \frac{B^2}{\mu_o} - \mathbf{u}\cdot\mathbf{B}\frac{B_n}{\mu_o}\right] = 0 \tag{1.12}$$

From Maxwell's equations, Equation 1.13 stems from the requirement that the magnetic field across the boundary is continuous whereas Equation 1.14 comes from Faraday's law, assuming a static $\mathbf{B}$. For ideal single-fluid MHD with isotropic pressure, the RH conditions uniquely determine the downstream state of the shocked plasma.

$$[B_n] = 0 \tag{1.13}$$

$$[u_n \mathbf{B_t} - B_n \mathbf{u_t}] = 0 \tag{1.14}$$

The first categorization of discontinuities depends on the flow across the shock surface. In general discontinuities have $u_n = 0$ while, necessarily shocks have $u_n \neq 0$. While there are many ways to satisfy the RH set of equations for either u_n, we focus here on those relevant to the discontinuities frequently observed in SIRs, namely forward and reverse shocks as well as tangential discontinuities.

Tangential discontinuities are characterised by $u_n = 0$ and $B_n = 0$. This means the discontinuity separates two plasmas of different thermal and magnetic pressures. Tangential discontinuities separate plasmas from different sources and as such are an accurate descriptor for the SI, which separates solar wind that was originally fast from coronal hole sources (*Krieger et al.*, 1973) from wind that was originally slow, from closed magnetic field regions such as streamers or pseudo-streamers (*Gosling et al.*, 1981; *Morgan et al.*, 2013).

Conversely, shocks are characterised by $u_n \neq 0$. Plasma flows into the shock at supersonic speeds, is decelerated and compressed. SIRs are bound by waves that steepen into shocks as the SIR propagates away from the Sun. A forward wave/shock, simultaneous increases in speed and pressure, bounds the leading edge and a reverse wave/shock, simultaneous increase in speed but decrease in pressure, bounds the trailing edge. *in situ* measurements show an increase in solar wind speed, density, pressure and magnetic field at the forward shock. The increase in magnetic pressure further categorizes this as a fast forward shock, corresponding with the magnetosonic fast characteristic wave mode. The observer would then pass through the SI and then the reverse wave/shock. The later consists of another increase in solar wind speed while the density, thermal pressure, and magnetic field decrease.

It is worth noting that the shock speed for the reverse and forward shock may not be the same, as the velocities and plasma characteristics on either side differ. Furthermore, these shocks propagate in opposite directions, effectively broadening the SIR. By contrast, the SI should be advected within the intermediate solar wind. In the reference frame moving with each shock, both shocks have supercritical inflow upstream and subcritical flow downstream. The downstream direction is within the SIR for both shocks. Passage through the shocks compresses and heats both the upstream slow and fast wind. The shock speeds which satisfy this have the forward wave propagating outward from the SI, away from the Sun. On the trailing edge of the SIR, the reverse wave propagates Sunwards, also away from the SI. Both shocks are fast.

There are two dimensionless parameters that characterise the strength of the shock - the compression ratio, which I'll denote as $r_{shock} = \rho_1/\rho_2$. The other is the Mach number; the ratio of the upstream solar wind speed to the characteristic speeds in the plasma. There are a number of characteristic speeds in a magnetized plasma,

such as the sound, Alfvèn, and magnetoacoustic speeds, and each has a corresponding Mach number.

1.3 Lyon Fedder Mobary (LFM) model

We now turn our attention briefly from the physical system being studied to the tool I have used to study it. The requirements for an MHD description to study SIRs has been presented in Section 1.2.1 and it has been argued that this is an apt descriptor for SIRs. I have studied these structures using a fully 3D, time-dependent, MHD model called the Lyon-Fedder-Mobarry (LFM) model, specifically its adaptation to heliospheric systems, the LFM-helio.

The LFM-helio, a MHD model of the inner heliosphere, is a version of the Lyon–Fedder–Mobarry (LFM) simulation code (*Lyon et al.*, 2004) adapted for heliospheric plasma and fields. The LFM-helio code uses the same numerical algorithms that underlie the conventional, magnetospheric LFM model, which was developed to study the interaction of the solar with the Earth's magnetosphere. As such, one of the distinctive features of the LFM model is its high resolving power. This enables the LFM to resolve MHD shocks and discontinuities in 1–2 simulation grid cells, a capability which distinguishes this model from other heliospheric MHD models. Its high resolving power makes the LFM-helio particularly well-suited to studies of SIRs and the evolution of discontinuities within them. The interested reader is referred to *Lyon et al.* (2004); *Zhang et al.* (2019) for the full description of the model's numerics but a brief description of the essential features will be given below.

One of the design choices made in building the LFM-helio was the implementation of a Total Variation Diminishing (TVD) numerical scheme. The TVD scheme is based on total plasma energy instead of primitive variables which allows for the resolution of discontinuities within 1-2 grid cells instead of 3-4 (*Lyon et al.*, 2004).

TVD schemes decide whether to use a high-order or a first order algorithm based on the local solution (*Lyon et al.*, 2004) and the "limiter" that is chosen. In the LFM-helio's case, this is the Partial Donor Cell Method (*Hain*, 1987). The Partial Donor Method is an aggressive limiter which, along with an 8th order TVD advection numerical schemes reduces the spurious extrema that are present in higher order scheme. Along with an 8th order numerical scheme, this improves the quality of the solution. It does so by allowing for high resolving power while minimizing spurious extrema that would be introduced when dealing with lower order schemes by setting a criterion for when to allow for diffusion and applying it only there.

The LFM was also designed with an adaptable grid that allows for higher spatial resolution in regions on interest, such as the bow shock. The only constraint on the grid of the version of the LFM used in this dissertation is that the cells be hexahedral. The simulations included in this dissertation involve a regular spherical grid. The LFM-helio is also a fully time dependent model but the simulations considered in this dissertation all have static input conditions that rotate, for an approximately steady state solution. Since SIRs are a relatively steady-state phenomenon, being prevalent on the declining phase of the solar cycle and at solar minimum when the global magnetic field evolves relatively slowly, this is an acceptable approximation.

In solving the MHD system of equations at each time step for each grid cell, taking differences of two large numbers may present numerical truncation issues which could have serious effects on the quality of the solution, particularly in situations where the physics is modified by the inaccuracy. One such case occurs while maintaining $\nabla \cdot \mathbf{B} = 0$. Some numerical schemes allow for a small, finite $\nabla \cdot \mathbf{B}$ and have found some small effects that are unphysical (*Powell et al.*, 1999; *Dai and Woodward*, 1998). Prioritizing $\nabla \cdot \mathbf{B} = 0$ was chosen as a design priority in the LFM-helio but achieving this with a TVD transport scheme with only cell-centered variables

makes this almost impossible (*Lyon et al.*, 2004). Instead, the Yee grid (*Yee*, 1966) is used, whereby the plasma n,$\mathbf{u}$, and P are defined at cell-centers but the magnetic flux is defined on cell faces and the electric fields are defined on the cell vertices.

Since the LFM-helio is an ideal MHD model, it solves the set of equations described in Section 1.2.1 although the equations have been reformulated in order to make them more numerically tractable, based on the considerations listed above. The form of equations solved by the LFM-helio is listed below.

$$\frac{\partial \rho}{\partial t} = -\nabla{\cdot}\rho\mathbf{u} \tag{1.15}$$

$$\frac{\partial \rho\mathbf{u}}{\partial t} = -\nabla \cdot \left(\rho\mathbf{u}\mathbf{u} + \bar{\mathbf{I}}P\right) - \nabla{\cdot}\left(\bar{I}\frac{B^2}{8\pi} - \frac{\mathbf{B}\mathbf{B}}{4\pi}\right) \tag{1.16}$$

$$\frac{\partial E_P}{\partial t} = -\nabla \cdot \left(\mathbf{u}\left(\rho u^2 + \frac{\gamma}{\gamma - 1}P\right)\right) - \mathbf{u} \cdot \nabla{\cdot}\left(\bar{I}\frac{B^2}{8\pi} - \frac{\mathbf{B}\mathbf{B}}{4\pi}\right) \tag{1.17}$$

$$\frac{\partial \mathbf{B}}{\partial t} = -\nabla \times (\mathbf{u} \times \mathbf{B}) \tag{1.18}$$

where

$$E_P = \rho u^2 + \frac{P}{\gamma - 1} \tag{1.19}$$

To solve these coupled PDEs, they are broken into their components and solved one direction at at time, which allows reuse of computational routines. The plasma and the magnetic field computations are handled by separate subroutines, for the cell centers and faces respectively. The workhorse of the code that does the numerical computing is written in Fortran and the code has been updated and runs in parallel. The simulation domain is divided between processors into spatial blocks of cells and solved separately, using the edges of the next region as a boundary condition.

The communication between cell blocks is done in OpenMP using Message Passing Interface.

Since the LFM-helio simulates supersonic solar wind, what is input at the inner boundary propagates out without having time to reverberate back towards the input conditions. The outer boundaries, both radially and in the polar direction, allow for outflow. The azimuthal boundary is periodic. As such, the inner boundary is a unique and important part of the code. The inner boundary condition of LFM-helio assumes supersonic and super-Alfvènic solar wind and thus must be located beyond these critical points in the solar corona. Since the numerical scheme is 8^{th} order in space, there must be four cells on either side of the boundary considered. This requirement is satisfied by the use of 4 ghost cells beyond the inner boundary.

The simulations in this dissertation were run on a regular spherical grid with the inner boundary located at 21.5 solar radii, $R_\odot$, (0.1 AU) and the outer boundary at 215 $R_\odot$ (1 AU) or 430 $R_\odot$ (2 AU), unless otherwise noted. The grid extends to 80° heliographic latitude, excluding a cone centered at each pole. As noted previously (*Pahud et al.*, 2012), this is not a fundamental limitation of the model. The magnetospheric version of the code spans the entire 3-D simulation domain and so does an upgraded version of LFM-helio (*Merkin et al.*, 2016a,b). The inertial coordinate system is used.

The version of the LFM-helio described above, with a regular hexahedral grid was used throughout this dissertation. Both realistic and idealized time-independent inner boundary conditions were used. The inner boundary conditions and validation will be discussed in Chapter 2.

The rest of the dissertation is structured as follows. Chapter 2 describes the procedure and inherent assumptions made in creating inner boundaries for realistic simulations of the solar wind in the inner heliosphere. A set of realistic inner bound-

aries is used to validate the LFM-helio model by comparing simulations with *in situ* observations, made by ACE and MESSENGER spacecraft in the ecliptic plane and made by the Ulysses spacecraft outside of the ecliptic plane. The sensitivity to the inner boundary is explored. It is shown that the LFM-helio reproduces the large and meso-scale characteristics of the solar wind in the inner heliosphere and that the global model results depend most strongly on the global distribution of magnetic field strength. This emphasizes the importance of accurately recreating the polar magnetic strength, which is difficult to measure from Earth, in synoptic maps. This becomes crucial in predicting the extent and timing of various solar wind streams.

Having validated the LFM-helio, Chapter 3 focusses on the evolution of SIRs and investigates the differences in SIR structure observed between solar cycle 22 and solar cycle 23. The observations of SIRs typically encountered in solar cycle 22, and previously in the space age, were consistent with SIRs being planar structures, driven by the fast wind originating from low-latitude extensions of polar coronal holes. SIRs in both hemispheres were tilted equatorward. Observations of SIRs during solar cycle 23 showed significantly less regularity in the pattern of meridional tilts, which has been attributed to the relative preponderance of equatorial coronal holes in this interval. Chapter 3 demonstrates the importance of latitudinal structure of HSS on the evolution of SIRs in the inner heliosphere. This is done by comparing the SIRs occurring in CR 2058 and CR 2060, which are driven by HSS with markedly different latitudinal structures. The distribution of CHs is not the only difference between the minima of solar cycles 22 and 23; not only was the solar wind more tenuous and cooler, but the strength of the magnetic field was significantly weaker than in previous cycles. The cases from Chapter 2 , which vary the parametric relationship between MHD parameters, are used to investigate the sensitivity of SIR evolution on the interrelationship between solar wind speed and the plasma parameters.

Chapter 4 attempts to exploit the numerical rigor of the LFM-helio numerics to study the discontinuities present in the solar wind. First, the SI is located within a realistic simulation and tracked using four definitions found in the literature. The null point in the azimuthal flow deflection of the solar wind at the SI is found to be the most reliable method at multiple distances within the inner heliosphere. We then attempt to locate Forward and Reverse shocks, as the exact location and timing of shock formation is still an open question. The parameters which have the strongest influence are also poorly understood. A number of idealized simulations are run in order to investigate the importance of global geometry and to simplify the problem, when in reality, there are likely multiple contributing factors.

Finally, Chapter 5 summarizes the results of the dissertation, contextualizes and extrapolates the results, and proposes some future work.

Chapter 2

LFM-Helio: Inputs and Validations

Global modeling of the solar wind generates a simulated state of the solar wind plasma everywhere in the solution domain at any given time. The comprehensive nature of simulated data, impossible to achieve with *in situ* measurements, facilitates the study of large scale solar wind phenomena. Single spacecraft measurements convolve spatial and temporal variations in heliospheric plasmas, resulting in difficulty detangling the advection from the evolution of structures. Combining data from multiple spacecraft allows some separation of temporal and spatial effects. The distance between the spacecraft determine an effective resolution.

In the solar wind, spacecraft anywhere other than at L1 have vast distances between them. This is not the case in the magnetosphere. Dedicated multi-spacecraft missions such as CLUSTER (ESA, (*Acuña et al.*, 1995)), THEMIS (*Angelopoulos*, 2008), the Van Allen Probes (RBSP, *Spence et al.* (2013), and MMS (*Fuselier et al.*, 2016). *Burch et al.* (2016) have attempted to separate temporal and spatial variations in the magnetospheric system. No such dedicated array of spacecraft has yet been launched into the solar wind. Despite this, studies have used opportune times of proximity or alignment of spacecraft to probe the spatial evolution of large scale solar wind structure. *Winslow et al.* (2016) used a longitudinal alignment of MESSENGER and ACE to study the interaction of CMEs and streams, *Phan et al.* used ACE and Wind observations to study the physical extent of reconnection X-lines near L1, and *Simunac et al* (2012; 2009), attempt to probe the smaller scale

time-dependent variations of SIRS whereas *Siscoe and Intriligator* (1993) used the much further separated IMP, Pioneer 10, and Pioneer 11 to determine the large scale structure, evolution and interaction of SIRs. However, these observations do not have the spatial and temporal resolution needed to unambiguously discriminate between evolutionary effects.

More success has been had using radial motion or alignment of spacecraft at greater separations in order to understand evolution of solar structures with increasing heliocentric distances. Evolutionary trends emerge (*Gosling et al.*, 1978; *Richter and Luttrell*, 1986; *Siscoe and Intriligator*, 1993; *Goldstein et al.*, 1996) but local evolution and causes of variability remain illusive. Global MHD models, in providing the state of the heliospheric plasma at all times over the simulations grid, are a useful tool for gleaning insight into the large scale phenomena, evolution, and variability of the inner heliosphere.

In order to understand the evolution of large scale structures in the heliosphere, the structures must be realistically simulated. A model's accuracy depends on the inclusion of the necessary and relevant physics and on the accuracy of the input at the inner boundary since heliospheric MHD models propagate these conditions outwards. As has been shown by (*Linker et al.*, 2010; *Riley*, 2007; *Pahud et al.*, 2012), the predictive capabilities of such models are limited by the accuracy of the input. Despite this limitation, for realistic input conditions, a model's ability to recreate conditions observed *in situ* can be a powerful diagnostic test. This important consideration will be discussed in this chapter.

If however, the goal is not to recreate the solar wind during a particular interval but to understand general phenomena, then simpler inner boundary conditions (IBCs) may be favourable. Indeed, such idealized models have provided much insight into the basic behaviour of the solar wind (*Parker*, 1958; *Hundhausen*, 1973; *Pizzo*,

1978). Idealized IBCs also lend themselves more easily to comparison with analytical solutions (*Lee*, 2000).

Both styles of IBCs are used in this dissertation. Realistic IBCs are discussed in 2.1 and idealized IBCs are included later in 2.1.4. The former is useful for validating model output via comparisons with *in situ* measurements while the latter allows for bridging the gap between analytical solutions and real measurements as well as evaluating the influence of various isolated parameters.

2.1 Realistic Inner Boundary Conditions

Running realistic simulations of the inner heliosphere with the LFM-helio requires realistic IBCs. Throughout this dissertation, the LFM-helio's inner boundary is placed at 0.1 AU. This choice is arbitrary other than satisfying the requirement that it be beyond the distance at which the solar wind becomes supersonic and super-alfvenic. Providing an accurate IBC requires a realistic representation of the coronal conditions at 0.1 AU, which are difficult to determine. *in situ* measurements have not yet been made, although Solar Probe Plus (perihelion 9.5 $R_{\odot}$, launch 2018 : NASA) will directly probe the coronal plasma. While easier to execute, remote measurements are necessarily integrated along lines of sight of optically thin coronal plasma. While tomographic measurements use solar rotation and deconvolution techniques (*Jackson et al.*, 2011; *Frazin and Janzen*, 2002; *Frazin*, 2000), the spatial and temporal resolutions are low. In lieu of direct measurements of the corona, it is easier to measure the bright photosphere and extrapolate outwards. Coronal models are constructed from photospheric data to provide the conditions at 0.1 AU. The following sections discuss this process.

2.1.1 Magnetograms

Magnetograms are full disk maps of the solar magnetic field at the photospheric surface. Synoptic map magnetograms are built up by combining successive measurements, taking advantage of solar rotation to scan through heliographic longitudes. Although vector magnetic field measurements exist (*Wiegelmann et al.*, 2012; *Hayashi et al.*, 2015), most magnetograms consist of line of sight magnetic field strength measurements. The magnetograms used in this dissertation use line of sight magnetic field measurements and are provided by the Kitt Peak National Observatory and the Global Oscillations Network Group (GONG). It is worthwhile to discuss how these synoptic magnetogram maps are constructed.

Full solar disk measurements of spectral line Zeeman splitting (*Title and Tarbell*, 1975) are taken throughout the day. As the Sun rotates, approximately 13.2°/day as viewed from the Earth, subsequent images have different heliographic longitudes at disk center, where the data are most reliable. The line of sight magnitude of the magnetic field is likely a large fraction of the actual magnetic field strength near the center of the solar disk. The images are remapped into longitude from the central meridian, shifted to the appropriate Carrington longitude, and added to previous images. Overlapping images are convolved with a $cosine^4(longitude)$ weighing function as swaths of heliographic longitude are stitched together. The weighing function ensures that the most weight is given to data at disk center. Over a Carrington Rotation (CR), defined as one synodic period of the sun and lasting 27.27 days, 360°longitude are observed and stitched together into a synoptic map. An example of a synoptic map is shown in Figure 2.1.

While line of sight synoptic maps are widely used, there are several assumptions built in to their construction that merit discussion. *Riley et al.* (2014) gathers and compares the different decisions made during the construction of synoptic maps at

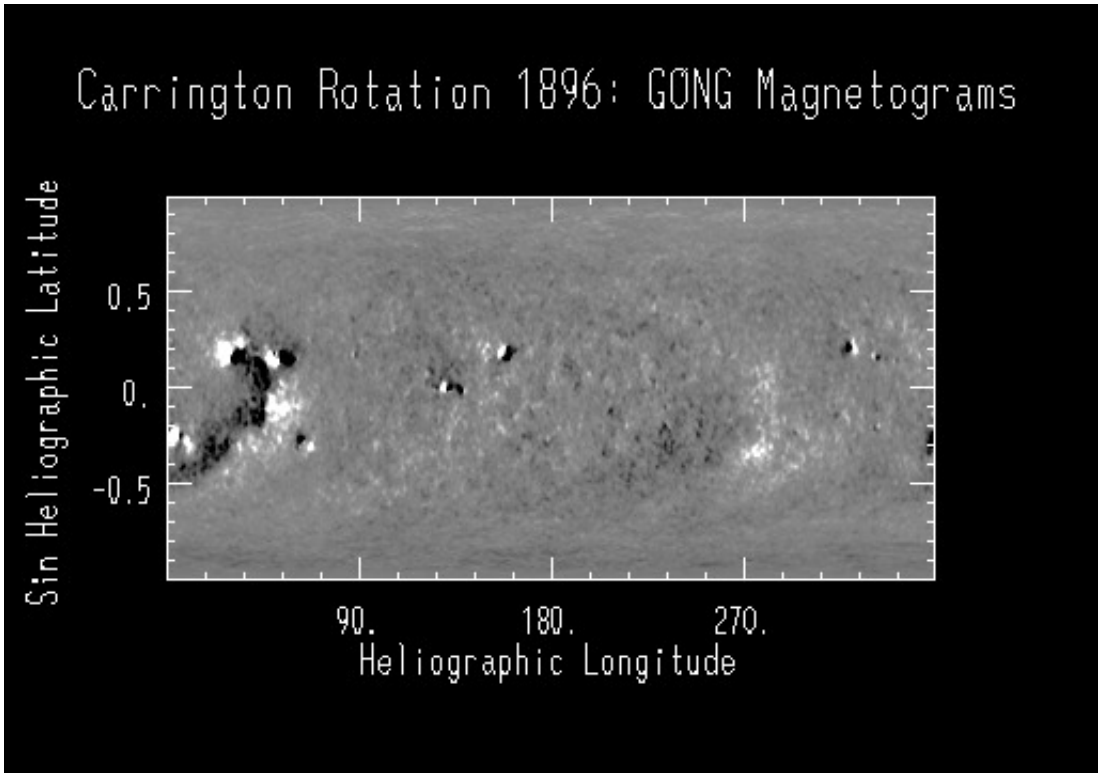

Fig. 2.1: Sample synoptic map showing the synoptic map of CR 1896 made by the Global Oscillation Network Group/National Solar Observatory/AURA/NSF. (http://gong.nso.edu/data/magmap/)

multiple observatories. While there are a number of significant differences, the important similarities are discussed here. The Zeeman splitting of spectral lines gives the line of sight magnetic field strength. This component is only a projection of the actual field strength, providing a lower limit and introducing a source of uncertainty. The magnetic field is frequently assumed to be radial to derive a field strength (*Riley et al.*, 2014). If the magnetic field is radial, the line of sight projection measures a large fraction of the total field strength near the center of the solar disk but this fraction decreases towards the limb. In building a synoptic map, the ambiguity of the eastern and western limb is reduced as the solar rotation brings different heliographic longitudes to disk center. Measurements of the magnetic field at the poles of the Sun, however, remain elusive. Polar field strength is frequently defined by fitting

an analytical function to lower latitude data and extrapolating to the poles. GONG, for example, uses a cubic polynomial fit at neighboring latitudes.

The construction of magnetograms further assumes a static magnetic field configuration. This assumption may be good during solar minimum on large spatial scales but does poorly during solar maximum. Even at solar minimum, the global magnetic field has some time dependence. By the time Carrington longitude 0°is measured, Carrington longitude 360°is 27.27 days old. This seam in longitude will have discontinuous segments and some data smoothing must be done. Another complicating factor is the differential rotation of the Sun. The Sun's sidereal equatorial rotation period is about 25 days while the polar rotation period is about 29 days. While all synoptic maps used in this dissertation use the static photospheric magnetic field approximation, new methods incorporating data assimilation, such as ADAPT (*Arge et al.*, 2010; *Merkin et al.*, 2016a) are beginning to address these effects.

Once the magnetic field strength and polarity at all latitudes and longitudes are populated, $\nabla \cdot B = 0$ must be enforced. While this must be true in nature, the time-dependence of measurements and errors introduced while reducing the data may introduce a flux polarity imbalance. Individual observatories use different methods to deal with each of the these issues and the resulting synoptic magnetogram maps may differ. Small differences in the maps produce differences in the subsequent coronal models which result in differences between heliospheric MHD models driven by them. This will be discussed in more depth in Section 2.2.2 and shown in Figure 2.8. Despite the differences in the resultant synoptic maps, all observatories produce a map of magnetic field strength over solar latitudes and longitudes that are frequently used to create coronal and heliospheric models that are accurate enough to reproduce many of the large scale structures observed in the inner heliosphere.

2.1.2 Coronal Models

Once the magnetic field over the full Sun is built up, the state of the corona must be determined in order to drive models of the inner heliosphere. The LFM-helio simulations included in this dissertation have an inner boundary at 0.1 AU and require the vector quantities of plasma velocity and magnetic field, as well as the scalar quantities of plasma density and temperature. There are traditionally two approaches to determining these parameters.

One approach, included for completeness but not used in this dissertation, is to simulate the corona with an MHD code (*Usmanov and Goldstein*, 2003; *Roussev et al.*, 2003; *Nakamizo et al.*, 2009; *Feng et al.*, 2010). This has been done many times with codes such as the MHD Around a Sphere (MAS) code (*Riley et al.*, 2001; *Owens et al.*, 2008; *Riley et al.*, 2006) and BATS-R-US (*Oran et al.*, 2015). These provide good qualitative agreement in terms of synthetic coronal observations at multiple wavelengths (*Downs et al.*, 2010), convolutions of plasma density and temperature as well as with white light corona images during eclipses (*Mikić et al.*, 2007).

An advantage of coronal MHD models is that they self-consistently solve for all required solar wind parameters. However if used, unretouched, to drive a heliospheric simulation, these coronal solution's parameters usually do not quantitatively reproduce the properties of the solar wind observed at 1.0 AU. Thus the parameters are typically tweaked (*Riley et al.*, 2001; *Owens et al.*, 2008). Another consideration is that they are computationally expensive and can be time-consuming to run.

The second approach, used frequently in the literature, is semi-empirical (e.g., *Detman et al.*, 2006; *Cohen et al.*, 2007; *Owens et al.*, 2008; *Merkin et al.*, 2011; *Pahud et al.*, 2012; *Wiengarten et al.*, 2013; *Shiota et al.*, 2014). Within this dissertation, the coronal model begins with a Potential Field Source Surface Model (PFSS) (*Arge and Pizzo*, 2000; *Arge et al.*, 2004; *Wang and Sheeley*, 1992). The PFSS uses spherical

harmonic fitting to the synoptic map data. It assumes that there are no volumetric currents and that all magnetic field lines are open and purely radial at a particular heliospheric distance, called the source surface. The PFSS model for the Carrington Rotations in this dissertation placed the source surface at 2.5 $R_{\odot}$. Beyond this distance, a single volumetric current is allowed, the Schatten current sheet (*Schatten*, 1972), separating magnetic field of opposite polarity. A meridional slice of a PFSS solution with and without the Schatten current sheet is shown in Fig. 2.2, from *McGregor et al.* (2008). The inner most circle represents the photosphere and the second circle depicts the source surface. The blue lines represent the PFSS solution over the entire radial domain. The red lines, by contrast, show the magnetic field lines when the Schatten current sheet is included. The Schatten current sheet extends into the heliosphere, where it is called the Heliospheric Current Sheet (HCS). A PFSS model below the source surface and a PFSS and Schatten current sheet beyond it are used in the Wang Sheely Arge (WSA) model, which in turn is used to drive the LFM-helio.

The WSA is an analytical solution that extends to arbitrary heliospheric distances. For use with the LFM-helio, the solution is truncated at 0.1 AU. At this distance the LFM-helio's inner boundary is beyond the critical point; the solar wind is supersonic and super-Alfvénic. The WSA however only provides the radial component of the magnetic field, B_r. To drive the LFM-helio all MHD variables need to be specified at 0.1 AU. Thus, the vector magnetic field, the plasma velocity, density and temperature are determined via empirical relations, observations at 1.0 AU mapped sunwards, and assumptions.

V_r is determined from an empirical relation that depends on both the expansion factor of magnetic flux tubes within the coronal solution (f_s) and the angular distance between the field line footpoint and the nearest coronal hole boundary (θ_b), as

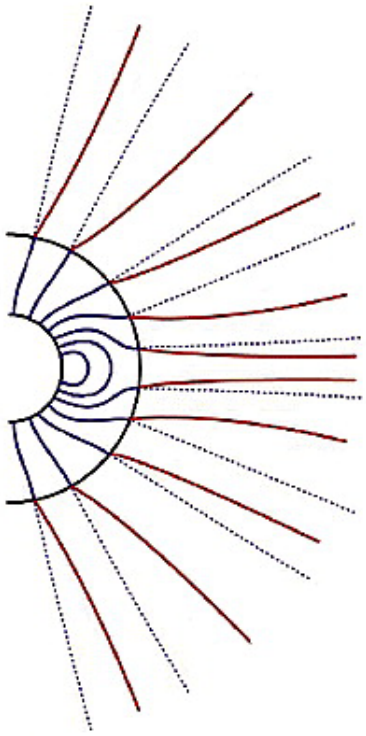

Fig. 2.2: From Fig. 1 in *McGregor et al.* (2008) showing a meridional slice of a PFSS solution in blue and the effects of including the Schatten Current Sheet (in red). The inner circle represents the photosphere while the outer circle represents the source surface.

described by *Arge et al.* (2004); *McGregor et al.* (2011a). Equation 2.1 quantitatively defines the empirical relation.

$$V_r(f_s,\theta) = V_0 + \frac{V_1}{\left(1+f_s^{2/9}\right)} \cdot \left(1.0 - 0.8\exp\left[-\left(\frac{\theta_b}{3.8}\right)^{3.6}\right]\right)^3 \tag{2.1}$$

where, in this dissertation, $V_0 = 200\ km/s$ and $V_1 = 750\ km/s$. The θ_b factor allows footpoints of field lines near a coronal hole boundary to be sources of slow solar wind, even if their expansion factor is small, while those which have footpoints well within the coronal hole generate fast wind (*Riley et al.*, 2011).

The boundary condition assumes corotation, such that the azimuthal component of the magnetic field is determined by $B_\phi = -(\Omega r_i \sin\theta/V_r)B_r$, where B_r and V_r

are the imposed radial components of the magnetic field and solar wind velocity respectively, obtained from the coronal model. The polar component, B_θ is set to zero at the inner boundary. r_i is the radius of the inner boundary, θ is the heliographic colatitude. Ω is the solar rotation rate. $\Omega = 2\pi/27.27$ days is the average synodic rotation period and $\Omega = 2\pi/25.38$ days is the average sidereal rotation period. Both were used in this dissertation and which was used for each run will be stated explicitly throughout. V_θ and V_ϕ are both set to zero at the inner boundary.

Once B and V are defined, assumptions must be made to assign the plasma number density and temperature at the inner boundary. As is done in other models (e.g. *Riley et al.*, 2001; *Pizzo*, 1982), the density is determined by assuming a scaling relation to solar wind speed, usually that fast wind is more tenuous than slow wind. Uniform momentum flux at the inner boundary is often invoked (*Riley et al.*, 2001) but we have instead used an empirical relation given by Equation 2.2 based on Helios data (*McGregor*, 2011; *Merkin et al.*, 2011; *Pahud et al.*, 2012).

$$n\,[\mathrm{cm}^{-3}] = 112.64 + 9.49 \cdot 10^7 \left(\frac{1.}{V_r\,[\mathrm{km/s}]} \right)^2 \tag{2.2}$$

The temperature is determined by invoking uniform thermal pressure at the inner boundary. Specifically, $n_0 T_0 = nT$, where $n_0 = 300\ cm^{-3}$ and $T_0 = 0.8\ MK$ are chosen for the fast solar wind, $V_r = 712\ km/s$. The temperature is then often obtained from thermal pressure balance over the inner boundary of the simulation (*Riley et al.*, 2001). We refer to this particular set of assumptions as the baseline. The LFM-helio's sensitivity to these assumptions will be discussed in Section 2.2.4. Once the plasma parameters have been defined at the inner boundary, these conditions are used to drive the global LFM-helio simulations of the inner heliosphere.

CR	Dates	Year	Observatory	Section(s)
1891	31/12–27/1	1994/5	Kitt Peak	2.2.4
1892	27/1–23/2	1995	Kitt Peak	2.2.4
1893	23/2–23/3	1995	Kitt Peak	2.2.4
1894	23/3–14/4	1995	Kitt Peak	2.2.4
1895	14/4–16/5	1995	Kitt Peak	2.2.4
2058	21/6–18/7	2007	Multiple	2.1.1
2060	14/8–10/9	2007	GONG	2.2.1
2068	20/3–16/4	2008	GONG	2.2.1

Table 2.1: List of Carrington Rotations, corresponding dates, and the sections in which the Carrington Rotations are discussed in this dissertation. Dates taken from $http://alpo-astronomy.org/solar/rotn_nos.html$ and synoptic maps input into the WSA model are taken from $https://www.nso.edu/data/historical-archive/$

2.1.3 Carrington Rotations

For realistic simulations, one Carrington Rotation is simulated at a time. Carrington Rotations have been standardized and catalogued (*Hill*, 2000). Carrington Rotation 0 (CR 0) began on October 13th, 1853. Each successive Carrington Rotation is recorded and numbered sequentially. Table 2.1 lists the Carrington Rotations used in this dissertation.

Figure 2.3 shows the inner boundary condition for CR 1892 and is representative of CR 1891–1895. These Carrington Rotations span from December 31st, 1994 to May 16th, 1995. This interval corresponds to the late declining phase of solar cycle 22 (*Gosling et al.*, 1995) and exhibits the characteristics expected of solar minimum. Namely, the solar magnetic field is dominated by the dipole moment, the magnetic and rotational axes are roughly aligned, and the evolution from one Carrington Rotation to the next is small. This magnetic configuration constrains high speed solar wind to high latitudes while the slow solar wind and the heliospheric current sheet undulate about the heliographic equator.

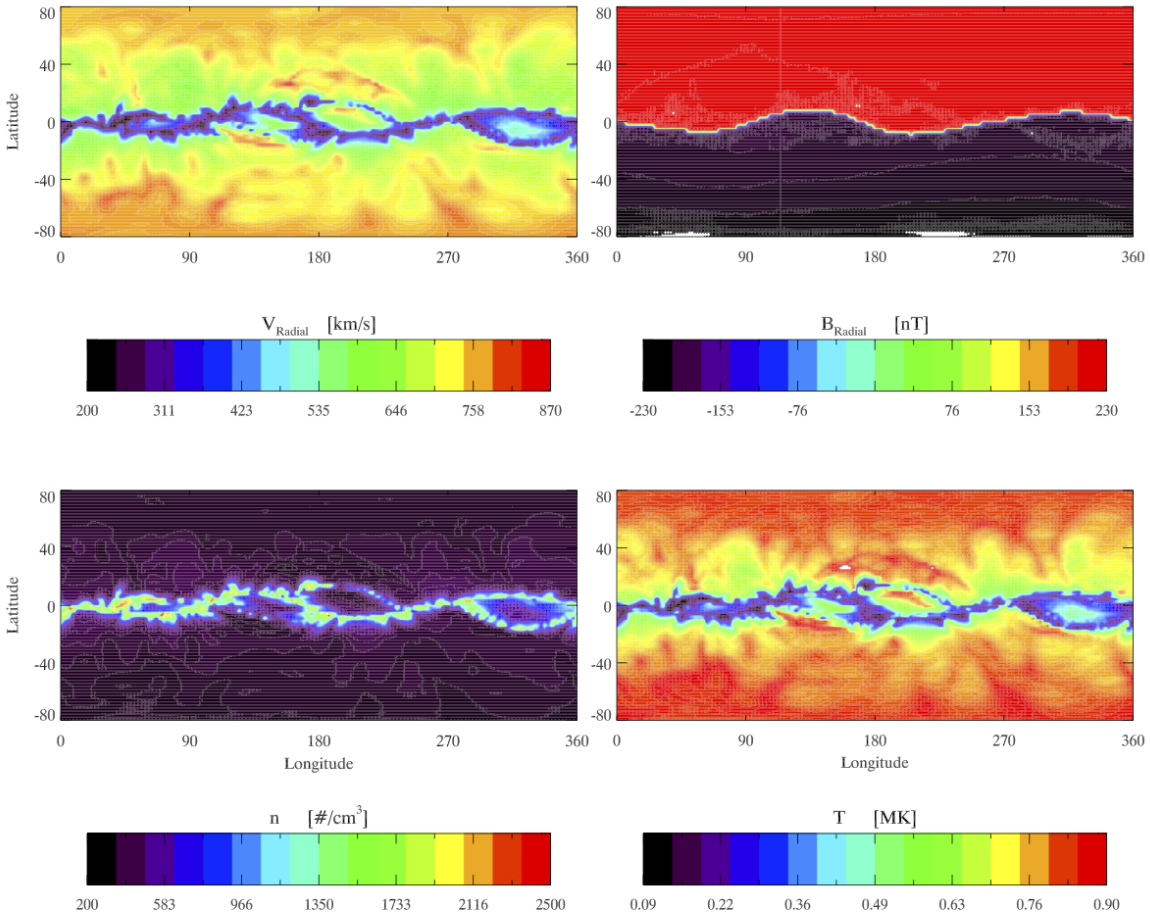

Fig. 2.3: Inner boundary condition for CR 1892.

The panels of Figure 2.3 show the radial component of solar wind velocity and magnetic field, the plasma number density and temperature at 0.1 AU clockwise from top left. Fast solar wind, with low densities and high temperatures, is constrained to high latitudes and is uniform, as expected. The magnetic field strength is uniform everywhere. The polarity reverses at the HCS. The HCS undulates about the heliographic equator and is embedded in slow, dense, and cool solar wind. Pseudostreamers, bands of slow wind that do not contain the HCS (*Wang et al.*, 2007;

Crooker et al., 2012; *Crooker and McPherron*, 2012; *Riley and Luhmann*, 2012), are present in the IBC.

While only CR1892 is shown, this interval is also representative of classical solar minimum conditions in its relative quiescence. The global structure of the solar wind changes slightly from CR1891 to CR1895 but the IBCs for each resemble each other, suggesting that large scale evolution is slow. This supports the assumption of a time stationary IBC, at least on large scales. This does not preclude smaller scale time dependent phenomena which may have an effect on comparisons with *in situ* measurements.

2.1.4 Idealized Simulations

While realistic boundary conditions are powerful tools for validating models, space weather predictions, and recreating complex space weather events, there is a lot going on. Another approach to understanding the evolution of the solar wind is to simplify the inner boundary to idealized conditions in a regime between analytical and realistic. This approach bridges the gap between analytic solutions and realistic models. The allow for incorporating complexity from simplifications necessarily made in analytic solutions such as reductions in spatial or temporal dimensions or oversimplification of spatial complexity. Experimental design of idealized 3D modeling allows for both 3D effects and temporal evolution while also allowing for isolation of parameters in a way that may not be separable or measurable in nature.

Indeed, idealized IBCs have frequently been used to deduce important characteristics of the solar wind (*Hundhausen*, 1972; *Parker*, 1958) and have been a useful tool for studying the effects of added complexity to models (*Pizzo*, 1978, 1980; *Pizzo*, 1982). While historically important, such idealized models are still useful and will be used throughout this dissertation. Four idealized IBCs are used in this dissertation and are described in detail in Chapter 4.

2.2 LFM-Helio Validation

There are multiple ways of validating a global MHD model such as the LFM-helio. While the magnetospheric version of the LFM has been in use for decades, it is worthwhile to validate the heliospheric adaptation. This may be done by comparing simulation results to analytical solutions, to simulation results from other models, and finally by comparing with *in situ* observations of the solar wind.

While all three will be discussed in this dissertation to varying extents, we begin with validation via *in situ* observations.

2.2.1 Comparison with in *situ* measurements

In this section, we do not pursue a particular scientific objective, rather, the goal is to subject the LFM-helio model to a validation exercise whereby the simulation results are compared with *in situ* data from the Advanced Composition Explorer (ACE), MErcury Surface, Space ENvironment, GEochemistry and Ranging (MESSENGER) and Ulysses spacecraft over the course of Carrington rotations 2060 and 2068, as well as CRs 1891–1895 respectively. All Carrington Rotations occurred during solar minimum, when the Sun was quiet and the inner heliosphere relatively undisturbed by transients. For each of the Carrington Rotations simulated, an inner boundary was created as described in Section 2.1. The LFM-helio was run to steady state over a simulation domain ranging from 0.1 AU – 2.0 AU, all 360°in longitude, and extending to ±80°. Data were extracted along the trajectory of the spacecraft in question and compared to *in situ* measurements. Sections 2.2.2 and 2.2.3 present and discuss the results of the model-data comparisons within the ecliptic plane and perpendicular to it, respectively.

2.2.2 In the Ecliptic

Results from the LFM-helio simulations for CR 2060 and CR 2068 afford a global view of the structure of the heliospheric plasma, flows and magnetic fields from 0.1 – 2.0 AU. This perspective of the solar wind helps to place *in situ* observations into a 3D context thus offering a more complete understanding of heliospheric processes. Figure 2.4 and Figure 2.5 provide an overview of simulation results for CR 2060 and CR 2068, respectively. Panels a) and b) in both figures show the distribution of the solar wind velocity and the radial component of the magnetic field at the inner boundary of the simulation (0.1 AU). Panels c) and d) show the same quantities at 1 AU heliocentric distance. In all panels, the HCS is shown as the iso-contour of zero radial magnetic field ($B_r = 0$). The solid black line shows the ACE spacecraft trajectory through the simulated heliosphere over the course of the Carrington rotation. ACE orbits L1, but since the Sun completes a full synodic rotation each Carrington rotation, the trace made by ACE appears to orbit the Sun.

The LFM-helio solutions at 1 AU reproduce the typically observed large scale characteristics of the solar wind during solar minimum: a relatively uniform, fast solar wind at high latitudes and a band of variable solar wind speed at lower latitudes. The slowest solar wind, in the vicinity of the HCS, undulates about the heliographic equator and extends to latitudes of up to $\pm$ 40°. This large scale behavior is imposed at the inner boundary by the coronal conditions obtained from the WSA model. The large scale structure corresponds to structure in the corona, although stream interaction regions develop self-consistently in the solar wind as do smaller-scale features, in particular in the HCS (*Merkin et al.*, 2011).

In CR 2060, the slow wind ($<$ 400 km/s, in blue) forms a narrow streamer band encapsulating the HCS but also bifurcates into pseudostreamers in a number of places, e.g. latitudinally extended "fingers" evident in Figure 2.4 at longitudes

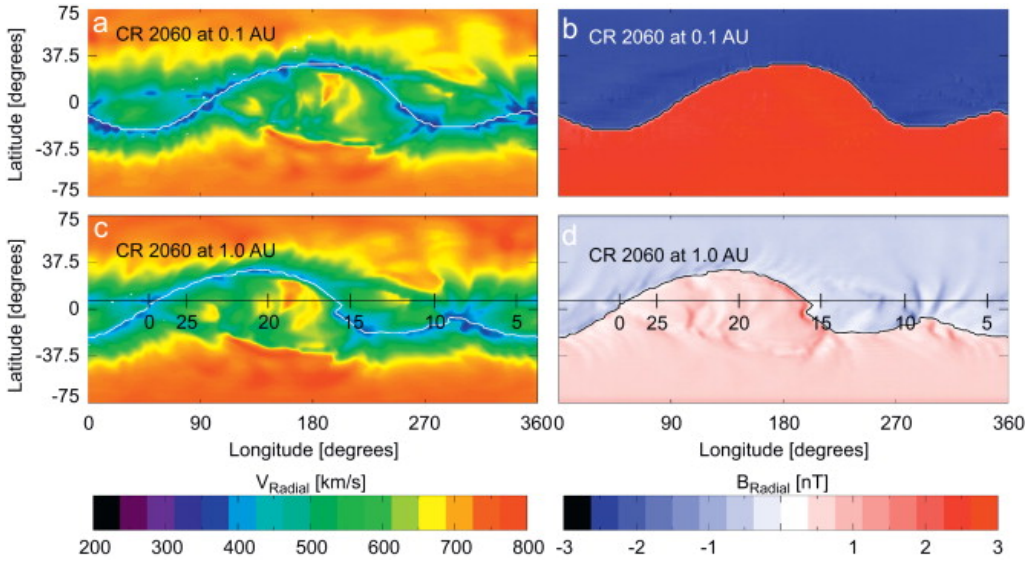

Fig. 2.4: Radial velocity (left) and magnetic field (right) at the inner boundary of the simulation at 0.1 AU (top row) and at 1 AU (middle row) for CR 2060. The HCS is calculated as the surface where the radial magnetic field vanishes and is shown as a white contour on the velocity panels (a) and (c) and black contour on the magnetic field panels (b) and (d). The ACE spacecraft trajectory is shown as a black line on the bottom panels (c) and (d), with days since the beginning of the CR indicated along the line.

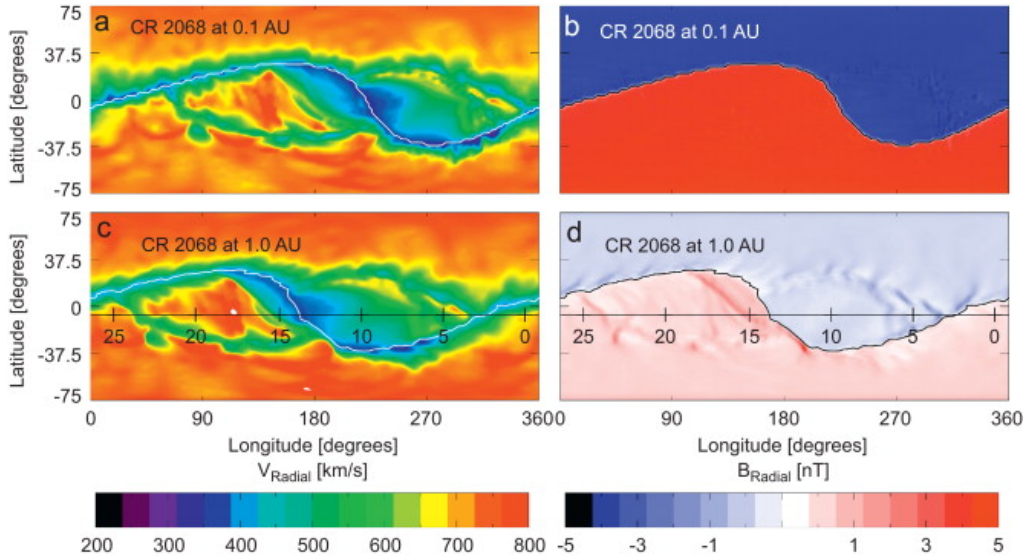

Fig. 2.5: Same as Figure 2.4 but for CR 2068.

315°–360°. For CR 2068, the slow wind streamer is quite broad relative to its size in CR 2060. An extended region of slow wind is present in the coronal solution (Figure 2.5 a), around 250° longitude and at 1 AU around 200° longitude. The low latitude high-speed streams differ between the two Carrington rotations. In CR 2068 the low latitude high-speed streams are faster, more uniform, and have a larger longitudinal extent. The large-scale high-speed stream covering a large portion of both Carrington rotations between 50° and 180° longitude appears to have persisted and intensified during the 6 months CR 2060 and CR 2068. The two streams also have different shapes of high speed stream fronts on the leading edge. Furthermore, the warp of the HCS is different between the two Carrington Rotations, changing with it the distribution of slowest streamer wind.

An important feature of the solutions, shown in panel b) of Figures 2.4 and Figure 2.5, is the strength of the magnetic field. The line of sight magnetic field strength is measured by the GONG observatory, concatenated into a synoptic map in order to create a coronal model. The radial field strength is obtained from the WSA solution at 0.1 AU is 60 nT and 80 nT for CRs 2060 and 2068, respectively. Using Parker's scaling relation, this gives 0.6 nT and 0.8 nT for the radial field at Earth, which is roughly a factor of five weaker than expected. While the source of this problem is unclear and may be associated with uncertainties in measurements of photospheric fields (*Riley et al.*, 2014; *Linker et al.*, 2017), we note that such low values of the magnetic field at the IBC will clearly affect comparisons of the LFM-helio magnetic field with ACE and MESSENGER measurements presented below.

The simulation-data comparisons for CR 2060 and CR 2068 focus on comparing the simulated solar wind velocity and magnetic field values with corresponding observations. Other MHD parameters, such plasma density and temperature, are strongly dependent on their specification at the inner boundary of the MHD simula-

tion. This specification relies on a number of assumptions used to derive the density and temperature from the velocity, which, in turn, is derived from the WSA magnetic field via an empirical relation (*Arge et al.*, 2004; *McGregor et al.*, 2011b) and will be discussed in Section 2.2.4. Due to this underlying uncertainty in the values of density and temperature, we concentrate here on velocity and magnetic field comparisons.

The global view in Figure 2.4 and Figure 2.5 contextualizes the configuration of the solar wind and facilitates comparisons between model results and *in situ* data, which for a single spacecraft provide the state of the solar wind at a point in space at a series of points in time. Figure 2.6 shows such time series obtained from the ACE spacecraft for the radial component of the velocity (a and b) and the radial component of the magnetic field (c and d). CR 2060 data are shown on the left column (a and c) and CR 2068, on the right, (b and d). Data from the ACE spacecraft is smoother 64 second resolution Level 2 data (*Stone et al.*, 1998). The ACE measurements are shown in black, while the LFM-helio simulated data are in red (radial velocity) and orange (magnetic field). For all panels, the x-axis shows the elapsed time in days, spanning an entire Carrington rotation. The spacecraft trajectory through the simulation is shown as the black line in the bottom panels of Figure 2.4 and Figure 2.5, also marked in days of the Carrington rotation. In order to obtain the simulation data along ACE trajectory, a virtual satellite was flown through the simulation domain and assigned the data, sampled on a cadence of about 10 min, from the grid cells where it was situated. The original data rates for ACE plasma and magnetic field measurements are of approximately one data point per 1 and 4 minutes, respectively. The ACE data is then resampled at a 10 minute rate, so as to agree with the virtual sampling cadence.

The ACE data for CR 2060 in Figure 2.6 shows two large high-speed streams, centered on days 14-15 and 20-21, and a third, less pronounced stream, centered on

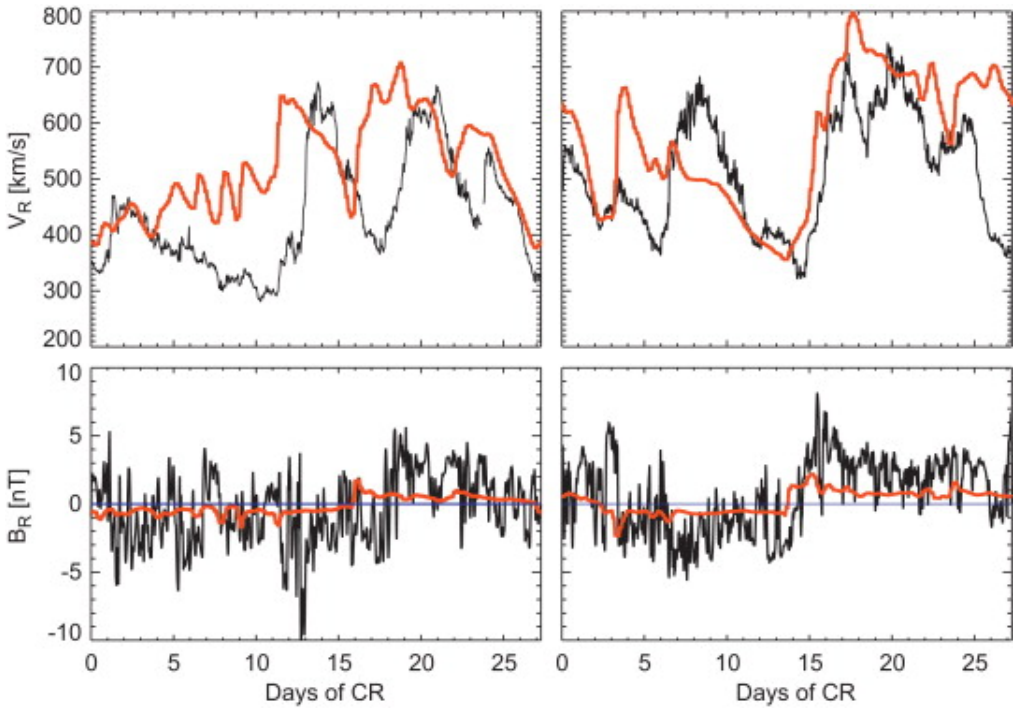

Fig. 2.6: Comparisons of the radial solar wind velocity (top row) and radial magnetic field (bottom row) between LFM-helio and ACE along the spacecraft trajectory. Both CR 2060 (left) and CR 2068 (right) are shown. *In situ* data are shown in black, while the model results are in red and orange.

day 24. The LFM-helio simulation reproduces all three streams with relatively good timing. Comparison with Figure 2.4 (panels c and d) reveals that the day 14 and day 24 streams, which appear as small yellow patches, are confined in space and a small error in their location or size in the simulation may lead to sizable discrepancy in a comparison with observations. Another interesting feature in Figure 2.6 is the double-peaked nature of the stream observed by ACE on days 20-21. The simulation clearly captured both of the peaks, and as shown in Figure 2.4 c), and this feature results from the bifurcated structure of the stream. The main discrepancy between the simulations and observations is the arrival times of fast streams at 1.0 AU; the simulated fast streams arrived at the ACE location approximately 2–3 days early. However, the steep rising slopes were captured well, indicating the compression re-

gions are reproduced by the LFM-helio. The trailing edges of the high speed streams are less steep and show better timing, indicating the rarefaction regions are also well reproduced by the model. Between days 4–11, the LFM-helio produces speeds that are 100-150 km/s too fast, on average. In addition, a number of pronounced oscillations are evident between days 5 and 10. Again referring to Figure 1c, it is obvious that the oscillations are due to the "fingers" of the slow wind (blue), also clearly present in the WSA solution at 0.1 AU (Figure 2.4 a).

The average and the maximum solar wind speeds are faster during CR 2068 than during CR 2060, in both simulations and observations. The observed high-speed streams also last longer than in CR 2060. The ACE measurements show two large streams having speeds greater than 650 km/s, centered on days 8 and 20 with a duration of approximately 5 and 10 days, respectively. The observed second stream reveals a complex three-peak structure. The simulation reproduces this second stream remarkably well, including the signature of the third peak observed on day 25. However, comparison with Figure 2.5 c shows that this third peak is actually not a part of the large-scale high-speed stream, rather, by day 25 the spacecraft has entered the high-speed wind from the southern coronal hole after passing through a band of slow wind on day 23. Unlike CR 2060, the double-peaked nature of the large-scale high-speed stream was not captured by the simulation in CR 2068. However, Figure 2.5 c reveals bands of variable speeds within the stream, suggesting that the two peaks could be caused by a slower wind band embedded within a faster flow, similar to CR 2060.

Overall, the LFM-helio reproduces the wind velocity distribution from day 15 through the end of the rotation, the simulated speed enhancement occurring only half a day before the observed arrival time. The first high-speed stream, however, is missed by the LFM-helio. The observations show a smaller velocity enhancement

with the peak speed of roughly 500 km/s observed on day 4. This enhancement is simulated, but with much higher maximum speed. Figure 2.5 c indicates the presence of a relatively small-scale high-speed stream that the virtual spacecraft passes through on day 4, which results in the peak on that day shown in Figure 2.6. The virtual spacecraft passes south of another stream between days 6 and 11. This could be the stream observed by ACE on day 8, suggesting that in reality this stream extended to lower latitudes.

Turning to the magnetic field comparisons (Figures 2.6c and d), we note that, given the lack of Alfvènic turbulence generated in the corona (e.g. Goldstein et al., 1995; Horbury et al., 2005) or transients of any kind in our specification of the inner boundary condition, the primary properties that allow a meaningful comparison with *in situ* data are the locations and timing of the major HCS crossings and the strength of the magnetic field. We note that results using the LFM-helio model suggest that, even in the case of smooth and static boundary conditions, simulations of progressively higher resolution may give rise to HCS structures self-generated in the solar wind (*Merkin et al.*, 2011). These structures, such as HCS folds and ripples, may lead to simulated sector boundaries separated in time by as little as 1 hour (or as little as the simulation resolution allows) in the vicinity of the HCS. Such multiple HCS crossings are also often registered by *in situ* spacecraft (*Blanco et al.*, 2006; *Neugebauer*, 2008; *Foullon et al.*, 2009).

We have noted above that we expect our simulation to produce radial field strengths significantly weaker than those observed due to the low field at the inner boundary of the simulation. Indeed, Figures 2.6c and d show simulated fields are about a factor of 3 lower on average than observed *in situ* ($\leq$ 1 nT vs. 3 nT). Small-scale variations are also missing, owing to the lack of transients and waves in the specification of the IBC; however, the model produces some variability although

not enough to result short duration polarity reversals. During each of CR 2060 and CR 2068, both simulated and *in situ* data contain two large-scale HCS crossings along the ACE trajectory.

For CR 2060, ACE observed sector boundary crossings on day 18 and again on day 27, while these occurred in simulations on days 16 and 27, respectively. The second crossing is captured exactly by the model, although this same crossing was also registered by the spacecraft on day 1 indicating that the HCS either moved over the course of the rotation or had fine scale structure. The timing of the other crossing is approximately two days early in the simulation. Comparisons with panel (a) shows that in both the observations and simulation the HCS crossing coincides with a minimum in velocity, again displaced by about 2 days. This difference is probably related to the high-speed stream in the model that occurred somewhat earlier (its westward edge being to the west/to the right in Figure 1c) than in reality. During CR 2068, ACE observed magnetic sector crossings and velocity minima on days 3 and 14. LFM-helio reproduced both HCS crossings and velocity minima to within one day of the observations. This better agreement correlates with the better prediction of high speed streams during this rotation.

Global models such as LFM-helio allow tracking of solar wind plasma and magnetic field as they evolve with the radial distance from the sun. While the accurate timing is an important aspect for predicting solar wind conditions at Earth, reproducing the correct interrelations between changes in plasma speed, density, and magnetic field is an important rubric for accurately simulating the physics taking place. It is then a useful exercise to examine the properties of our numerical solutions and assess their validity at different heliocentric distances. The MESSENGER spacecraft allows an excellent opportunity for such an evaluation of the simulated magnetic field; unfortunately the availability of MESSENGER solar wind plasma data is limited during

these Carrington Rotations since the spacecraft was in its cruise phase as it traveled towards Mercury.

At the beginning of CR 2060, MESSENGER was at a radial distance of 0.45 AU from the Sun, reached perihelion at 0.33 AU, and at the end was at a distance of 0.37 AU. During this interval, MESSENGER's heliographic latitude increased from -0.3° to 3.1° at perihelion, then decreased to 2.3°. Its heliographic longitude ranged from 6.9°, through 360° down to 121.6° due to the rotation of the sun and the orbital motion of MESSENGER. Conversely, for CR 2068, MESSENGER was at aphelion. Its radial distance from the Sun began at 0.69 AU, reached aphelion at 0.70 AU on day 4 of the Carrington rotation and decreased to 0.66 AU by the end. MESSENGER's latitudinal motion began at a heliographic latitude of -3.2°, decreased until aphelion at -3.3° and increased to -3.0° at the end of the Carrington rotation. MESSENGER spanned from 44.2°, through 360° to 58.1° heliographic longitude.

During the cruise phase, the MESSENGER magnetometer instrument (MAG) (*Anderson et al.*, 2007) was turned on only for segments of the Carrington rotations and cruise phase data were provided via private communication (D. Gershman) MESSENGER data are now situated at *Planetary Data System* (2016). In Figure 2.7, we plot the available *in situ* MESSENGER magnetic field data in black for CR 2060 (a) and CR 2068 (b). The LFM-helio simulated results along the spacecraft trajectory are shown in orange. As with the ACE comparisons, the LFM-helio underestimates the magnitude of the radial magnetic field. For CR 2060 and CR 2068, the average strength of the magnetic field observed by MESSENGER is 12 nT and 6 nT, respectively. Note that the spacecraft was further from the sun during CR2068, so that, despite the stronger coronal field, the measured field at MESSENGER was weaker than in CR 2060. The average magnitude of the simulated magnetic field is 4 nT for CR 2060 and 2 nT for CR 2068, a factor of about 3 weaker than observed.

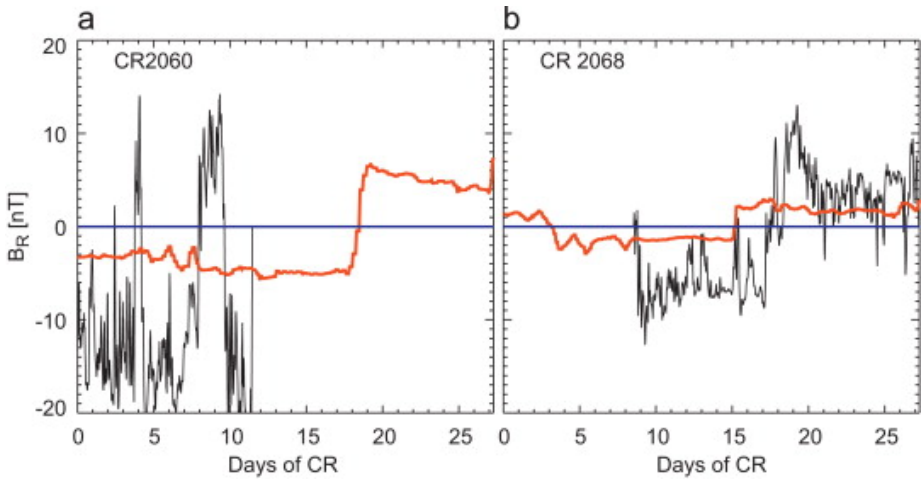

Fig. 2.7: Comparisons of the radial magnetic field between LFM-helio and MESSENGER along the spacecraft trajectory. Both CR 2060 (a) and CR 2068 (b) are shown. Observations are shown in black, while the model results are in orange.

In the 12 days of MESSENGER magnetometer data coverage for CR 2060, there are four magnetic sector crossings but most of the measurements show a negative polarity. The simulated data span the whole Carrington Rotation and show some fluctuations of the field corresponding to the observed short-term polarity reversals, but no reversal actually occurs. The switching of polarity on day 20 in the LFM-helio occurs when there is no MESSENGER data.

MESSENGER magnetic field data coverage for CR 2068 is more complete. *In situ* data show one major crossing of the magnetic sector boundary on day 18, which is reproduced by LFM-helio 1-2 days earlier. This agrees with the ACE comparison (Figure 2.6 d), where the HCS crossing also occurred in the simulation earlier than observed. The model results also show another crossing on day 4 (expected to occur based on Figure 2.6d), which cannot be confirmed by MESSENGER due to the lack of data.

For comparisons between simulations and observations, the primary question that arises is whether one learns something about the solar wind model or about

its IBC. For instance, the magnetic field comparisons with ACE and MESSENGER (Figure 2.6 c,d and Figure 2.7) demonstrate that the magnetic field in the solar wind model is too low, but it is a direct consequence of the coronal field from the WSA being weak at the inner boundary of the simulation which, in turn, is likely a consequence of uncertainties in measurements of the photospheric field, particularly, when it is weak. The scaling of the simulated field with radial distance from 0.1 AU to MESSENGER and then to ACE indicates that the MHD model correctly propagated what was input.

Further, in order to quantify the comparisons, i.e. whether they are "good" or "bad" and to what degree, one needs to have a sense of intrinsic uncertainties that are associated with these simulations. Figure 2.8 shows three LFM-helio calculations differing only in the observatory that constructed the synoptic magnetogram map used to in the WSA model, and provides a sense of error (*Pahud et al.*, 2012). This is sufficient to make our point: discrepancies between MHD simulations using IBCs generated using different observations of the photospheric magnetic field can be larger than the deviation of any given simulation from observations. Moreover, the same observatory can yield a better result in one instance, and worse in the other (*Bale et al.*, 2019). In this view, discrepancies between LFM-helio and ACE and MESSENGER observations shown in Figure 2.6 and Figure 2.7 lie well within the range of possibilities, and we conclude that our simulations produce a faithful representation of their coronal boundary conditions.

It is also worth noting that for the specification of our inner boundary condition we used stationary Carrington maps from the WSA model. Daily updated maps or more elaborate approaches including evolution of the field, such as the Air Force Data Assimilative Photospheric flux Transport (ADAPT) (*Arge et al.*, 2011), would likely result in significant improvement of data-model comparisons.

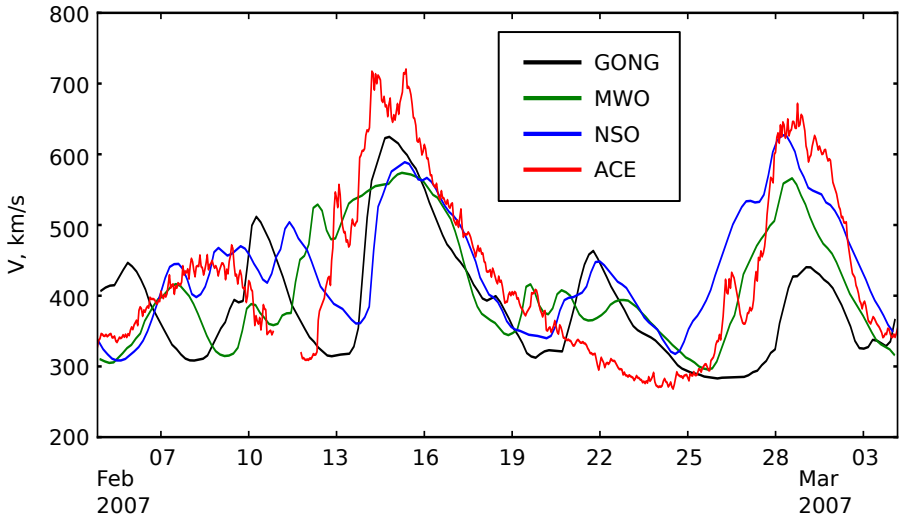

Fig. 2.8: ACE measurements of solar wind speed at L1 are shown in red, while three LFM-helio solutions are shown for the corresponding time period. Each solution corresponds to a different solar observatory, whose magnetogram product has been input into the WSA and the LFM-helio. Results fromt he GONG magnetogram are shown in black, those from MWO are shown in green, and those from the NSO are shown in blue. This gives a sense for the range of possible solution depending on the input magnetogram. Figure from *Pahud et al.* (2012).

One might wonder as to the value of such data-model comparisons if they inform us more about the particular specification of the coronal boundary condition than the solar wind model itself. There are a number of reasons these validation exercises are important. First, they provide a zeroth order quality check: whether major streams are reproduced, whether major sector boundary crossings are captured, etc. Secondly, the fact that a given solar wind model leads to significantly different results dependent on the coronal boundary condition does not mean that different solar wind models will produce the same result when given the same boundary condition. *In situ* measurements provide a baseline for such comparisons.

Finally, results presented here are only the first step toward more realistic modeling of the solar wind on smaller scales, particularly, during solar minimum. Higher resolution simulations (*Merkin et al.*, 2011) have shown the formation of

self-generated meso-scale structure in the solar wind not present in the laminar, smooth coronal boundary. Direct comparisons of such structures with *in situ* observations are not feasible, but climatological studies to this end, using statistical and spectral methods, have proved useful in magnetospheric research (*Guild et al.*, 2008a,b), and will undoubtedly benefit the field of inner heliosphere modeling as well (*Murray*, 2018).

Overall, these results give us confidence that the LFM-helio reproduces the state of the solar wind in the inner heliosphere near the ecliptic plane with some fidelity. It is useful to validate the LFM-helio simulations out of the ecliptic as well. We have done so in Section 2.2.3 by comparing LFM-helio simulations with observations from the Ulysses spacecraft, whose orbital plane is roughly perpendicular to the ecliptic.

2.2.3 Out of the Ecliptic

In this section, results from the LFM-helio for CR 1892 are shown and compared to *in situ* data from the Ulysses spacecraft, whose orbit is inclined nearly perpendicular to the ecliptic plane, in order to validate LFM-helio simulation results at latitudes beyond the ecliptic. Ulysses' perihelion is at 1.4 AU, so the simulation is run out to 2.0 AU in the radial direction. The inner boundary is constructed in the same way as in previous sections and a virtual spacecraft is flown through the simulated heliosphere. The simulated and observed data are compared.

Figure 2.9 shows v_r (a) and scaled B_r (b), $log_{10}(n)$ (c) and $log_{10}(T)$ (d) for CR 1892 at 0.1 AU and at 1.41 AU (e–h) as a function of latitude (-75° to +75°) versus longitude (0°– 360°). CR 1892 is qualitatively representative of CR 1891–CR 1895 spanning Ulysses' Fast Latitude Scan (FLS). Panels (e–h) show the solar wind at 1.41 AU, Ulysses' mean heliocentric distance during its FLS. The magnitude, shown by color, is indicated in the adjacent colorbars.

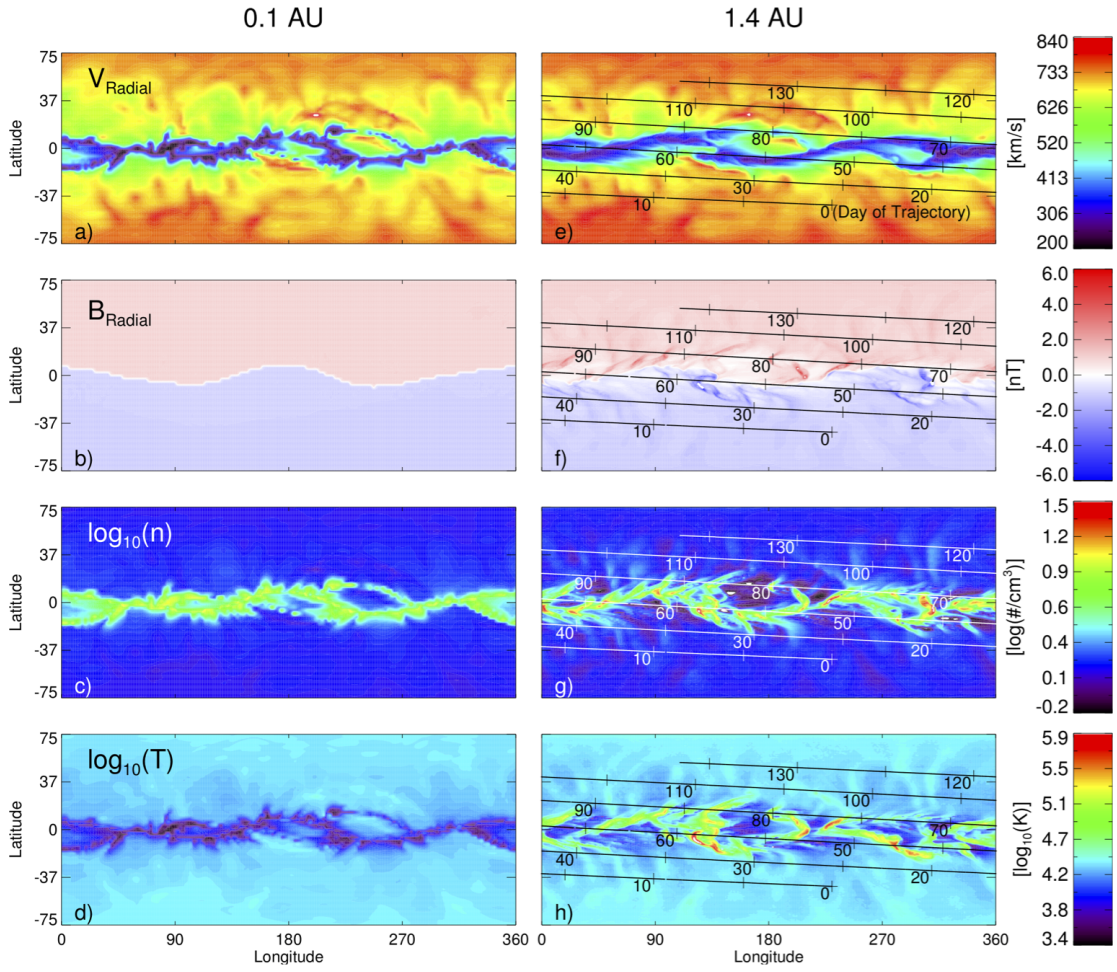

Fig. 2.9: Latitude-longitude plots of the LFM-helio solution for CR 1892, at the inner boundary (0.1 AU, left column) and at 1.41 AU (right column). Panels show the radial component of the solar wind velocity (a, e) and of the magnetic field (b, f), the logarithm of the plasma density (c, g) and of the plasma temperature (d, h). The black/white line indicates the projection of the Ulysses trajectory onto a spherical shell of radius 1.41 AU for all five Carrington Rotations. The tick marks denote five day intervals. Day 0 corresponds to the first day of CR 1891. The density and magnetic field have been scaled by r^{-2} and the temperature by $r^{-4/3}$ at the inner boundary to allow for the color scales to correspond to values at 1.41 AU.

Panels a) and e) of Figure 2.9 show that the simulated global structure of v_r is consistent with data from Ulysses' first FLS (*McComas et al.*, 1995). High latitudes are populated by high speed solar wind (red), while mid- and low-latitudes contain a band of slow solar wind (blue/black), interspersed with higher speed plasma, producing a latitudinal extent of variable solar wind speed. The band of slow wind undulates about the heliographic equator and is bifurcated over much of its extent. B_r, shown in b) and f), is scaled by r^2 so that the plots share a color bar. Outward directed magnetic field is shown in red while inward directed magnetic field is shown in blue. The white line separating inward magnetic field from outward magnetic field represents the HCS, the reversal of magnetic polarity embedded in the band of slow wind. The bifurcated branches of slow wind not containing the HCS are heliospheric extensions of coronal pseudo-streamers (*Riley and Luhmann*, 2012; *Crooker et al.*, 2012). Panels c) and g) show the logarithm of density scaled by r^2 and panels d) and h) show the plasma temperature scaled adiabatically as $r^{4/3}$, assuming the adiabatic index γ=5/3. Since semi-empirical relations based on solar wind speed determine the plasma density and temperature at the inner boundary, the slow wind is dense and cool while the fast wind is tenuous and hot.

Figure 2.9 shows that the large scale structure in v_r input at the inner boundary, such as the shape and latitudinal extent of the slow wind band, remains at 1.41 AU. The effects of dynamical evolution caused by the solar wind streams of different speeds interacting are most apparent in panels f),g), and h). Towards the right in this figure, solar rotation radially aligns solar wind of different speeds and creates SIRs (*Gosling and Pizzo*, 1999). When slow wind precedes fast wind, the latter compresses and heats the plasma ahead of it, forming a pressure ridge which accelerates the slow wind and decelerates the fast wind. If fast wind precedes slow wind, a rarefaction region forms and the slow, dense wind accelerates into the evacu-

ated region behind the high speed stream. Features at 1.41 AU are easily understood when these dynamics are taken into account.

Magnetic field, plasma density and temperature at high-latitudes remain uniform to 1.41 AU due to relatively uniform solar wind speeds there. In contrast, at heliographic latitudes between -40° (south) and 40° (north) the variability in solar wind speed has caused numerous SIRs. The magnetic field has developed localized intensifications (saturated color) generally corresponding with the compressed and heated plasma (yellow and red), qualitatively consistent with the frozen-in conditions and the Rankine-Hugoniot conditions for ideal MHD. Conversely, rarefaction regions are tenuous, cool, and have low magnetic field strength. Stream interactions have also introduced meso scale structure to the HCS, which is input as a relatively smooth surface at 0.1 AU (*Merkin et al.*, 2011). By 1.41 AU, irregular deformations have formed along the extent of the HCS.

The diagonal lines overlaid on panels d–h of Figure 2.9 show a projection of Ulysses' FLS trajectory onto the spherical surface at 1.41 AU. Ulysses traveled northward in an orbital plane roughly perpendicular to the ecliptic. Since the Sun rotates five times under the spacecraft during the FLS, in a frame of reference rotating with the Sun, the Ulysses trajectory spirals westward and northward. At the beginning of CR 1891 (day 0), Ulysses is at heliographic latitude -40°, well within fast solar wind at high southern latitudes. On day 43, Ulysses enters the band of slow wind. Ulysses remains in the band of variable solar wind speed for the next 45 days then re-enters high speed solar wind populating the northern high latitudes. Although Figure 2.9 shows the entire FLS trajectory overlaid on the LFM-helio results for CR 1892, Carrington Rotations 1891, 1893-1895 have also been run and were used for validation as discussed below.

Figure 2.10 shows simulated data taken from each of the corresponding Carrington Rotations concatenated and compared to Ulysses observations. In descending order, v_r, B_r, n and T are shown over the FLS. Hourly Ulysses data, from the Solar Wind Over the Poles of the Sun (SWOOPS) ion sensor (*Bame et al.*, 1992) and the magnetic field investigation (*Balogh et al.*, 1992), are shown in black, smoothed by a three hour running boxcar average. Simulated data for each Carrington rotation are shown in a different color: CR 1891 (red), 1892 (yellow), 1893 (green), 1894 (blue), and 1895 (indigo). The width of the colored lines shows the maximal range of values in the cells adjacent to the one occupied by the simulated Ulysses trajectory, two in each of the (r, θ, ϕ) directions, and gives a sense of the magnitude of local variability and an estimate of uncertainty in the simulation results. Since transitions between fast and slow solar wind are abrupt, a small change in position can result in vastly different simulated results at Ulysses. A wide band of color indicates sharp gradients within a small spatial extent. The vertical hatched green band marks the passage of an Interplanetary Coronal Mass Ejection (ICME) that was embedded in the slow-fast boundary (*Riley et al.*, 2001; *Gosling et al.*, 1995). Due to the static inner boundary, such transient phenomena are not included in these runs and thus we do not expect the simulation to agree with observations during this interval.

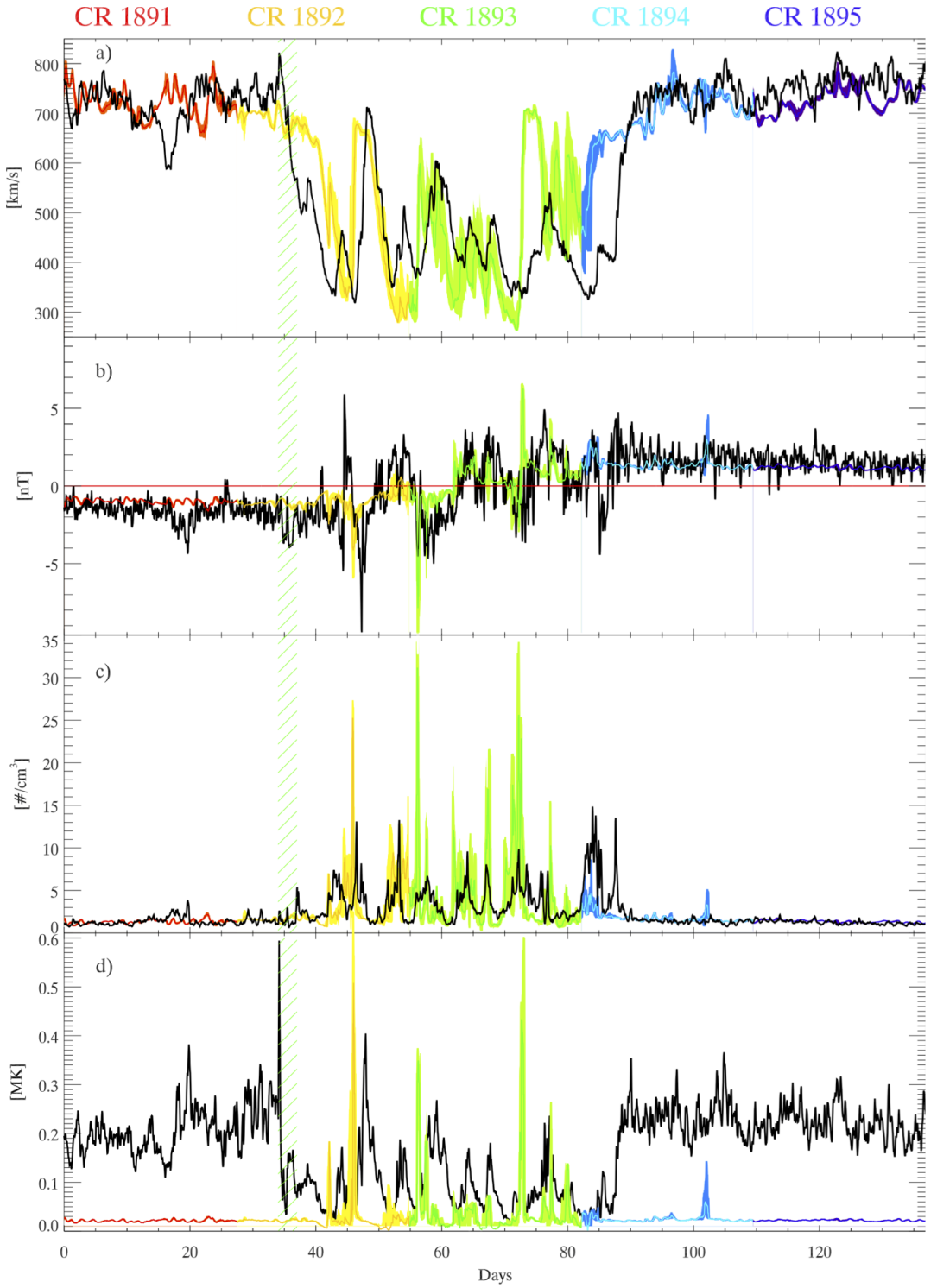

Fig. 2.10: Comparison of Ulysses observations (black) and LFM-helio simulated data (colors) for solar wind v_r (top), B_r (second row), plasma density (third row) and plasma temperature (bottom) for the five Carrington Rotations constituting Ulysses' Fast Latitude Scan.

In terms of the global structure of solar wind speed, the top panel of Figure 2.10 shows that the LFM-helio simulations agree with Ulysses observations at heliospheric distances between 1.3–1.6 AU. It is worth noting that the velocity structure input at 0.1 AU is propagated to Ulysses' orbit, and exhibits evolution on small and meso-scales. The global, large scale structure is retained out to 2.0 AU and is predetermined by the WSA solution for B_r and the subsequent derivation of v_r. For these simulations, Equation 2.1, is used. The FLS begins and ends with fast solar wind (days 0–35 and 95–135). Both observations and simulations have mean speeds of 750 km/s and small scale variations of amplitude 100 km/s. Days 36–94 of the FLS are spent in the band of variable solar wind speed, where measured solar wind speeds vary from 300 km/s to 700 km/s. The ICME that coincides with the entry into the slow wind renders the precise timing ambiguous. Despite the timing differences, the steepness of the transition of v_r from fast to slow wind in the simulations is similar to that observed by Ulysses. Inside the streamer belt, observed slow wind 'troughs' have speeds of 330 km/s interspersed with high speed streams. Simulations have slower minimum speeds (290 km/s) but otherwise reproduce approximately the right number and amplitude of high speed streams. The slopes on the forward edge, and particularly the trailing edge, of the high speed streams are well reproduced within the band of variable solar wind speed.

As seen in the second panel in Figure 2.10, the model reproduces the polarity reversals and amplitude of small scale variations in B_r observations but the mean magnitude of B_r is too small. Within the high speed wind, the average $|B_r|$ is observed to be 1.5 nT whereas the simulations produce an average $|B_r|$ of approximately 1 nT. The variations in simulated magnetic field amplitude correspond causally to SIRs, as the field strength input at the inner boundary is uniform. The peaks in magnetic field slightly precede the arrival of high speed streams, consistent with the

compressed plasma being located ahead of the high speed stream (*Gosling et al.*, 1978; *Gosling and Pizzo*, 1999). Although differences in small scale polarity inversions are evident, most observed polarity inversions lasting more than a day are reproduced in the simulation. Ulysses crossed the HCS on day 64, with short duration polarity reversals of B_r before and afterwards. In the LFM-helio simulations, the sector boundary crossing occurs one day earlier. As can be seen in the magnetic field panel of Figure 2.9, Ulysses remains near the HCS during days 40–90. If the simulated HCS were more warped or distorted, the Ulysses trajectory could have crossed the boundary more frequently or traversed regions of stronger field, as seen in observations.

The third panel of Figure 2.10 shows the observed and simulated proton number density measured along the FLS. In the fast wind, the simulations reproduce both the average values and low levels of variability seen in the observations. In the high speed wind, the mean n is 1.5 cm^{-3} with small scale variations of 0.5 cm^{-3}. Within the band of variable solar wind speed, Ulysses measures several high-density peaks. The density peaks are a result of the slow solar wind being inherently denser than the fast wind combined with the plasma compressions due to SIRs. The LFM-helio simulated density also has approximately the correct number, width and timing of density peaks. In the simulation result, the densest peaks are concurrent with the largest peaks in B_r and correspond to plasma regions that have been compressed in SIRs. Many of the peaks have wide bands of color, indicating that there is a large span between the maximum and minimum density in cells adjacent to Ulysses' trajectory, suggesting regions of sharp density gradients. Often, if simulations do not agree with observations, the range of nearby densities in the LFM-helio will overlap with what is observed.

The last panel of Figure 2.10 shows that proton temperature has the largest discrepancy between simulations and observations. In the fast wind, the simulated temperature is an order of magnitude too low and lacks the observed large amplitude (0.05 MK) fluctuations. There is better agreement in the band of variable solar wind speed. Physical reasons the simulated temperature is too low, particularly in the hot wind, may be that (i) the temperature at the inner boundary is too low which is possible since it is poorly constrained observationally at 0.1 AU, (ii) assuming an adiabatic index of γ=5/3 is inaccurate, (iii) the LFM-helio does not include physical heating mechanisms, such as electron hear conduction, dissipation of Alfvènic turbulence known to be prevalent in the fast wind (*Belcher and Davis Jr.*, 1971), or some combination of the above.

Section 2.2.4 addresses the effects of increasing the temperature at the inner boundary and of using γ=3/2 instead of γ=5/3. The different γ parameterizes some of the missing physics in the formulation of the LFM-helio code, such as the lack of heat conduction, kinetic effects, and dissipative turbulent heating, known to be important in heating the fast wind. The omission of these processes is recognized as a source of error but not addressed further in this dissertation.

A small but suggestive discrepancy between the simulations and observations is that the magnitude of the simulated peaks in magnetic field, plasma density and temperature is typically larger and the duration is shorter than those observed. This is likely due to the leading edge of the high spreed streams being too steep in the simulations and creating SIRs that are too compressed.

Overall, however, the simulations are in reasonable agreement with the Ulysses observations. The mean values of v_r, B_r and n in the high speed solar wind are particularly well matched, with the temperature constituting the largest departure from measurements. Within the band of variable solar wind speed, the amplitude

and frequency of variations generated by the model are similar to those in the Ulysses measurements despite differences in the timing and duration of specific features. We conclude that the LFM-helio reproduces the large-scale structure of the heliosphere during CRs 1891– 1895 well. Conversely, fluctuations on the order of a day are retained by the non-diffusive numerical scheme of the LFM-helio. This model's ability to capture sharp transitions and retain this amount of structure, dynamically advected to Ulysses' orbit, allows the reproduction of not only the large scale structure of the solar wind but also the qualitative characteristics of the day-scale variability.

2.2.4 Sensitivity to the Inner Boundary Conditions

We now turn our attention to the sensitivity of the LFM-helio results to the assumptions made at the inner boundary. The results for CR 1891–CR 1895 discussed above were derived using the set of assumptions we refer to as the baseline, which assumes the empirical relation between velocity and density based on Helios data (Equation 2.1) and uniform thermal pressure at 0.1 AU. Assumptions are necesary to populate the plasma parameters at the inner boundary of MHD models. Similar assumptions to the ones stated above are often used as reasonable methods of assigning values for the density and temperature required at the inner boundary of MHD models in the absence of *in situ* measurements. The assumptions may be justified; uniform momentum flux is suggested from Ulysses results (*Riley et al.*, 1997) and non-radial gradients in thermal pressure at the inner boundary would be quickly minimized by the resulting flow (*Riley et al.*, 2001). In order to limit the number of runs performed, we focus on CR 1892 to test the LFM-helio's sensitivity to a variety of assumptions that are described below. We chose CR 1892 because it is the only Carrington rotation during the FLS which contains measurements from the high latitude fast wind, a transition between high latitude wind and the band of variable solar wind speed, as well as a high speed stream despite also contain-

ing an ICME. The different assumptions made affect the density, temperature, and magnetic field strength at the inner boundary as well as the value of the adiabatic index.

The variations of the physical assumptions made at each inner boundary used in this section are listed in Table 2.2. The first column contains the names we assign each run. For the first five runs, v_r and B_r are determined in the same way: B_r is taken directly from the WSA solution, while v_r is computed using 2.1. The top two panels on the left in Figure 2.9 show v_r and B_r thus obtained at the inner boundary. The sixth case includes an additional step; after determining v_r from the formula in 2.1, B_r is made proportional to v_r. Hence, in the B_R run, regions of fast solar wind are also regions of strong magnetic field.

The density is either obtained from Equation 2.2 (Baseline, T, $P_{\rm tot}$, B_R and γ runs) or by assuming a uniform momentum flux, $nv_r^2 = n_0 V_0^2$, where $n_0 = 300$ cm^{-3} and $V_0 = 625$ km/s (nV^2 run). The temperature at the inner boundary is based on one of three assumptions: (i) uniform thermal pressure, $nT = n_0 T_0$, where $T_0 = 0.8 \cdot 10^6$ K (Baseline, nV^2, B_R, and γ runs); (ii) uniform temperature $T = T_0$ (T run); and (iii) uniform total pressure (thermal plus magnetic), $nkT + B^2/8\pi = n_0 k T_0 + B_0^2/8\pi$, where $B_0 = 300$ nT ($P_{\rm tot}$ run). Assumption (iii) is a more rigorous version of (i) and includes the contribution of the magnetic field into the pressure balance. Assumption (ii) has little justification and is intended to test the sensitivity of the global solution to the specification of plasma temperature at the inner boundary. All runs use an adiabatic index of γ=5/3 except for the γ run which uses γ=3/2 but is otherwise the same as the Baseline run.

The T and $P_{\rm tot}$ runs differ from the Baseline run only in the treatment of the plasma temperature at the inner boundary. The uniform temperature in the T run results in a slow wind that is hotter by a factor of about 8 and a fast wind that is cooler

by roughly a factor of 0.8 than in the Baseline run. The $P_{\rm tot}$ run has temperatures that are about 3 times hotter than the Baseline run at the inner boundary. In the nv^2 run, the fast wind is about 33% more tenuous and the slow wind is about 15% denser than in the Baseline run. The new density is used to determine the temperature, so relative to the Baseline run the fast wind is correspondingly slightly hotter while the slow wind is slightly cooler. The B_R run differs from the Baseline run only in the magnitude of the magnetic field at 0.1 AU. In the γ run, the IBCs are identical to the Baseline run but the value of the adiabatic index throughout the heliosphere is 3/2 instead of 5/3.

Run Name	n	B_r	T	γ
Low Resolution				
Baseline	Helios	WSA	nT uniform	5/3
nV^2	nv^2 uniform	WSA	nT uniform	5/3
T	Helios	WSA	T uniform	5/3
$P_{\rm tot}$	Helios	WSA	$nT + B^2/8\pi$ uniform	5/3
γ	Helios	WSA	nT uniform	3/2
B_R	Helios	WSA, scaled to v_r	nT uniform	5/3
High Resolution				
Baseline	Helios	WSA	nT uniform	5/3

Table 2.2: Description of simulation runs performed for Carrington rotation 1892. The rows represent the different set of assumptions made at the inner boundary for each of the runs. The first column specifies the run identifier used throughout the text of the paper. The columns show how the variables in the column titles are determined in a given simulation run. In all cases, v_r is determined by Equation 2.1. The constants in the table are as follows: $n_0 = 300$ cm^{-3}, $V_0 = 625$ km/s, $T_0 = 0.8 \cdot 10^6$ K, $B_0 = 300$ nT.

LFM-helio results were generated for CR 1892 for each run listed in Table 2.2 from 0.1–2.0 AU. The global structure of the solar wind for all runs resembles that of the Baseline shown in Figure 2.9 and are not shown individually. Figure 2.11 shows

simulated data along the Ulysses trajectory during CR 1892 (days 27–54 of the FLS) and Ulysses observations in the same format as Figure 2.10. Ulysses observations are shown in black. Simulation results from the Baseline, nV^2, $P_{\rm tot}$, T, γ, and B_R runs are shown in red, yellow, green, cyan, purple, and blue, respectively. From top to bottom, the panels show v_r, B_r, n, and T. As before, the vertical hatching spanning days 34–37 marks the passage of an ICME (*Riley et al.*, 2001; *Gosling et al.*, 1995). Since the comparison between the Baseline run and Ulysses FLS observations has been discussed in the previous section, we focus here on the relative differences between runs. Overall, since the assumptions listed in Table 2.2 do not change the variables at the inner boundary by much, all simulations resemble each other for all variables more than they resemble Ulysses data. Still, the relative differences between runs can be instructive. It is important to note that the v_r input at the inner boundary is identical for all runs and any differences seen in this variable are due to differing dynamical evolution.

The Baseline and nV^2 runs are nearly identical in all panels of Figure 2.11. This is not surprising since the density and temperature differ only slightly at the inner boundary. The γ run, only differing from the Baseline run by using a smaller value for the adiabatic index, results in simulations that are nearly identical at Ulysses for the all variables shown, except temperature which is higher everywhere except in SIRs. The relatively hot slow wind at the inner boundary of the T run accelerates the slow wind to higher speeds at Ulysses than in the Baseline run. The P_{Total} run, which increased the temperature everywhere at the inner boundary by a factor of 3, produces solar wind that is 30 km/s faster and is about three times hotter at Ulysses than in the Baseline run.

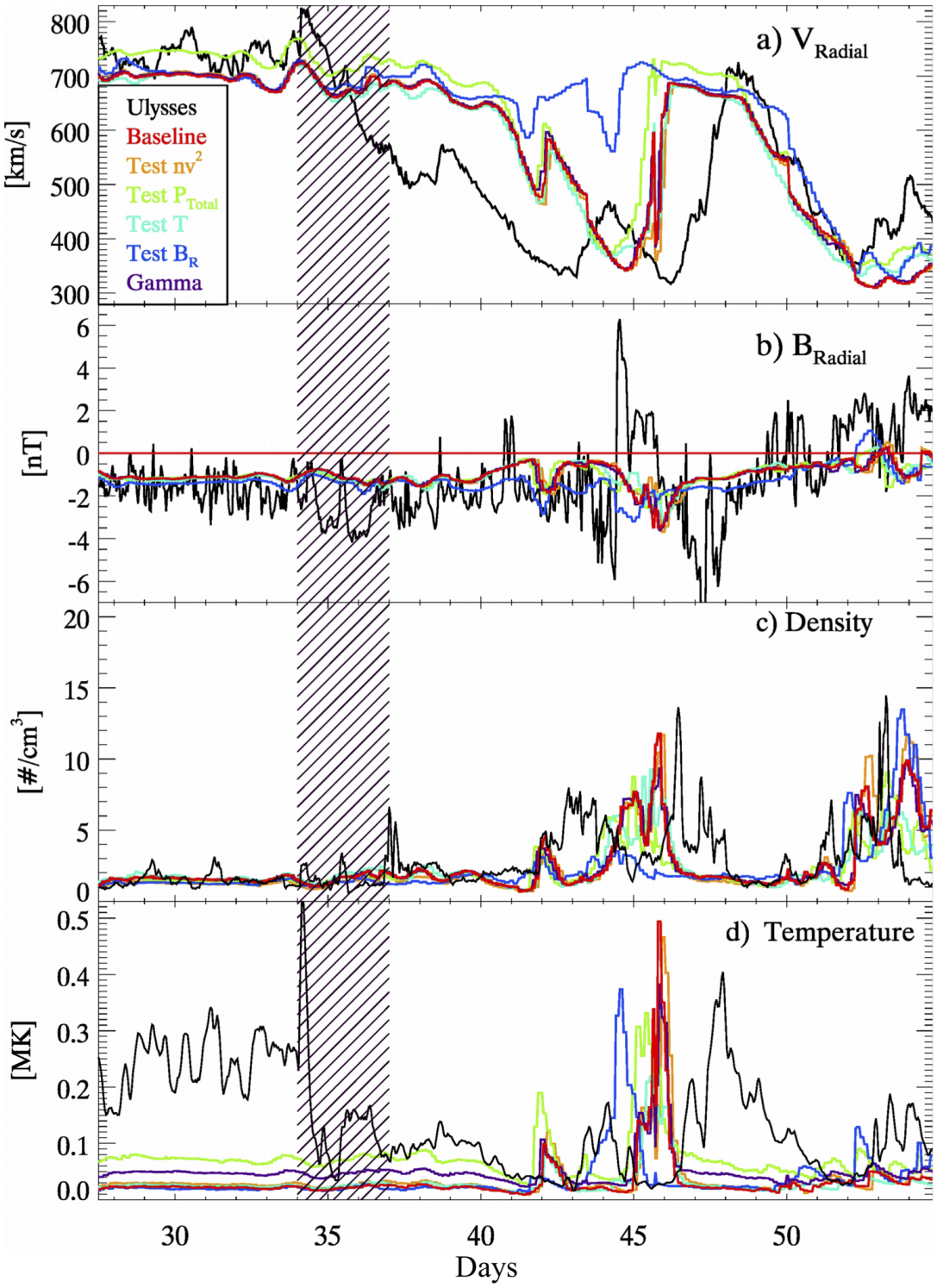

Fig. 2.11: Comparison of Ulysses observations (black), smoothed with a three hour running boxcar average, during CR 1892 with corresponding LFM-helio simulated results (colors). Each color represents one set of assumptions made at the inner boundary, described in Table 2.2.

The compressed plasma in the SIR, centered on day 46 in the third and fourth panels of Figure 2.11, is not compressed or heated as much as the plasma in the Baseline run for the T, γ, and P_{total} runs. In the T run, this is due to the smaller speed difference driving the interaction. In the P_{Total} and γ runs, the slow wind plasma is hotter, so there is more thermal pressure to resist compression and heating from the high speed stream. The increased solar wind speed in the P_{Total} run creates a Parker spiral that is less tightly wound and results in an earlier arrival time of the high speed stream (day 45).

The B_R run differs the most from the Baseline. The increased field strength in the fast wind improves the agreement between simulated and observed B_r, as can be seen in the second panel of Figure 2.11. This also increases the magnetic pressure at high latitudes, producing a global pressure gradient which compresses the band of variable solar wind speed. The narrower band of slow wind is seen in the top panel, where simulated v_r misses the initial entry into slow wind and instead samples high speed solar wind until day 50.

Figure 2.11 highlights two points; the first is that the LFM-helio does a good job at reproducing the Ulysses Fast Latitude Scan data for CR 1892 for most sets of inner boundary conditions considered here, capturing large scale features and also qualitatively the meso-scale variability. The second point is that the simulated data strongly resemble each other, with variations more similar to each other than with observations. The B_R run, the only run to affect the magnetic field strength, produces the largest difference. The compression of mid- and low-latitude heliospheric structures causes significant delay in the timing of Ulysses' entry into the band of variable solar wind speed. This result highlights the importance of accurate measurements of polar photospheric magnetic fields in a model's ability accurately simulate the solar wind and to predict space weather events. This is also illuminating in the

context of solar cycle 23's weak minimum and solar wind, which includes weak polar fields and a slow solar wind.

2.3 Sensitivity to Preset Values

All runs in the previous sections require preset values for n_0 and T_0, B_r at the inner boundary. B_r comes from the WSA model. Values for n_0 and T_0 describe the number density and temperature of the fast wind and have been chosen from a reasonable range of values at 0.1 AU. While the set of LFM-helio simulations in Figure 2.11 reproduce Ulysses measurements of velocity and number density, the magnetic field strength and temperature are underestimated in all runs. The temperature underestimation could be due to T_0 being too low at the inner boundary or the temperature decreasing too rapidly with increasing distance from the Sun. This is characterised by γ parameter. In order to address the underestimation and to test the LFM-helio's sensitivity to these preset values, we run another set of simulations. Using the Baseline set of assumptions, the values for T_0 and B_r are increased, using both γ=5/3 and 3/2, as listed in Table 2.3. Figure 2.12 is in the same format as Figure 2.11 with Ulysses measurements in black and the Baseline run in red. The orange line shows the $T1$ run (T_0=3.2 MK), while the green line shows the effects of also setting γ=3/2 (run $T1\gamma$). The blue line (run $T1\gamma B$) shows the effect of also increasing B_r by a factor 1.5.

As before, increasing plasma temperature at the inner boundary results in hotter plasma, more acceleration of the plasma, and in faster speeds at Ulysses (Figure 2.12, panels a) and d)) while leaving the density and magnetic field strength nearly unchanged (panels b) and C)). The new runs have solar wind speeds 50–60 km/s faster at Ulysses than in the Baseline run but are still within the range of Ulysses observations. The speed of the slow wind is sometimes overestimated (day 45) and at other

Run Name	γ	T_0 [MK]	B_r [nT]
Baseline	5/3	0.8	300
$T1$	5/3	3.2	300
$T1\gamma$	3/2	3.2	300
$T1\gamma B$	3/2	3.2	450

Table 2.3: Description of simulation runs performed for Carrington rotation 1892. The rows represent the different sets of preset values used at the inner boundary for each of the runs. The first column specifies the run identifier. The columns show how the variables in the column titles are determined in a given simulation run. n_0=300 cm^{-3}, V_0=625 km/s.

times (day 52) agrees better with measurements than Baseline run. The faster solar wind speeds also result in earlier arrival times of high speed streams. The uniform increase in the thermal pressure maintains pressure balance in the latitudinal and longitudinal directions while accelerating the solar wind away from the inner boundary of the simulation, resulting in a globally faster solar wind and a more loosely wound Parker spiral.

Figure 2.12 shows that setting T_0=3.2 MK produces better agreement to temperature measurements at Ulysses. For all variables, the runs with T_0=3.2 MK at the inner boundary show temperature fluctuations at Ulysses on the scale of roughly a day that are both more frequent and have larger amplitudes than the Baseline case. The $T1\gamma$ and $T1\gamma B$ runs provide the best agreement to temperature measurements of the high speed wind without significantly affecting the other variables. Both runs also provide reasonable agreement with measured temperatures in the slow solar wind. The apparent disagreement in simulated and measured temperatures on day 37–42 in Figure 2.12 d) is due to the simulated results still sampling hot, high speed wind. The Ulysses trajectory skims the boundary between fast and slow wind, so minor differences between runs can result in different simulated speeds. Small latitudinal variations in the sharp boundary between fast and slow solar wind in the runs

cause the difference in timing of the entry into the slow wind and the short duration high speed streams therein.

The $T\gamma B$ run, shown in blue in Figure 2.12, increases B_r uniformly, as opposed to scaling it with solar wind speed as done in the B_R run. This increases the magnetic pressure uniformly at the inner boundary and does not compress the band of variable solar wind speed. As such $T\gamma B$ run generates a solution that is globally more similar to the Baseline that the B_r run. As expected and as is shown in Figure 2.12 b), the magnitude of B_r has increased and better agrees with observations. v_r along the Ulysses trajectory for CR 1892 is changed only during the initial entry into the slow wind. Density and temperature are unchanged save the timing differences due to the slight differences in the velocity profile.

For runs $T1$, $T1\gamma$, and $T1\gamma B$, the amount of plasma compression occurring in the SIR is reduced relative to the Baseline run, as can be seen in Figure 2.12 c). The peak density in these simulations better agrees with the observations than the Baseline simulation. This is likely due to increased thermal and magnetic pressures in the plasma resisting the compression caused by the dynamic pressure of the high speed stream. The plasma does, however, get much hotter than in the Baseline case.

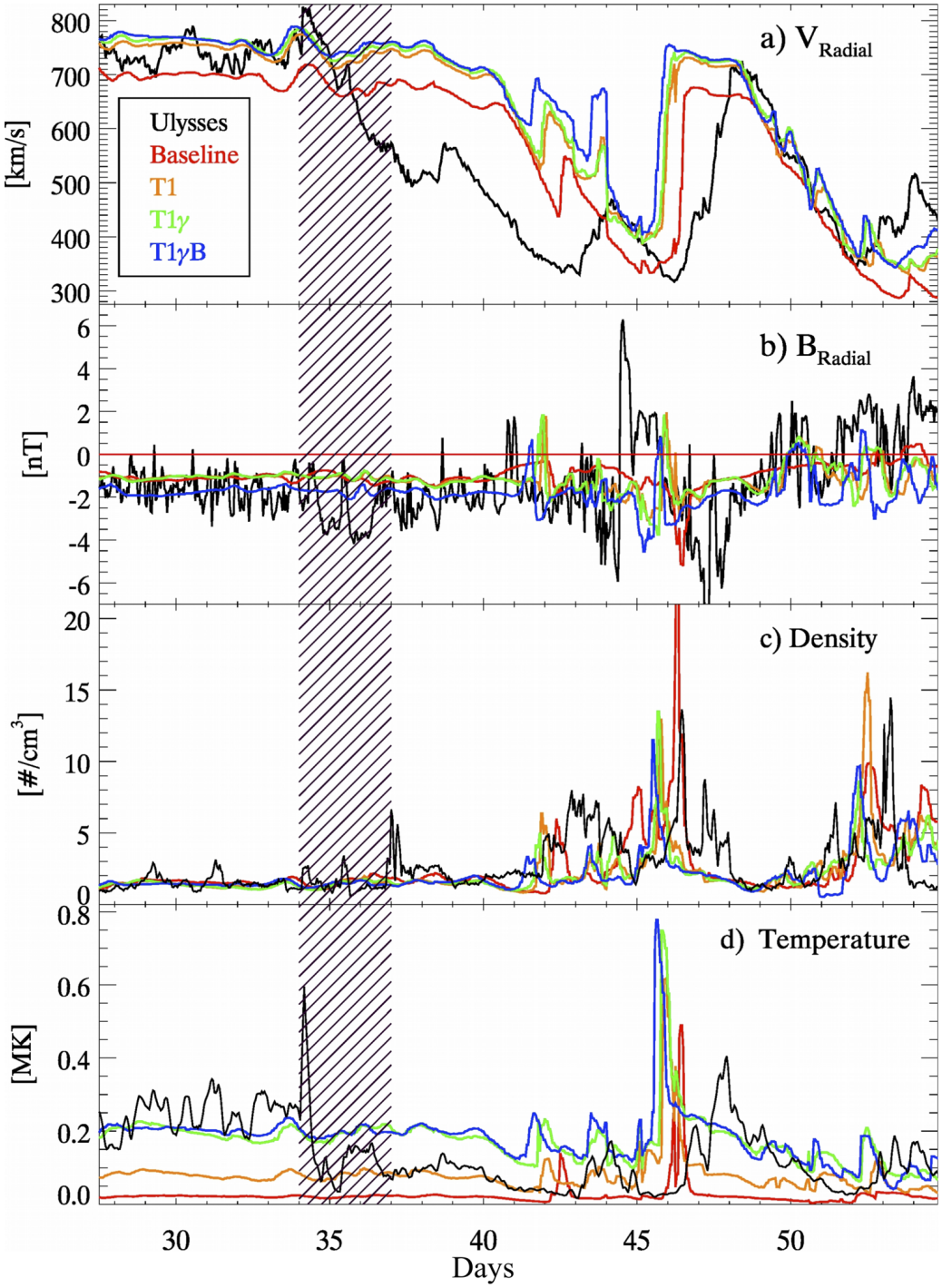

Fig. 2.12: Comparison of Ulysses observations (black), smoothed with a three hour running boxcar average, during CR 1892 with corresponding LFM-helio simulated results (colors). As indicated in the legend, the red line shows the "Baseline" case, identical to that in fig. 2.11. The orange, green, and blue lines represent runs $T1$, $T1\gamma$, and $T1\gamma B$, respectively, as in Table 2.3.

Comparing Figures 2.11 and 2.12 shows two things. The first is that all of these runs produce simulated data that are similar to each other and are also in reasonable agreement with Ulysses data. The second is that the result are more strongly affected by increasing the preset values for T and B_r at the inner boundary than by varying the physical assumptions made there. It is worth noting again, however, that the physical assumptions used to assign density and temperature at the inner boundary do not change the relative value of these variables by much. The preset value for T_0 at the inner boundary has a large effect on both the simulated solar wind speed and temperature.

2.4 Summary and Conclusions

We have presented a validation and sensitivity study for the heliospheric adaptation of the Lyon-Fedder-Mobary (LFM) magnetohydrodynamic (MHD) code, the LFM-helio. The LFM-helio is a 3D, global MHD model that simulates the supercritical flow of the solar wind. The model is driven at its inner boundary by the WSA model results for v_r and B_r. The Baseline run specifies the plasma density at 0.1 AU from an empirical fit to Helios data and the plasma temperature by assuming a uniform thermal pressure at the inner boundary. Using the Baseline set of assumptions, the LFM-helio results were generated from 0.1–2.0 AU. Simulated data were extracted along spacecraft trajectories and compared with MESSENGER and ACE observations in the ecliptic for CR 2060 and CR 2068 as well as with Ulysses observations, perpendicular to the ecliptic plane, for CRs 1891–1895.

Simulated large scale, global features agree with observations. High speed streams are reproduced and the timing of arrival is roughly matched. For the FLS, the entry into and exit from the band of variable solar wind speed is matched within a few days, which is comparable or better than other heliospheric MHD models. The

Baseline run underestimates the magnitude and variability of B_r, particularly for CR 2060 and CR 2068, but the timing of HCS crossings matches to within a few days. Simulated number density agrees well with measurements, although density peaks in compression regions are too narrow and too dense. The simulated temperature is colder than observations, particularly in the fast wind which is roughly an order of magnitude too cold.

To test the sensitivity of global results to the assumptions made at the inner boundary, variations on the assumptions were made for CR1892. The nv^2 run assumes uniform momentum flux over the inner boundary, while runs P_{Total} and T keep the Helios fit for density but assume uniform total pressure (thermal plus magnetic) and uniform temperature, respectively, at the inner boundary. The resulting changes in density and temperature are not large. The γ run keeps the Baseline density and temperature at the inner boundary but assumes an adiabatic index of 3/2 for the plasma. For the B_R run, $|B_r|$ is scaled to the solar wind speed so that high speed wind is also the source of stronger magnetic field, since this is where the largest discrepancy occurred.

Our primary conclusion is that the LFM-helio is a robust tool for simulating the solar wind in the inner heliosphere and that the LFM-helio reproduces the state of the heliosphere accurately, when considering the limitations in specifying an accurate inner boundary. The ability of the LFM-helio to capture small scale structure and steep gradients make it an excellent tool for investigating steady state structures such as SIRs.

Furthermore, the resultant simulations of the large scale structure of the heliopshere do not differ substantially between runs except the B_R run. The largest effects were found for assumptions concerning the temperature and the magnetic field strength distribution at the inner boundary. A hotter temperature at 0.1 AU

resulted in higher solar speeds and a hotter plasma at Ulysses. The increased magnetic pressure at high latitudes at the inner boundary in the B_R run created a global pressure gradient which compressed the band of solar wind variability and had the largest effect on the large scale structure of the heliosphere and on the prediction of arrival times for high speed streams. This emphasizes the importance of the polar magnetic field.

The LFM-helio's sensitivity to the choice of preset values for temperature in the fast solar wind and the magnetic field strength at the inner boundary was also tested. We found that, while using the Baseline set of assumptions, increasing the preset temperature by a factor of four (T_0=3.2 MK) resulted in higher solar wind speeds and hotter temperatures at Ulysses, leaving the density and magnetic field unchanged. These simulated results also agreed with Ulysses temperature observations better. Using T_0=3.2 MK and γ=3/2 provides the best overall agreement between simulations and Ulysses observations of v_r, n, and T. Also increasing the magnetic field strength by a factor of 1.5 at the inner boundary results in better agreement with B_r measurements for both magnitude and amount of variability.

It is possible for a given solar wind speed configuration at the inner boundary of MHD models, through judicious choice of n_0,T_0, and B_r parameters, to quantitatively match the range of values for each of the variables measured *in situ* observations during the Ulysses FLS. While the minimum and maximum values of B_r, n, and T may be matched, the global structure of the solar wind is dependent on the configuration of the coronal magnetic field and the way the velocity is derived from it. The width of the slow wind band and the sharpness of the transition between fast and slow solar wind are sensitive to the parameter choices in made Equation 2.1. Though outside the scope of this dissertation, the parameters in Equation 2.1 determine the magnitudes of speed but also the angular extent of sources of slow wind. Though

this Equation has been calibrated for agreement with Helios, OMNI, and Ulysses data (*McGregor et al.*, 2011a), the velocity distribution input at the inner boundary largely is the dominant source of error in the ability to predict solar wind speeds at particular locations.

While accurately reproducing solar wind observations has received much attention in the field and certainly is an important skill needed to accurately predicting space weather impinging on Earth's magnetosphere, we have demonstrated that the ability of any given model to achieve this depends on both the physics included and perhaps to a larger extent, the accuracy of what is input at the inner boundary. I assert here that the LFM-helio has been validated and its sensitivity to variations in parameters characterized. The LFM-helio is used in the next chapters to investigate the physical processes involved in the evolution of SIRs within the inner heliosphere.

Chapter 3

Evolution of SIRs in the inner heliosphere: In Ecliptic

3.1 Motivation

The solar wind is inherently four dimensional, having large scale structure which depends on heliocentric radial distance, latitude, longitude, and time. In Chapter 1.1.1, the decision to remove the time-dependence when investigating SIRs was justified; there being a first order equivalence between time and azimuthal rotation. Indeed, coronal configurations during solar minimum are typically long-lasting, meaning that the global pattern of the solar wind source is roughly the same for several Carrington rotations. The slow evolution of the coronal configuration during solar minimum and during the declining phase bolster this equivalence and motivate the use of a static inner boundary for LFM-helio simulations of CR 1892, CR 2058, and CR 2060. These Carrington Rotations, which will be discussed throughout the chapter, occur during the declining phases of solar cycles 22 and 23, respectively.

During solar minimum and the declining phase of the solar cycle, the approximate alignment of the solar magnetic and rotational axes introduces some symmetry between northern and southern hemispheres. This coronal configuration places open magnetic field lines, coronal holes, at the poles and closed field lines near the heliographic equatorial plane, generating uniform fast solar wind at high latitudes. Slow wind is produced near the heliomagnetic equator, which extends out to form the

heliospheric current sheet (HCS). The HCS often forms a warped sinusoid about the heliographic equator, and the slow wind typically reproduces this general form.

Consider for example the minimum of solar cycle 22, coronal holes filled the heliographic polar areas and low latitude extensions of the polar coronal holes were prevalent. This magnetic topology generated uniform fast wind at high latitudes with fingers of fast wind extending to low latitudes. In contrast, isolated equatorial coronal holes were prevalent during the minimum of solar cycle 23. This generated fast wind at the poles and island sources of fast solar wind at low latitudes. The equatorial coronal holes also created a bifurcated band of slow wind - the familiar streamers with the HCS embedded and also pseudostreamers which did not include a reversal in IMF. Both coronal configurations introduce complexity to mid and low latitude solar wind. Mid and low latitudes are therefore populated by variable solar wind speed for both typical and the recent, more peculiar solar minima. Both complex solar wind speed source patterns, coupled with solar rotation, produce SIRs. Mid and low latitudes are hence the foremost regions of prevalence and thus interest for understanding the development and evolution of SIRs during the declining and minimum phases of the solar cycle.

Furthermore, low heliographic latitudes encompass the ecliptic plane - the plane in which the Earth orbits the Sun. The ecliptic is tilted by approximately 7° with respect to the heliographic equator and as the Earth orbits over the course of a year, the sub-solar point of the Earth on the Sun ranges from 7° above or below the heliographic equator. The angular separation between the sub-solar point and the heliographic equator is known as the solar B angle, θ_B. Thus the span of $\pm$ 7° about the heliographic equator is of particular interest since, over the course of a year, it is solar wind from this narrow band that flows over Earth's magnetosphere.

The solar wind conditions impinging on the Earth's magnetosphere may drive space weather, whether the solar wind conditions are transient, such as ICMEs, or steady state, as the SIRs considered in this dissertation. The interest in both understanding and being able to predict space weather result in a particular focus on the ecliptic plane. Hence, the vast majority of in situ observations are from near the ecliptic plane and as such, phenomena occurring there have been studied carefully.

There is a relative abundance of both spacecraft observations and simulations concentrating on this plane. In Section 3.1.1, I will summarize observations of SIRs in the ecliptic plane in the inner heliosphere, and review some previous simulations in this plane. In section 3.2, SIRs occurring during CR 2058 and CR 2060 are compared in order to qualitatively discuss the influence the shape of the HSS has on the resulting structures and their evolution. This section also addresses latitudinal variability for SIRs with different large scale structures. The effects of changing plasma parameters, as described in Chapter 2, on SIR evolution is discussed in Section 3.3.

3.1.1 Observational Background

Observations of SIRs in the ecliptic at 1.0 AU reveal common signatures. First, the driver of the SIR is a significant and sudden increase in solar wind speed, creating a sharp gradient in solar wind dynamic pressure. Usually, the solar wind speed increases by a few hundred km/s over an average of 36 hours (*Jian et al.*, 2006; *Badruddin and Falak*, 2016). Concurrent with increasing speed, enhancements in solar wind density and temperature are observed, since the wind ahead of the high speed stream (HSS) is being compressed, heated, and accelerated. The compressed and heated plasma creates a region of high thermal pressure relative to the surrounding solar wind plasma. The compression of solar wind plasma also intensifies the magnetic field such that the region of high thermal pressure is also a region of high magnetic pressure. The resulting pressure gradient transfers momentum from

the fast wind, decelerating, compressing and heating it. Wind that was originally fast and wind that was originally slow, once swept up into the SIR, both have intermediate speeds. The two solar wind populations are separated by a tangential discontinuity called the stream interface (SI). The high pressure regions, and more particularly the pressure gradients on either side of the maximum, driven in response to gradient in dynamic pressure, produce forward and reverse waves on the leading edge and trailing edge of the SIR respectively. These waves steepen with increasing distance from the Sun and may develop into forward and reverse shocks (*Gosling and Pizzo*, 1999).

The forward and reverse waves are roughly aligned with the Parker spiral on a global scale. Since the pressure waves are at an angle relative to the radial flow of the unperturbed solar wind, they drive flow deflections within the SIR. In the azimuthal direction, slow wind is deflected in the direction of solar rotation and fast wind is deflected in the opposite direction. In the polar direction, the magnitude and orientation of the deflection depends on the shape of the HSS. Observationally, the magnitude and direction of deflected flows tangential to the SI surface, which is assumed to be planar, are used to deduce the orientation of the SIR as a large-scale structure. This approach for large scale structures is supported by the theoretical work of *Pizzo* (1982), who has shown this for idealized coronal conditions. The effects of more complex high speed streams on the evolution of SIRs in the ecliptic plane will be discussed qualitatively in Section 3.2.

The strength of SIRs is often characterised by the extrema for various plasma parameters. As such, the maximum density, temperature, and speed of flow deflections are also frequently considered in the literature. Other such parameters are the amplitude of speed increase, orientation and timing of the forward wave, reverse wave, and SI, as well as whether or not the waves have steepened into shocks. While

in situ observations at distances other than 1 AU are sparse, the evolution of the SIRs as parameterized by their extrema is of much interest for space weather predictions.

Near the Sun, the alignment of fast wind behind slow is established. Before this configuration creates a region of enhanced pressure, the fast wind catches up to the slow wind and drives the compression unimpeded. A peak in density, temperature, and magnetic field is subsequently created and the local enhancement in thermal and magnetic pressure counteract the dynamic pressure gradient which tends to compress the transition from slow to fast wind. Hence there is competition between the compression and steepening of the SIR and subsequent broadening. In the inner heliosphere, the steepening dominates while further out, around 5 AU, the broadening dominates. At 1 AU, typically SIRs are still developing.

In terms of evolution of density and temperature, since the solar wind is expanding adiabatically into the heliosphere. Theoretically, in the absence of dynamical effects, the density scales as r^{-2} and the temperature scales as $r^{-4/3}$ if γ=5/3. Including the dynamical effects of SIRs, the peaks in scaled density and temperature within a SIR increase with increasing distance from the Sun, as the SIR is continually driven by the dynamic pressure of the HSS. This relative increase in pressure exerts a larger force and drives faster flow deflection.

Hence, in the inner heliosphere SIRs become increasingly pronounced as they propagate away from the Sun. The forward and reverse waves which bound them develop into shocks, which themselves propagate away from the SI. The distance between forward and reverse waves/shocks at 1.0 AU, on average is approximately 0.4 AU (*Jian et al.*, 2006). The normal to the surface of the forward wave, reverse wave, and SI of the same SIR are roughly the same. The general features of SIRs are fairly consistent over a large range of heliospheric distances and throughout all phases of the solar cycle. Each SIR is composed of a region of compressed, heated

plasma coincident with a rise in solar wind speed and exhibiting significant non-radial flow bound by forward and reverse waves. These features become more pronounced as the SIR flows away from the Sun but the particular characteristics of any given SIR vary.

The amount of plasma compression, for example, increases with increasing heliospheric distance but the maximum density observed at 1.0 AU varies from SIR to SIR or even for the same SIR but observed by different spacecraft at 1 AU. Even for recurrences of the same HSS, characteristics such as the maximum density, timing of arrival, and orientation of the SIR normal differ (*Simunac et al.*, 2009; *Rouillard et al.*, 2009). These observations are incongruent with the simplistic model of a static solar wind, often invoked during solar minimum, and early, large scale observations of SIRs. Qualitatively repetitive patterns have indeed been observed in the ecliptic plane (*Crooker et al.*, 1999; *Gosling and Pizzo*, 1999), and support the long duration of solar wind sources during solar minimum, with the same high speed stream pattern recurring when observed from a particular vantage point. The quantitative particulars of such observations vary for the same HSS between spacecraft and between Carrington rotations.

These quantitative variations in SIRs are attributed to either to small scale structure of the HSS, or to the evolution of the coronal holes, dynamical evolution of the HSS, or small scale transients. The importance of small scale structure, and the latitude of the observer, will be explored later in this chapter.

3.2 Influence of Global Structure

In this section, we qualitatively discuss the influence of global solar wind structure on the observational patterns in the ecliptic plane. To highlight the effects of global structure of the HSSs, we consider HSSs of different shapes that are flow-

ing into similar background solar wind. Specifically, the HSSs considered are from CR 2058 and CR 2060, during the declining phase of solar cycle 23 and separated by less than a month. The temporal proximity of these intervals during solar minimum implies that, given the slow change in global coronal configuration, these two Carrington Rotations should be fairly similar. Furthermore, we choose to compare what would be considered the recurrence of the HSS near the equatorial plane in CR 2058. The top panels of Figure 3.1 show the global configuration of v_r as a function of latitude and longitude at 0.1 AU. Subsequent rows show the evolution of v_r as a function of latitude and longitude in increments of 0.5 AU out to 2.0 AU as propagated through the LFM-helio.

Simulations for CR 2058 and CR 2060 were run on a low resolution grid, $[192, 96, 192]$ cells in the radial, polar, and azimuthal directions respectively. The grid spacing is sub 2° X 2° X 2 $R_\odot$ resolution from 0.1 AU - 2.0 AU. The panels in Figure 3.1 show v_r as a function of latitude and longitude for CR 2058 (left) and CR 2060 (right) at increasing heliospheric distances from the Sun from 0.1 AU (top), 0.5 AU, 1.0 AU, 1.5 AU and 2.0 AU. In both cases, as can be seen by comparing subsequent rows, the interaction between streams smooths some of the structure at the interface between fast and flow wind. The HSS of interest located just below the heliograpic equator and at longitudes denoted by a row of diamonds.

Similarities between Carrington Rotations include uniform, high speed solar wind at high latitudes, above 40°, an undulating band of slow wind with a large deviation northward, with a thin pseudostreamer encircling an equatorial source of faster wind within which are nested two small sources of high speed wind faster than 700 km/s, located just below the heliographic equator between longitudes 300°–20°. One of these sources is patchy and abuts the HCS and the other is enclosed by slow wind. This latter HSS is considered in detail here since the pattern of low speed

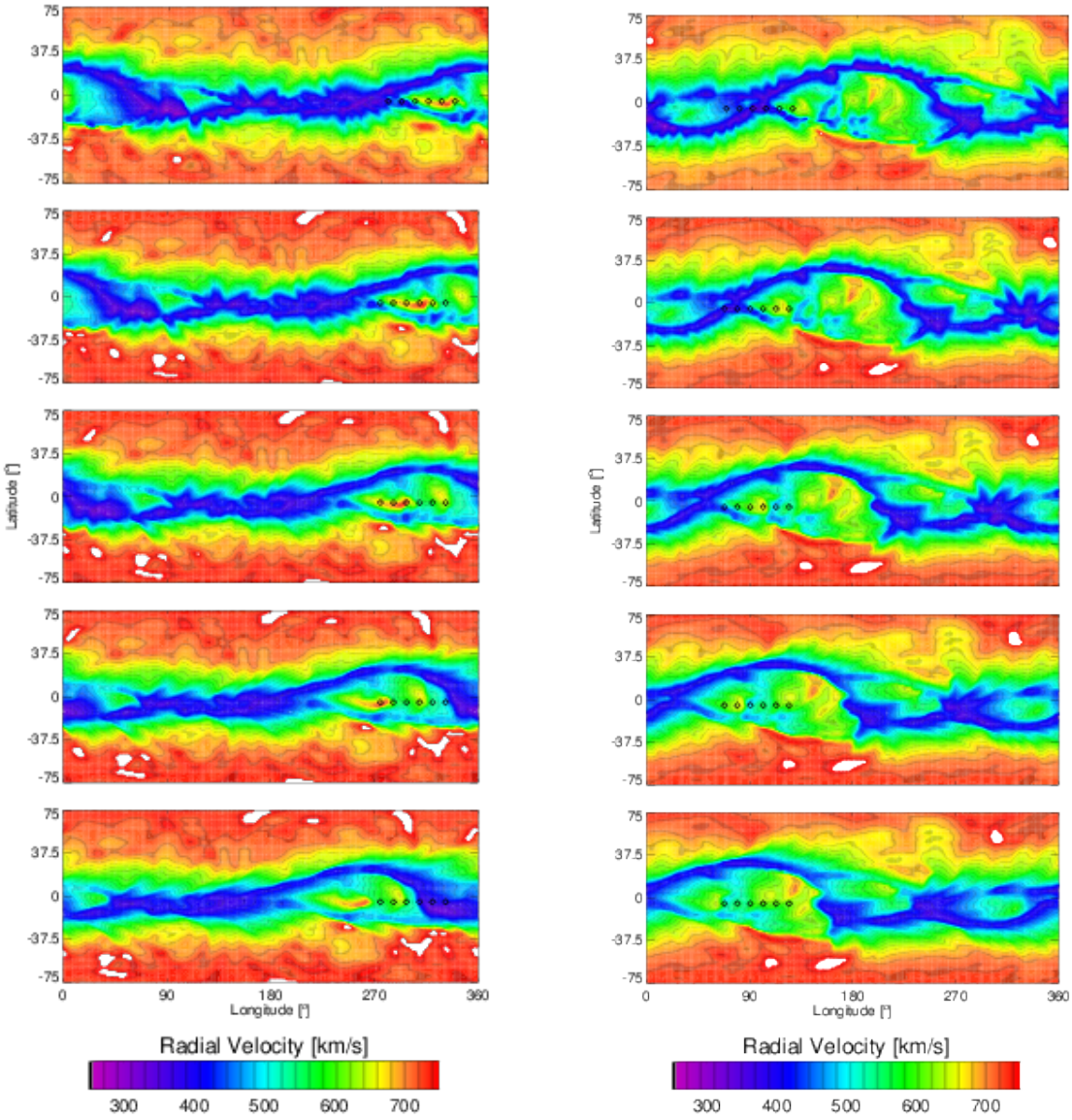

Fig. 3.1: Latitude vs Longitude plots of v_r at five different heliographic distances; 0.1 AU, 0.5 AU, 1.0 AU, 1.5 AU, and 2.0 AU, for CR 2058 (left) and CR 2060 (right). The black diamonds represent the latitude and longitude from which data as a function of radius is extracted.

wind that precedes it is similar for both Carrington Rotations, and so both HSSs are flowing into similar solar wind.

On global scales, the bands of slow winds in these Carrington Rotations differ. In CR 2058, the band of slow wind is relatively wide and all pseudostreamers remain near the streamer belt. The equatorial HSS being examined is elongated; it spans a wide longitudinal extent but is narrow in latitudinal extent. CR 2060, shown as the right column in Figure 3.1 has slow wind that is narrower along its entire extent and the bifurcation of the pseudostreamers extend to further separations from the streamers. While there is still only one equatorial HSS that exceeds 700 km/s, the same source as in CR 2058, it has evolved. Its shape in CR 2060 is slightly smaller in longitude but broader in latitude and the highest speed attained has decreased compared to its equivalent in CR 2058.

In order to understand the differences in evolution of SIRs due to the shapes of HSSs that drives them, it is important to understand the 3D shape of each HSS. To this end, each is presented in a different projection. Figure 3.2 shows v_r for CR 2058 (left) and CR 2060 (right) as a function of radial distance from the Sun and longitude in a cone of constant latitude, 3.75° south of the heliographic equator but within the range of the heliographic angle, θ_B, the range of inclination of the ecliptic relative to the heliographic equator.

As can be seen in Fig. 3.2, the difference between distributions of solar wind speeds in the plane 3.75° south between CR 2058 and CR 2060 is striking. During CR 2058, most of the solar wind present is slow ($<$ 400 km/s) with two broad bands of fast solar wind ($>$ 600 km/s). The fastest wind in this plane is faster than 700 km/s. Each interval of slow and fast wind has a fairly wide longitudinal extent, which will translate into long duration intervals as observed at 1.0 AU. In contrast, most of the wind present in the same plane for CR 2060 is fast, with three wide

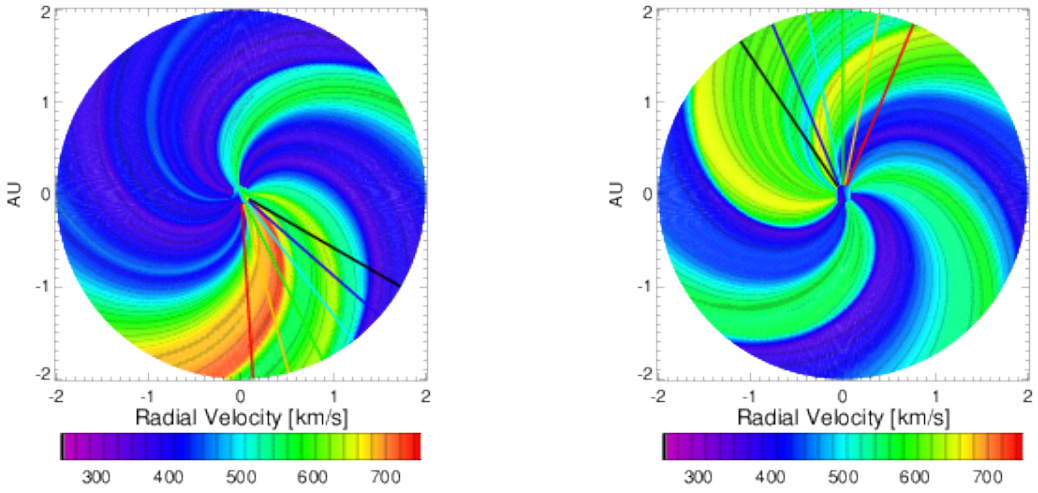

Fig. 3.2: Radius - Longitude plots of v_r at a constant latitude of 3.75° south of the heliographic equator, for CR 2058 (left) and CR 2060 (right). The lines of different color at a constant latitude correspond to the black diamonds in Fig. 3.1.

bands of slow solar wind. The slow wind in this plane is not as slow and the fast wind is not as fast as in the same plane during CR 2058. We can already see that the large scale structure of the solar wind has greatly affected what will be observed in a particular latitudinal cone near the ecliptic. We will qualify how this will affect the local evolution of SIRs.

In order to highlight the importance of the latitudinal extent of the HSS driving the SIRs, meridional slices offer a useful perspective. Figure 3.3 and Figure 3.4 show v_r as a function of heliographic distance and latitude at six different longitudes, each of which is represented by the coloured lines in Fig. 3.2 and/or diamonds in Fig. 3.1. Conversely, the cone of constant latitude in Figure 3.2 is indicated by the black lines transecting the HSS in Figure 3.3 and Figure 3.4. Each meridional slice shows the global structure of v_r at different longitudes and hence different distances and evolutionary stages of the SIR.

Consistent with previous comparisons, in Figure 3.3, the maximum speed of the HSS of interest during CR 2058 is faster than its counterpart during CR 2060,

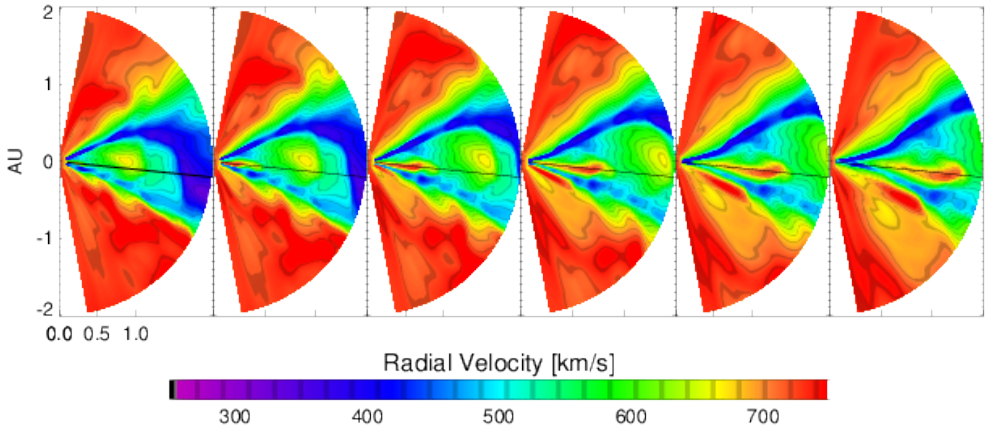

Fig. 3.3: Slices through the global LFM-helio solution for CR 2058. Six meridional slices show the structure of v_r, transecting the SIR at different heliospheric distances show the evolution of the latitudinally narrow HSS.

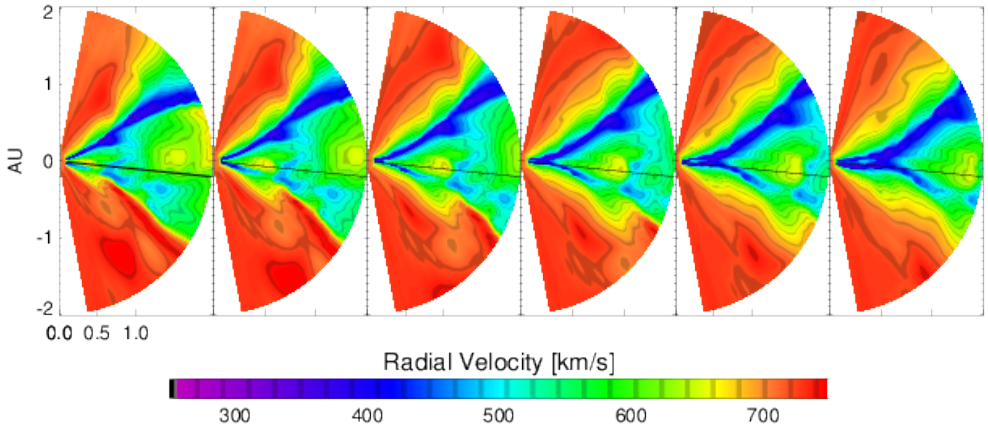

Fig. 3.4: Slices through the global LFM-helio solution for CR 2060. Six meridional slices show the structure of v_r, transecting the SIR at different heliospheric distances show the evolution of the latitudinally broader HSS.

shown in Figure 3.4, and maintains a narrower latitudinal extent. One expects the different shapes of HSS will exert different distributions of dynamic pressure on the solar wind ahead of the structures. Both figures show the progression, in subsequent panels, of the HSSs propagating away from the Sun. In CR 2058, there is a large extent of slow solar wind ahead of the HSS, followed by a latitudinally broad HSS, a narrow band of slow wind, and then the narrow HSS of interest, appears in the third panel. As the narrow high speed stream catches up to the slow wind, it seems to pierce through the narrow band of slow wind ahead of it - although the acceleration from the rarefaction wave caused by the first HSS may contribute. Similarly, the HSS of interest in CR 2060 is separated from a preceding HSS by a narrow band of slow solar wind. In both Carrington Rotations, the HSS of interest is preceded by another HSS and a narrow band of slow wind. Although the amplitude of the velocity jump is not the same between the two, the conditions into which the HSS flows are similar.

3.2.1 Local SIR Evolution: CR 2058

We now focus on the local evolution of the SIR. To do so, we look at other MHD parameters that are frequently used to characterise SIRs in observations, such as the peaks in density, temperature, and magnetic field strength as well as the magnitude of the flow deflections. We focus on a subset of the latitudinal and longitudinal ranges at different heliospheric distances. Figures 3.5 and 3.7 show, from left, v_r, nr^2, $Tr^{3/4}$, and $B_r r^2$ from the inner boundary, 0.1 AU, to 2.0 AU at the same distance intervals as in Figure 3.1. Figures 3.6 and Figure 3.8 show all three components of the solar wind velocity in the RTN coordinates, where R is the radial direction, T is the azimuthal direction and N is the polar direction with the Sun at the origin. v_r is shown in the left column, V_ϕ is shown in the central column and V_θ is on the right.

The progression shown in the panels of each figure show the qualitative differences between the respective SIRs due to the shape of the HSS.

The top left panel of Figure 3.5 shows the HSS that will drive the SIR of interest. As mentioned earlier, it is preceded by another high speed stream, separated by a narrow band of slow solar wind: a tendril of a pseudostreamer. The other panels in the top row show that, as defined at the inner boundary, the slow wind is denser and hotter than the fast wind and the radial component of the magnetic field is uniform. The HCS, the white line separating magnetic field of opposite polarity, is embedded in the slowest, densest solar wind. Subsequent rows show the evolution of the SIR as it flows to increasing heliospheric distances. The separation between the HSS and the preceding slow wind decreases, the HSS accelerates wind ahead of it and by 1.0 AU has passed through the tendril of slow wind. Alternatively, one can think of this perforation of the pseudostreamer as the local plasma being accelerated by 50–100 km/s to an intermediate speed although the slow wind persists at adjacent latitudes. The peak plasma density at any of these distances is low relative to many SIRs, barely reaching $25/cm^3$ by 2.0 AU. This stands out in comparison to the HSS ahead of the one being considered by roughly 45° longitude, which is compressing the solar wind near the HCS in two bands. In this SIR, the peak densities are over $70/cm^3$. At 2.0 AU, the peak temperatures, however, are comparable in the two SIRs within CR 2058. Interestingly, the heating begins closer to the Sun for the narrow HSS than for the other. All inhomogeneity in $B_r r^2$ beyond 0.1 AU is due to dynamical evolution. The compression of the magnetic field is similar to that of the plasma density, namely B_r is not particularly intensified in the SIR driven by the narrow HSS.

The small peak density of the SIR in question may be understood by considering the shape of this particular HSS. The narrow latitudinal extent of this HSS means

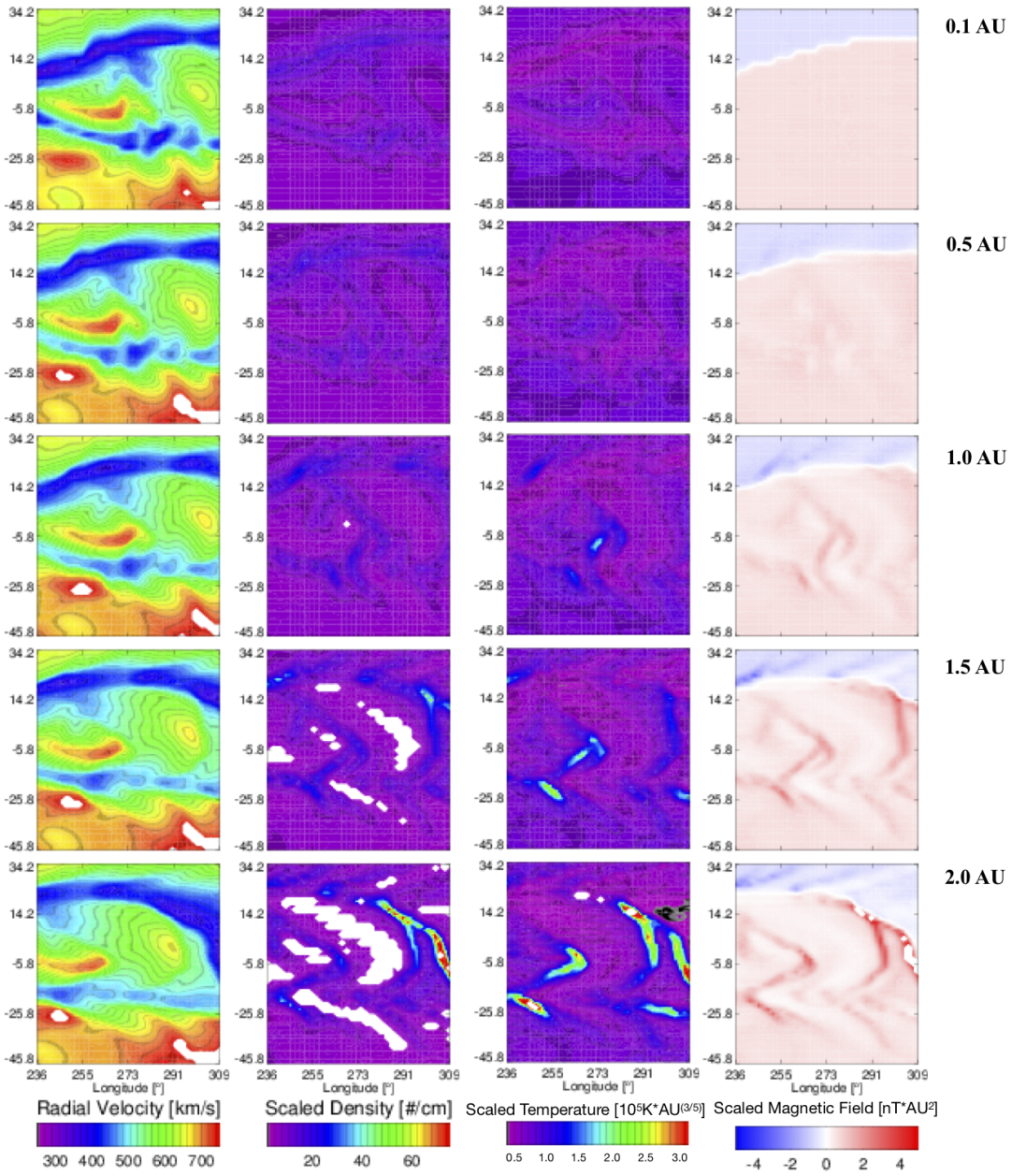

Fig. 3.5: Latitude vs longitude panels showing the detailed evolution of the SIR due to the narrow HSS during CR 2058. The columns show different plasma characteristics; v_r,nr^2, $Tr^{3/4}$, and $B_r r^2$. The rows represent the state of the solar wind at distance progressively further away from the Sun. Value that extend beyond the indicated color range are shown in white.

that it will be particularly efficient at deflecting flow in the polar direction. The amount of flow deflection can be seen in Figure 3.6, which is presented in the same format as Figure 3.5. The flow deflection in the azimuthal direction is shown in the central column while the flow deflection in the polar direction is shown in right hand column. The top row shows that there is negligible flow deflection at the IBC. The SIR in question exhibits a peculiar double-deflection flow feature in the azimuthal and polar velocities ahead of the HSS within 0.7 AU. The middle counter-streaming deflections cancel out and by 1.0 AU, where only the two-flow deflection pattern that is expected remains. At 1.0 AU, the slow wind is deflected in the direction of solar rotation (positive V_ϕ) while the fast wind is deflected in the opposite direction. The white space separating them is used to identify the SI both observationally and throughout this dissertation. This SIR exemplifies potential complications in using this SI identification method. Remarkably, the flow deflections in the polar direction - typically thought to be slower than their azimuthal counterparts (*Gosling and Pizzo*, 1999) are of the same magnitude and are well-ordered. The polar flow deflections correspond with expectations for a HSS stream with a normal oriented northward (negative on these plots) driving slow flow north and fast wind southwards and vice versa on the southern side of the narrow HSS. It may also be worth noting that the flow deflections for the SIR that abuts the HCS, shown as the white trace on the scaled magnetic field columns of Figures 3.5 and 3.7, have slower flow deflections, which bolsters the argument that the efficient deflection of plasma slows the compression and heating process. Finally, it is interesting that the HSS being considered generates a flow deflection wake, also seen in the increased density and temperature. While the flows speeds have roughly equal amplitudes in the azimuthal component, the deflection of the flow in the polar direction are stronger away from the HSS than towards.

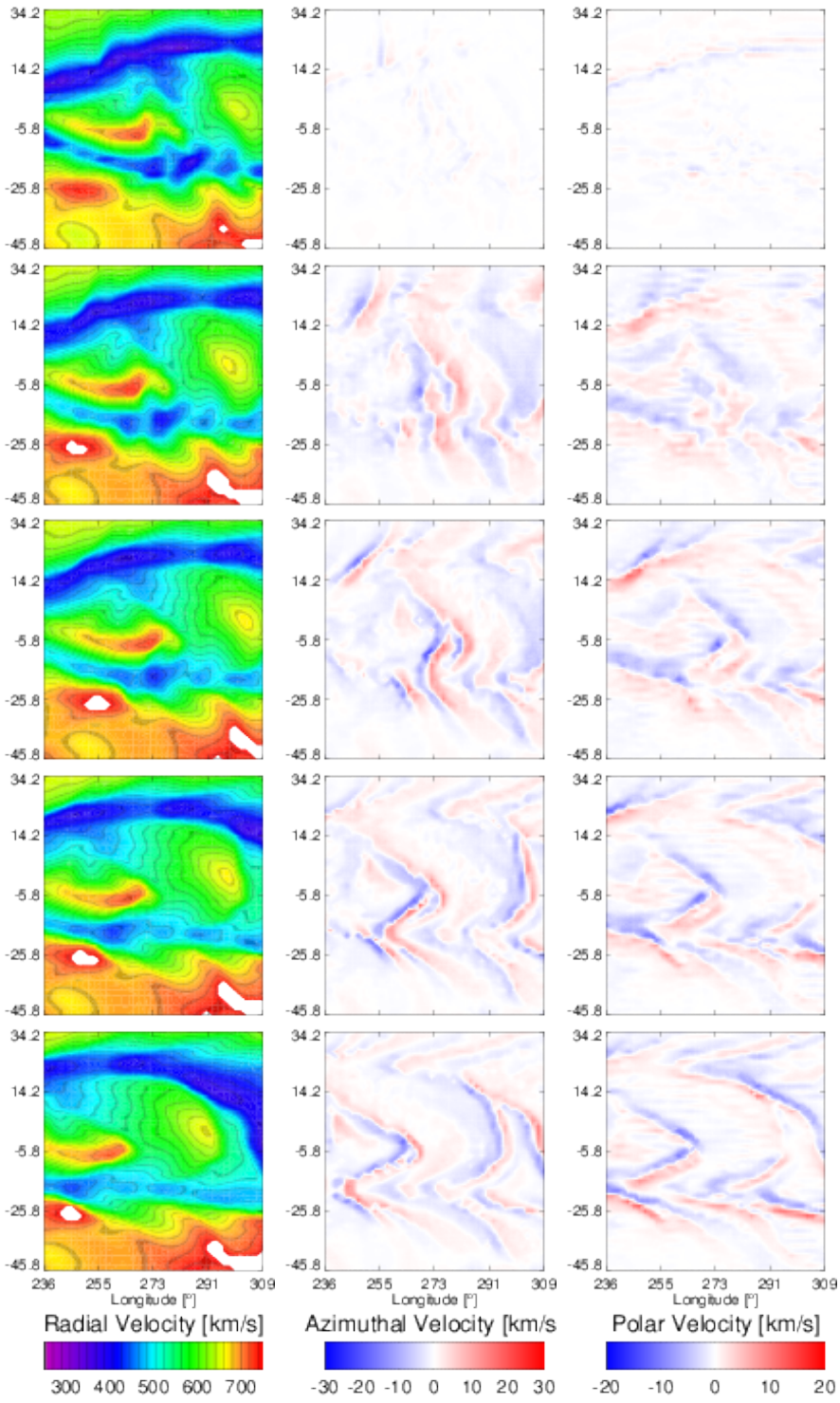

Fig. 3.6: The format is the same as Figure 3.5 except showing the flow deflection driven by the HSS. The columns show different components of plasma velocity; v_r,v_ϕ, and v_θ. The rows represent the state of the solar wind at distance progressively further away from the Sun.

3.2.2 Local SIR Evolution: CR 2060

While the two SIRs in CR 2058 show different evolution, the HSSs not only have different shapes but are also flowing into different preceding heliospheric conditions. The leading HSS is abutting the HCS and band of wide slow, dense wind, which also affects the evolution of SIRs. In order to compare HSSs flowing into similar heliospheric conditions, namely a thin tendril of slow, pseudostreamer wind, in turn preceded by a band of fast solar wind, we consider the same equatorial HSS as in CR 2058 but during its CR 2060 incarnation. Although the upstream conditions are similar, the recurrent HSS has evolved. In CR 2060, the HSS is not as fast but is broader in latitudinal extent than in CR 2058. Figure 3.7 shows the evolution of the CR 2060 SIR in the same format as Figure 3.5. The leftmost column shows v_r. As in CR 2058, the HSS of interest catches up to the slow wind ahead of it but in CR 2060 it does not accelerate it to intermediate speeds or appear to pass through it. Rather, both the fast wind and slow wind decrease in longitudinal extent and decelerate and accelerate, respectively, to intermediate speeds. The middle two columns show that the SIR has a substantial peak density and temperature by 1.0 AU and the right hand column shows that the magnetic field compression is strongest locally at the SIR.

As is evident in Fig. 3.7, the SIR in CR 2060 is blunt, in that it spans a range of latitudes at a particular longitude. This SIR resembles the idealistic spiral tilted planar surface of Fig. 1.2. The densest, hottest, and strongest magnetic fields are roughly co-located and are confined to the leading edge of the HSS.

As done in CR 2058, we now look at the amount of flow deflection generated by the SIR as a measure of its ability to remove plasma from the compressed region. Figure 3.8, in the same format as Figure 3.6, shows V_ϕ (middle column) and V_θ (right column) at increasing heliospheric distances. Since the HSS in CR 2060 is broader

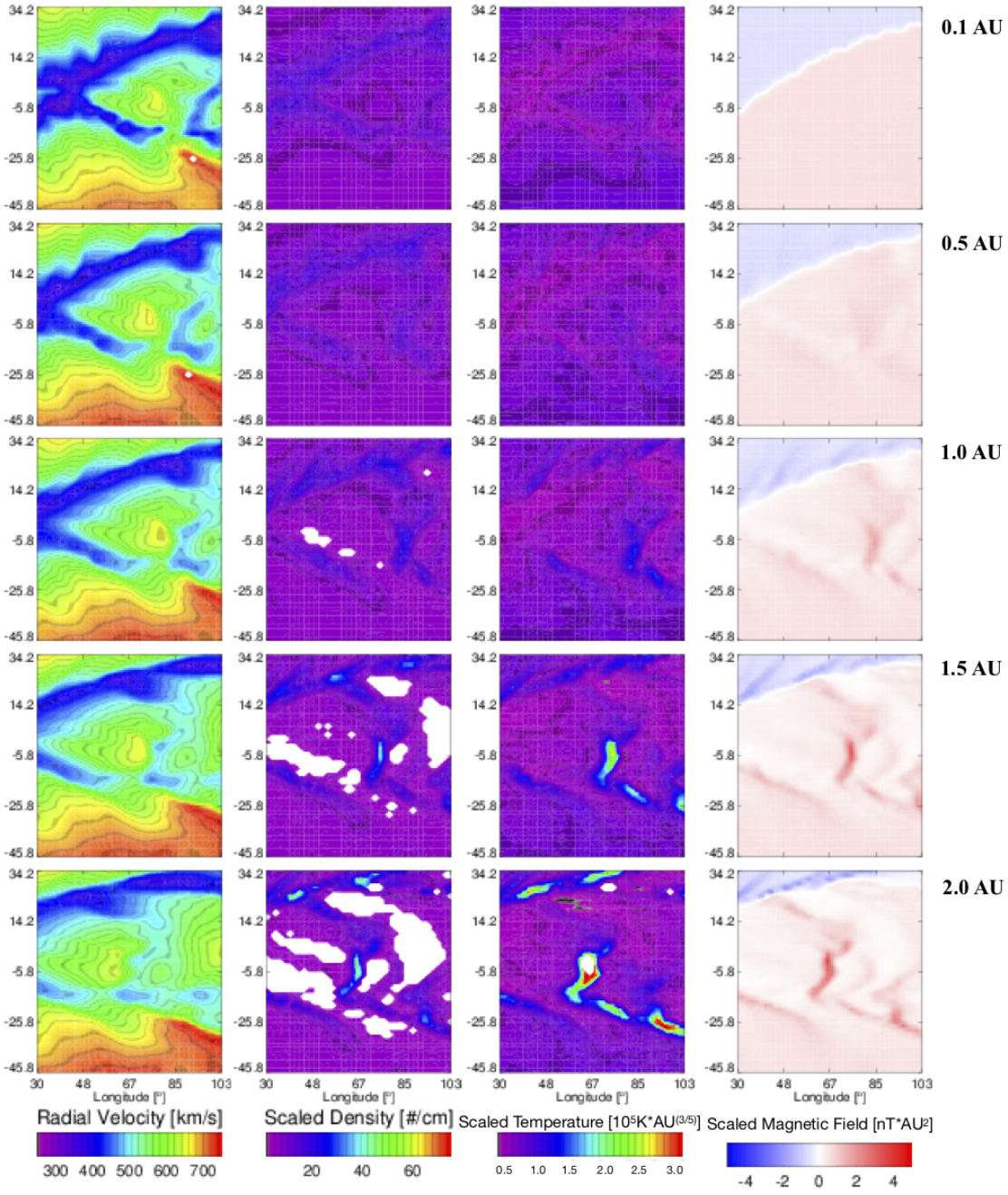

Fig. 3.7: Same as Figure 3.5 but for the HSS during CR 2060.

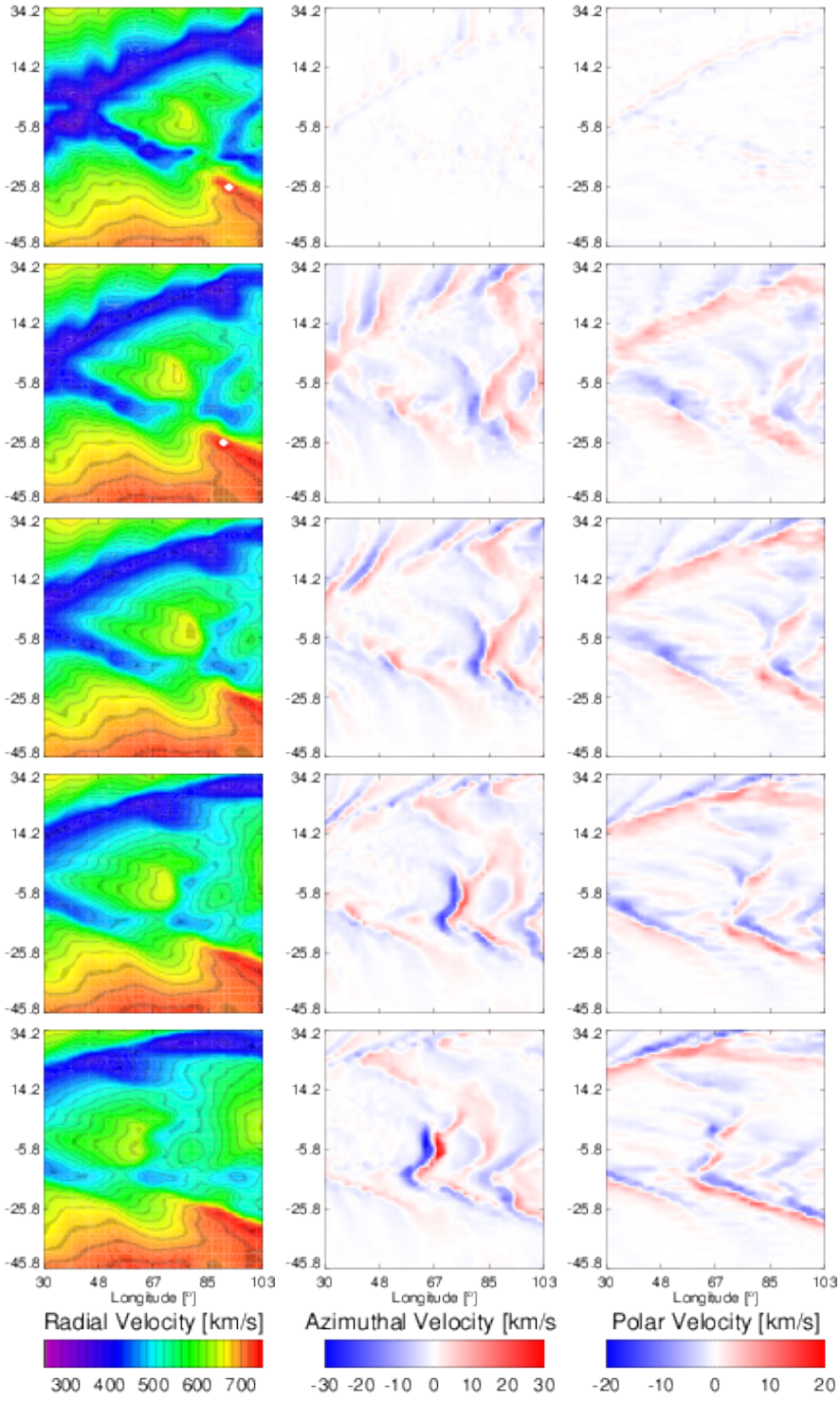

Fig. 3.8: Same as in Figure 3.6

in latitude, a larger extent of its interface surface with slow wind will have a normal with little or no polar component. Plasma deflections to the north and south are expected to be slower than in CR 2058 at all distances. The right hand column in Figure 3.8 confirms this; the deflected flow in the polar direction in the SIR are neither fast or particularly well-ordered. In terms of determining the location of the SI, the small-scale structure in V_θ would make measurements of maximal vorticity location dependent on latitude. In terms of V_ϕ, there is some flow deflection ahead of the SI in the direction of solar rotation for a larger latitudinal extent than in the opposite direction. The deflection in V_{phi} has a larger magnitude than in CR 2058 and the flow deflection in the azimuthal direction displaces the plasma back into the path of the SIR. The total flow deflection is smaller in CR 2058 than in CR 2060, which is consistent with the latter SIR having higher peak plasma density and temperature than the SIR in CR 2058.

The comparison of these SIRs during CR 2058 and CR 2060 is helpful in understanding the variation in observational signatures of SIRs in the ecliptic at 1.0 AU. Even for similar v_r vs time profiles, the amount of plasma compression and heating may depend on the shape of the HSS and the normal of the SI. A HSS that fills a smaller latitudinal range may be effective at driving flow deflections, through directional pressure gradients, while a HSS that is more blunt will drive a SIR with more compression and heating.

It is also clear from Figure 3.5 and Figure 3.7 that the local measurements of a spacecraft trajectory transecting either of these SIRs could differ substantially, even if separated by 1–2 degrees in latitude. This latitudinal shift is on the order of the variation in θ_B between subsequent Carrington rotations. Namely, small differences in spacecraft position may result in vastly different *in situ* observations. This is demonstrated quantitatively in Figure 3.9 for CR 2058 and Figure 3.10 for CR 2060,

which show simulated observations from five imaginary spacecraft separated in latitude only. The red line shows what would be observed by a spacecraft at a θ_B within the ecliptic (red) and what spacecraft 2° and 4° north (shades of blue) and south (shades of purple). The simulated parameters shown are v_r, nr^2, $Tr^{4/3}$, V_ϕ, and $|B|$ at 1 AU (left) and 2 AU (right). Note that the vertical scales are adjusted with distance.

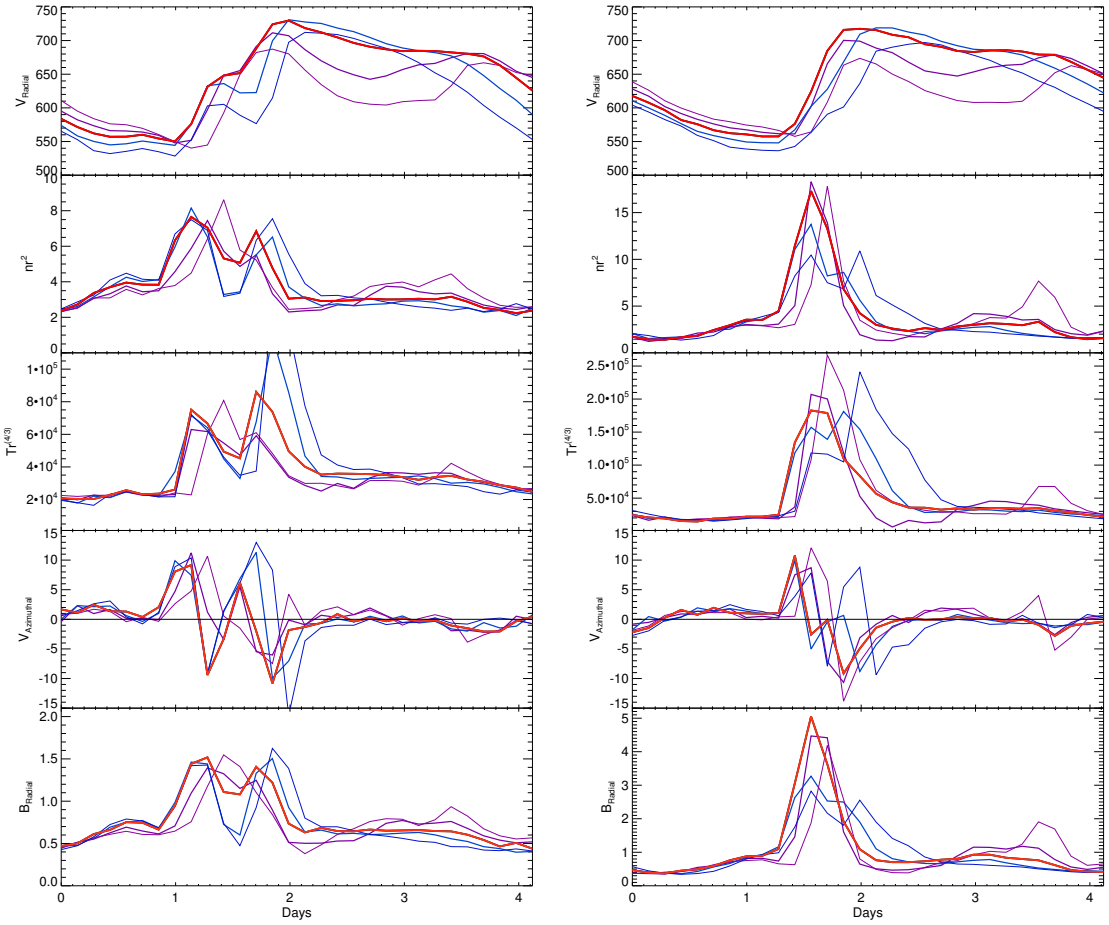

Fig. 3.9: Panels show v_r, nr^2, $Tr^{4/3}$, V_ϕ, and $|B|$ as would be measured by an in situ spacecraft as the SIR advects over it at 1.0 AU (left) and 2.0 AU (right). The red trace shows the observations in a particular plane. The blue traces show what the observations would have been 2° and 4° degrees northward and the purple lines show what the observations would have been for 2° and 4° southward.

In CR 2058, there is a lot of variability in v_r, n, T, V_ϕ, and $|B|$ as a function of latitude. The solar wind speed preceding the SIR is similar but the maximum speed attained, the monotonicity of v_r, and the timing of the peak speed vary with latitude. The speed profiles to the north and to the south are markedly different and the profile in the ecliptic is intermediate. Consequently, at 1.0 AU the amplitude and timing of the peak density and temperature can differ by up to half a day. The density enhancement and amplification of magnetic field to the north is double peaked whereas the density enhancement in the south has one prominent peak which occurs between the two at the more northern latitudes. The plasma temperature observed also depends on strongly on latitude. V_ϕ changes directions multiple times within the SIR and the SI is thus ambiguous to identify, using this method and indeed would also be for any of the methods discussed in Section 1.1.1. The characteristics of this particular SIR in CR 2058 vary considerably with latitude, though the amount of variability decreases from 1.0 AU to 2.0 AU.

The v_r measurements in CR 2060 shown in Figure 3.10, which has a SIR broader in latitude, show similar time profiles at all sampled latitudes at both 1 AU and 2 AU. The velocity profiles over the 8° of latitude centered on the ecliptic are remarkably similar to each other at 1.0 AU, particularly northward. The arrival times of the high speed stream agree within a few hours, and the arrival time of the SI agrees within the same range. At 2.0 AU, the v_r profiles are still remarkably similar, though the preceding slow wind differs in lowest speed attained by approximately 50 km/s. The arrival times of the peak density, temperature, SI as defined by V_ϕ and peak strength of the magnetic field coincide well at 1.0 AU and are nearly identical by 2.0 AU. The uniformity of this SIR across 8° is in stark contrast with that of CR 2058. We may also see that the identification of the location of the SI for this SIR yield an unambiguous location that would indeed be planar.

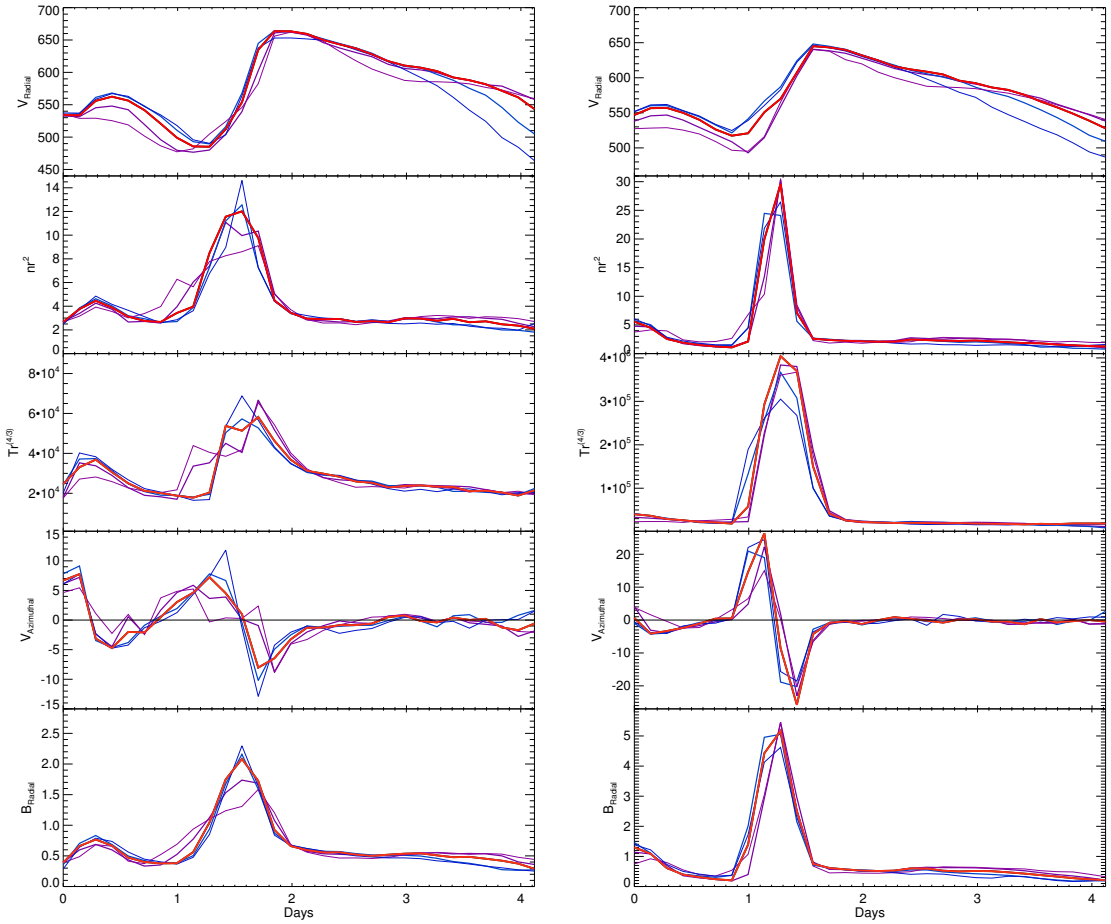

Fig. 3.10: Same as in Figure 3.9 but for the HSS in CR 2060.

The variability in observed parameters, as shown in Figures 3.9 and 3.10, demonstrates that even small differences in latitudinal positions may explain the variability in observations of the same SIR made by different spacecraft. For example, *Simunac et al.* (2009) compared observations from STEREO A, ACE, and STEREO B that displayed variability and timing differences inconsistent with a corotation of a planar SIR. The timing differences were larger than attributable to a rotational offset and the tilt of the SIR, as calculated from ACE observations. The conclusion drawn was that there must be some time variability in the solar wind that alters the SIR locally. There is inarguably time-variability in the solar wind, due to slow, rapid or

complex evolution of its coronal source (*Luhmann et al.*, 2008; *Arge et al.*, 2010) and small-scale transients being intermittently released (e.g. *Rouillard et al.* (2009)), particularly in the slow solar wind (*Yu et al.*, 2016). While this is a contributing factor, as evidenced in the difference of in the IBCs for CR 2060 and CR 2058, the results presented in this section argue that it is not a necessary factor when comparing observations of the same instance of the SIR by multiple spacecraft. We show that even in a steady-state simulation, a large amount of variability may be observed due solely to latitudinal structure.

The comparison of the same HSS during CR 2058 and CR 2060 illustrate that the dynamical evolution of SIRs, both on large and small scales, depends on the large scale structure of the HSS. While the high speed streams that were selected, as well the immediate surrounding solar wind, were as similar as possible for two different Carrington rotations and realistic solar wind models, there are still factors that differ between these cases. The relative contributions of these differences are unknown. Section 3.2 qualitatively described the differences in SIR evolution due to the global shape of the high speed stream by means of realistic examples. Admittedly, this approach is illustrative but lacks rigour.

In order to systematically characterize these effects, Section 4.2 studies the role of HSS shape more quantitatively via idealized IBCs. The large scale shape of the HSSs are not the only parameters to vary however, there is also the steepness of the gradient in v_r at a particular latitude as well as the properties of the plasma the HSS is flowing into. The shape of the HSS and the relative proportions of plasma density, temperature, and magnetic field strength between the fast wind and slow wind varies from SIR to SIR and also as a function of latitude within a SIR. The vast range of combinations makes predicting exact characteristics of a particular SIR very difficult. The underlying physics which could be gleaned despite such variability

may be buried beneath the attempts to accurately reproduce parameters at the inner boundary. We argue that these parameter variations are useful in characterising their importance during SIR evolution, given their effect on the magnetosonic and Alfvén speeds. The choice to study the effect of these parameters is bolstered by the surprising nature of the minimum of solar cycle 23, which exhibited a slightly slower, more weakly magnetized, colder and more tenuous solar wind. Indeed, this was the longest, deepest, and quietest solar minimum of the space age (*Solomon et al.*, 2018).

The solar wind contained the slowest average solar wind speeds, the corona was colder and the global magnetic field was weaker than any of the space-age solar cycles. SIRs were still observed but their characteristics had changed. From this perspective, it is interesting and worthwhile to investigate the influence of varying the plasma parameters at the inner boundary and quantifying their influence on the evolution of SIRs in the inner boundary. This is precisely what was done for a particular HSS during CR 1892 and will be discussed further in Section 3.3.

3.3 Influence of Plasma Conditions at the inner boundary condition

In this section, we revisit CR 1892 but focus more on the evolution of a particular SIR. We discussed the LFM-helio's success in reproducing the large-scale global structure of the solar wind for CR 1891–1895 in Section 2.2.3 and the sensitivity of the global solutions to the parameters set at the inner boundary of the LFM-helio in Section 2.2.4. We now turn to the effects that the various assumptions and variation of parameters listed in Table 2.2 and in Table 2.3 and their respective effects on the evolution of SIRs in the ecliptic plane. Although these particular variations in n, T, γ, and B_r are artificially constructed, they are nonetheless instructive in informing

us how the relationships between these parameters affect the evolution and local structure of SIRs.

In addition to the theoretical understanding of how changes in density, temperature, adiabatic index, and magnetic field strength affect the evolution of SIRs, this study attempts to quantify the importance of the characteristic speeds in the evolution of SIRs. An increase in magnetic field strength at the inner boundary of the LFM-helio will propagate throughout the solution domain and will necessarily increase the Alfvén speed throughout. Increases in density and/or temperature will also affect the sound speed. While the changes in characteristic speeds may not affect some quantitative parameters such as the maximum density or temperature attained, they may influence the evolution of the forward and reverse waves that bound the SIR, hence affecting its width.

Observationally, as discussed in Section 1.1.1, SIRs are bound by a forward wave on their leading edge and by a reverse wave on their trailing edge. Both are characterised by an increase in solar wind speed but the former involves a concurrent increase in plasma pressure while the latter involves a decrease in plasma pressure. The steepness of the waves determines whether or not these have developed into shocks and at which heliospheric distance they might do so. The phenomenology of shock development is still not well understood on a case by case basis and will be discussed in Chapter 4.

3.3.1 Evolution of SIR in CR 1892 Baseline Case

Before investigaing the effects of varying parameters at the inner boundary and their influence on the evolution of a SIR, we focus on the Baseline case. A particular high speed stream complex in CR 1892 that lies within the ecliptic plane is chosen and its evolution is described in Section 3.3.1. The differences that arise when the other assumptions are used at the inner boundary are discussed in Section 3.3.2.

Figure 3.11 shows v_r 5° north of the equatorial plane from 0.1 AU–2.0 AU. The black concentric semi-circles indicate the radial distances at which quantitative data has been extracted, namely: 0.1 AU, 0.5 AU, 0.8 AU, 1.0 AU, 1.2 AU, 1.5 AU, 1.8 AU, and 2.0 AU. Data is extracted from right to left, and shown color-coded on the right hand plot in Fig. 3.11. A spacecraft samples the solar wind of decreasing heliographic longitude as a function of time. The solar wind structure of interest is composed of two HSSs, the first abuts the heliographic streamer while the second flows into a pseudostreamer. The first HSS is relatively narrow and is preceded by a vast extent of sub-400 km/s solar wind. The shell of constant latitude, 5° above the heliographic equator in this case, shows that the first HSS, as with other HSSs of narrow longitudinal extent, is decelerated to intermediate speeds. The first HSS is followed by a narrow band of slow, pseudostreamer wind and then a second, wider extent of even faster wind. This second HSS also decelerates also but remains faster than 700 km/s within 2.0 AU.

The right hand side of Fig. 3.11 shows v_r quantitatively for both HSSs. A hypothetical spacecraft would encounter these solar wind streams from right to left, with decreasing heliographic longitude as a function of time. At the inner boundary, the first HSS has wind faster than 500 km/s that spans approximately 20° in longitude while the second HSS spans approximately 35°. The second HSS is roughly 100 km/s faster than the first. The increase in v_r is 300 km/s for the both the first and second HSSs. The angular separation between peak velocities is roughly 40° at the inner boundary. As the simulated HSSs flow outwards into the heliosphere, the dynamical evolution of the SIRs erodes the v_r profile. Both HSSs steepen on their leading edge, meaning that the jump from slow wind to the peak speed occurs over a compressed longitudinal distance. Conversely, the trailing edge of the HSSs is stretched and smoothed. The longitudinal extent of high speed wind decreases as a

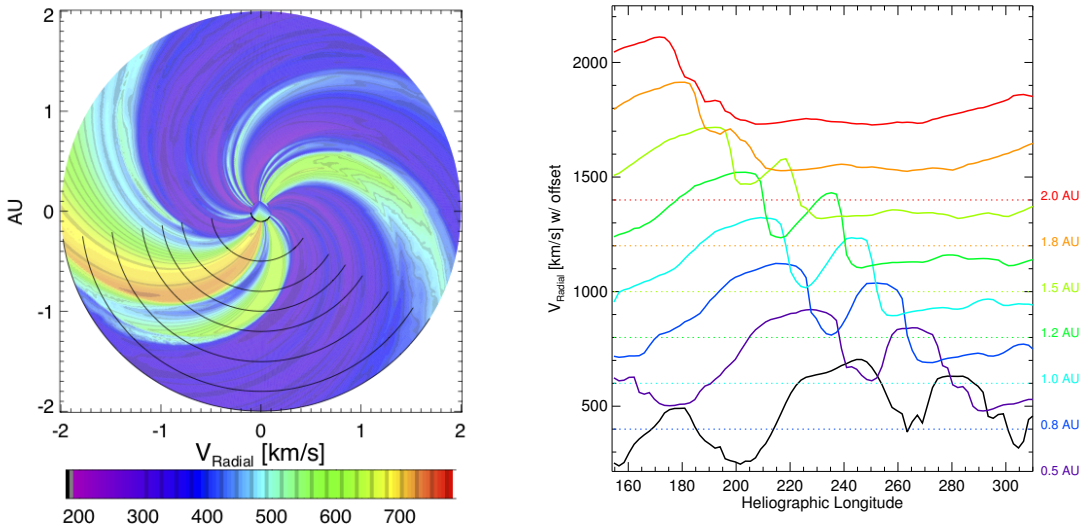

Fig. 3.11: Baseline v_r as a function of r and ϕ at 8° north of the heliographic equatorial plane from 0.1 AU to 2.0 AU for the Baseline case as described in Section 2.2.4 on the left. On the right is v_r as a function of longitude at each of the black concentric semi-circles on the contour plot. Each colored line represent v_r at a different radius, indicated on the right by the offset line (the horizontal dashed line), transecting the SIR at different stages of evolution. The black line indicates the inner boundary condition. The colored lines are offset from each other by 200 km/s, for visual clarity, the solar wind is not accelerating. The offset x axis is shown as a dotted line of the appropriate color for each radius.

function of increasing distance from the Sun. This occurs in an obvious manner for both streams until 1.5 AU, beyond which, the first HSS is nearly unidentifiable as it has been evolved into a large extent of intermediate speed wind. By 2.0 AU, the second HSS has evolved into a narrow saw-tooth shaped pulse of fast wind, with a speed increase of over 300 km/s.

As will be shown later, the gradients in pressure have significantly redistributed the momentum flux of the solar wind within 2.0 AU. Before delving into this, however, it is instructive to understand the evolution of the other solar wind parameters that are frequently observed and reported in the literature or used for space weather

predictions; namely the solar wind n, T, and B_r. The solar wind flow deflections will also be considered.

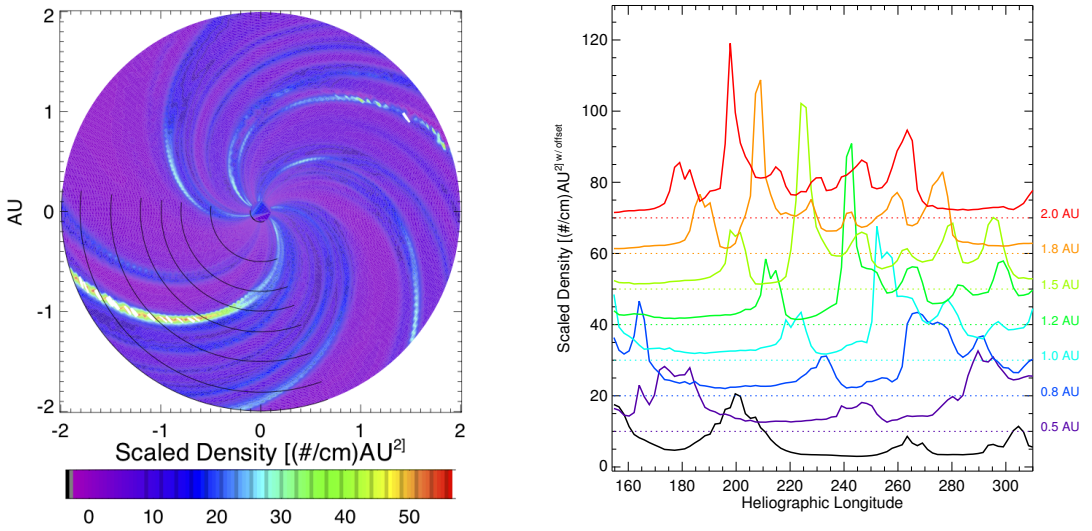

Fig. 3.12: Same as Fig. 3.11 but for scaled number density, nr^2. Each colored line represent $n * r^2$ at a different radius, indicated on the right of the plot, transecting the SIR at different stages of evolution. The colored lines are offset from each other for visual clarity and as such seem falsely accelerated. The offset x axis is shown as a dotted line of the appropriate color for each radius.

The empirical relation used to define n at the inner boundary dictates that the slow wind is denser than the fast wind. As can be seen in the scaled density shown in Figure 3.12, the solar wind scaled number densities at the inner boundary preceding the first and second HSSs respectively, normalized to 1.0 AU, are about just above and just below 10 AU^2/cm^3, respectively. The fast wind for both have $n \approx 4/cm^3$. As the SIRs evolve, the scaled number density ahead of the first HSS, although being preceded by fluctuations, is increasingly compressed ahead of the fast wind. The peak density increases from $20(AU^2/cm^3)$ at 0.5 AU, through $35(AU^2/cm^3)$ at 1.0 AU, reaching and maintaing a maximum of just above $50(AU^2/cm^3)$ between 1.2 AU – 2.0 AU. Considering the density of the plasma immediately preceding the

first density enhancement, the compression ratio extends from 1.3–4.2 for the first HSS.

The density enhancement due to the second HSS is narrower in longitudinal extent for the radial distances considered and has much lower peak densities. It is also simpler, a single peak in density, as the plasma being swept up is made uniform by the preceding rarefaction wave. The peak density is smaller than in the first SIR, despite the similar speed increase, attaining a maximum value of 18 (AU^2/cm^3) and a maximum compression of about ≈ 9. Thus, despite having a lower peak density than the first SIR, the second SIR drives a stronger compression. Finally, it is clear from the heliographic longitude of the density peaks that the SIRs are getting closer. The angular separation at 0.1 AU is 40°. This decreases with distance from the inner boundary and is just over 20° at 2.0 AU.

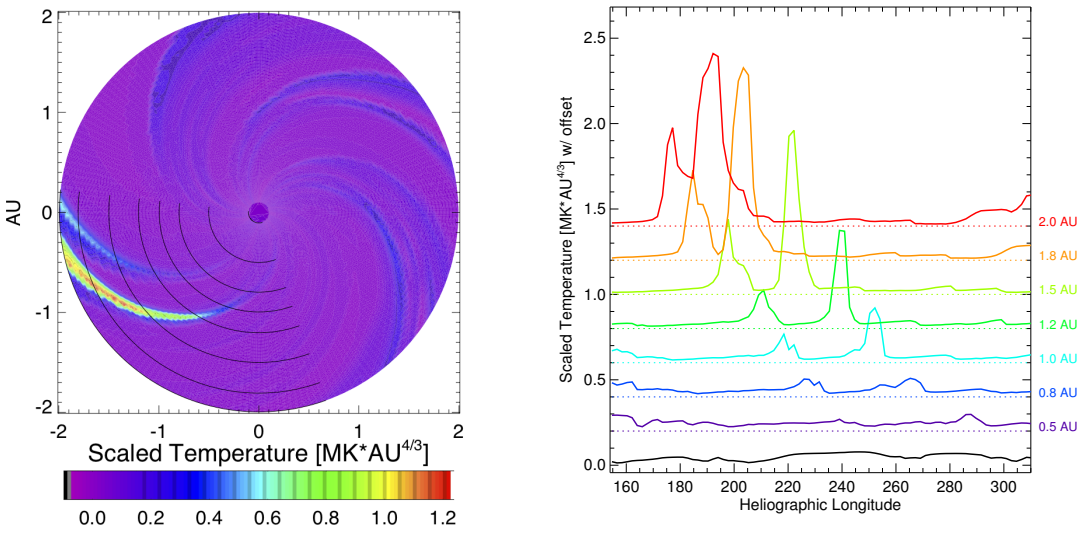

Fig. 3.13: Same as Fig. 3.11 but for scaled temperature, $Tr^{4/3}$. Each colored line represent $Tr^{4/3}$ at a different radius, indicated on the right of the plot, transecting the SIR at different stages of evolution. The colored lines are offset from each other for visual clarity and as such seem falsely accelerated. The offset x axis is shown as a dotted line of the appropriate color for each radius.

Figure 3.13 shows that the simulated temperature for the solar wind for the Baseline CR 1892 is fairly uniform, and too cold, except for SIRs, within which it is compressively heated. It is worth mentioning again here that the kinetic heating processes present in the solar wind are not included in the ideal MHD method of the LFM-helio. There is very little variation in the temperature at any distance, other than the heating due to compression. Withing the SIRs, as with nr^2, the enhancement due to the first SIR is greater than the second, with peak normalized temperatures of 1.1 $MKAU^{4/3}$ and 0.6 $MKAU^{4/3}$ respectively. Both temperature peaks occur behind, meaning at smaller heliographic longitudes, than the corresponding peaks in densities. This ordering is typical of *in situ* observations of SIRs (*Gosling and Pizzo*, 1999; *Jian et al.*, 2006).

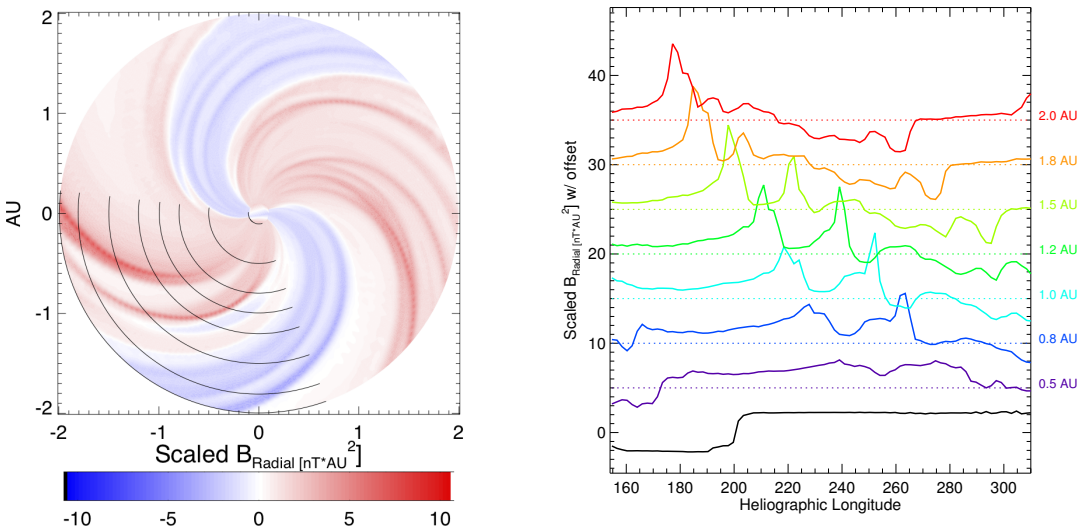

Fig. 3.14: Same as Fig. 3.11 but for $B_r r^2$. Each colored line represent $B_r r^2$ at a different radius, indicated on the right of the plot, transecting the SIR at different stages of evolution. The colored lines are offset from each other for visual clarity and as such seem falsely accelerated. The offset x axis is shown as a dotted line of the appropriate color for each radius.

The B_r^2 input at the inner boundary in the Baseline case is uniform. Therefore, any deviation from uniformity is completely due to the dynamical evolution. Fig-

ure 3.14 shows that indeed, the regions of largest B_r occur within the SIRs. The polarity of both SIRs is the same, namely positive B_r but that the first SIR evolves in proximity of the HCS. Furthermore, the plane considered in these figures transects a warped and inclined HCS. The high density Heliospheric Plasma Sheet (HPS) which surrounds the HCS, skimmed by path of interest, explains the variations in density seen in Figure 3.12 ahead of the first SIR, where no significant variation of v_r is seen in Figure 3.11. Similar to n and T, the first SIR evolves more rapidly, then once this HSS has eroded away, the second SIR has a stronger B_r signature. At 1.0 AU, the peak B_r reaches 7–8 nT. The strongest normalized B_r is $\approx 9\ nT$ and occurs at 1.8 AU. By 1.5 AU, the second SIR keeps compressing the plasma and magnetic field and becomes more compressed than the first, which seems to have been 'pulled apart'.

Observationally, the arrival time of the SI is often determined using $V_\phi = 0$ and the orientation of the SI is determined using the assumption that the flow deflection magnitudes are symmetric with respect to a planar SI. Figures 3.15 and 3.16 show V_ϕ (top) and V_θ in the same plane as Figures 3.11 – 3.14. While it is obvious that there are small scale deflections at all longitudes, the largest flow deflections in this plane occur at the two SIRs being considered. Furthermore, V_ϕ and V_θ are small within 0.8 AU and grow to be significantly larger than background variations at 1.2 AU and beyond. Azimuthally, the deflection occurs in the same direction for both SIRs, as the slow wind ahead of the SIR is deflected in the direction of solar rotation according to the Parker spiral angle, and the fast wind behind is deflected anti-sunward.

For V_θ, the deflection occurs in opposite directions for the first and second SIR. As the first HSS erodes away, no longer driving the SIR, and the second HSS catches up to the first, the negative V_θ deflections evolve closer together and by 2.0 AU, have eliminated any positive flow. This would suggest SIRs with opposite orientations.

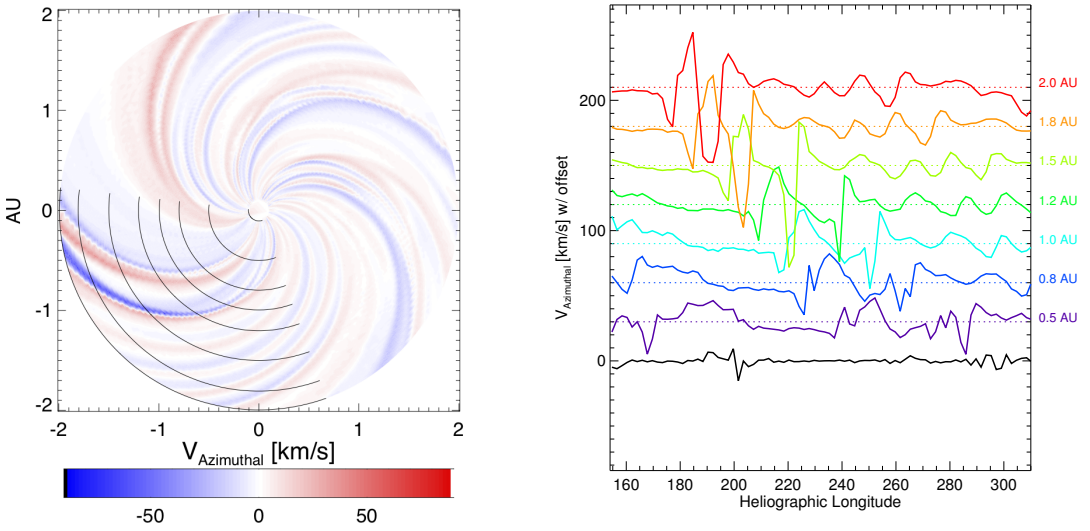

Fig. 3.15: Same as Fig. 3.11 but for V_ϕ (top). Each colored line represent V_ϕ at a different radius, indicated on the right of the plot, transecting the SIR at different stages of evolution. The colored lines are offset from each other for visual clarity and as such seem falsely accelerated. The offset x axis is shown as a dotted line of the appropriate color for each radius.

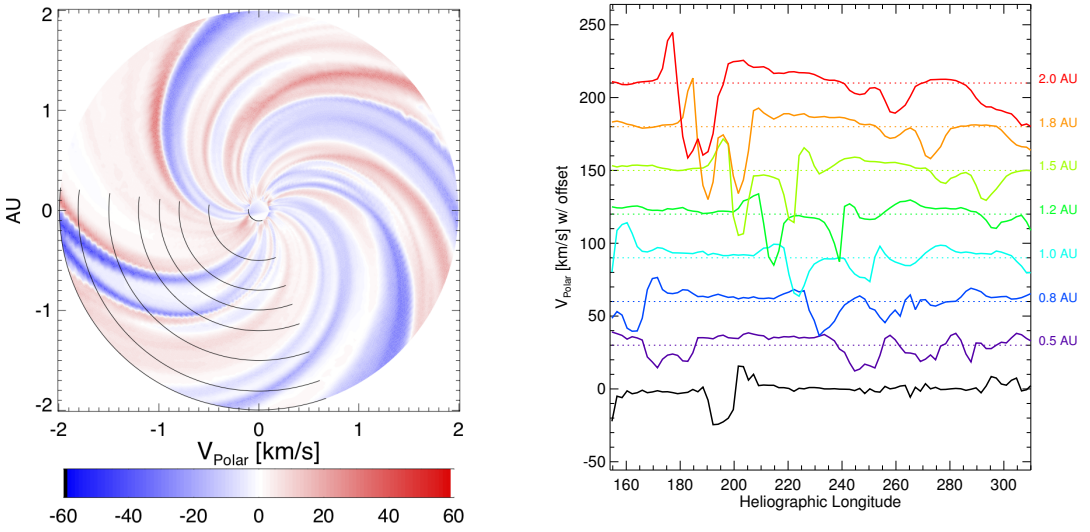

Fig. 3.16: Same as Fig. 3.11 but for V_θ. Each colored line represent V_θ at a different radius, indicated on the right of the plot, transecting the SIR at different stages of evolution. The colored lines are offset from each other for visual clarity and as such seem falsely accelerated. The offset x axis is shown as a dotted line of the appropriate color for each radius.

In order to better understand the large scale shape of the SIRs in three dimensions, and in particular the latitudinal shape and orientation, consider Figure 3.17. v_r,P_{mag}, and P_{therm} are shown in the r-θ plane at longitudes that transect the SIRs at different distances and thus, stages of evolution. The top row shows v_r and specifically the shapes of the HSSs that are driving the SIRs of interest. Visible in all of the panels is a thick band of slow wind, containing the HCS, which is warped and tilted as it flows out to 1.0 AU. The fast wind behind it drives the first SIR discussed above and is consistent with the classic model of SIR formation (*Gosling and Pizzo*, 1999; *Crooker et al.*, 1996). Behind the first HSS is a narrow band of slower, pseudostreamer wind which is followed by a latitudinally narrow band of fast solar wind.

The bottom two columns of Figure 3.17 show the logarithm of the thermal and magnetic pressures. The thermal pressure is determined by the polytropic relation as defined in Equation 1.3, where for the Baseline $\gamma = 5/3$, and hence decreases as $r^{-10/3}$. The scaling with distance of the magnetic pressure depends on the amplitude of the components of $\vec{B}$. B_r falls off as r^{-2} and is the dominant component within 1 AU, beyond which B_ϕ, which falls off as r^{-1}, dominates due to the winding of the Parker spiral. B_θ falls off as r^{-1} also but since we set this to 0 nT at the inner boundary and only small flow deflections will drag field into that component, this is a smaller contribution.

In general, the signature of the SIRs in P_{therm} and P_{mag} are clear and roughly two orders of magnitude stronger than the pressures in the surrounding plasma. There is a region of high P_{therm} extending southward in the two leftmost panels that is also prominent in P_{mag}. As alluded to earlier, the first SIR has roughly the shape expected for polar coronal holes, namely almost planar and inclined towards the heliographic equator (*Pizzo*, 1982; *Crooker et al.*, 1996; *Riley et al.*, 2003; *Gosling*,

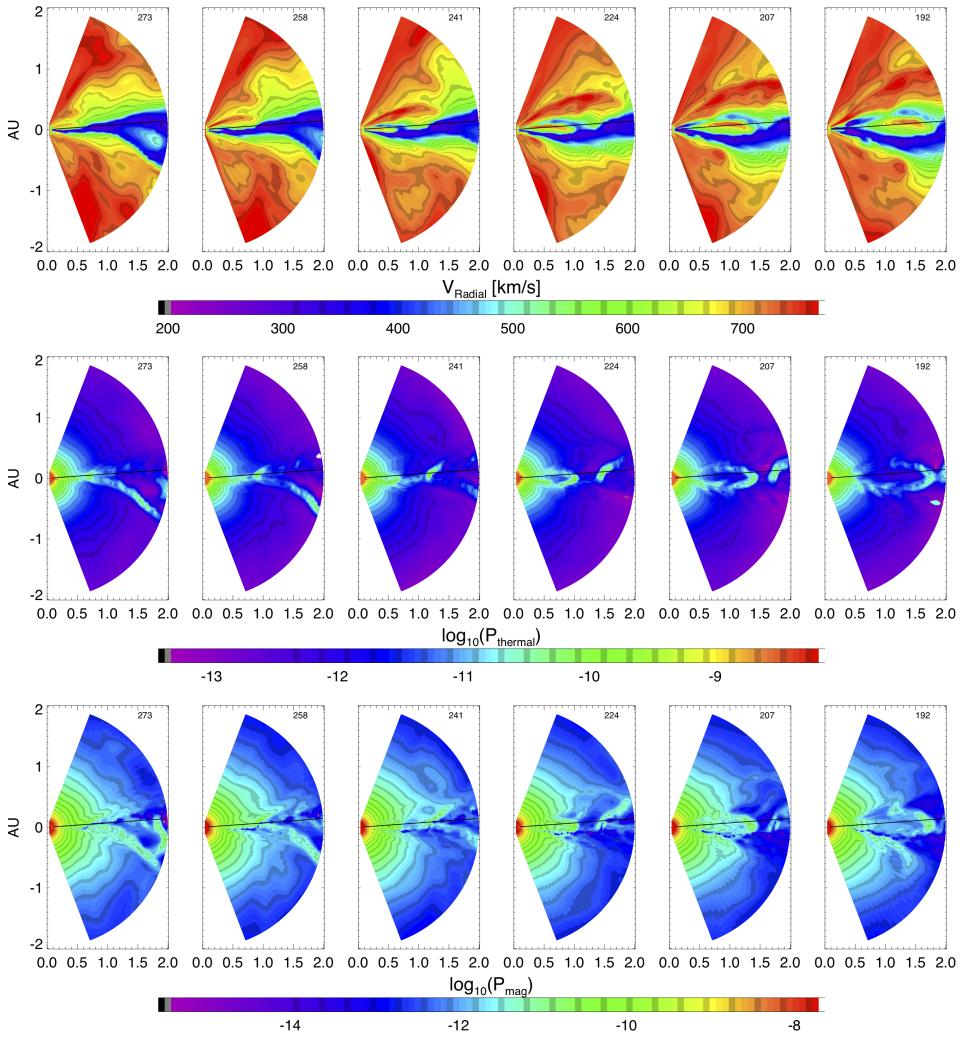

Fig. 3.17: Offering another view of the SIRs being considered, these plots show solar wind parameters as a function of r and θ. The top row shows v_r, the subsequent rows show the logarithm of the thermal pressure and magnetic pressure respectively. The small numbers on the top right of each plot indicates the longitude being shown. Note that the pressure plots do not have the same color bar.

1993; *Riley et al.*, 1996). The second SIR is driven by a latitudinally narrow HSS, expected for small equatorial coronal holes, and drives an arrowhead-shaped SIR, as seen in simulations (*Pizzo*, 1982; *Riley et al.*, 2003) and *in situ*. We then turn to the differences in SIR evolution caused by small variations in the plasma parameters and canonical variables, as imposed during the parameter sensitivity study. This will highlight the effects of changing the plasma parameters on the evolution of a SIR which had identical velocity profile input at the inner boundary, therefore isolating effects due to frame independent plasma parameters.

3.3.2 Evolution of SIR in CR 1892 : Parameter Sensitivity

This section will focus exclusively on the effects of the differences made about the properties of the plasma and magnetic field as described in Chapter 2.2.4. It is worth emphasizing here that the v_r input at the inner boundary is identical for all of these cases. Therefore any differences in v_r beyond the inner boundary are consequences of the differences in dynamical evolution due to differing plasma density and temperature at the inner boundary. It is worth a reminder at this point, that the set of assumptions used here and listed in Table 2.2 do not change the plasma properties by a large amount. Hence, as noted in Section 2.2.4, the effects of the sensitivity study are small on global scales, with the exception of Case B_R. However, the effect on the specific features of SIRs is investigated here. Though this investigation tests the LFM-helio's performance and sensitivty, it further has the important application of shedding insight into the observational differences between SIR observations in the ecliptic plane between Solar Cycle 22 and Solar Cycle 23.

Explicitly, the observations from near the ecliptic plane of SIRs during Solar Cycle 22 were fairly consistent. The SIRs observed were usually tilted along the Parker Spiral angle for the solar wind speed of the SI, were inclined towards the heliographic equator relative to the hemisphere of the source HSS. Namely, the classical

four-stream two-sector pattern of the tilted dipole solar wind model would have SIR normals pointing Southward from a high speed stream originating in the northern hemisphere and vice versa. In general, this is what has been observed. The peak temperature, density, total pressure of most SIRs fell within a normal distribution (*Jian et al.*, 2006). Most frequently, the forward and reverse waves have not yet steepened into shocks at 1.0 AU.

Solar cycle 23 surprised observers by being host to solar wind that had the same speed as in previous cycles but was otherwise weaker. The magnetic field, as observed *in situ* at 1.0 AU, was roughly 30% weaker than in Solar cycle 22. The density of the slow wind was also lower and the temperature was cooler. The reason for this is still not understood and is outside the scope of this dissertation but is thought to be a consequence of the relative dominance of the quadrupole moment of the solar dynamo over the dipole moment of previous solar cycles. As a result, the magnetic field at the poles of the Sun were weaker than in previous cycles and equatorial coronal holes were more prevalent than in previous cycles. The additional open magnetic field lines at low latitudes divert the HCS and create current-free bands of slow wind, pseudo-streamers. Pseudostreamers and the SIRs they precede have already been discussed in an indirect way in this dissertation. The focus of this section is the effect of small variations in plasma density and temperature on the evolution of SIRS. This is done in a comparative way, relative to the Baseline case of CR 1892.

Since *in situ* observations of SIRs also typically include the peak value of the parameters, such as density, pressure, and magnetic field strength, these will also be calculated relative to the SIR in Baseline. While the velocity profile at the IBC is identical for all cases, the characteristic speeds for all cases differ, which affects how

the pressure ridge of the SIRs propagates and steepens. This will change to location, size, and characteristics of the SIR.

We begin with the difference between each of the cases and the Baseline. Figure 3.18 shows v_r in the equatorial plane for each of the cases with v_r from the Baseline subtracted, after the runs have been rotationally aligned. It can be seen that Cases nv^2 and Baseline have nearly identical velocity structures from 0.1 AU to 2.0 AU in the equatorial plane, shown here, and at all latitudes. Cases P_{Total}, T, and B show substantially more variation, where typically the v_r is larger (blue) in these cases than in the Baseline, though there are regions where the wind is slower (red). The dashed and dotted lines are contours of different speeds in the Baseline run. The spirals of faster wind in the test cases result from both faster high speed wind and the Parker spiral being less tightly wound, resulting in SIRs that arrive before they do in the Baseline case. Hence, the differences shown in Fig. 3.18 combine differences in azimuthal position, or observationally in timing of arrival times, and in amplitude. Any difference in the velocity profile is due to the dynamical effects of the assumptions made at the inner boundary.

In order to differentiate between temporal and spatial differences, let's now consider Figure 3.19. This figure shows v_r as a function of longitude for several radial distances from the sun, indicated in the top left of each panel, for each of 8 cases. The distances considered are 0.1 AU, 0.5 AU, 0.8 AU, 1.0 AU, 1.2 AU, 1.5 AU, 1.8 AU, and 2.0 AU. The radial sampling is higher near and after 1 AU both because this is the region of most *in situ* observations and because this is the region of interest for shock formation. The cases considered are the low and high resolution versions of the Baseline set of assumptions. Cases nv^2, P_{total}, T,B, and γ are all in low resolution while case $T3$ N $Scales$ and $T3$ B $Scales$ are in high resolution. The difference in resolution is coincidental; the runs were generated a

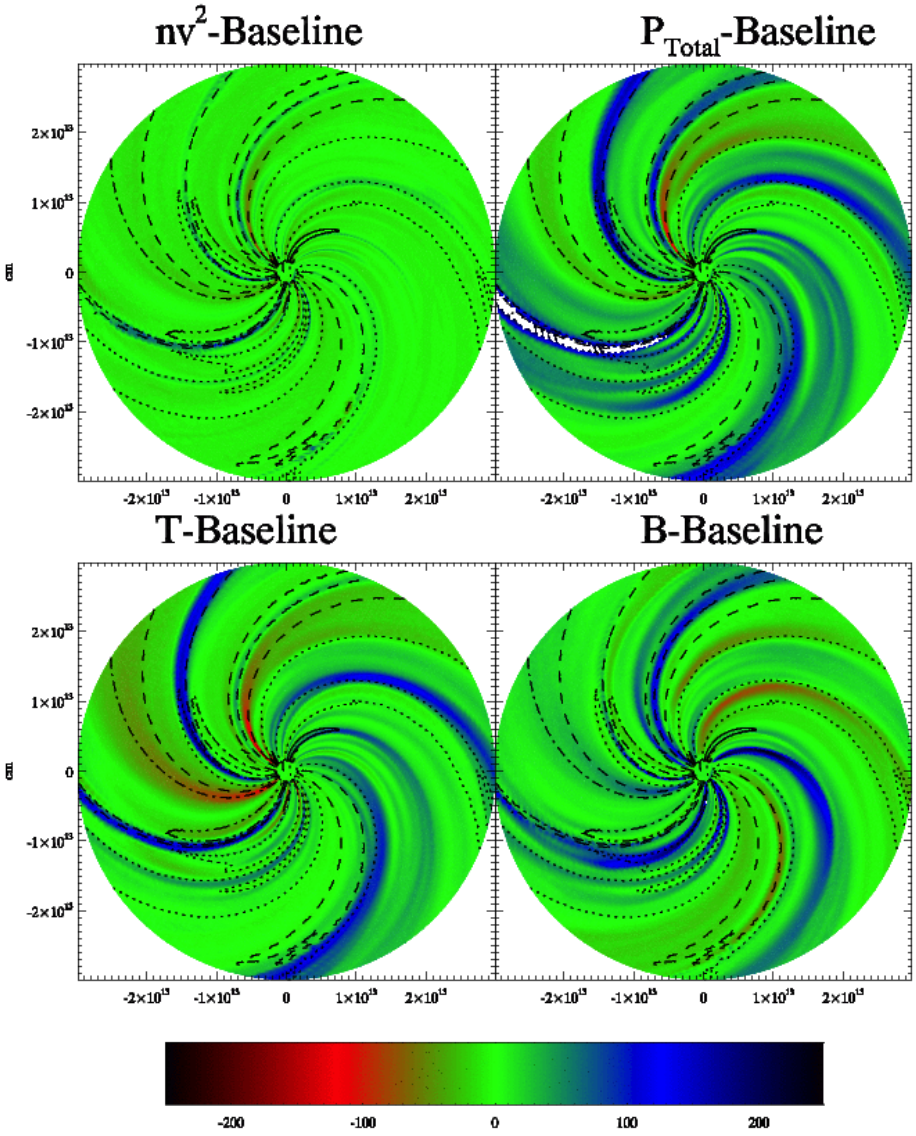

Fig. 3.18: Difference in v_r between each of the cases in the parameter sensitivity study and the Baseline case in the equatorial plane. Blue represents the test cases having faster winds, and red represents slower wind. The differences are caused by a combination of differing amplitudes and spatial offsets, all due to the effects of the inner boundary conditions. The dashed and dotted black lines are contours of constant solar wind speed in the Baseline case.

few years apart and were motivated by different inquiries. The advantage to having done so being able to compare the low and high resolution Baseline cases. The two are identical at the inner boundary and evolve in very similar ways from 0.1 AU to 2.0 AU. As defined at the inner boundary, all low resolution cases have the same v_r at 0.1 AU and the consequences of the different assumptions lead to slightly differing SIR evolutions at larger distances. The high resolution Baseline case is very similar at the inner boundary to the low resolution Baseline case with the exception of some fine scale structure, shown as some small fluctuations about the low resolution case. The high resolution parameter cases have each increased the temperature at the inner boundary by a factor of 4 and scaled the density or the magnetic field linearly with velocity, in $T3$ N $Scales$ and $T3$ B $Scales$ respectively. In all cases, the differences in v_r profile for the SIRs become more pronounced as a function of distance.

The Baseline, T, and nv^2 cases remain very similar, even out to 2.0 AU, which can also be seen in Figure 3.18. Case γ is nearly identical to the Baseline speed profile throughout. The HSS in case nv^2 arrives slightly after that in the Baseline and the first high speed stream has been dynamically evolved away. Case T, on the other hand, retains more of the first HSS, making the speed increase at 2 AU more step-like. Case B retains a faster initial, meaning larger longitude, HSS out to 2.0 AU, meaning that the speed increase at 2.0 AU is more step like than even Case T. The second HSS is very similar to the Baseline. Case P_{Total}, with its increased temperature at the inner boundary, accelerates the solar wind to higher speeds, which increases the amplitude of the maximal high speed wind for both high speed winds. This leads to faster HSSs that arrive 5°–10° in longitude before the HSS in the Baseline. This offset in longitude corresponds to between $\approx 1/2$– 1 day's difference in arrival time of the HSS if we assume the synodic rotation period for the solar wind arriving at Earth. Similarly, Case $T3$ N $Scales$ and $T3$ B $Scales$ also have faster speed maxima,

which are comparable or faster than the fastest wind in P_{Total}. These cases evolve differently than the Baseline for the first and second HSSs, the first remaining a distinct peak in velocity.

Since v_r is the parameter that is kept the same in each case, it is instructive to look at the parameters that have been changed at the inner boundary, namely, the number density and the temperature of the plasma. The scaled number density is shown in Figure 3.20 in the same format at Fig. 3.19. The top left panel shows the number density at the inner boundary, and that it has not changed by much more than $5/cm^3$ at the inner boundary (scaled to values at 1 AU), which corresponds to a 25% increase in the maximum value. As the SIRs evolve out, the peak density for all cases increases, and furthermore, the density corresponding to the first SIR is larger than for the second. This is due to the fact that the first HSS is compressing dense wind ahead of it, while the second HSS is compressing wind that is also being rarefied by the first HSS. It is clear from the jumble of lines shown here, that peak density reached is different for each of the cases and these differences become more pronounced with increased distance from the Sun. The different azimuthal locations for the HSSs in the cases shown here lead the peak density locations to be offset for a given radial distance. For most of the cases, the peak scaled density increases from 0.1 AU–1.2 AU, reaching a maximum scaled value of 50–70 $/cm^3$. With the exception of Case B, the scaled peak density remains constant beyond that point.

The temperature input at the inner boundary, shown in the top left panel of Figure 3.21, varied more significantly between cases. Case P_{Total} is hotter than the other low resolution cases. Cases $T3NScales$ and $T3BScales$ have much hotter plasma at the inner boundary. For all cases, compressive heating becomes apparent by 0.8 AU. The scaled peak temperature amplitude increases slowly from 0.8 AU - 1.2 AU, beyond which it increases rapidly out to 2.0 AU. Cases P_{Total}, B have the

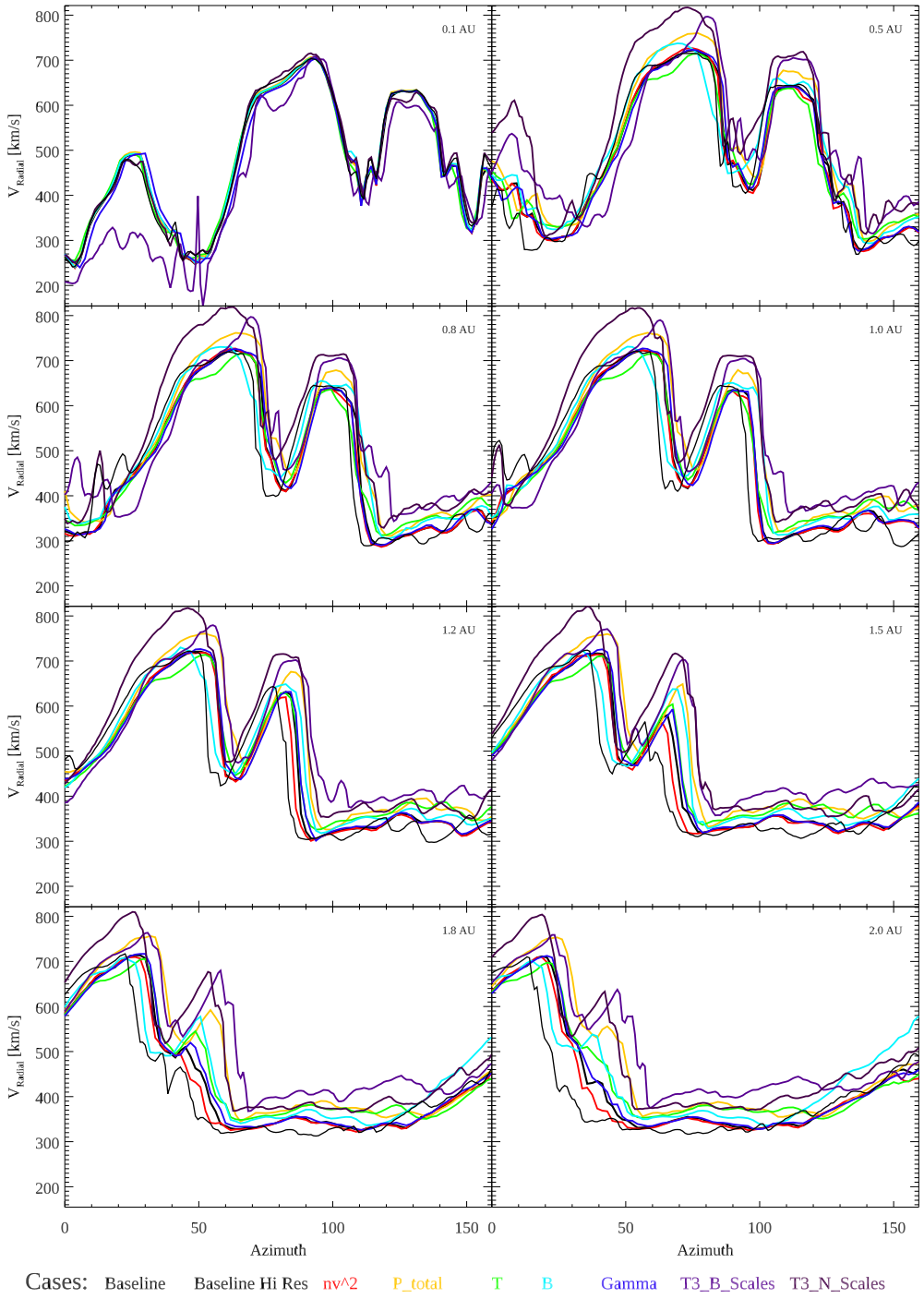

Fig. 3.19: v_r of the SIRs for each of the cases in the parameter sensitivity study and the Baseline case as a function of azimuth, indicated on the x axis, and radial distance from the Sun, indicated in the top left corner of each panel. Cases include the original low resolution cases, as well as the Baseline case at high resolution, and a high resolution case in which the temperature and magnetic field strength at the inner boundary have been increased. Each case is color coded and the legend is across the bottom of the figure.

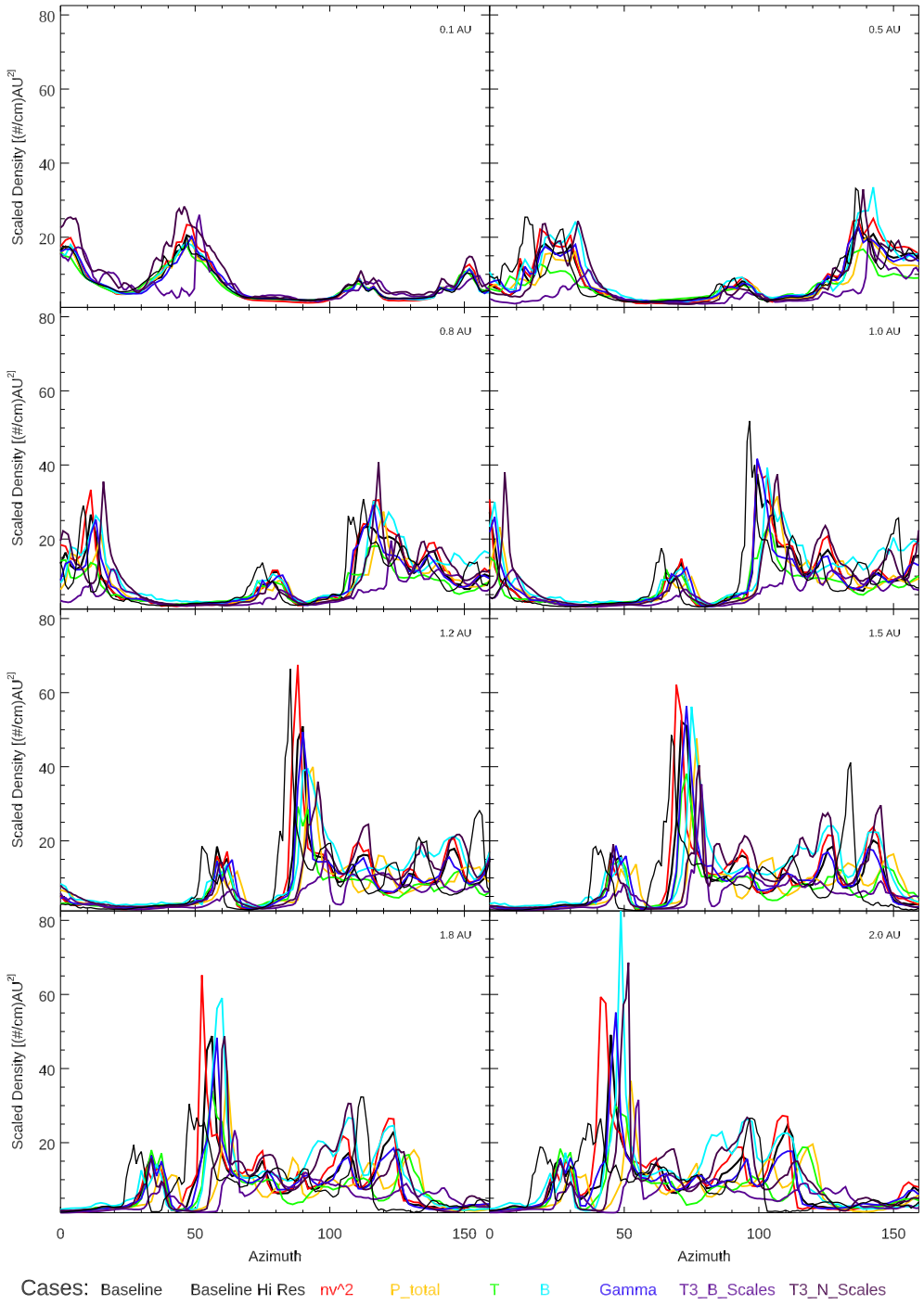

Fig. 3.20: n of the SIRs for each of the cases in the parameter sensitivity study, as shown in Fig. 3.19. Cases shown here include the original low resolution cases, the Baseline case at high resolution, and a high resolution case. All panels have the same range of amplitudes. Cases are color coded in the legend across the bottom of the figure.

highest temperature plasma in the SIR at 2.0 AU, while Case T, γ, and the high resolution runs are cooler than the Baseline. Hence, for elevated temperatures at the inner boundary, the plasma temperature remains hotter out to at least 2 AU but the amount by which it does so decreases. As with the the density, the location and width of the hot SIR plasma is offset in each of the cases due to small changes in position of the gradient in v_r.

The rate of increase in density is larger in the inner heliosphere whereas the rate of increase in temperature is larger beyond roughly 1.2 AU. This has not been documented in literature, perhaps due to the dearth of observations of the same SIR at multiple distances from 0.8–1.2 AU. In contrast, for all cases, the peak in density occurs before the peak in temperature for all cases simulated here, which is frequently observed in SIRs. In general, the cases that have higher peak densities also have higher peak temperatures.

While the simulated densities for all cases matched the observed densities both at the Helios and ACE orbits, the temperature and the magnetic field magnitude were both underestimated. As can be seen in Figure 3.22, an increase by a factor of 2-3 in magnetic field strength at the inner boundary will retain the rough factor of 2 of increased strength at 1.0 AU but that ratio lessens by 2 AU in all but the most compressed fields within the SIRs. Interestingly, the high-resolution cases $T3BScales$ and $T3NScales$ have similar magnitudes to Case B, which is much weaker at the inner boundary, from 0.8 AU to about 1.8 AU everywhere except within SIRs. In summary, the large increase in $|B|$ at the inner boundary results in stronger magnetic fields everywhere, particularly within the compressions of SIRs relative to the background field.

The differences in density, temperature, and magnetic field strength between cases combine to mean that the SIRs will therefore have different peak thermal

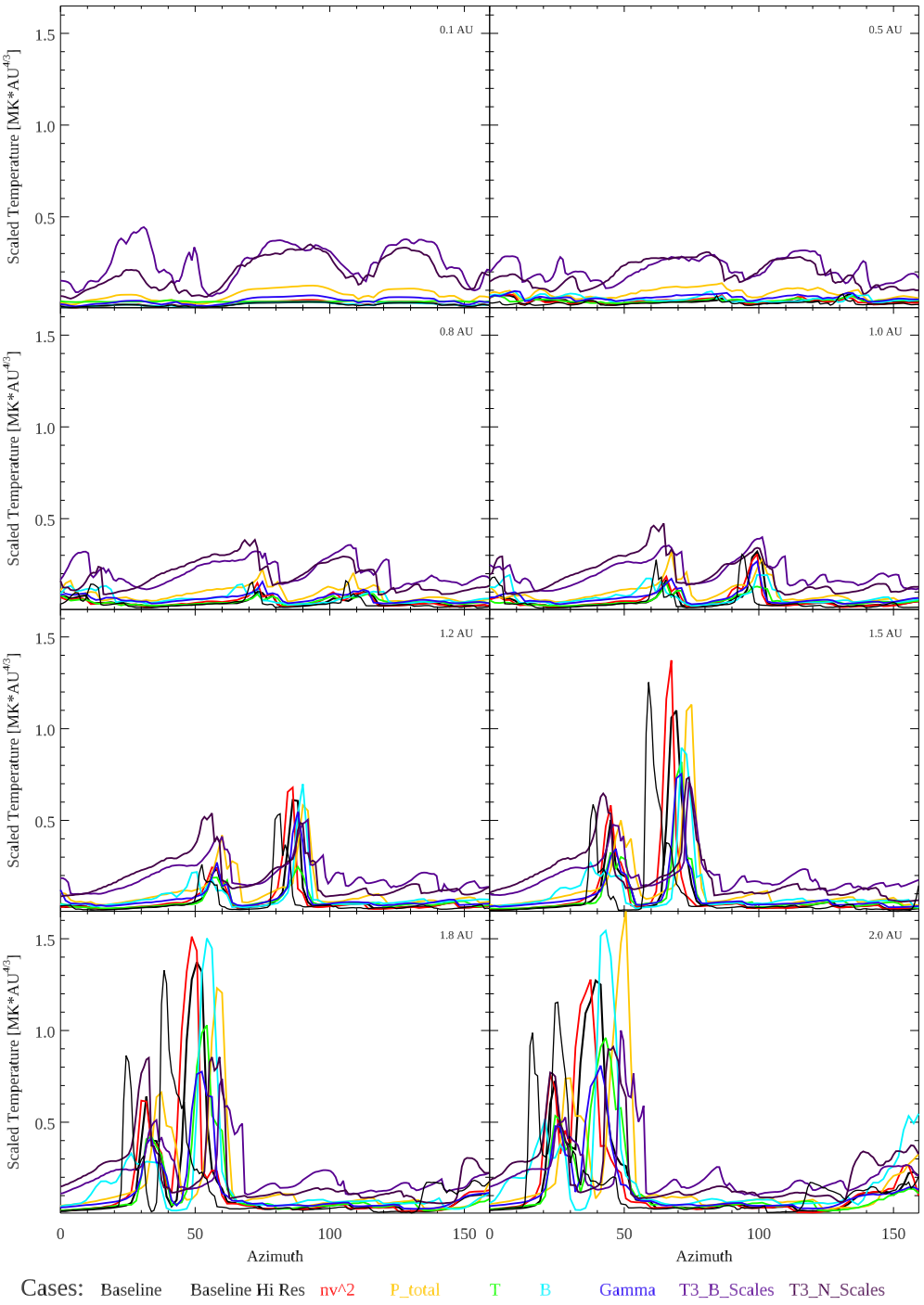

Fig. 3.21: T of the SIRs for each of the cases in the parameter sensitivity study, as shown in Fig. 3.19. All panels have the same range of amplitudes. Cases are color coded in the legend is across the bottom of the figure.

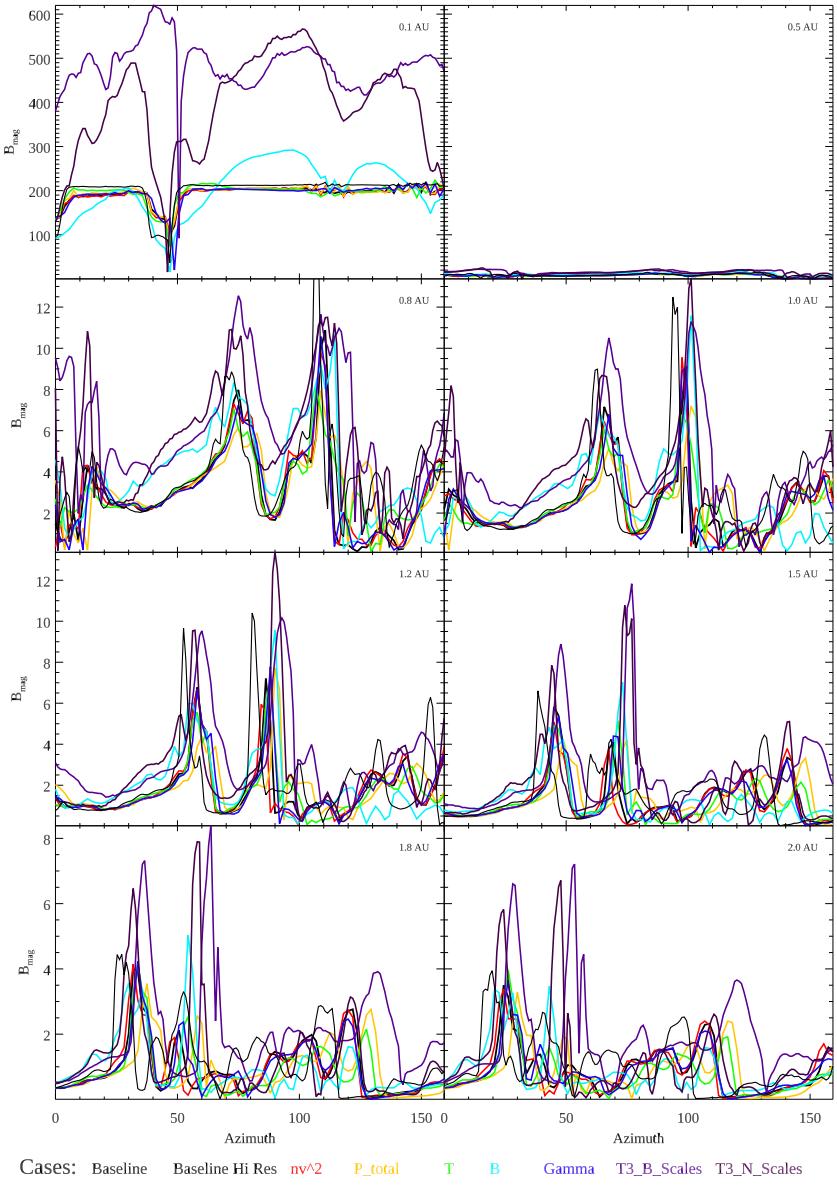

Fig. 3.22: $|B|$ of the SIRs for each of the cases in the parameter sensitivity study, as shown in Fig. 3.19. Note that each row has the same amplitude in y-axis but the range decreases for lower rows. Cases are color coded and the legend is across the bottom of the figure.

pressures, which differ by up to a factor of 3. Likewise, there are also differences in magnetic and dynamic pressures between the cases. The differences in pressures, and specifically the differences in gradients in pressures, will decelerate and deflect flows by different amounts, generating different characteristics of SIRs. Furthermore, the characteristic speed in the plasma will determine how rapidly the pressure waves travel and whether shocks are able to develop. The sound and Alfvén speeds are dependent on the parameters that have been changed substantially. Therefore, the characteristic speeds differ between the cases considered and are shown in Figure 3.23 and Figure 3.24, respectively.

Both the sound speed and the Alfvén speed have a factor of 2-3 between the Baseline case and the cases with the fastest characteristic speeds at the inner boundary, namely the $T3BScales$ and $T3NScales$. For c_{fast}, Case P_{total} has speeds at the inner boundary that are just as fast as $T3NScales$, though it decreases with distance more rapidly than either of the high resolution cases. These high resolution cases maintain a faster overall sound speed out to 2.0 AU in the ambient solar wind but in the compressed with of the SIRs beyond 1.2 AU, the characteristic speeds are not as fast. In contrast the Alfvén speed of the ambient solar wind is similar for all cases beyond 1.5 AU, the $T3BScales$, $T3NScales$, and B cases having higher c_A at smaller heliospheric distances than the other cases. At all distances, the cases with higher c_A at the inner boundary have the fastest c_A within the SIRs at all distances considered here.

Figure 3.19 through Figure 3.24 together show that for the same input solar wind speeds, variations in density, temperature, and magnetic field at the inner boundary, and of γ within the LFM-helio will develop SIRs with differing local peak densities, temperatures, and pressures. Furthermore, the differences between cases increase with increasing distance from the Sun. While the jumble of lines shown in

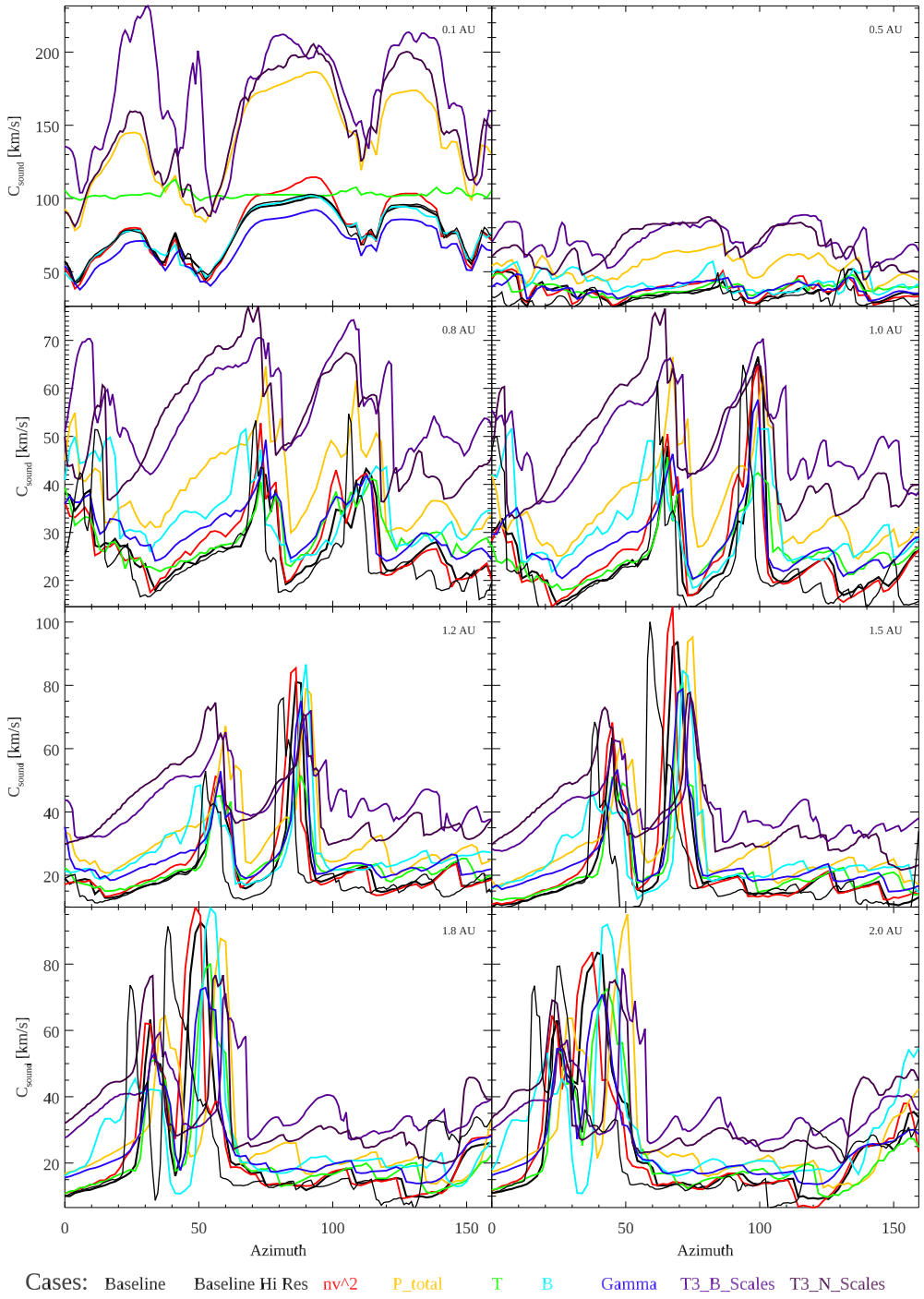

Fig. 3.23: c_s and of the SIRs for each of the cases in the parameter sensitivity study, as shown in Fig. 3.19. Cases are color coded and the legend is across the bottom of the figure.

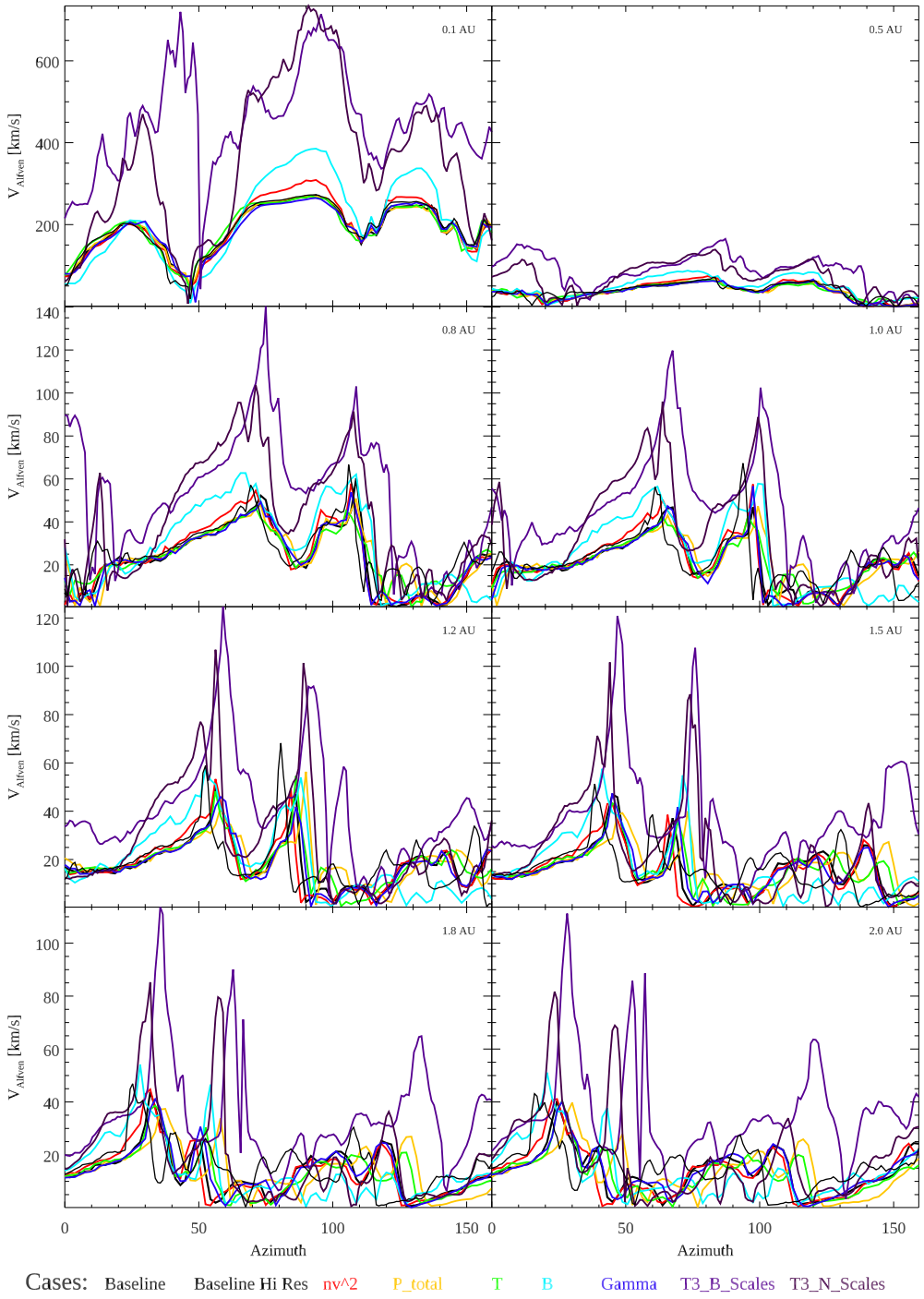

Fig. 3.24: C_A of the SIRs for each of the cases in the parameter sensitivity study, as shown in Fig. 3.19. Cases are color coded and the legend is across the bottom of the figure.

these figures show what a spacecraft would see for each simulated case at each of the distances, a line by line comparison is not be the most efficient way to quantify the differences between all the case. Differences between cases primarily take the form of either timing/azimuthal differences or offsets or differences in magnitudes. Both types of difference arise from differences in dynamical evolution and for now, they will be considered together. To get an estimate of difference between the Baseline case and each of the parameter sensitivity cases, a modified Euclidean norm has been used to quantize the differences between cases. While this approach masks differences in timing, other measures such as the variance, root mean square error, correlation coefficients, and skill scores have been used to intercompare models and to compare simulations with *in situ* data (*Owens et al.*, 2008; *Owens and Riley*, 2017; *Owens et al.*, 2017).

The modified Euclidean norm was calculated using Equation 3.1. For each grid cell along the azimuthal trajectory, 83 cells in total for the low resolution simulations, the variance between the value of the variable in the case being considered and the baseline case was calculated. The square root is taken and is normalized by the sum of the values of the Baseline case for the same variable over the same range. Finally, this is multiplied by 100 to get an approximation of a percent difference in areas under the curve. This modified Euclidean norm is a combination of the mean square error and the skill score as used in *Owens et al.* (2008), modified such that the Baseline simulation is used as the reference data set instead of *in situ* observations. It is again worth noting that this cumulative difference may be caused by either a change in magnitude, an offset in azimuth, or a mix of both, but since the comparisons considered here have all been aligned at the inner boundary, any and all differences arise from evolutionary effects due to the changes in plasma parameters. Each of the low resolution cases have been compared with the low resolution baseline case,

the high resolution cases have been compared with the high resolution baseline case. For completeness, the high resolution and low resolution baseline cases have been compared. To do so, the high resolution case was sampled every second grid cell in the azimuthal direction in order to effectively match resolutions.

$$\text{Euclid}\,[\,\%\,] = 100 \times \frac{\sqrt{\sum_i \left(Case\,(i) - Baseline\,(i)\right)^2)}}{\sum_i \left(\,|\,Baseline\,(i)\,|\,\right)} \tag{3.1}$$

Let us begin by examining the modified Euclidean norm for v_r. Figure 3.25 shows the result of Equation 3.1 for each distance shown in Figures 3.19. It is clear that at 0.1 AU, the percentage for all cases is less than 1.5 %, and most cases are below 0.5 %. This is reassuring since identical velocity profiles are input at the inner boundary. Any differences arise from the calculations done in the ghost cells of the LFM-helio. For most cases, the modified euclidean norm increases as a function of distance but remains within a two percent difference within 2.0 AU. v_r for cases nv^2, γ, and T all remain quite similar to the Baseline case for all distances even out to 2.0 AU. This is consistent with the small changes made in density and temperature at the inner boundary. Case P_{Total} changes the temperature at the inner boundary by more than case T, thereby accelerating the wind to higher speeds and the effects on v_r persist out from 0.1–2.0 AU. Case B compresses the entire band of variable solar wind speeds and the effects on the SIR persist out to 2.0 AU as well, though the modified Euclidean norm of both of these cases differ from the Baseline by between 1–2%. Finally, the cases that show the largest differences in Euclidean norm are the high resolution Baseline, and the high resolution Scaled cases. In these cases, the smaller scale structure that is input at the inner boundary and propagated outward, contribute to the differences. But even these only reach a difference of 2.5%. These small differences are reassuring since identical v_r have been input at the

inner boundary for each of these cases and the dynamical evolution of the solar wind is primarily driven by v_r.

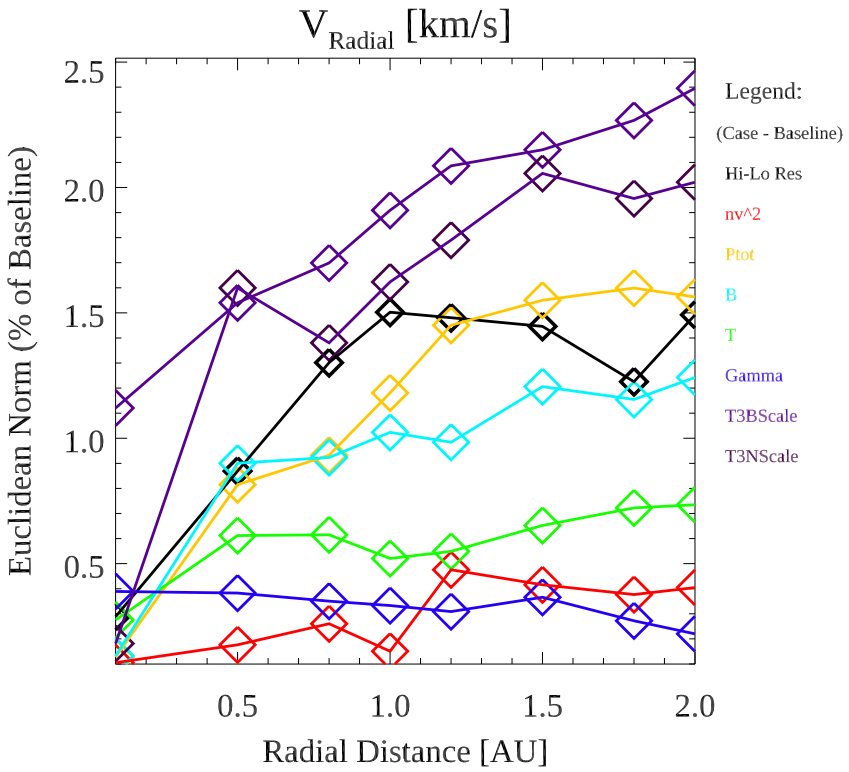

Fig. 3.25: Euclidean norm for the difference between v_r in each of the parameter sensitivity runs and the Baseline run. Cases are compared with the Baseline of the same resolution. The low resolution runs are:nv^2, P_{tot}, B, T, and $Gamma$, and the high resolution runs are: $T3BScale$, $T3NScale$. For completeness, low resolution and high resolution runs for the Baseline case are also compared ($Hi - LoRes$, in black). Each case is color coded, as in Fig. 3.19. The legend is on the right of the figure.

It is instructive to now look at the parameters that have been changed at the inner boundary and how these evolve out into the heliosphere. This is shown in Figure 3.26 for the solar wind number density and temperature. This more clearly shows that all of the low resolution cases run had a 2% or less Euclidean norm difference from the Baseline at the inner boundary, while the higher resolution cases had a Euclidean norm difference of about 4%. All cases increase their percent difference as

a function of increasing heliospheric distance, but at different rates. Case Γ remains quite similar to the Baseline all the way out to 2.0 AU whereas case nv^2 is similar to the Baseline within 1 AU but then evolves to be appreciably different past 1 AU. Cases T and B show steady increases in Euclidean differences but at different rates whereas cases P_{total} and the higher resolution runs seem to level off after 1.2 AU. Notably, the difference between the high and the low resolution runs shows the most difference, perhaps because of the cumulative effect of small scale structures. The high resolution parameter runs were compared with the high resolution baseline, so the effect of these smaller scale fluctuations will not be present. All cases have a modified Euclidean norm difference between 4–12%

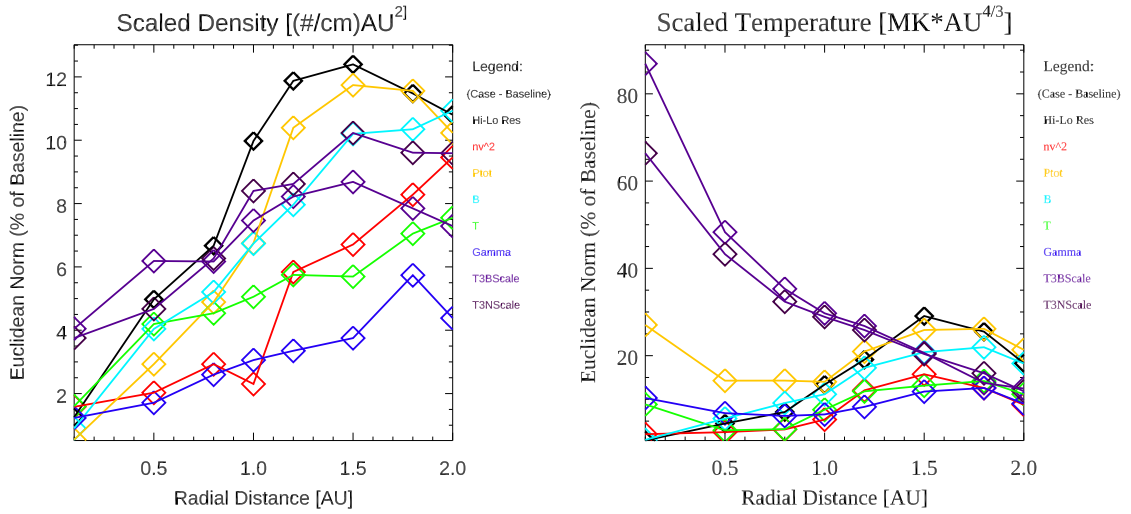

Fig. 3.26: Euclidean norm for the difference between n and T in each of the parameter sensitivity runs and the Baseline run. Cases are compared with the Baseline of the same resolution. For completeness, high and low resolution runs for the Baseline case are also compared. Each case is color coded, as in Fig. 3.19. The legend is on the right of the figure.

The behavior of the modified Euclidean norm for the scaled temperatures, in contrast, is markedly different. The right hand side of Figure 3.26 shows that the temperatures for each of the cases varies greatly at the inner boundary, from 10%

or less for all of the low resolution cases except case P_{Total}, which has a modified Euclidean norm of about 35 %, while the high resolutions cases have percent differences of 65% and 85%. For all of the low resolution cases, the percentage norm decreases slightly from 0.1 AU to 0.5 AU, remains quite steady out to 1.0 AU, and then increases. Between 1.5–1.8 AU, many of the low resolution runs seem to attain a maximum in modified Euclidean norm, ranging from 10–30%, and decrease again by 2.0 AU. This behavior is perhaps indicative of differences in temperature at the inner boundary being smoothed out in the inner heliosphere, before dynamical effects process the plasma. Once the stream interactions begin to compress the plasma, the difference in sound speed may alter the evolution of the SIR relative to the Baseline case. The high resolution runs, in contrast, have a steady decline in modified Euclidean norm, down to 20% at 1.5 AU. The large differences in the inner heliosphere are due to the high resolution runs having significantly higher temperatures at the inner boundary. As the solar wind expands and cools, the $T3$ runs, undergo compressive heating, but the maximum temperatures in the SIRs are similar to those in the Baseline case. The differences in temperature of unperturbed wind decrease as the solar wind flows past 1.0 AU, which decreases the euclidean difference of these runs, bringing the measure into the range of the other low resolution cases.

Figure 3.27 shows the modified Euclidean norm percentages but for the magnitude of the magnetic field in the same format as Figure 3.25. This resembles the plot for the density in both pattern and in magnitude. Once again, most of the low resolution cases are input with a less than 5 % difference, while the high resolution runs, which were purposely input with higher magnetic field strengths have differences from 8–11%. The cases with higher total pressure at the inner boundary, cases B, P_{Total},$T3NScales$,and $T3BScales$, have the largest Euclidean norms. The high resolution runs decrease in differences within 0.5 AU but then increase up to

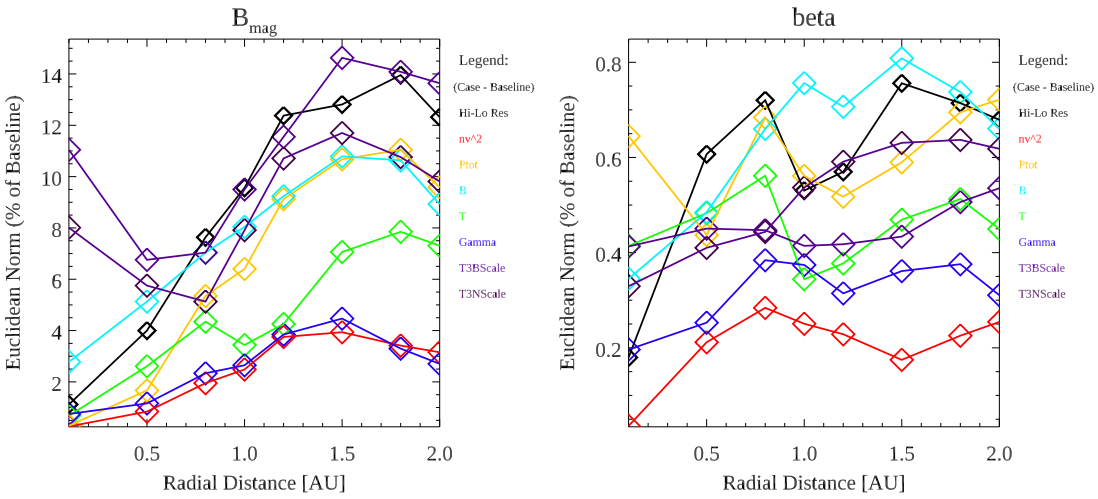

Fig. 3.27: Euclidean norm for the difference between B_{mag} (left) and β (right) in each of the parameter sensitivity runs and the Baseline run. Cases are compared with the Baseline of the same resolution. For completeness, high and low resolution runs for the Baseline case are also compared. Each case is color coded, as in Fig. 3.19. The legend is on the right of the figures.

1.5–1.8 AU but all cases differ by less than 15% between 0.1–2.0 AU. While the individual cases, when considering the modified Euclidean norm for n and B, differ, the overall pattern is similar, which is roughly what we would expect for plasma where the field is frozen-in, but where compression will effect each of the thermal and magnetic pressures slightly differently.

Finally, we consider the characteristic speeds within the plasma, c_s and c_A, shown in Figure 3.28. Considering first c_s, shown on the left hand side of the Figure, there is a 10% range in Euclidean norms for the sound speed input at the inner boundary. The high resolution Baseline case and the low resolution case B both have the same c_s at the inner boundary as the low resolution Baseline case, while Cases nv^2 and γ are only about 1% greater. Case T has a 4% increase at the inner boundary while Cases P_{total}, $T3NScales$, $T3BScales$ have a 7.5–10% increase. As the plasma flows outward into the heliosphere in all of these cases, the evolution

of the sound speed varies with each of these cases relative to the Baseline. The modified Euclidean norm for cases nv^2 and γ increases slowly, reaching a maximum of approximately 4% between 1.5–1.8 AU. The difference in case T drops from 4% to $< 2\%$ from 0.1–0.5 AU and then evolves much like Cases nv^2 and γ. Similarly, Case P_{total} drops from 9% to $< 6\%$ from the inner boundary to 0.5 AU, remains consistently about 6% different from the Baseline case out to 1.0 AU, then increases again out to 1.8 AU. The modified Euclidean norm for the high resolution baseline case increases up to 10% different at 1.5 AU. The scaled high resolution cases, where the input temperature was four times that of the Baseline and the density and magnetic field scaled with speed, maintain an 8–10% difference to 1.5 AU and then become more similar to the Baseline case. While the differences in c_s relative to the Baseline case as a function of distance may seem fairly small, this characteristic speed determines whether the jump in solar wind speed, moving in the frame of the shock/pressure wave, is sub- or super- sonic and hence distinguishing whether the transition from slow wind to fast wind is separated by a shock. While the range of Euclidean norm differences in sound speed range from 0–10-%, the Euclidean norm differences in v_r are at most 2%, implying that although the velocity profiles are similar, the sound speeds vary more, which may mean that the prevalence of shocks in the difference cases may vary and may vary as a function of distance.

The right hand side of Figure 3.28 shows the modified Euclidean norm for c_A relative to the Baseline case as a function of heliospheric distance. All of the low resolution cases, except Case B, differ by less than 1% at the inner boundary, as does the high resolution Baseline case. Case B has a 3% difference from the Baseline case, arising mainly from differences in magnitude. Each of the aforementioned cases increase up to either 2% for cases nv^2 and γ, to 4% for case$T$, and $\approx 8\%$ for cases P_{tot} , B, and the high resolution baseline run. The high resolution runs

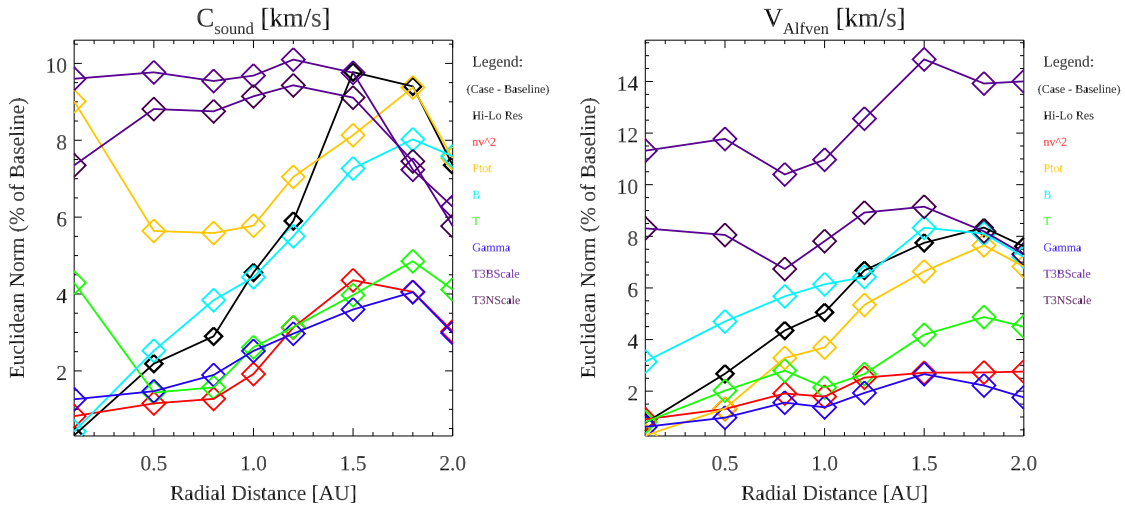

Fig. 3.28: Euclidean norm for the difference between c_s (left) and c_A (right) in each of the parameter sensitivity runs and the Baseline run. Cases are compared with the Baseline of the same resolution. For completeness, high and low resolution runs for the Baseline case are also compared. Each case is color coded, as in Fig. 3.19. The legend is on the right of the figures.

have Euclidean norms of 8% for $T3NScales$ and 11% for $T3BScales$ and the inner boundary. These cases each have a minimum, of 6.5% and 10% respectively, at 0.8 AU, then increase to a maximum of 9% and 15% respectively at 1.5 AU. As with c_s, the differences in Alfvèn speed between cases becomes most significant when compared to the Eucledian norm differences in v_r and the former's role in shock development. In combination with c_s, the magnetosonic fast speed varies more and will regulate the presence of fast shocks.

Thus far, the effects of varying parameters within the HSS have been discussed as applied to realistic SIRs, namely for particular SIRs within CR 2058, CR 2060, and CR 1892. The first two have demonstrated that the shape of the HSS affects the evolution of the subsequent SIR. In particular, for an equatorial source of fast wind, the latitudinal extent of the HSS affects the amount and direction of flow deflection as well as the peak density of the SIR. The SIRs in CIR 1892, having the

exact same shape at the inner boundary are shown to evolve differently depending on the density, temperature, and magnetic field strength input at the inner boundary. Though it is clear that both HSS shape and plasma parameters affect the evolution of the SIR, there are many components contributing to these differences. To elucidate the effects of certain characteristics, we turn to idealized IBC in order to quantify the contributions of HSS geometry.

Chapter 4

Evolutions of SIRs and Latitudinal Dependence of SIRs: Idealized IBCs

4.1 Motivation

In situ observations of SIRs near the ecliptic plane are plentiful and have been summarized in Section 3.1.1. *In situ* observations of SIRs away from the ecliptic, in contrast, have so far been scarce. As before, the advantages of in situ data are the precise, local and quantitative measurement of the solar wind plasma but this comes at the cost of having a single, small trajectory of sampled SIR, where spatial and time dependent effects are indistinguishable. Time-dependent imaging techniques have been used to study the three dimensional structures of SIRs. For example, the interpretation of white light images and tomographic reconstructions, such as measurements of Thomson Scattering by the Solar Mass Ejection Imager (SMEI) and those used in interplanetary scintillation (IPS) measurements, observe the large scale structure of SIRs at a range of heliospheric distances. This technique encompasses a larger spatial scope but involves a convolution of time and longitudinal structure in the solar wind. As such, even simplified global MHD models play an important role in understanding the out-of-ecliptic evolution of the solar wind and the structures within it, and is particularly well suited to SIRs.

In terms of observations out of the ecliptic, in addition to the white light imaging data, there are a select few *in situ* observations that enable the study of the local

evolution of SIRs at high latitudes in the inner heliosphere. Given its orbit being nearly perpendicular to the equatorial plane, the Ulysses spacecraft has made observations of SIRs at distances between 1.5–5.2 AU. At larger heliospheric distances, the Voyager spacecraft have made observations off the ecliptic plane beyond the orbit of Saturn but the inclination is more moderate. Measurements of SIRs in the inner heliosphere are somewhat more frequent but have historically been mainly confined to by-products of planetary missions en route to their inferior planet. The recent Parker Solar Probe mission is a notable example, dedicated to solar wind measurements. It orbits within the inner heliosphere, studying the origin of the solar wind, but mostly in the ecliptic plane. Solar Orbiter, launched February of 2020, does not have orbital perihelion as close as the Parker Solar Probe but will be the first spacecraft in the inner heliosphere to leave the ecliptic, its orbital inclination will reach to $\pm$ 30° heliographic latitude in 2028. Solar Orbiter data will reveal *in situ* characteristics of SIRs in the inner heliosphere at mid-latitudes for the first time.

Although observations of SIR evolution beyond the planets' orbital planes are few, data from both *in situ* and imaging spacecraft show that the variable solar wind speed drives SIRs at a range of latitudes. At solar minimum, the latitudinal range which encompasses the band of solar wind variability is about 40° (*McComas et al.*, 2000). Ulysses' first full orbit coincided with solar minimum. Its observations of shocks indicated that both forward and reverse shocks occur within a latitudinal range equal to the maximum latitudinal extent of the HCS. At latitudes poleward of the HCS, forward shocks were no longer observed but reverse shocks were still present for the first Ulysses orbit (*Gosling and Pizzo*, 1999). This pattern of spatial distribution was explained using the corresponding observations of the SIR orientations. The observations of shock prevalence were explained by invoking that forward shocks propagate away from the Sun and equatorward while reverse shocks propagate

toward the Sun and poleward. SIRs are assumed to be planar and parallel to the SI, whose orientation is calculated from the speeds of deflected (non-radial) solar wind. The normal of the SI's and thus the SIR's were calculated and predominantly pointed equatorward during the declining phase of solar cycle 22 (*Gosling et al.*, 2001). This was consistent with the idealized tilted dipole configuration typical of an idealized solar minimum, which is simulated in the Slow Sine case in the LFM-helio.

Conversely, during Ulysses' second full orbit at solar maximum, evidence for the dynamical evolution of the solar wind persisted at all latitudes. This was consistent with sources of slow and fast wind being distributed at solar maximum. Surprisingly, observations of SIRs made during Ulysses' third orbit, during the declining phase of solar cycle 23, differed from those taken during the declining phase of solar cycle 22. The meridional inclinations of SIRs were observed to be both poleward and equatorward over a wide range of latitudes, for both forward and reserve shocks. These observations were no longer consistent with SIRs expected to arise from the tilted dipole, two sector, four stream pattern of the solar wind. Furthermore, the prevalence of shocks at high latitudes decreased and the ratio of forward and reverse shocks differed between the declining phase and minima for solar cycles 22 and 23. Explicitly, forward shocks were observed at higher latitudes than reverse shocks (*Gosling et al.*, 2001). The change in shock rate and orientation of shocks as a function of latitude suggests that the structure of the SIRs themselves differed from solar cycle 22 to solar cycle 23. This is further supported by the change in global structure of the heliosphere between the declining phases of solar cycle 22 and 23, as indicated by both the different average coronal structure between the two solar cycles and from *in situ* observations of the solar wind properties.

The different coronal structure between solar cycles is seen clearly in the distribution and size of coronal holes. In the declining phase and the minimum of

solar cycle 22, the coronal holes were large, coherent, and well-centered on the heliographic poles. Despite occasional protrusions to lower latitudes, the high speed wind and open magnetic were confined to high latitudes. The slow wind was roughly constrained in a wide, undulating band which contained the HCS. Hence, the tilted dipole configuration was a good approximation and the idealized Slow Sine case is used to reproduce the characteristics of spatial positioning and orientation of the SIRs during solar cycle 22.

In contrast, during the declining phase of solar cycle 23, the polar coronal holes were both smaller in size and weaker in magnetic field strength. The resulting solar wind had a weaker interplanetary magnetic field, was more tenuous, and cooler than winds of equivalent speed in the previous cycle. Furthermore, there were persistent equatorial coronal holes that were sources of low-latitude high speed streams, notably causing a band of pseudostreamers in addition to the slow wind streamer belt. This global change in distribution of solar wind speed sources leads to different configurations of SIRs and therefore, also of the shocks that are driven. The idealized Steamer-Pseudostreamer case approximates the distribution of solar wind during this cycle.

The structural differences of the sources of fast solar wind between solar cycles have been hypothesized to cause the differences in the extent and directionality of the SIRs observed at Earth as well as those observed off the ecliptic at heliospheric distance larger than 1.0 AU. The following sections of this dissertation examine this hypothesis by examining the evolution of SIRs at a wide range of latitudes. In this process, we also examine the oft quoted assumption that SIR structure is isotropic and homologous between 0.2–2.0 AU.

Finally, as posed by *Richardson* (2018), although the evolution of SIRs has been well investigated at 1.0 AU and beyond, this dissertation addresses the question

of how near the Sun are SIRs, and the structures within, well defined? Does the structure depend on latitude? The new results from the Parker Solar Probe shed much insight into the sources of the solar wind, both fast and slow. The upcoming Solar Orbiter results will tell us much about the inner heliosphere at mid-latitidues. Being able to distinguish fast wind from slow will aid in our understanding of the processes within the solar wind in the inner heliosphere and the evolution of SIRs therein.

In order to characterise effects of global heliospheric structure on the evolution of SIRs, I use the four idealized solar wind speed configurations to study the properties and latitudinal extent of the SIRs that arise in each high speed stream morphology.

4.2 Evolution of Idealized SIRs - Latitudinal Dependence

As shown in Chapter 3, the evolution of SIRs is affected by several factors whether it be the shape of the high speed streams or the relationship between the solar wind speed, density, or temperature. The realistic cases discussed in Chapter 3 demonstrate the effects of these factors in the evolution of SIRs. The SIRs considered also include features that render the evaluation of the effect of any one parameter difficult. Many complicating factors are present and contribute to the local evolution of the SIR. For example, small scale spatial structure on the boundary between fast and slow wind results in localized effects in the ensuing SIR (*Pizzo*, 1982). Furthermore, the HSS flows into non-uniform and evolving 'background' solar wind, such that for the same HSS, a portion of the latitudinal extent flows into the HCS but not all.

In order to characterise the contributions of the global shape of the high speed stream to the subsequent evolution of SIRs, four idealized simulations have been run: Fast Bands, Fast Circles, Slow Sine, and Streamer-Pseudostreamer. The inner

boundary conditions and the resultant SIRs are described in turn in Sections 4.2.1, 4.2.2, 4.2.3, and 4.2.4. These idealized velocity configurations have different latitudinal structures and whether this drives differences in resulting SIRs is investigated. Despite perhaps seeming simplistic for a model such as the LFM-helio, these idealized runs are useful for comparison with results with analytical studies and idealized cases as simulated by other models. Furthermore, these idealized cases often capture the large scale features that recur over multiple Carrington rotations during a particular solar minimum. As mentioned in the previous section, the global structure of the heliosphere changed between the declining phases of solar cycle 22 and 23. In the former, the tilted dipole configuration was a good approximation. The tilted dipole configuration consists of an offset between the solar rotational and magnetic axes, resulting in high speed wind at high latitudes and a band of slow wind about the heliomagnetic equator, which undulates about the heliographic equator. This case is represented by the Slow Sine case discussed in Section 4.2.3. In contrast, during the declining phase of solar cycle 23, equatorial coronal holes are sources of low-latitude high speed streams. On their own, equatorial coronal holes are simulated in the Fast Circles case. Solar cycle 23 was noteworthy for the presence of bands of pseudostreamers in addition to the slow wind streamer belt, bifurcating the band of slow solar wind. This is simulated with the Streamer-Pseudostreamer case.

4.2.1 Fast Bands

The first and simplest idealized IBC, called Fast Bands and shown in Figure 4.1, is meant to recreate in 3D the results of a 2D model, having excluded any latitudinal dependence for the HSS. This allows for comparison with 2D models and with analytical solutions. By design, most of the solar wind is slow, dense, and cool. Bands of high speed solar wind of constant angular longitudinal width extend over all simulated latitudes (80° North to 80° South). The bands of fast wind have different

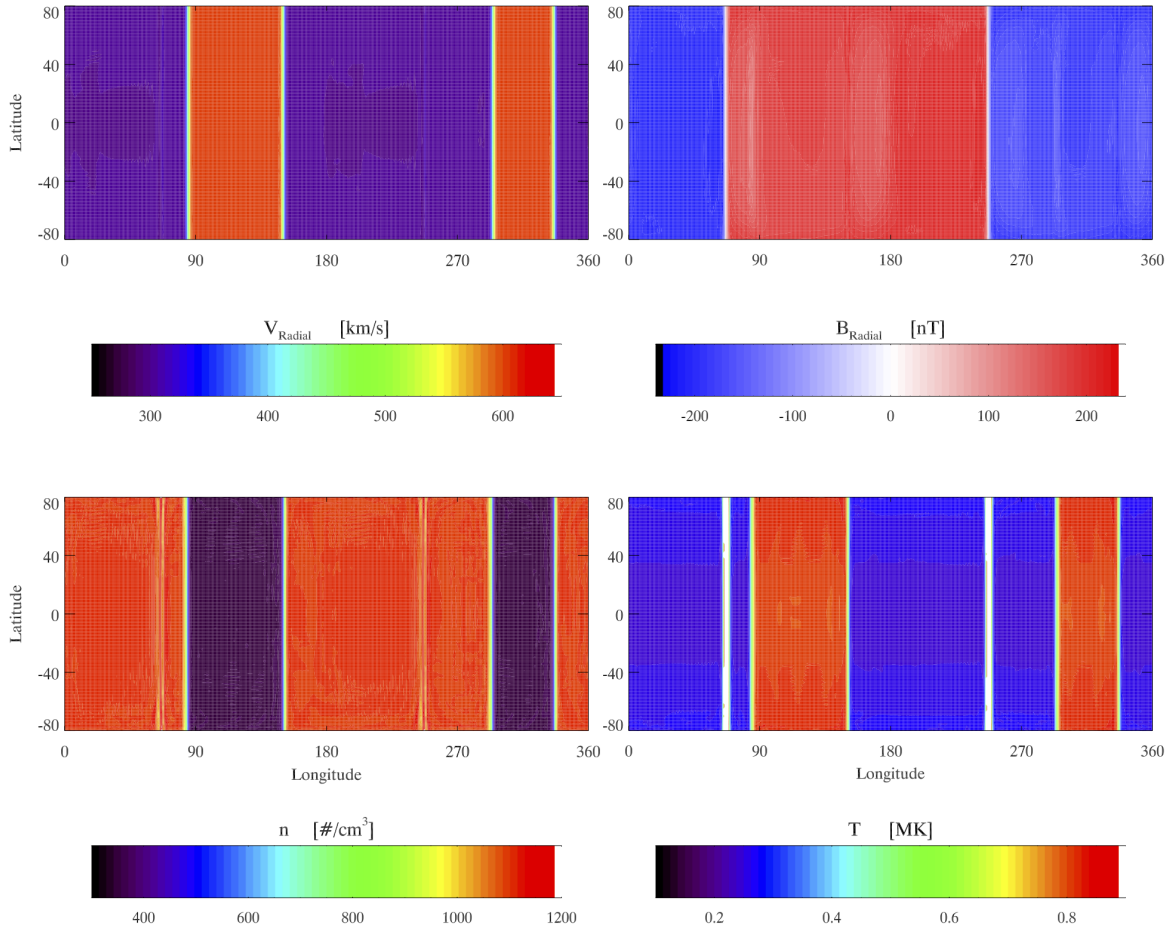

Fig. 4.1: Idealized inner boundary condition - Fast Bands. Bands of constant longitudinal width drive SIRs in a manner that has no latitude dependence as 2D analog.

angular widths, with the wider band having a larger "reservoir" of dynamic pressure with which to drive SIRs. This was done purposely to test whether the longitudinal extent of the HSS alone affects the evolution of the SIR in the inner heliosphere.The HCS has been given the unusual shape of bisecting the heliosphere azimuthally and placed 'vertically', at constant longitudes, in order to eliminate the interaction of the HCS with the SIR, as it has been shown to happen (*Merkin et al.*, 2011).

Figure 4.1 shows the radial components of the velocity and magnetic field (top left and right, respectively) as well as the number density and temperature (bottom left and right, respectively) of the solar wind at the inner boundary. The transitions between wind speeds have the functional form of a hyperbolic tangent over 8 grid cells in the azimuthal direction, and are symmetric for the leading and trailing sides of the HSS. The wide and narrow bands of fast wind extend over different lengths in longitude but both span the entire latitudinal range simulated. This isolates the importance of the longitudinal width of the high speed driver of SIRs. The slow wind has a speed of 300 km/s and the fast wind of 600 km/s. At the inner boundary, the wide band of fast wind extends $\approx 70^{\circ}$ in longitude and the narrow band extends $\approx 40^{\circ}$. The radial component of the magnetic field at the inner boundary has uniform magnitude of 200 nT. The azimuthal component of the field is determined from corotation, and the polar component is set to zero. The number density and temperature were defined in the same way as the Baseline case for CR 1892, namely an empirical relationship between n and V_R and requiring a uniform total pressure. Note that the HCS is hot because it is a region of, theoretically, zero magnetic pressure.

Figure 4.2 shows the evolution of V_R as a function of distance as seen in shells of constant radial distance (left) and in the equatorial plane. The diamonds in the latitude-longitude plots span approximately the range of longitudes shown as the concentric arcs in the equatorial plane, as shown in the right hand panel. Though not shown explicitly, this range of distances and longitudes are also sample at several latitudes. It is worth noting here that the data available for this simulation was for a time step before the initial conditions in the simulation had time to completely be swept off the LFM-helio grid, which cause the sudden changes at distances greater than 1.5 AU. For this case, we will only consider the radial range from 0.1–1.5 AU.

Both panels in Figure 4.2 show the essential characteristics of SIRs expected in the solar wind speed. The bands of fast solar wind, shown in orange, are preceded by a band of intermediate speed solar wind, show in green and cyan. This band of intermediate speed contains both accelerated slow wind and decelerated fast wind and increases in radial width as the SIR develops at larger heliospheric distances. Though not the focus of this dissertation, it is worth noting that the rarefaction wave is also present and seen as the band of intermediate solar wind speed, in yellow, green and cyan, trailing the HSS. As expected, the rarefaction wave has a much larger radial extent that the SIR.

Figure 4.3 shows the SIR in detail in the equatorial plane at 1 AU as a function of decreasing heliographic longitude. Reading the plots from right to left corresponds approximately to what a spacecraft at L1 would encounter, as indicated on the top x-axis. The top panel shows the V_R profile, including a HSS whose leading edge (right) creates a SIR. On the trailing edge, the fast wind outpaces the slow, forming a rarefaction wave. The two subsequent panels show the solar wind number density, nr^2, and the plasma temperature $Tr^{4/3}$, both scaled to 1 AU. The fourth panel shows the non-radial deflection of the solar wind speed; V_ϕ and V_θ are shown by the solid and dashed lines respectively. $|B|$ is shown in the fifth panel and P_{total} is shown in the sixth panel. The vertical lines delineate four distinct regions in the SIR. Region 1 corresponds to undisturbed slow solar wind, region 2 is solar wind that was originally slow but has been accelerated, compressed, heated, and deflected by the pressure wave of the SIR. Region 3 is fast wind that has been decelerated, compressed, heated, and deflected as well. Finally, Region 4 is undisturbed fast solar wind.

Since characteristics of this SIR correspond well with SIRs observed *in situ* and simulations discussed in previous chapters, it is valuable to point out some features

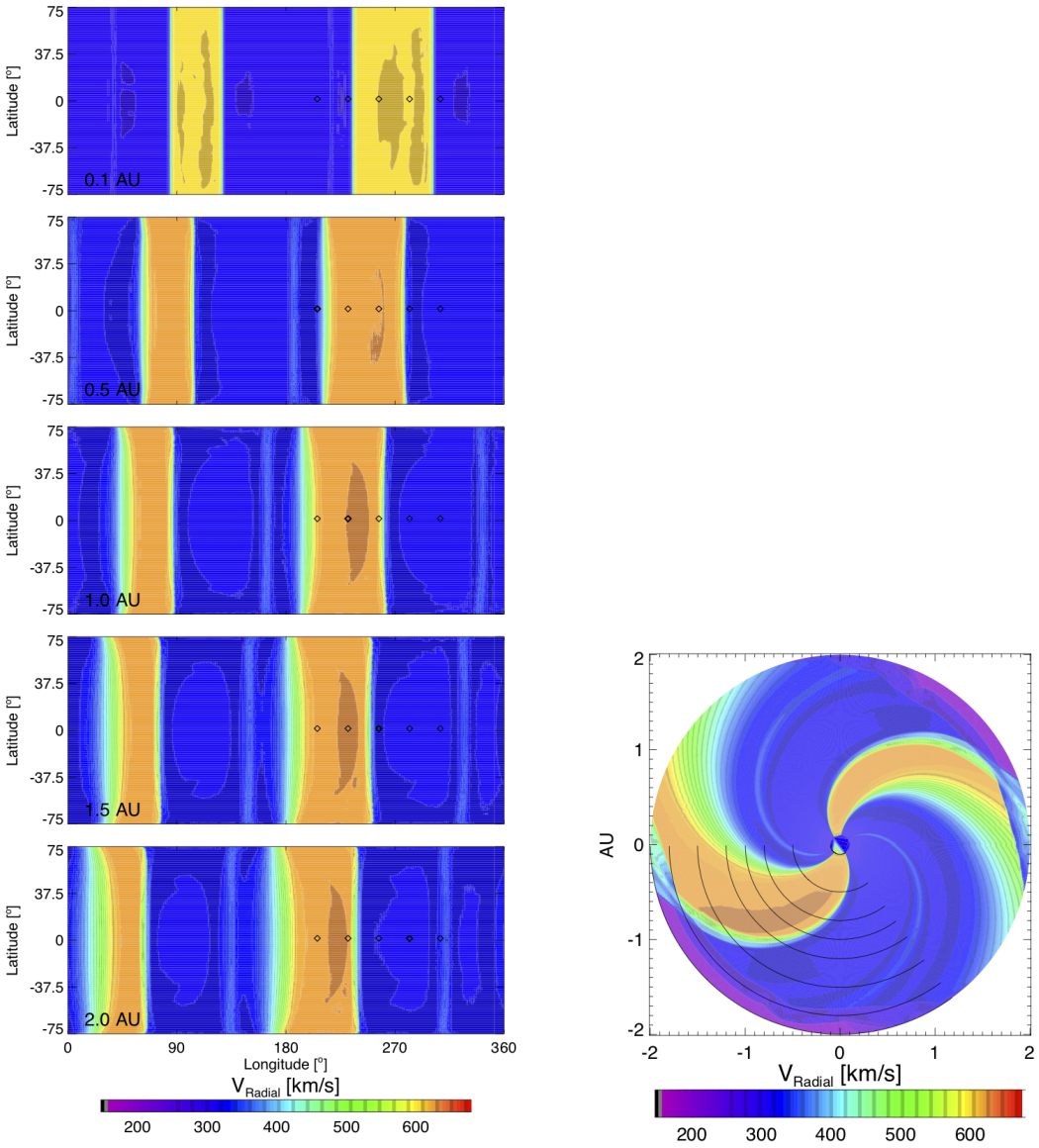

Fig. 4.2: V_R as a function of latitude and longitude at 0.1, 0.5, 1.0, 1.5, and 2.0 AU (left) and as a function of radius and longitude in the equatorial plane (right) for highly idealized vertical bands of fast wind, as an approximation for the 2D case.

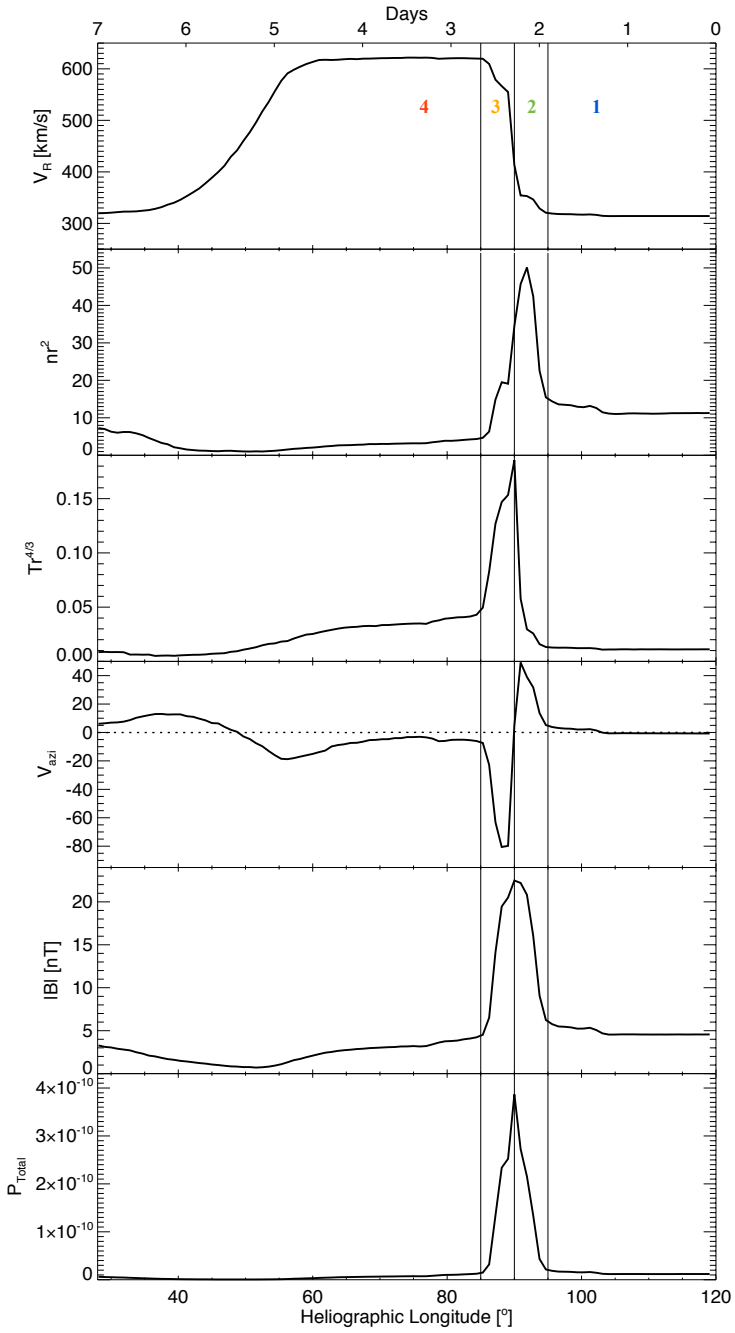

Fig. 4.3: Idealized Fast Bands SIR structure at 1 AU in the equatorial plane. From top to bottom, panels show V_R, nr^2, $Tr^{4/3}$, V_ϕ (solid) and V_θ, $|B|$, and P_{Total} as a function of heliographic longitude. Four regions of the SIR are indicated and correspond to undisturbed and slow solar wind (1), compressed and accelerated slow wind (2), compressed and decelerated fast wind (3) , and undisturbed fast solar wind (4) .

that will be focussed on throughout this chapter. In particular, the V_R profile as a function of time exhibits the two-step like behavior with a forward and reverse wave developing on either end of the speed increase. We have defined the Steam Interface (SI), the distinction between Regions 2 and 3, here as where $V_\phi = 0$, as found in a separate simulation study as being a reliably identifiable, unique feature of SIRs. The SI occurs here within intermediate speed solar wind (approximately 400 km/s, within the observational range). Another frequently used identifier for the SI is the peak in P_{total} (*Jian et al.*, 2006). The two definitions are co-located here but this is not always the case in LFM-helio simulations or *in situ*. The SI is identified, the peak in n frequently occurs ahead of it, as seen in this simulation and the peak in T is most frequently observed after the SI, whereas the peak in $|B|$ coincides with the SI. For example, in *Borovsky and Denton* (2010), a superposed epoch analysis of 27 CIRs occurring between 2003 and 2008 was conducted. Numerous studies using superposed epoch analyses of SIRs over multiple solar cycles and for several spacecraft have found similar patters. For example, *Belcher and Davis Jr.* (1971) and *Gosling et al.* (1978) found the same relative placement of peaks in Mariner 5 data. It is worth noting that there are exceptions, such that *Gosling et al.* (1972) found that the density peak arrives after $V_\phi = 0$ superposed epoch analysis of Vela data as well as variations for individual SIRS at 1 AU (*Richardson*, 2013). In the aforementioned study, the SI is defined as the location of maximum vorticity within an SIR, the placement of the peaks in temperature and field strength are the same.

Now that the salient features of the SIR have been highlighted at 1 AU in the ecliptic plane, we test whether the features observed in typical SIRs depend on the longitudinal width of the HSS that is driving them. Figure 4.4 shows V_R, nr^2, $Tr^{4/3}$, and V_ϕ, in the top left, top right, bottom left, and bottom right respectively. Each is shown as a function of longitude, as a hypothetical stationary spacecraft at a fixed

radial distance would observe the advecting SIRs. The SIR at each radial distance, shown in different colors, are plotted with a vertical offset so that simulated data are visually separated. The longitudinal shifts are due to the winding of the SIR along the Parker spiral. The format is the same as Figure 3.11. Each of the colored lines shows both the simulated data for the wider band of fast wind (thick line) and the narrower band of high speed wind (fine line) in the ecliptic and are aligned such that the leading edge of the HSS at the inner boundary is superposed, meaning that the longitudinal offset between the SIRs is constant with heliospheric distance. It is clear that in the equatorial plane, the SIR driven by the narrow and wide bands of fast wind are identical out to 1.5 AU. For this simulation, the orange (1.8 AU) and red (2.0 AU) lines shows an initial condition that has completely been blown off the simulation grid. These are not part of the SIR evolution simulations but do show the range of compression, heating, and deflection attainable. Turning our attention back to the distances within 1.5 AU, though not unexpected for supersonic flow, the structure and location, or alternatively arrival time, of the SIR does not depend on the width of fast wind driving it, as long as the fast wind front is the same and has not been eroded by the rarefaction wave. The SIR is nearly identical in all parameters.

The SIRs generated by the Fast Bands display the characteristics observed in SIRs at all distances considered, regardless of HSS width. The V_R profile, shown in the top left panel of Figure 4.4, shows the leading edge of the HSS steepening, developing step-like features, the forward and reverse waves bounding the SIR, which may steepen into shocks. The peak in nr^2 increases with distance as the SIR becomes more compressed and, consistent with *in situ* observations, is located on the slow wind side of the compression region. Similarly, the peak plasma scaled temperature continuously increases with distance, with the peak located on the fast wind side of the SIR. The region of compressed plasma and field broadens with increasing

heliospheric distance from the Sun. The compression of the radial component of the magnetic field has a broader peak than that in the density. The non-radial components of solar wind velocity exhibits the prograde and retrograde deflections observed *in situ*, with the slow wind deflecting in the direction of the Sun's rotation and the fast wind deflection being larger and in the opposite direction. As expected for this geometry, there are no polar component to the flow deflection in the equatorial plane.

The plot for all parameters at all distances considered shows that the SIR is nearly identical for HSSs of different widths, as long as the rarefaction wave has not yet caught up with the reverse wave. This suggests that as long as the V_R profile on the leading edge is the same, the extent does not immediately affect the evolution of the SIR, at least in the Fast Bands case. This is not surprising since the compressed plasma in the SIR does not know about the extent of wind behind it, since the solar wind is supercritical. It is therefore only once the peak speed of the HSS has decreased due to erosion by the rarefaction wave that the evolution of the resulting SIRs will begin to differ. This will occur earlier for the narrower bands of high speed streams, but the width of 30° considered here is not narrow enough for the effect to occur within 1.5 AU, as opposed to the narrow bands of the SIRs in CR-1892 discussed in Section 3.3.1.

In brief, the Fast Bands SIR simulation effectively recreates the canonical characteristics of SIRs with no inclination relative to the ecliptic plane. The expectation is that the parameters of the SIR are identical at all latitudes since V_R at the inner boundary is the same at all latitudes. To confirm this, Figure 4.5 shows the evolution of the SIR driven by the wide band of fast solar wind as a function of heliographic longitude for several heliospheric distances and latitudes. This is the same SIR shown in only the ecliptic plane in Figure 4.4 but without the vertical offset. The longitudinal

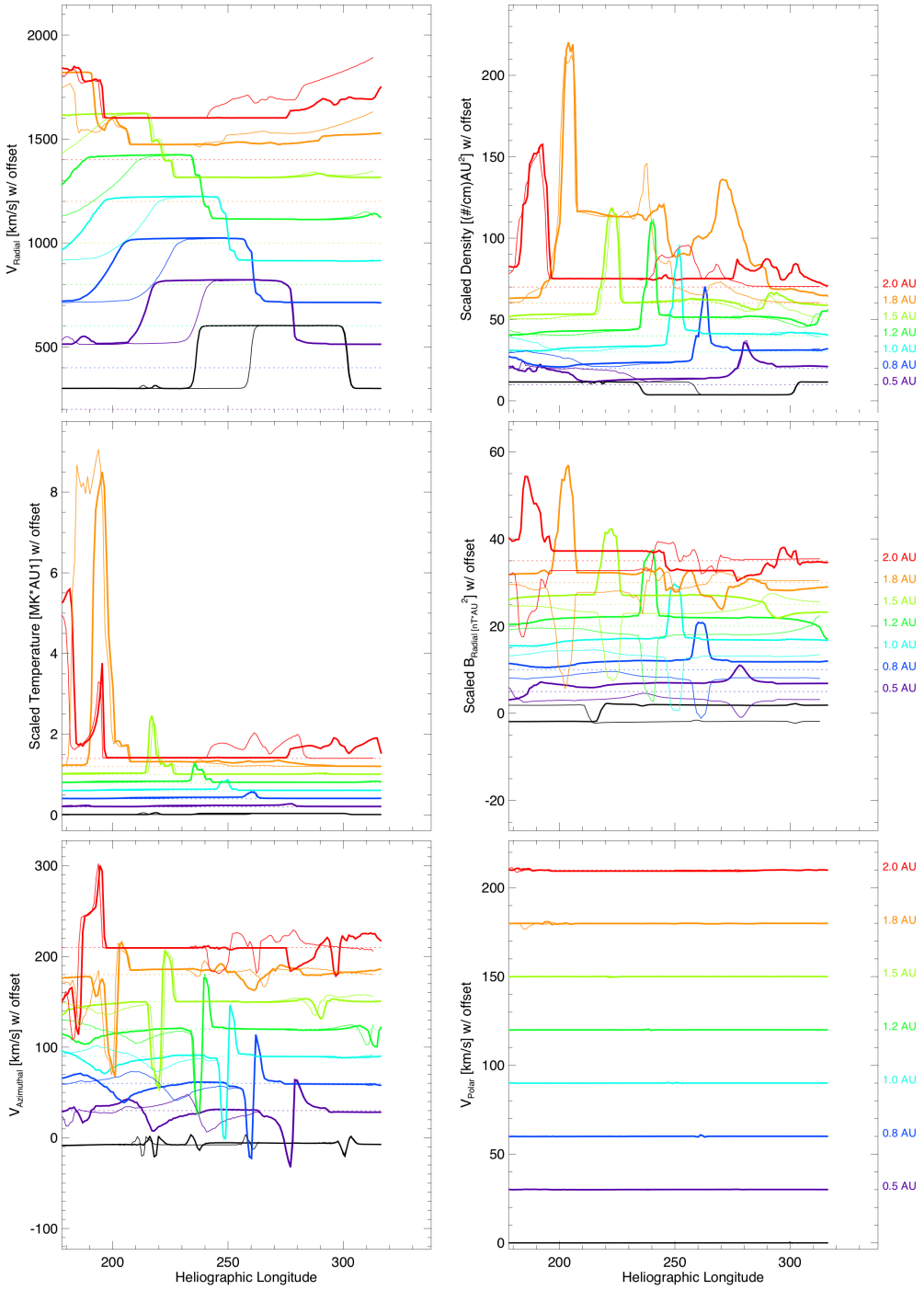

Fig. 4.4: V_R, n, T, B_R, v_ϕ, and v_θ as a function of heliographic longitude in the equatorial plane for highly idealized vertical bands of fast wind, as an approximation for the 2D case. The black line represents the inner boundary condition. The thick lines and thin lines show the evolution of the SIR driven by the wide and narrow bands of fast wind, respectively.

offset of the SIR arises from the winding of the Parker spiral. Each color represents the path through the SIR at a different radial distance, and the multitude of lines in the same color represent each of the 31 latitudes sampled, at equal intervals, between $-60°$ –$+60°$. Each panel shows one of the six parameters shown in 4.4.

Having shown that the longitudinal widths of fast wind do not affect SIR evolution, provided the peak speed has not been decreased by erosion, we use the idealized Fast Bands wide-band case to study the dependence of SIRs on heliospheric distance and latitude. To confirm that there is no latitudinal dependence, Figure 4.5 shows the same solar wind parameters as a function of heliographic longitude, radial distance (color), and latitude (multiple lines of the same color). In the top left panel, shown in black, the V_R profile at 0.1 AU is identical for all latitudes. As the solar wind propagates outward, at 0.35 AU (purple) and at 0.5 AU (indigo), there is evidence of the acceleration in the inner heliosphere but the shape of the SIR is still nearly identical for all latitudes being considered, as seen by the fact that the set of lines for V_R is narrow and all have the same shape. Generally, the profiles don't show an obvious increase in density, temperature, or magnetic field until at least 0.35 AU, which is the minimum distance at which an observer could tell that an SIR is developing. Slight differences in V_R as a function of latitude arise at distances of 0.65 AU and beyond, as seen in the progressive increase in spread of lines on the same color at leading edge.

Similar trends can be seen in B_R, n, and T, scaled to 1 AU. Each variable is identical at all latitudes at the inner boundary. As the SIR evolves with increasing heliospheric distance, the variables each develop the characteristics discussed in Figure 4.4, but the magnitude of the effects differ at increasing latitudes. These differences increase at larger heliospheric distances. This is unexpected for the Fast Bands case. Specifically, the timing of arrival and the sharpness of the increases in all

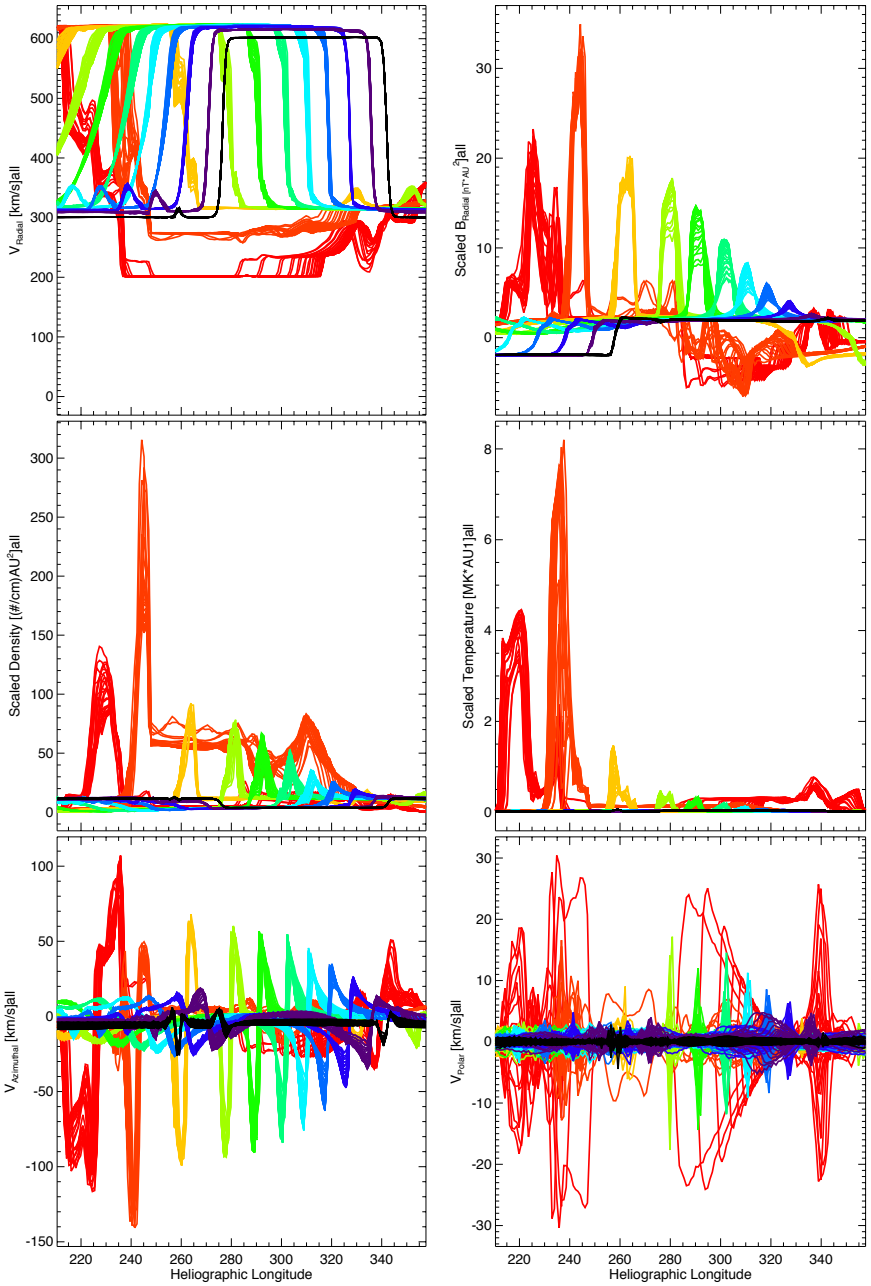

Fig. 4.5: Idealized Fast Band SIR parameters as a function of radial distance and latitude. The top row shows V_R, scaled $B_R r^2$. The second row shows scaled n and T while the third row shows v_ϕ and v_θ. The colors represent radial distances (0.20, 0.35, 0.50, 0.65, 0.80, 1.00, 1.20, 1.50, and 2.00 AU) and lines of the same color represent different latitudes, from $\pm$ 60°. The spread in lines of the same color shows that there is some latitudinal dependence on the evolution of the SIR. The distances 1.5 AU and 2.0 AU are problematic and should be ignored in this case.

SIR parameters considered, as well as the magnitudes of the peak density, temperature, and radial magnetic field strength depend on latitude. Once the SIR evolves to roughly 1.5 AU , the difference in plasma and field compression can be as much as 30%.

Furthermore, the expected deflections from the Fast Bands case is in the azimuthal direction but none in the polar direction. The corresponding panels in Figure 4.5 show that this is not the case. The V_ϕ panel shows the expected prograde-retrograde deflection, with a magnitude increasing rapidly within 1 AU and then more slowly beyond, as the SIR normal becomes more radially aligned. The fast wind deflection is nearly twice as fast as the deflected slow wind, implying a similar deflection angle for both slow and fast wind. Unexpectedly, V_θ is not 0 everywhere but exhibits evolutionary features similar to V_ϕ. V_θ is roughly 0 km/s at the inner boundary at all latitudes and remains 0 km/s in the solar equatorial plane. However, at higher latitudes, v_θ is non-zero at radial distances as small as 0.2 AU and increases with increasing distance from the Sun, which is unexpected from this geometry of high speed wind. Despite not being as fast as v_ϕ flow deflections, the polar component is still a clear, systematic flow deflection.

4.2.2 Fast Circles

Fast Circles is the second idealized case considered. As the name suggests, the inner boundary is constructed with slow wind everywhere except for two circles of high speed solar wind, centered on the heliographic equator. As in the Fast Bands case, the regions of slow and fast wind are uniform, having speeds of 300 km/s and 600 km/s, respectively. Both Fast Bands and Fast Circles have the same speed hyperbolic transition in V_R from slow to fast, and a vertical HCS embedded in the slow wind away from the speed transitions, so as not to affect the SIR's evolution. Furthermore, the circles of high speed wind have the same longitudinal extent as the

Fast Bands in the equatorial plane. Thus, the cases are identical in the equatorial plane and the effect of the large scale shape will be what causes any difference there. The IBC is shown in Figure 4.6.

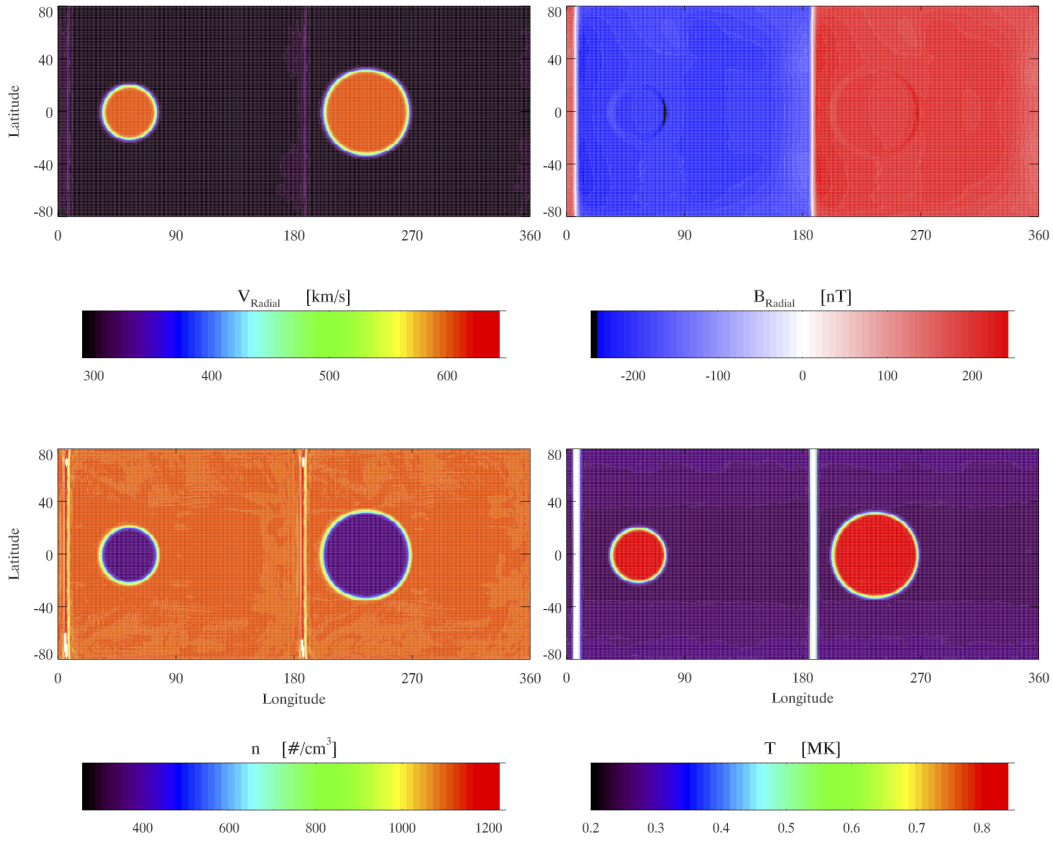

Fig. 4.6: Idealized inner boundary condition - Fast circles. High speed circles of different sizes drive SIRs and allow for deflection in the meridional plane.

Since the boundary between slow and fast solar wind has a latitudinal inclination, this configuration of HSSs should drive meridional deflection of plasma and so introduces 3D effects to an otherwise highly idealized solar wind configuration. This geometrical choice was motivated by earlier idealized studies by *Pizzo* (1982), in order to compare results from a validation motivation. From a more physical motivation, by the occasional presence of equatorial coronal holes (*Abramenko et al.*,

2010) would suggest that high speed sources centered on the equatorial plane warrant further investigation. These sources of low latitude high speed solar wind are more prevalent at solar maximum and also, atypically, during the solar minimum of solar cycle 23. The SIRs resulting from the Fast circles case are shown in Figure 4.7 in the same format as Figure 4.2, as a function of latitude and longitude at select distances, as well as in the equatorial plane. For this simulation, the results from 0.1–2.0 AU are valid. In the left-hand plot, of V_R at different latitudes, the SIR is seen to develop on the leading edge (right side) of the circular HSSs, as for both the big and small circles, the jumps in velocity increase and the region on intermediate solar wind speed broadens for most of the latitudinal extent of the HSS. The rarefaction waves that follow the HSS are also evident. In the equatorial plane, the winding of the SIRs roughly trace the Parker spiral, though there are differences in the equatorial plane seen between the big and small circle. The difference in the $r - \phi$ panel provides the first hint that, even in the equatorial plane, there will be differences in the evolution of the SIR driven by these HSSs. Thus, even for identical conditions at the inner boundary at that latitude, the introduction of some large scale structure will affect the local evolution of a stream.

Figure 4.8 shows the evolution of the SIR parameters quantitatively for the both the Big and Small Fast Circles in the equatorial plane in the same format at Figure 4.4. The V_R profiles of the Wide and Narrow HSSs evolve identically out to 1.5 AU. Beyond this, the narrow HSS seems to arrive earlier than the big circle case by 2-3 grid cells. Assuming that the Sun rotates through the 384 azimuthal grid cells in the synodic period of 27.27 days, the static pattern of solar wind would take about 1.7 hours to rotate through a grid cell azimuthally. Thus a 2-3 grid cell offset corresponds to a 3.4-5.1 hour arrival time difference.

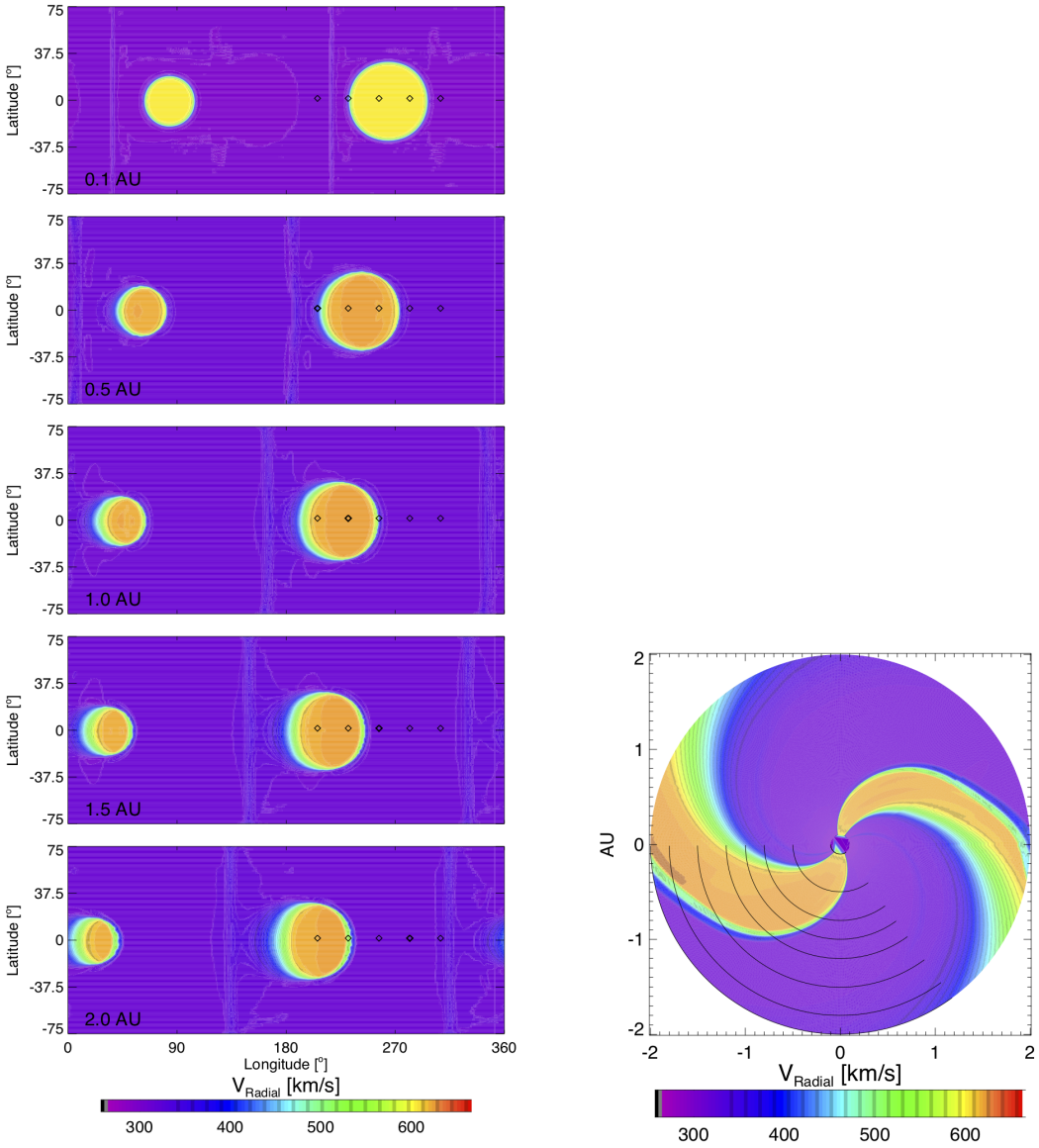

Fig. 4.7: V_R for highly idealized circles of fast wind, as an approximation for the 2D case.

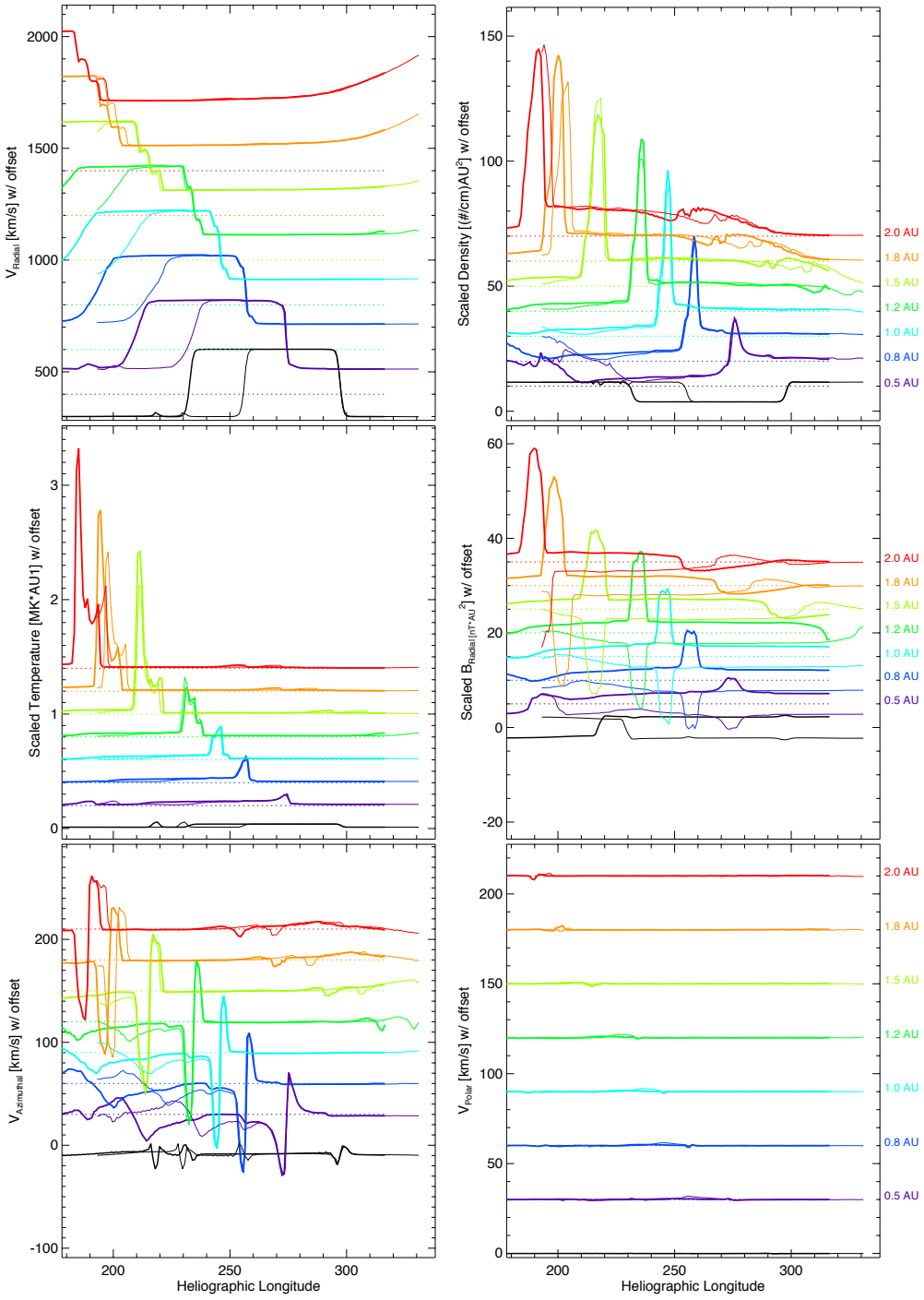

Fig. 4.8: V_R, nr^2, $TR^{4/3}$, $B_R r^2$, v_ϕ, and v_θ in the equatorial plane for SIRS driven by the Fast Circles case. The thick and thin lines are driven by the Big and Small circles HSS, respectively.

The other variables shown in Figure 4.8, are also shown as a function of heliographic longitude and radial distance for the SIRs from both the Big and Small circles, in the same format as Figure 4.4. nr^2 is shown in the top right, $Tr^{4/3}$ and $B_R r^2$ make up the second row, and the solar wind flow deflection in the azimuthal and polar directions make up the third row. The SIR evolution in nr^2 in the equatorial plane is nearly identical between $0.1 - 1.5\ AU$, for the SIRs driven by the Big and Small circles. Beyond 1.5 AU, the SIR from the small circle case arrives before the Big circle case, despite having similar magnitudes. The difference in timing is consistent throughout all of the SIR parameters. Similarly for scaled temperature, $Tr^{4/3}$, the evolution for both widths of circles strongly resembles those shown for the fast bands, however, there seems to be less heating in the small circle than in the big circle. The evolution of B_R for both the large and small circles of high speed is the same in magnitude but opposite in orientation as each of the HSSs is located in sector of different polarity. The flow deflection in the azimuthal direction is very similar to that in the Fast Bands case, as would be expected in the equatorial place. The deflections in the polar deflection are small but locally, the fast wind inclination is perpendicular to the equatorial plane and locally, we would expect no V_θ at this heliographic latitude.

Beyond the equatorial plane, however, the differences between the Fast Bands and Fast Circles cases are evident, primarily because the inner boundary and hence evolution of the Fast Circles cases is latitude dependent whereas the Fast Bands case is not. The latitudinal dependence of the evolution in V_R of the circular high speed streams is shown in Figure 4.9; the top row shows the V_R profile as a function of adjusted heliographic longitude for the big circles of high speed wind and the bottom row shows the same for the small circle. A latitude-dependent offset has been applied to the leading edge of the HSS, so as to analyze the SIR in a superposed epoch

analysis. The columns, from left to right, show V_R at $0.2, 1.0$ and 1.9 AU. Each of the colors show V_R at different heliographic latitudes. The black lines show V_R in the equatorial plane, with the other colors showing V_R at latitudes increasing in steps of 3 grid cells, being roughly equivalent to 4-5°, to higher heliographic latitudes, as indicated in the legend. The superposed epoch shift calculates the longitudinal offset, as a function of latitude, for the point in the speed profile at which $V_R = 450$ km/s at the inner boundary. This same shift is then applied at all distances, thus any offset in high speed stream initiation is a result of evolution and not of initial curvature of the high speed stream. This is called the Latitude Corrected Epoch longitude. As a result of this, the trailing edges at higher latitudes are offset, as expected for the diminishing longitudinal width of the high speed stream at higher latitudes.

Focussing our attention on the leading edge of the high speed streams in Figure 4.9, which drive the SIR, we can begin to see latitude dependent evolutionary effects for both the Big and Small Circles by 1 AU, especially for those latitudes where the HSS does not attain a speed of 600 km/s. The SIR at these latitudes has a less steep leading edge and the peak speed arrives later. This is consistent with a smaller speed differential driving the SIR and is not surprising for SIR evolution. Though the results for the SIRs driven by the large and small circles are homologous, it is worth noting that even in the equatorial plane, the large and the small fast circles drive SIRs that differ near 2.0 AU. The leading edge of V_R in, and near, the equatorial plane occur at larger heliographic longitudes, corresponding to earlier arrival times, and have a stronger step-like structure for the small circle SIR. It is worth noting that the Small Circle HSS has been mostly eroded at all latitudes at this point. Unfortunately, the Narrow Fast Band case does not extend to this distance and direct comparison is not feasible with the simulations that have been run since the initial conditions had not yet blown off the grid in the allotted simulation

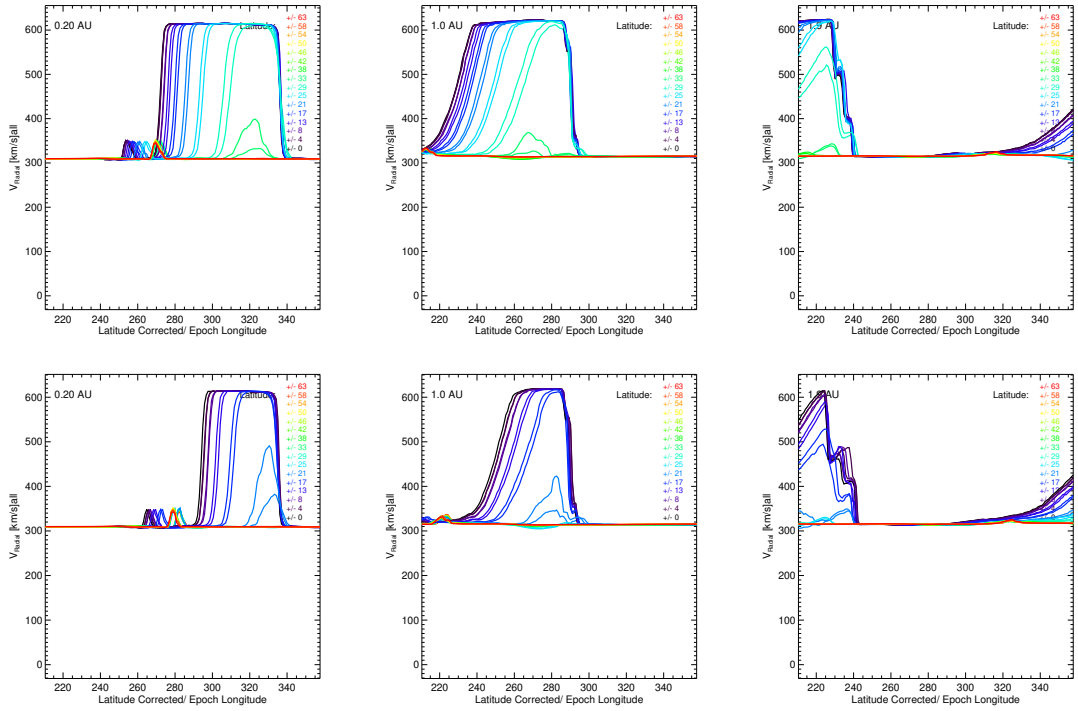

Fig. 4.9: V_R for highly idealized circles of fast wind, both big and small, at different distances and latitudes. The top row shows the evolution of the SIR driven by the big circle HSS at three heliospheric distances; 0.2 AU, 1.0 AU, and 1.9 AU (left to right columns) at several different latitudes, shown in different colors. The bottom row shows the same data but for the SIR driven by the small circle HSS.

time. This means that, even for identical local V_R profiles, the large scale shape of the HSS will have an effect on the local evolution of SIRs. The effects are largest and accrue the fastest once the maximum value of V_R is decreased.

Figure 4.10 shows meridional slices of the idealized SIR driven by the Big Circle at six different longitudes, transecting the SIR at increasing distances from the Sun. The top row shows V_R, with a cone of high speed wind driving the SIR within the latitudinal bounds set at the inner boundary ($\pm$ 35°, shown in the black lines). The thickening band of dark blue through yellow show the broadening region of intermediate speed in the SIR. The middle row shows the number density of the solar wind, scaled to 1 AU at the same longitudes as V_R. This projection shows that

the SIR initially shows the strongest compression near the equatorial plane, and the increased plasma density grows in latitudinal extent with increasing distance from the Sun. Just beyond 1 AU, the compressed plasma spans the range of latitudes containing the high speed wind. By 2 AU, the density enhancement extends beyond the range of latitudes where the SIR is driven, wrapping around the edge of the HSS. Therefore, the SIR-driven compression of solar wind plasma expands in latitude as the SIR propagates away from the Sun. Observationally, this would correspond to *in situ* data showing a region of enhanced density with no corresponding increase in solar wind speed. Furthermore, the extension of the SIR density is consistent with the suggestion by that SIRs, and hence also the shocks driven by them, propagate to higher latitudes. Similarly, the bottom row of Figure 4.10 shows the plasma temperature, scaled to 1 AU. The heating of the plasma begins moderately, is more prominent in the fast-wind side of the SIR, as is consistent with *in situ* observations, but remains constrained within the range of latitudes directly driven by fast solar wind. Both the density and temperature have the strongest enhancements within the range of latitudes where the SIR is directly driven, demarcated by the wedges drawn on each panel.

The reader's eyes cannot help but to be caught by the irregularities seen in the panels for Figuure 4.10 at distances greater than 1.5 AU. These may be the result of instabilities, such as the Kelvin-Helmholtz instability, as it has been observed in LFM simulations before (*Merkin et al.*, 2013). The analysis needed to determine whether and which type of instability is certainly worthwhile but is outside the scope of the current work.

Figure 4.11 shows the non-radial solar wind speed in the Fast Circles case. The top row shows meridional slices of V_ϕ, in the same style and location as in Figure 4.10 and the bottom row shows V_θ. As the SIR propagates away from the

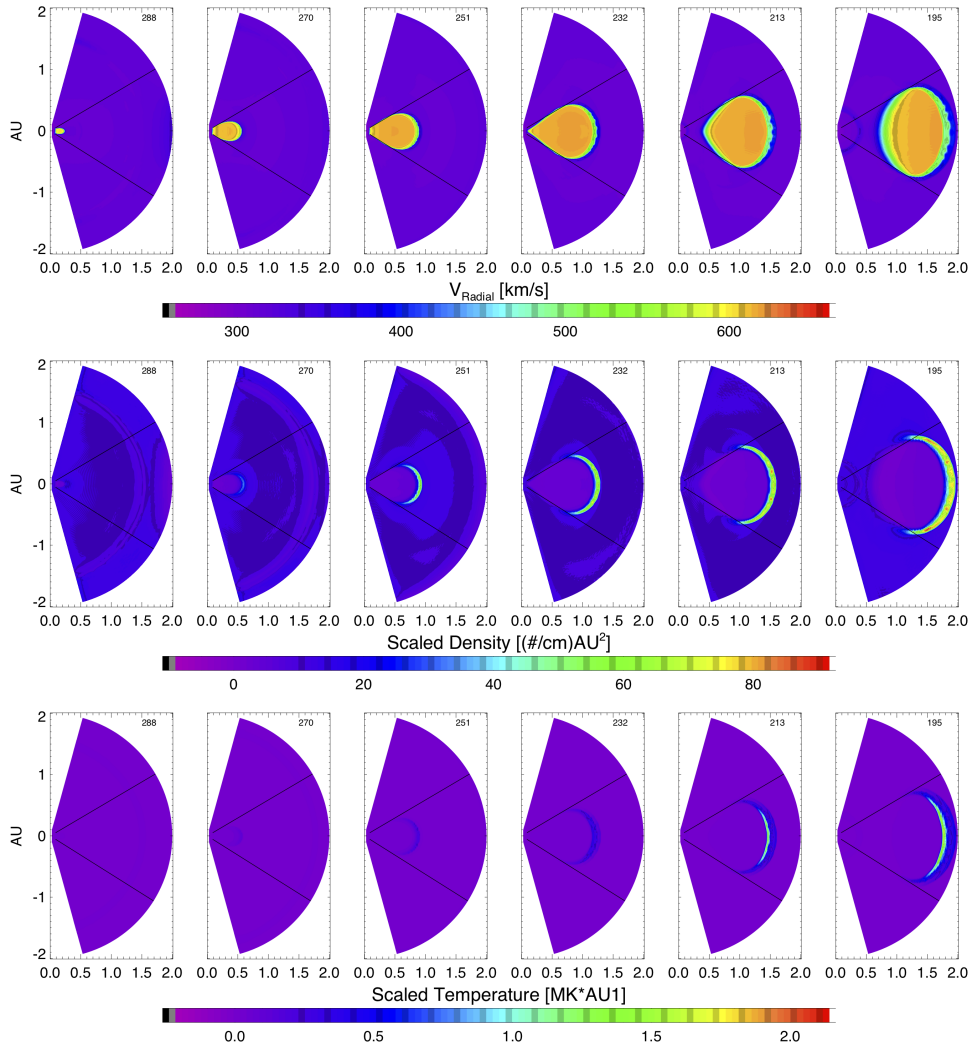

Fig. 4.10: The plots show meridional slices of the SIR driven by the Big Circle case. The rows show V_R, nr^2, and $Tr^{4/3}$ at longitudes indicated in the top right of each panel. Each longitude transects the SIR at different heliospheric distances, showing the evolution of the SIR as a function of distance and latitude.

Sun, the expected east-west deflection is present in the SIR, with a well defined and continuous region of $V_\phi = 0$. This surface of flow reversal is frequently used as an observational signature of the stream interface and these panels support the conceptualization that this surface is continuous and roughly parallel to the SIR orientation. The azimuthal flow magnitude is fairly uniform as a function of latitude and is constrained to the range of latitudes where the SIR is directly driven by high speed wind. For V_θ, there is stagnation in the equatorial plane, given that the SIR normal is not tilted at this latitude. At larger latitudes in the northern hemisphere, the slow wind is deflected northward while the fast wind is deflected southward. The converse occurs in the southern hemisphere. These deflection flows, driven in proportion to the latitudinal tilt of the SIR, are strongest at high latitudes, near the edges of the HSS. The northward deflection continues beyond the extent of the fast wind in the northern hemisphere, as does the southward flow in the southern hemisphere.

Hence, the Fast Circles case shows that the evolution of SIRs changes once the SIR and rarefaction wave decrease the maximum speed and that this occurs, unsurprisingly, at smaller heliographic distances for narrow HSSs than wide HSSs. The SIR evolves as expected for both the Fast Circles and Fast Band Cases, with the Fast Circles cases exhibiting the pattern of flow deflection expected of a tilted HSSs. Furthermore, the SIR plasma compression and polar flow deflection extend beyond the directly driven region of the SIR, causing the structure to expand in latitude with increasing distance from the Sun. Given the characteristic and latitudinal dependences seen here, we turn now to the canonical solar minimum solar wind configuration, which we have idealized in the Slow Sine run.

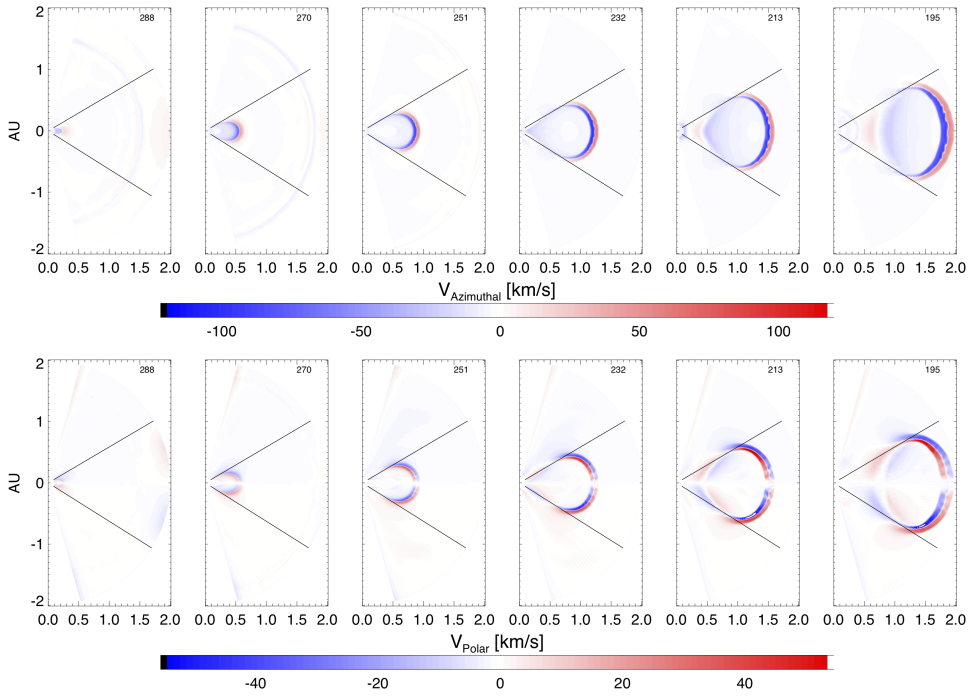

Fig. 4.11: Meridional slices of V_ϕ and V_θ driven by the SIR driven by the Big Circle case in the same format as Fig. 4.10.

4.2.3 Slow Sine

The inner boundary of the Slow Sine case shown in Figure 4.12, represents the idealized version of the canonical solar minimum. Uniform high speed solar wind populates high latitudes while a sinusoidal band of slow solar wind undulates about the heliographic equator. The fast wind is tenuous and hot while the slow wind is dense and cool. The HCS is embedded in the middle of the band of slow wind. As viewed from Earth, this reproduces the two sector, four stream pattern typical of solar minimum (*Crooker et al.*, 1996). Slow Sine is the most common configuration of idealized solar wind and has been modeled by others (*Riley et al.*, 2006; *Pizzo*, 1982).

Observations of the solar wind near the heliographic equator would consist of a period of fast wind then a period of slow wind, with the same magnetic polarity,

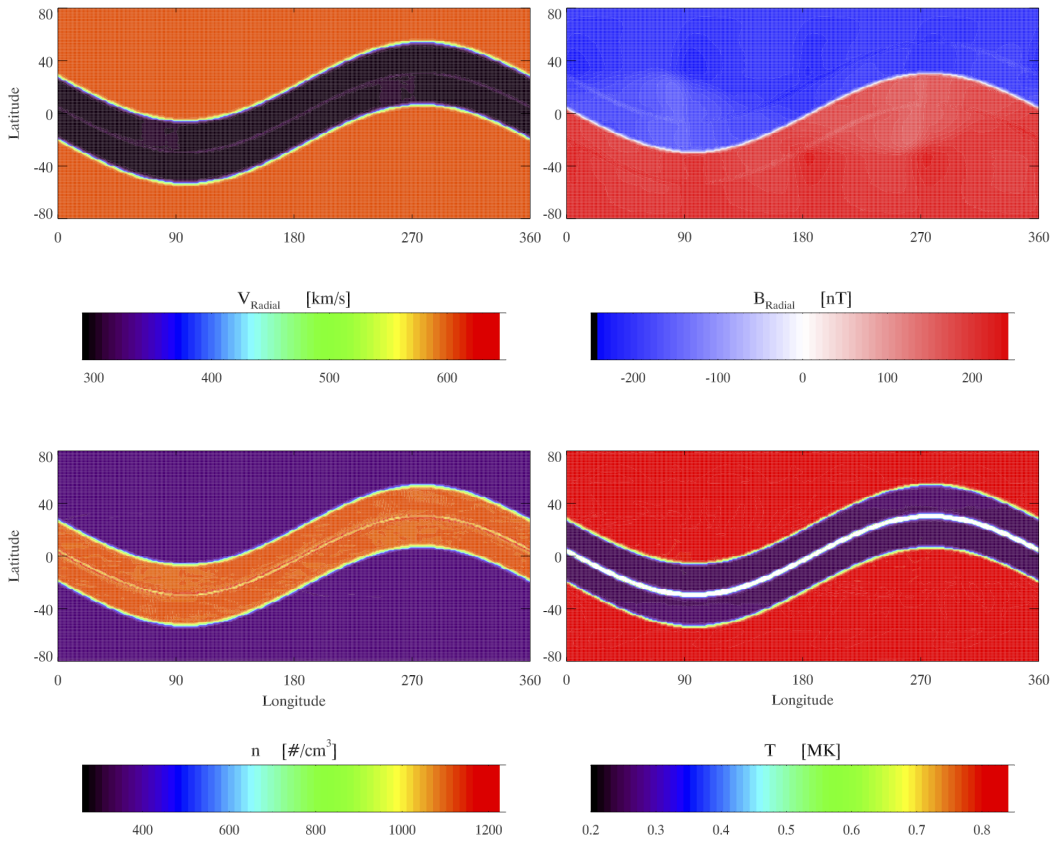

Fig. 4.12: Idealized inner boundary condition of Slow Sine. Clockwise from top left, the panels show V_R, B_R, T, and n. High speed, hot, tenuous solar wind populates high latitudes while the band of slow, dense, solar wind containing the HCS, undulates about the heliographic equator.

followed by a reversal of magnetic polarity within the band of slow wind, and finally a transition back into the fast wind. The pattern then repeats with the opposite polarity. This configuration of wind will create two large, planar, inclined SIRs where the fast wind follows the slow wind. Figure 4.13 shows V_R as a function of latitude and longitude at five different heliospheric distances (left) and as a function of radius and longitude in the equatorial plane (right). The SIRs are expected to develop where the fast wind flows behind the slow, namely whenever the fast wind is immediately

to the left of the slow wind at a particular latitude. Looking at the structure of V_R in Figure 4.13, a SIR would form northward of the HCS between longitudes of 280° and 80° and another SIR will form southward of the HCS between longitudes of 100° and 260°. Both SIRs will be inclined towards the equator, consistent with observations of SIRs during solar cycles 22.

Other than having bands of fast wind with a larger longitudinal extent, the plot on the right of Fig. 4.13 resembles the equivalent plot in Figure 4.2 and Figure 4.7. A significant difference between the Slow Sine case and the previous two is that, since the extent of slow wind is less, the HCS is embedded in the center of the slow wind band, as is physical. The SIRs develop near the HCS in this idealized case. While SIRs frequently occur following a crossing of the HCS or HPS, its influence was not intended to be included in these idealized cases. However, it is unavoidable to some extent in the Slow Sine and Pseudostreamer-Streamer case considered in Section 4.2.4. The band of slow wind was chosen to be wide enough to avoid direct interaction within 2.0 AU.

Quantitatively, Figure 4.14 shows the evolution of the SIR in the same format as Figure 4.4. The top left panel shows V_R. As with the previous cases, the minimum and maximum solar wind speeds at the inner boundary are 300 km/s and 600 km/s, respectively. The transition from fast wind to slow is also a hyperbolic tangent but oriented latitudinally in Slow Sine, as opposed to longitudinally as in the Fast Bands case and Fast Circles. Though this choice better recreates the variations seen in more realistic simulations of solar wind and with observations, it introduces some artificial jaggedness in the longitudinal direction as well as a slower rise in the V_R profile as a function of longitude. The jaggedness in V_R is smoothed by 0.8 AU. The two sections of longitude, one for the SIR north and south of the HCS, cut through different longitudinal extents of fast wind. The SIRs driven by both extents of high

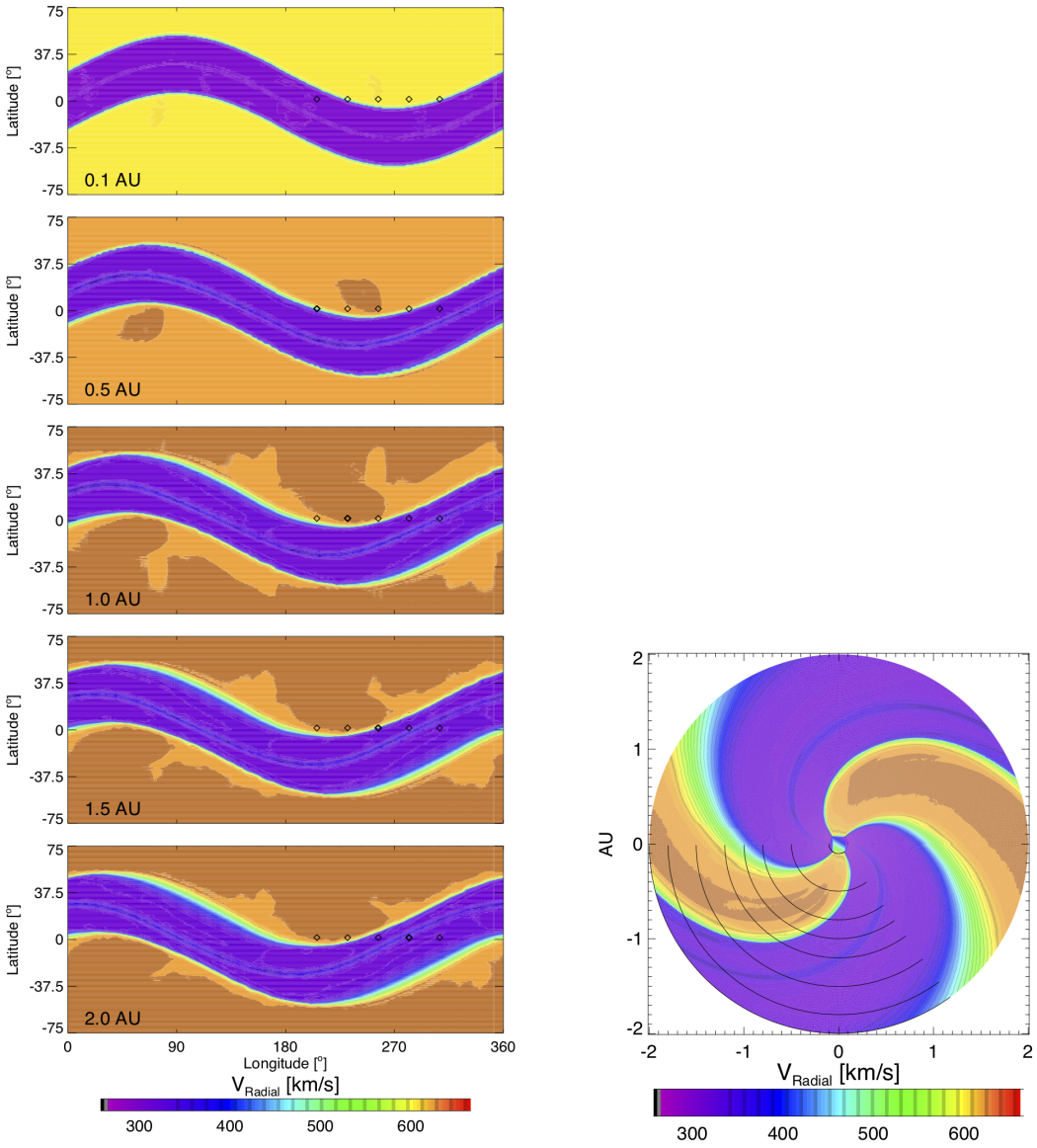

Fig. 4.13: V_R for the idealized Slow Sine case, as an approximation for the classical two sector, four stream case.

speed wind evolve identically between 0.1 and 2.0 AU, but these SIRs have the speed increase steepen out to 1.5 AU before they develop any step-like structure, as seen by 0.8 AU in the Fast Bands and Fast Circles cases. Similar to the Wide Fast Band and Wide Fast Circle, the HSS still contains an extent of fast solar wind by 2.0 AU, the erosion not being an issue at these heliospheric distances.

The top right panel of Figure 4.14 shows that nr^2 for both the northern and Southerm SIRs evolve the same, increasing in peak density and in width with increasing distance from the Sun. The SIR evolves differently than the SIRs in Fast Circles and Fast Bands. For each of the distances considered, the maximum density of the SIR is less in Slow Sine than in the other cases. Explicitly at 1.0 AU, the peak density of the Fast Circles case is ≈ 65 $/cm^3$ whereas it is ≈ 30 $/cm^3$ in the Slow Sine case. At 2.0 AU the respective peak densities are 75 cm^3 and 60 $/cm^3$. Furthermore, the density peak is broader and more structured. Similarly, B_R in the Slow Sine case has a broader extent of compressed magnetic field and smaller values at the peaks than in the other cases. The lower peak values and the broader compression regions are partially due to the smaller gradient in V_R which drives the SIR. The smaller bump in density that precedes the SIR is the density increase related to the HCS. The same trend is seen in T, where the peak temperatures in the SIR are 1.5 and 3 times as high in the Fast Circles case as they are in the Slow Sine case at 1.0 AU and 2.0 AU. The temperature peaks are broader and also are singly peaked out to 2.0 AU, whereas in the Fast Circles case, the temperature profile has two peaks beyond 1.5 AU, with the second one being hotter.

Other significant differences between the Slow Sine and the Fast Bands and Circles cases occurs for V_ϕ and V_θ. For Slow Sine V_ϕ, as with all other variables, the peaks are smaller and more broad. The deflection in the polar direction is a more pronounced dipolar signature, is broader, and has a larger magnitude than

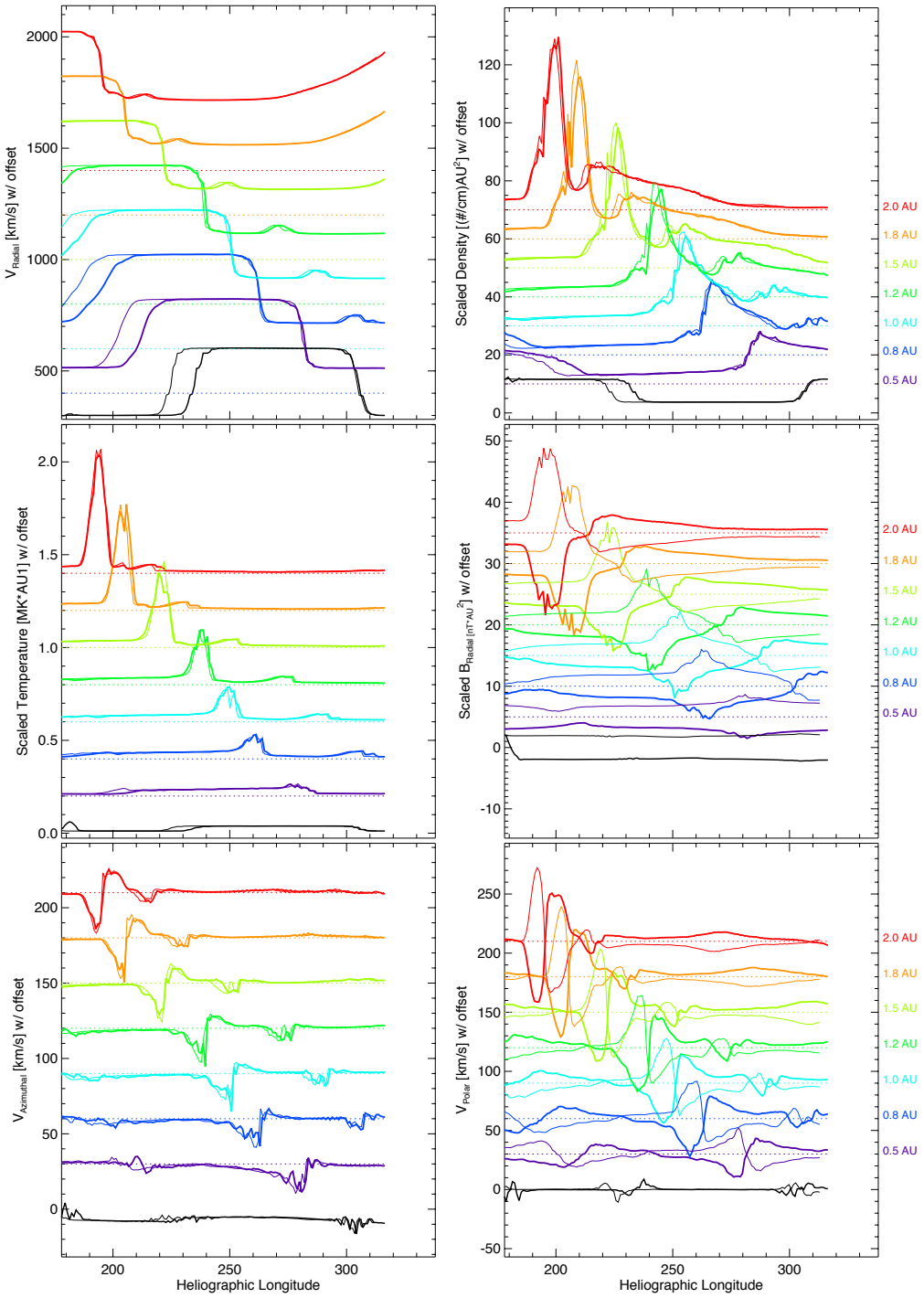

Fig. 4.14: V_R, n, T, B_R, v_ϕ, and v_θ for highly idealized as an approximation for the classical Slow Sine case.

the azimuthal flow deflection. The azimuthal flow deflections maintain the same amplitude beyond 1.0 AU but become broader out to 2.0 AU. For Fast Circles at 1.0 AU in the equatorial plane, the slow wind is deflected azimuthally at 60 km/s in the direction of solar rotation and the fast wind is deflected at 90 km/s in the opposite direction in narrow peaks. V_θ is less than 10 km/s in the equatorial plane. The azimuthal deflection is only $\approx$ 10 km/s and 25 km/s at 1.0 AU and they increase slightly in speed to 15 km/s and 25 km/s by 2.0 AU. Furthermore, this is the first case to show significant solar wind deflection in the polar direction in the equatorial plane. At 1.0 AU in the equatorial plane, the deflection in the polar direction is faster than in the azimuthal direction. V_θ becomes faster at larger heliospheric distances and attains speeds of 40 km/s for the deflected slow wind and 50 km/s for the fast wind. The flow deflection in V_θ are oppositely oriented and are consistent with the orientation of the SIR that drives them. The magnitudes of flow deflections supports the use of this method to deduce large scale inclinations of SIRs, at least locally.

It is worthwhile to also investigate how this more realistic configuration of fast wind drives SIRs as a function of latitude. As in the analysis for the Fast Circles case, Figure 4.15 shows V_R as a function of adjusted heliographic longitude at several latitudes at 0.1 AU, 1.0 AU, and 1.9 AU. The leading edge of the HSS has been aligned by the intermediate speed of 450 km/s at the inner boundary. As can be seen in the top left panel, the lines at all latitudes indeed overlap to form a narrow line at 0.1 AU. It is worth noting here that the latitudes considered span both hemispheres and thus include both a northern and southern fast wind source. The evolution of the V_R profiles depend on latitude. At high latitudes, the magnitude and longitudinal extend of slow wind both decrease as the rarefaction region from the preceding sector of fast wind accelerates it. This process is also occurring at mid-latitudes but at latitudes less than 46°, the slow wind is not completely eroded by 2.0 AU. For most

latitudes considered, the high speed stream driving the SIR remains intact in the region of interest.

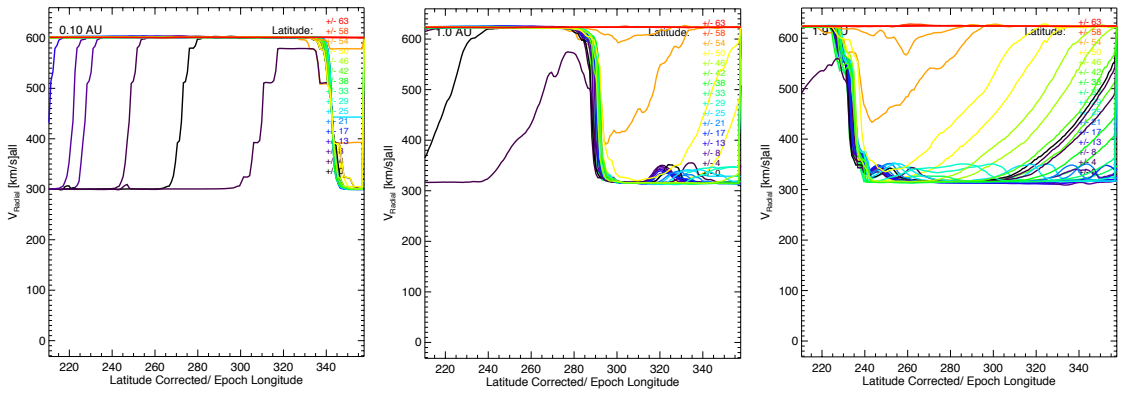

Fig. 4.15: V_R for highly idealized band of slow streamer at different distances and latitudes. The three heliospheric distances 0.1 AU, 1.0 AU, and 1.9 AU (left to right columns) at several different latitudes, shown in different colors.

As in the Fast Circles case, any spread in the leading edge of the SIR beyond 0.1 AU is therefore an evolutionary effect, and indicates a change in the tilt of the SIR as a function of distance. Indeed, this spread is present, increases with heliospheric distance, and is systematic by latitude. The SIR at low latitudes is consistently behind the SIR leading edge at high to mid-latitudes, which suggests that SIRs inclination increases with increasing distance from the Sun, which has not been suggested before. Explicitly, at 1.0 AU, the leading edge at 50° is at least 5° in longitude ahead of its equatorial counterpart. For structures corotating with the Sun, this implies an arrival time of more than 8 hours earlier than expected from inclination and corotation alone.Though a smaller difference than the accuracy of current models, it is still an interesting and notable phenomenon. Furthermore, the difference increases with increasing heliospheric distance.

With so much variation in V_R, Figure 4.16 shows the large range of variability in solar wind density, temperature and magnetic field strength is hardly surprising. The numerous lines on these plots show that there are clear patterns of increasing

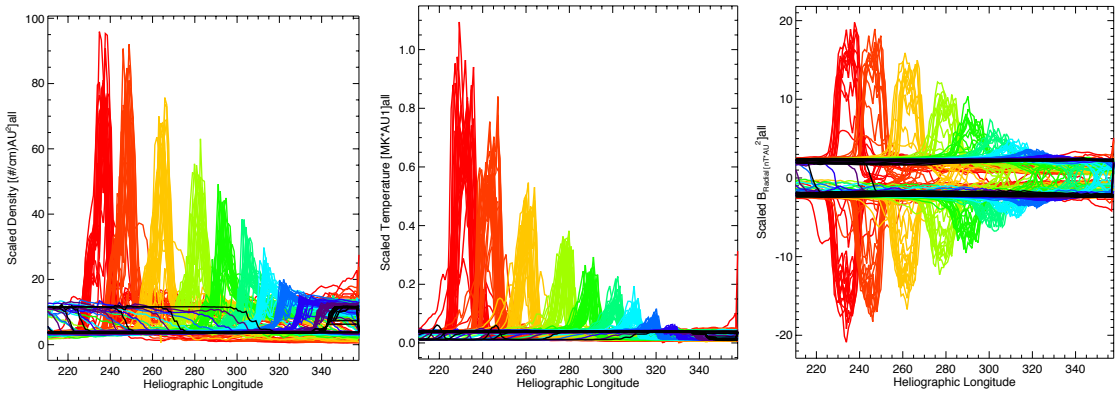

Fig. 4.16: nr^2 is shown in the left panel, $Tr^{4/3}$ is shown in the centre, and Br^2 is shown in the right panel as a function of latitude for several heliospheric distances, differentiated by color and labelled in the legend on the right of each panels.

density, temperature, and magnetic field strength within the SIRs driven by Slow Sine, as seen by the envelopes of the lines shown. There is also a large amount of variability in peak values, in widths, and in arrival times as a function of latitudes at each distance considered. For all latitudes, the variation in the near-inner heliosphere ($0.1 - 0.3$ AU) for parameters nr^2, $Tr^{4/3}$, and Br^2 are not discernible despite the transition from fast wind to slow wind. Thus, for missions in the inner heliosphere gathering data to parameterize SIRs in the early stages of their development, the transition in V_R is an obvious signature but the signatures in plasma properties that are normally associated with SIRs may be difficult to identify *in situ*.

To understand the latitudinal variation in Figure 4.16, Figure 4.17 shows meridional slices of the SIR at different distances in the same format as Figure 4.10 for both the northern and southern SIR. The placement of the SIR is offset from the equatorial plane and begins forming most strongly at mid-latitudes, where the width of intermediate speed wind increases, and then becoming stronger at low latitudes and at higher latitudes, only beyond 1AU. Both the density and the temperature exhibit similar evolution. Hence, in the case of a tilted HCS, the SIRs do not form

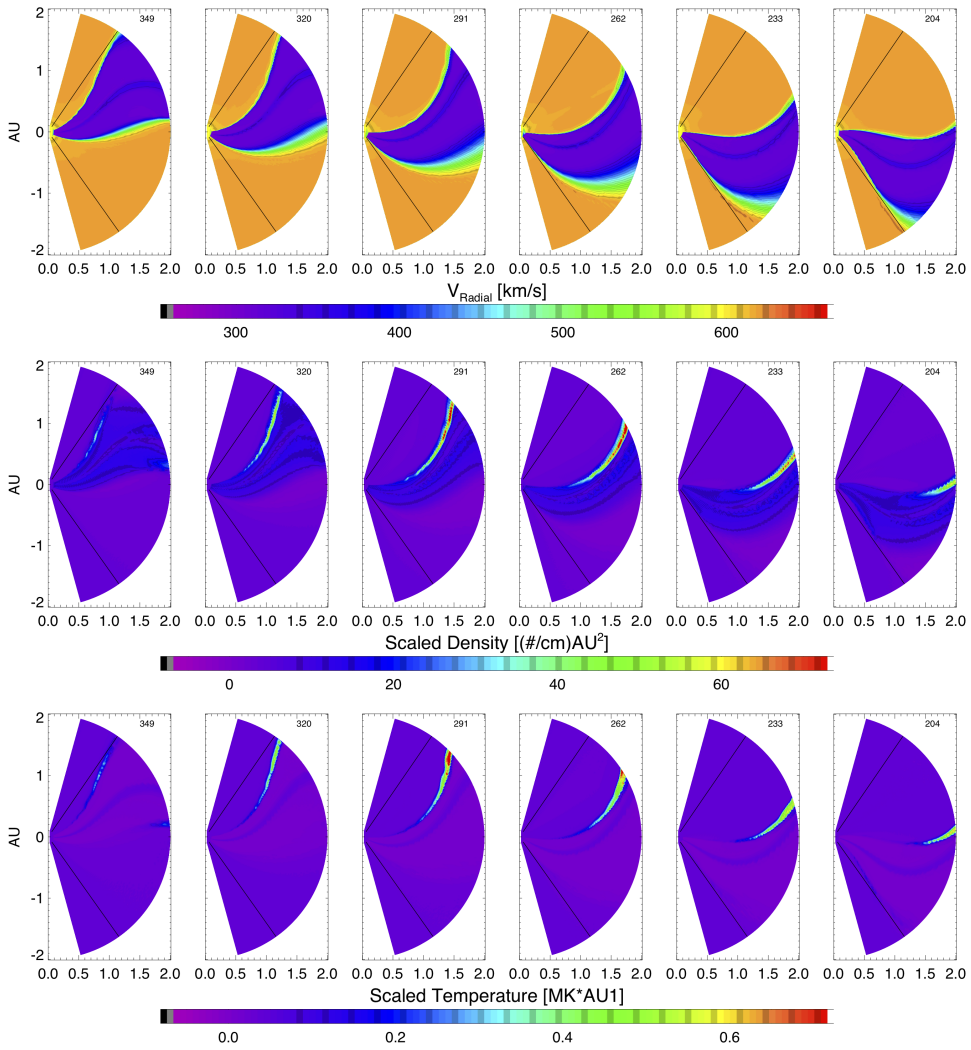

Fig. 4.17: The plots show meridional slices of the SIR driven by the Slow Sine case. The meridional slices show V_R, nr^2, and $Tr^{4/3}$ at particular longitudes, indicated in the top right of each panel. Each longitude transects the SIR at different heliospheric distances, showing the evolution of the SIR as a function of distance and latitude.

very strongly within the wedge of heliographic latitudes bounded by the ecliptic but are much more pronounced at high latitudes.

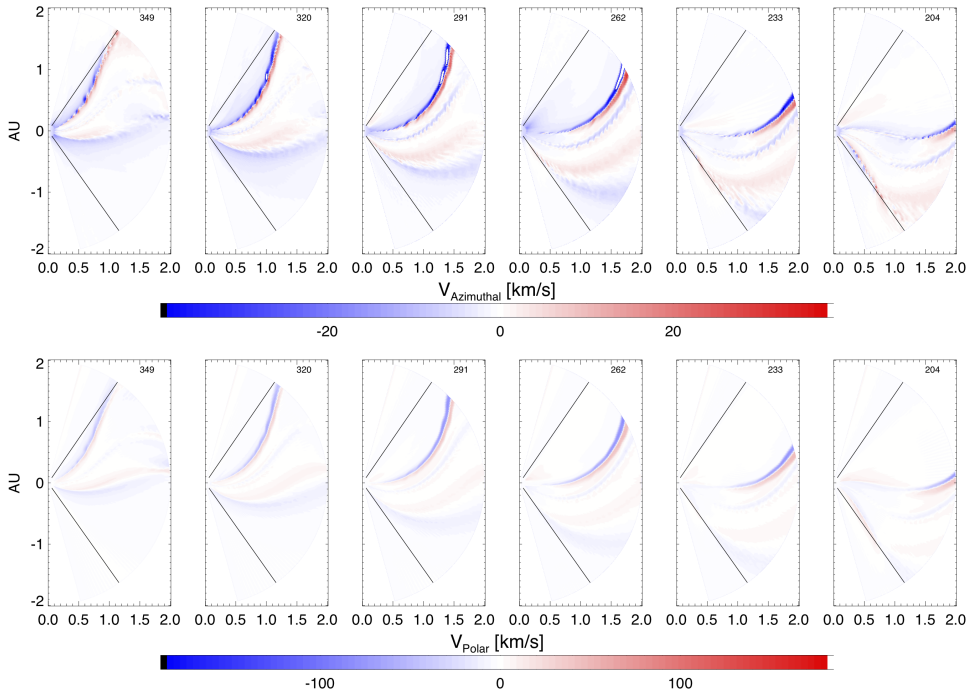

Fig. 4.18: The plots show meridional slices of the SIR driven by the Slow Sine case. The meridional slices show V_ϕ,V_θ in the same format as Fig. 4.10.

Figure 4.18 shows the deflection of solar wind flow within the SIR. The azimuthal flow that is driven by the SIR has the characteristic prograde - retrograde dipolar signature along the entirety of the SIR, as does the the north-south deflection in the polar flow. In the Slow Sine case, the deflected flow is asymmetric with the deflected slow wind consisting of a wider spatial extent than the deflected fast wind for the full latitudinal and radial extent of the SIR. Slow Sine is the first of the idealized configurations for which this is true.

With the evolution we have seen thus far in mind, we turn to the final idealized inner boundary condition.

4.2.4 Streamer Pseudostreamer

The fourth idealized case, Streamer-Pseudostreamer, is the most complex of the idealized cases. Its inner boundary condition is shown in Figure 4.19. Streamer-Pseudostreamer is similar to the Slow Sine case with the addition of a band of slow solar wind that does not contain the HCS, a pseudostreamer (*Wang et al.*, 2007; *Crooker et al.*, 2012; *Crooker and McPherron*, 2012; *Riley and Luhmann*, 2012). As shown in the top left panel of Figure 4.19, the IBC consists of high speed solar wind everywhere except for slow wind undulating about the heliographic equator, in the form of two sine waves in anti-phase. Only one band of slow wind contains the HCS; the idealized streamer. The other band of slow wind contains uniform magnetic polarity, which makes it a pseudostreamer. Both the streamer and pseudostreamer have the same latitudinal width and speed magnitudes. The streamer-pseudostreamer run is motivated by the preponderance of pseudostreamer structure during the declining phase of solar cycle 23 (*Lee et al.*, 2011; *Luhmann et al.*, 2009). In nature, there are studies that show that pseudostreamers may be thinner, and slightly faster than streamers but this can be difficult to ascertain unambiguiously *in situ*.

Unfortunately, for the inter-comparison between cases, the Streamer-Pseudostreamer case was initially conceptualized for a different purpose and so contains some differences with respect to the other idealized cases. It is used here to elucidate the structure of SIRs driven by an idealized version of the coronal state during solar cycle 23, but some important differences warrant direct discussion. Explicitly, for Fast Bands, Fast Circles, and Slow Sine, the fast solar wind is set at 600 km/s and the slow solar wind is 300 km/s. The shape of the transition between fast and slow wind is a hyperbolic tangent of constant width. For the Streamer-Pseudostreamer case, the slow wind was also set at 300 km/s but the fast wind was set at 720 km/s and the shape of the transition is parabolic, in order to more closely

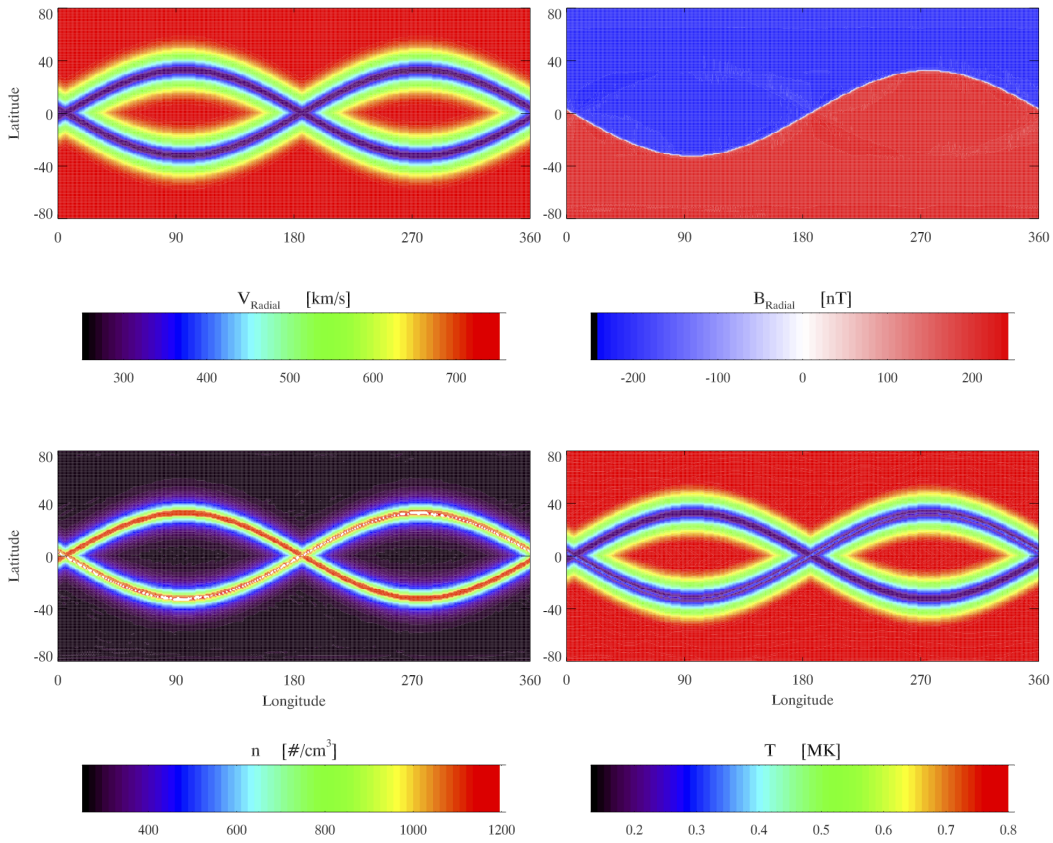

Fig. 4.19: Idealized inner boundary condition-Streamer-Pseudostreamer. High speed solar wind populates most of the inner boundary except where there are bands of slow wind, one containing the HCS, undulating in anti-phase about the heliographic equator. The relationship between V_R, n, and T is the same as in all previous cases.

match observed speeds for the fast wind. The speed transition thus spans a larger extent, with more intermediate speed wind than is thought to be present at 0.1 AU, and has a different functional shape. In order to leave enough room for a source of high speed wind in the equatorial plane in these runs, without the slow wind extending to latitudes significantly more poleward than observed, both the streamer and pseudostreamer bands were made narrower than the extent of slow wind in the other cases.

Despite the differences in V_R, the relationship between it and the other parameters are the same as in the previous idealized cases. The magnitude of B_R is uniform at the inner boundary, changing in polarity functionally as a hyperbolic tangent that spans 8 grid cells. B_ϕ is determined from corotation, and B_θ is set to zero. The number density is determined from V_r as in Equation 2.2. As before, the temperature is determined by assuming a uniform total pressure (P_{tot}=P_{therm}+P_{mag}).

The panel on the right hand side of Figure 4.20 shows V_R in the equatorial plane. This case resembles the others with four solar wind streams, two each of fast and slow, except that a larger fraction of the solar wind in the equatorial plane is fast, which is not often the case observationally. It is worth noting that the latitude of the terrestrial sub-solar point varies between $\pm 7°$, which would increase the proportion of time the Earth would be immersed in slow wind. Despite this disparity with observations, due to the narrower bands of slow wind and the oblong shape of the HSS, the evolution of the SIR proceeds as expected. The left hand side of Figure 4.20 shows V_R as a function of latitude and longitude at five heliographic distances. SIRs, seen the fast wind catching up to the slow wind, develop both on the interior and exterior of the streamer-pseudostreamer bands. The SIRs in the equatorial plane will be driven by HSSs that have an oblate circle cross-section in shape, mildly reminiscent of the chili-pepper shaped high speed stream discussed in Section 3.2.1. In the left hand plot, the fast wind can be seen accelerating the the slow wind towards the right (higher longitudes) and the corresponding rarefaction regions towards the left, resulting in a relative longitudinal offset between fast and slow wind.

Figure 4.21 shows the quantitative evolution of the SIRs in the equatorial plane. Despite the longer azimuthal extent of the transition from minimum to maximum speed at the inner boundary, the speed differential is larger, and the V_R profile evolves

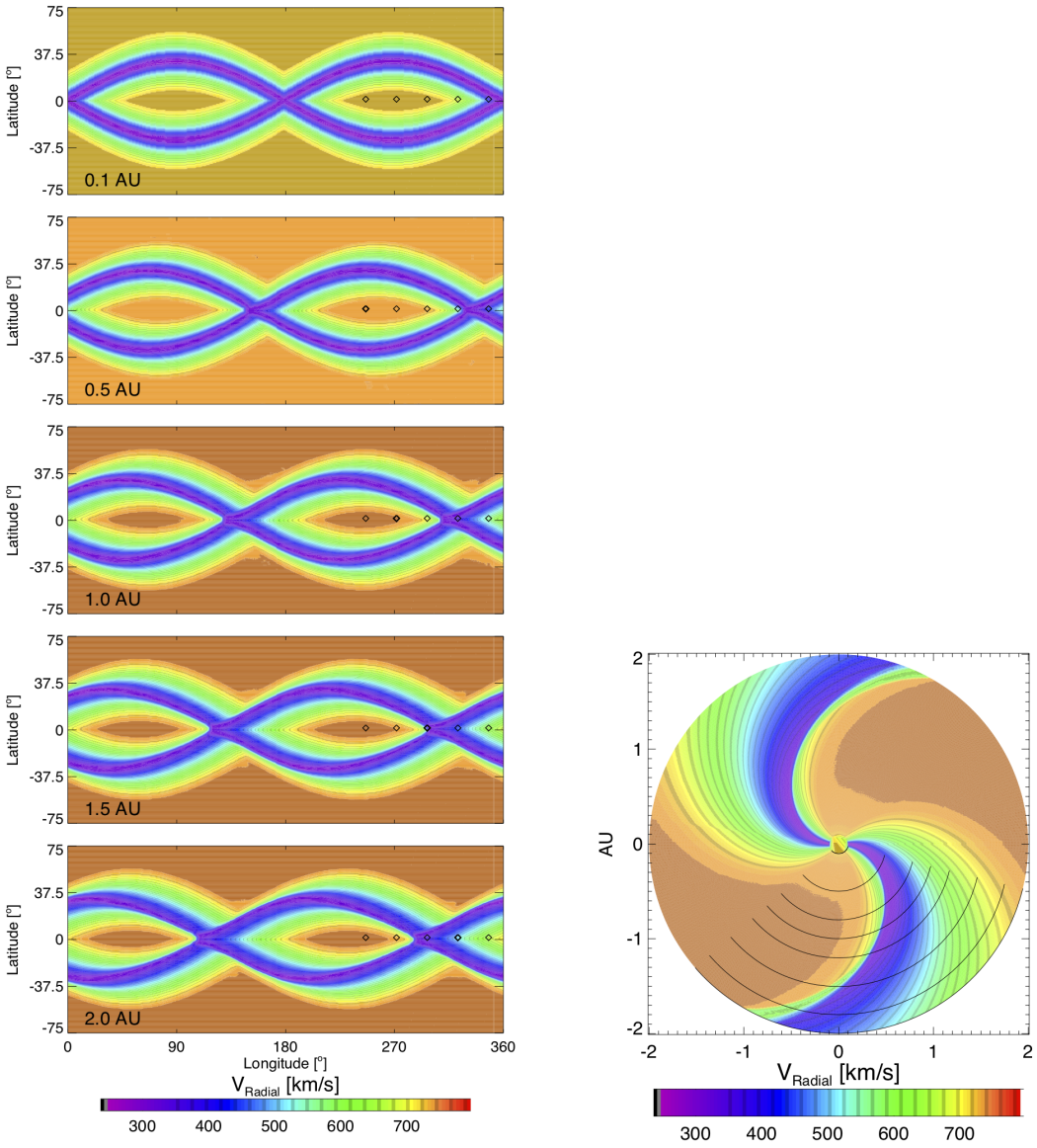

Fig. 4.20: V_R for highly idealized sinusoidal bands of slow wind, as an approximation for prevalence of pseudostreamers as seen in recent solar cycles.

to have the step-like increases in V_R by 1.5 AU, as seen in cases Fast Bands and Fast Circles in the equatorial plane and at higher latitudes for Slow Sine. The faster maximum speed, or rather the larger difference in maximum and minimum speeds, causes the evolution to be stronger within a particular distance. It is also worth noting that since the band of slow wind here is narrow, the SIR abuts a rarefaction region from the preceding HSS at 2.0 AU.

Despite a larger difference in speeds, the panel on the top right of Figure 4.21, the peaks in number density for the Streamer-Pseudostreamer case are intermediate between those of the previous cases. The compression of the plasma occurs more strongly within 1.0 AU, increasing the peak density rapidly. Within 1.2 AU, the peaks are preceded by a slow ramp-up as they are in the Slow Sine case but otherwise, the peaks are narrow and more similar in shape to those in Fast Circles. The scaled temperature in this case resembles that of Fast Circles in shape, notably that it is double-peaked by 1.5 AU, but seems to heat at a different rate with respect to heliospheric distance.The heating is less in Streamer-Pseudostreamer than other cases within 1.0 AU, but is comparable the other cases out to 1.5 AU and then exceeds it beyond that.

The compression of B_R in the equatorial plane also resembles the width and amplitude of the Fast Circles case more than the Slow Sine case at all heliospheric distances. A notable difference between this case and all others, however, is that the HCS is embedded in the SIR. The signature in B_R is thus an increase in magnitude, then a sharp polarity reversal and continual increase in magnitude. The HCS crossings are symmetric about the equator for each of the SIRs in the equatorial plane. The HCS is often observed to precede or be embedded within a SIR *in situ*.

Though the buildup of flow deflection is slow in the inner heliosphere for the Streamer-Pseudostreamer case, by 1.0 AU, V_ϕ in the equatorial plane has a strong,

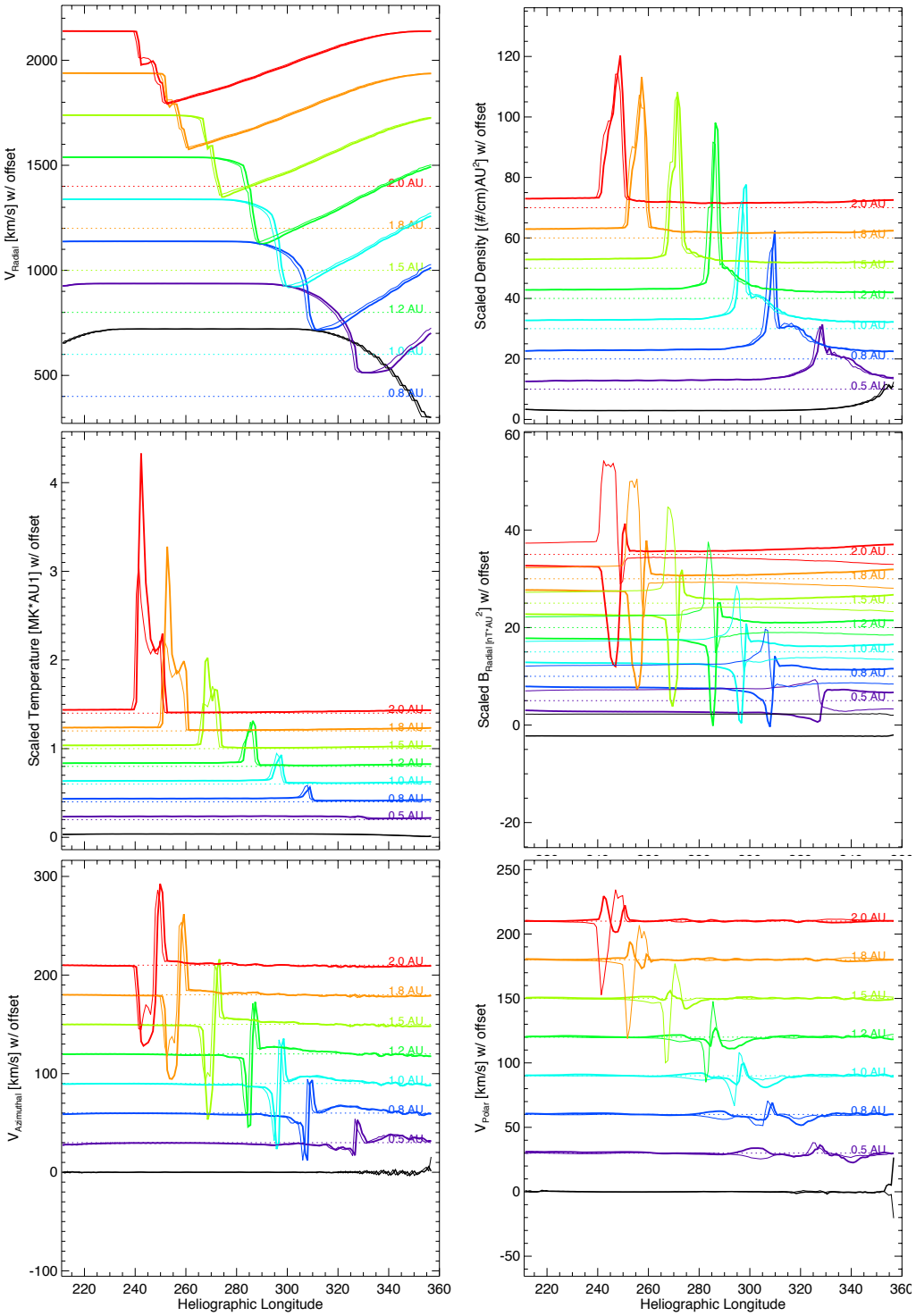

Fig. 4.21: V_R, n, T, B, $v_\theta$and v_ϕ for highly idealized as an approximation for the streamer-pseudostreamer case.

dipolar signature. There is also a slight asymmetry between SIRs considered in this plane for this case. Considering V_θ, here the Fast Circles case has barely any deflection and Slow Sine has significant deflection in the polar direction, whereas the Streamer-Pseudostreamer case is intermediate and becomes asymmetric between SIRs. V_θ for the SIR shown by the narrow lines remains small, $\leq 20\ km/s$ for one SIR. For this SIR, V_θ matches the other roughly out to 0.8 AU, but then develops differently into a series of small deflections, the order of which depends on heliographic distance. The flow deflection for the SIR shown by the solid lines has the typical bimodal shape and has amplitudes between 10–60 km/s. This asymmetry arises from small scale complexity that develops at the intersection of several SIRs and is a good example of how even idealized, relatively simple shapes of V_R can drive complex structure.

In order to put the SIR structure from Figure 4.21 into a global perspective, Figure 4.22 shows meridional slices of V_R, nr^2, and $Tr^{4/3}$ in the same format as Figure 4.10. The two leftmost columns show the SIRs caused by the high latitude HSSs, similar to those cause by the Slow Sine case. Here, we have latitudinally symmetric SIRs that are inclined and form most strongly at mid-latitudes, in compression but especially in temperature, as described earlier.The last 4 columns show the SIR driven by the oblong shaped HSS flowing into an extent of slow solar wind. There is strong compression and heating at the nose of the structure by about 1.0 AU and also on the top and bottom of the eyelet shape, although heating occurs at larger distances for this stretch of SIR.

Finally, Figure 4.23 shows the solar wind flow deflections around a complex SIR configuration in the same format as Figure 4.11. V_ϕ shows the consistent prograde deflection on the slow wind side of the SIR and retrograde deflection on the fast wind side, with a continuous and roughly smooth surface of $V_\phi = 0km/s$ separating the regions. As with the Slow Sine SIR, the widths of deflected wind are not the same

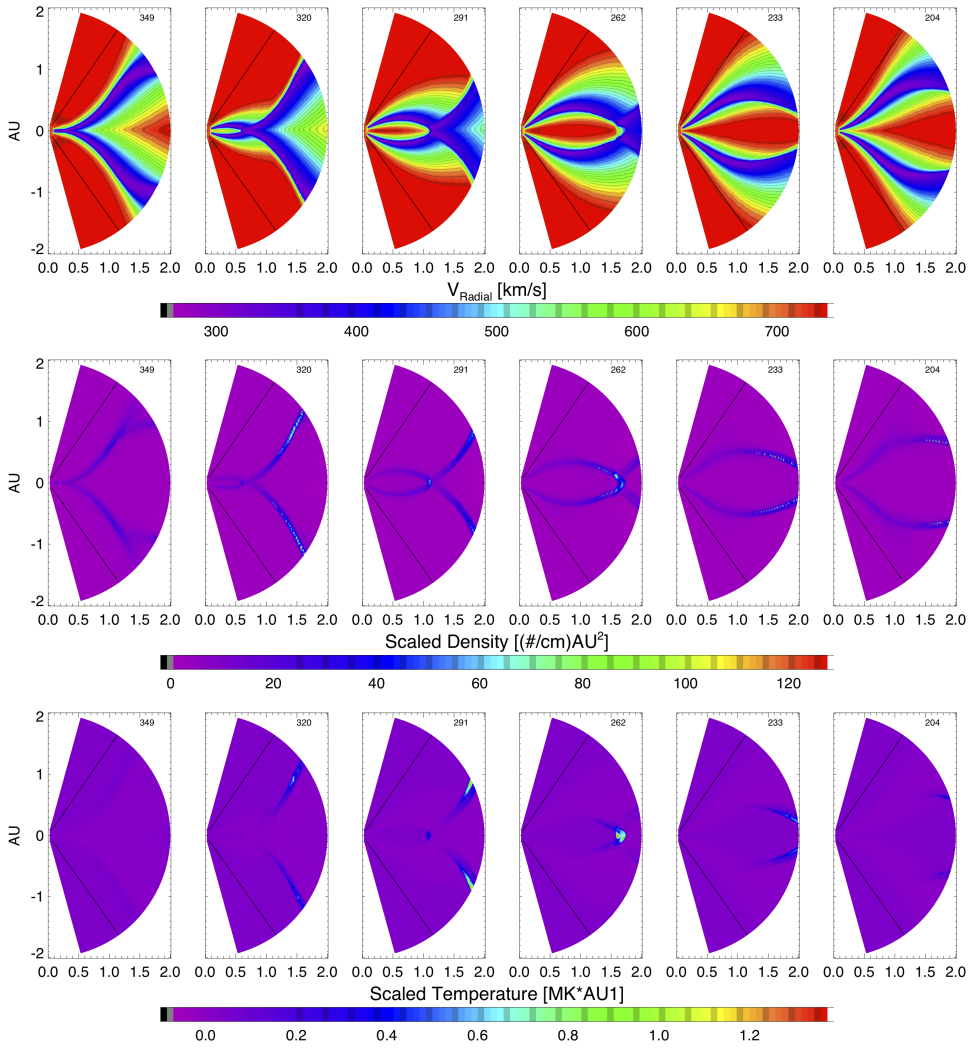

Fig. 4.22: The plots show meridional slices of the SIR driven by the Big Circle case. The meridional slices show V_R, nr^2, and $Tr^{4/3}$ at particular longitudes, indicated in the top right of each panel. Each longitude transects the SIR at different heliospheric distances, showing the evolution of the SIR as a function of distance and latitude. The broadening of the SIR's region of intermediate speed, dense, and hot solar wind is evident.

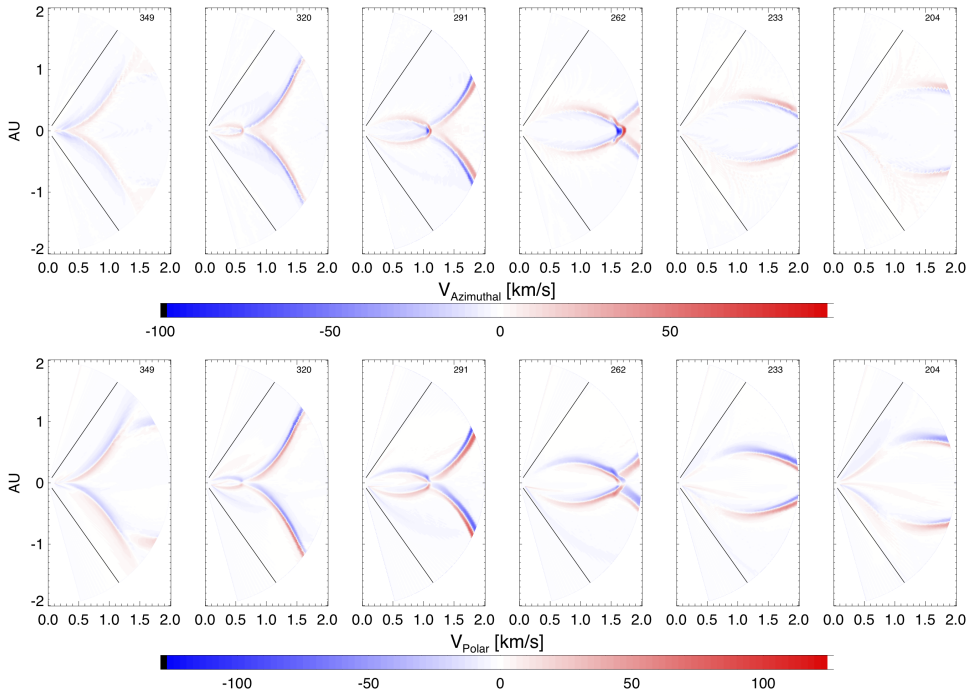

Fig. 4.23: The plots show meridional slices of the SIR driven by the Big Circle case. The meridional slices show V_ϕ,V_θ in the same format as Fig. 4.10. The SIR evolution and subsequent deflection of solar wind speed is evident.

size. Here, the region of deflected fast wind is narrower than that for the slow wind for the high latitude HSS-driven SIRS.The opposite is true for the SIR driven by the equatorial HSS. The same relative sizes of deflection is true for V_θ, which deflects the the solar wind northward or southward qualitatively according to the inclination of the front. Interestingly, the polar flow deflection near the equatorial plane is not well formed until almost 1.5 AU, though this is also seen for the compression and heating, so it may just take a while for the HSS between the band of streamer and pseudo-streamer to develop enough pressure to deflect flow. It is also worth noting that despite the SIRs not having much compression or heating at the intersection of SIRs, the flow deflection from each SIR persists in these locations and could make for a complex flow signature.

Despite the complexity, and the differences in its IBCs, the Streamer-Pseudostreamer case still reproduces general qualitative and quantitative characteristics of a SIR in the inner heliosphere. Indeed the characteristics and of SIRs in the equatorial plane and at all latitudes for the four idealized cases have been presented. We have seen that the SIR evolution begins to differ significantly once the peak speed plateau has been eroded, and that the small Fast Circle evolves differently near 2.0 AU than the big Fast Circle SIR. In both Fast Circle cases, the SIR expanded in latitude as a function of distance (as opposed to scaling with latitude) and that for these cases, and for the Slow Sine case, the SIR inclination changed as a function of increasing heliospheric distance. Both of these observations are not frequently part of the consideration when interpreting SIR observations *in situ*. Even though these corrections may be slight, they represent a shift in the morphological representation of SIRs. Given these considerations, we now turn to comparing the SIRs driven by the idealized cases to compare quantitatively.

4.3 SIR Comparisons

The analysis of the idealized cases has shown that highly idealized inner boundary conditions, input to the LFM-helio model, reproduce the large-scale features expected in an SIR. Further, the SIR's properties and evolution do not depend on the longitudinal width of the source HSS, at least out to 1.5 AU, as long as the stream is wide enough to have not been eroded by the rarefaction wave. High speed stream sources with longitudinal widths of 30° or larger will drive SIRs to at least 1.5 AU in identical manners. Although there is some variation in SIR structure as a function of latitude for the nominally 2D Fast Bands case, the V_R profile driving the SIR remains the same at all latitudes. With these results in mind, we turn our at-

tention to a slightly more realistic case, for which we expect there to be a latitudinal dependence to the structure of the SIR.

An explicit, direct comparison of the SIR driven by the Fast Bands and the Fast Circles cases is shown at 1 AU in the equatorial plane, in Figure 4.24. The SIR is shown in the same format as Figure 4.3. The parameters that are frequently reported for *in situ* observations are shown as a function of heliographic longitude, or approximate arrival time as shown on the top x-axis, with the regions of undisturbed slow wind, compressed slow wind, compressed fast wind, and undisturbed fast wind shown from right to left. The black curve shows the SIR driven by the Fast Bands case and the red lines show the SIR driven by the Fast Circles case. In the equatorial plane, the inner boundary conditions are identical. As can be seen by the curves at 1 AU, there are some small differences between the SIRs driven by the wide Fast Band and wide Fast Circle cases but the overall structure and amplitude of the SIR is the same. Since the narrow version of the Fast Band and Fast Circles evolved identically to the Wide equivalent cases, we can state that the evolution of the SIR in the equatorial plane within 1AU does not depend on the width of the high speed stream or the large-scale structure of the HSS. The differences in SIR structure seen in the equatorial plane between the Wide and Narrow Fast Circle cases at 1.5 AU, as seen in Figure 4.8 and beyond means that global structure begins to have an affect on the SIR structure locally beyond 1.5 AU.

Although Figures 4.5, and the meridional slices show that SIR evolution is latitudinally dependent for each of the parameters, they do not elucidate what the dependence is quantitatively. In order to analyze the SIR's dependence on latitude and distance, omitting the potentially different winding of the Parker spiral for the SIRs for the moment, the strength of the SIR is measured. The values of the peak density, peak temperature, and peak magnetic field strength are used to characterise

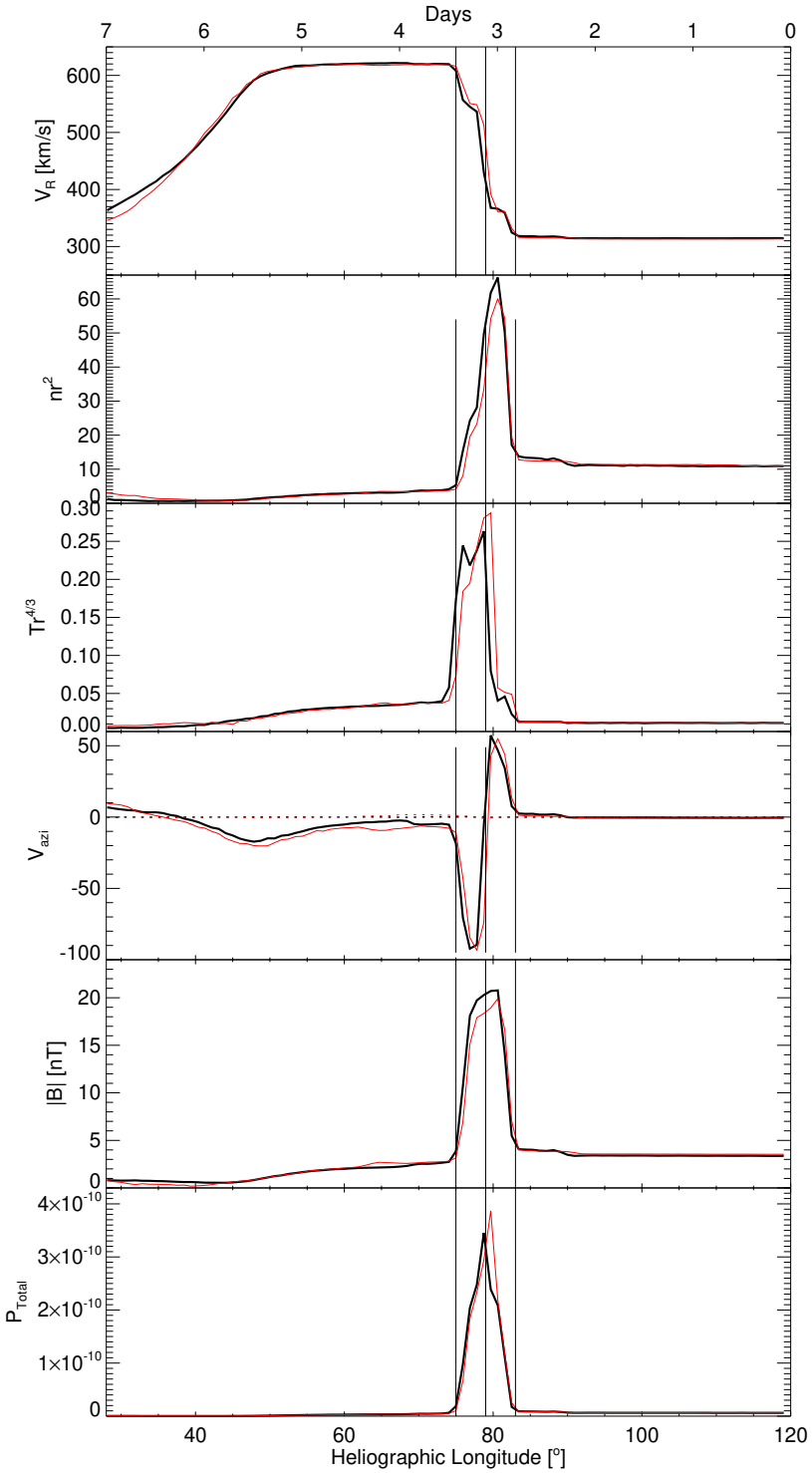

Fig. 4.24: Direct comparison of SIR at 1 AU in the equatorial plane produced by the Fast Bands and Fast Circles idealized wide cases, shown in black and red respectively. From top to bottom, the panels show V_R, nr^2,$Tr^{4/3}$, V_ϕ, $|B|$, P_{Total} as a function of heliographic longitude, or alternatively arrival time (top axis). The vertical lines show the same four delineated regions as Figure 4.3.

the strength of the SIR at each latitude and distance. These peak value are inter-compared for the Wide and Narrow cases for the Fast Bands and Fast Circles cases as well as the Slow Sine, and Streamer-Pseudostreamer cases. The peak value was selected from the data along the arc traced with decreasing longitude, containing a single SIR, for a given latitude and distance for each of the parameters considered. All idealized cases had the same distances and latitudes analyzed for consistency.

The result of such an analysis for the peak density scaled to 1 AU, for each of the SIRs is shown in Figure 4.25, which shows the peak density for each latitude, along the x-axis, and distance, shown in different colors, for the SIR driven by each Idealized case. The top row shows the peak scaled densities from the SIR driven by the wide (left) and narrow (right) band of fast wind. The second row shows the peak density for the SIRs driven by the Big Circle (left) and the Small Circle (right), as can be seen from the different latitudinal extends of each. Finally the bottom row shows the peak density of Slow Sine on the left and of Streamer-Pseudostreamer on the right. In all but the Fast Bands cases, there are latitudes where the peak scaled density is set to 0. Note that this is not because the density at these latitudes was 0 but rather that the analysis was only carried out in locations where the SIR was present.

The peak density between the Wide and Narrow Fast Bands is nearly identical at all latitudes up to 1.2 AU, with peak scaled number densities reaching between $70-75\ AU^2/cm^3$. The increase in peak density grows within 1.0 AU but the increase levels off after that. The same pattern occurs, with about the same magnitudes, for the Big and Small Fast Circles case. Beyond 1.2 AU, the SIR driven by the Small Circle does not compress the solar wind plasma as much as the Big Circle, even in the equatorial plane. It is worth remembering though that the HSS has been eroded and the plateau of fast wind is no longer present. It is also worth noting, that the

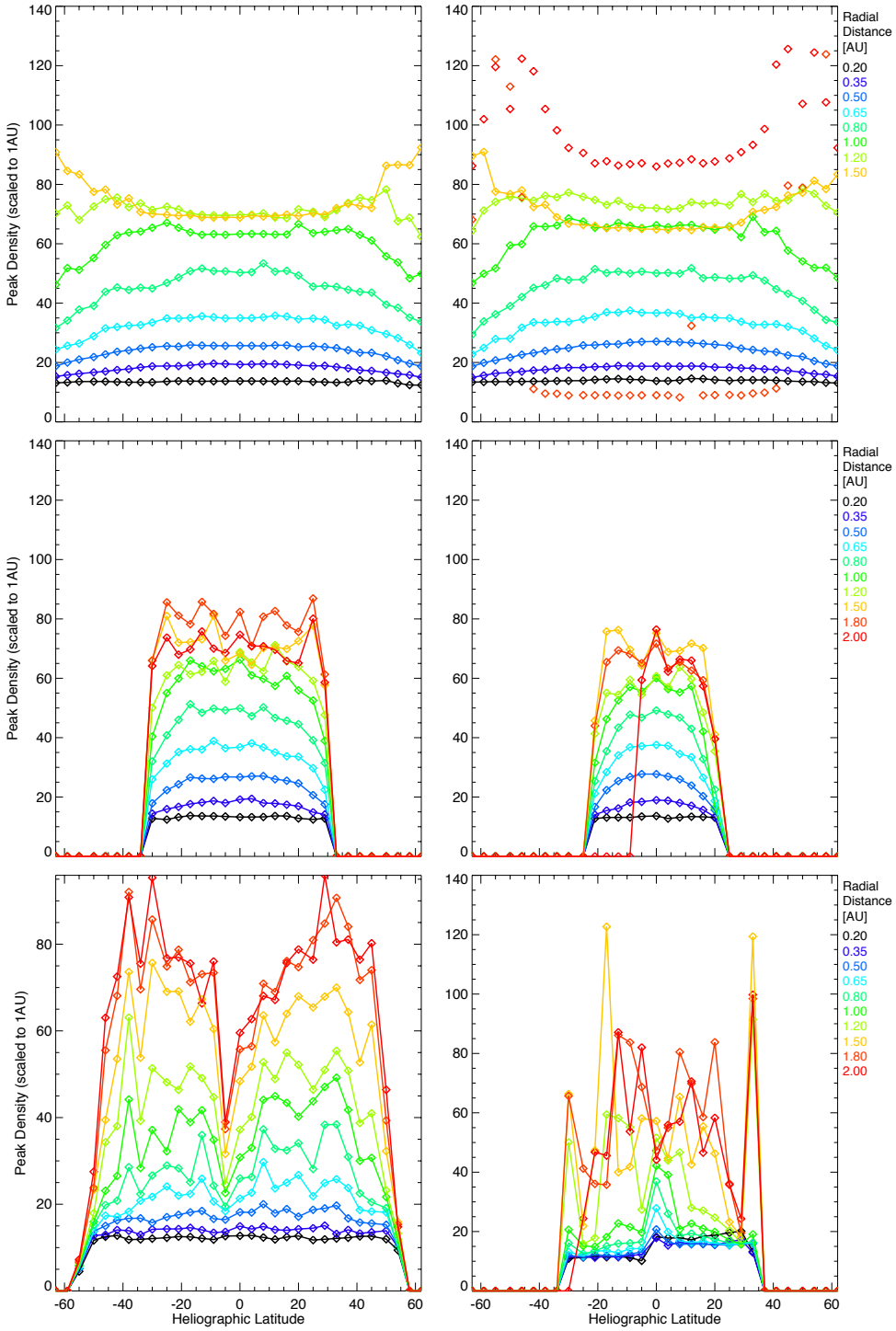

Fig. 4.25: Maximum scaled density for each of the SIRs as a function of radial distance, shown in different colors and indicated in the legends on the right, and heliographic latitude, shown along the x-axis. The top row show the peak values for Fast Bands, the second row shows Fast Circles. The bottom left plot is Slow Sine and the bottom right is Streamer-Pseudostreamer.

peak density in the Big Circle case is slightly latitude dependent. Within 0.5 AU, the peak in density has a weak latitudinal dependence. At larger heliospheric distances, the latitudinal dependence becomes more pronounced and then by 2.0 AU, the high latitudes also have high densities.

The Slow Sine case compresses the solar wind more slowly in the inner heliosphere than the other cases. For example, whereas the Fast Circles SIR has peak densities of nearly 35 AU^2/cm^3 at 0.65 AU, the Slow Sine case has peak scaled number densities of 25 AU^2/cm^3. The peak scaled densities increase at all latitudes more rapidly in the outer heliosphere however, and ultimately, the peak densities of the Slow Sine case are higher at 2.0 AU than the Fast Circles case. Restated, despite having the same δV_R as the Fast Circles case, Slow Sine produces SIRs that are more dense than Fast Circles, so that the maximum density reached by the SIR does not only depend on the change in solar wind speed between slow and fast solar wind. As was discussed in Section 4.2.3, the largest densities occur at high latitudes, near the maximum latitudinal extent of the band of variable solar wind speed. The drop in peak density seen at roughly -5° is due to following the northern hemisphere SIR to its minimal latitudinal extent and then switching the SIR considered, hence the large jump.

The same jumping between SIR regions occurs for the Streamer-Pseudostreamer case, shown on the bottom right of Figure 4.25. Near the heliographic equator, the SIR that is driven by the ECH is considered and latitudes beyond that, the SIRs driven by the high latitude fast wind are considered. This panel shows that the density of the equatorial source of fast wind drives the densest SIRs at distances within 1.2 AU but that beyond that the high latitude SIRs drive denser SIRs. Despite the δV_R being larger for this idealized case than any of the others, the peak densities are significantly lower than all other idealized cases, reinforcing the point that the

difference between fast and slow wind is not the sole determinant for the strength of the SIR. This idealized case has a large area of intermediate speed, and hence density and so it may take longer for the compression to 'catch up' to the density of the slow wind in other cases. The catching up seems to occur beyond 1.2 AU, where at mid-lattitudes, the peak densities are comparable to the other cases.

Comparing the four idealized cases suggests that SIRs driven by different HSS geometries evolve differently, and evolve in a latitude-dependent manner, reaching different peak densities. Further, the rate of compression seems to be dependent on geometry, the transition between fast and slow wind, or both but that the difference in V_R is not enough to be the sole determinant.

Since the magnetic field is frozen into the plasma in ideal MHD, we turn now to the maximum magnetic field strength for each of the SIRs in the idealized cases in Figure 4.26. This figure is in the same format as Figure 4.25. In this case, since B is a vector field and the components do not scale with r in the same way, the unscaled magnitude is shown. Hence, in all cases, the magnetic field strength is similar at 0.2 AU, near the inner boundary which received identical B_R input values. For all idealized cases, $|B|$ falls rapidly with distance from the Sun, since within 1 AU, the B_R component dominates and this scales as $1/r^2$ and beyond this, B_ϕ dominates and scales as $1/r$. A combination of the softening of the drop off of $|B|$ and the compression due to the SIR results in a slowing of a decrease in amplitude beyond roughly 0.65 AU.

The Wide and Narrow Fast Bands cases have nearly identical peak B measurements out to 1.5 AU at all latitudes. As with the density, the Big and Small Fast Circles drive SIRs with also nearly identical peak $|B|$, with the Big Circle compressing B slightly more. Both Circles cases have very similar compressions to the Fast Bands case. Also consistent with the compression in plasma, the Slow Sine case does not

compress B as much as the other idealized cases, and so the magnetic field strength is weaker at all distances and latitudes and the difference is particularly pronounced within 1.0 AU. The same is true for the Streamer-Pseudostreamer case. Here again the two cases with difference V_R transitions drive SIRs with weaker $|B|$ than the Fast Bands and Fast Circles case, suggesting once again that the geometry of the HSS and perhaps the shape of width of the transition from slow to fast wind may have an effect. It seems the size of the jump in speed in the Streamer-Pseudostreamer is not enough to compensate. The peak strength of the magnetic field does not decrease much in amplitude after 1.0 AU, meaning that the compression essentially 'keeps up' with the expansion of the field into the heliosphere.

Next, we consider the heating in the SIRs in each of the idealized cases. The peak temperature in the SIR attained at a particular latitude and distance, scaled to 1.0 AU, is shown in Figure 4.27 in the same format as Figure 4.25. In all idealized cases, the peak temperature increases slowly from 0.2 AU to 0.65 AU. The Fast Bands cases have SIRs with peak temperatures that increase rapidly beyond 1.0 AU and heats the most between $\pm 20°$. The Fast Circles case also experience significant heating beyond 1.0 AU, in a latitudinally dependent way. Both Fast Circles cases heat the plasma in the SIR to higher temperatures than any of the other cases, particularly between 1.2 AU and 1.5 AU. The SIR driven by Big Circle reaches higher peak temperatures than that driven by Small Circle, perhaps due to the Small Circle case having eroded through the HSS plateau. The peak temperature depends strongly on latitude, reaching the highest temperatures near the equatorial plane. The peak temperature, on the other hand is similar between the Big Circle and Small Circle from $0.1 - 1.2$ AU and then the SIR driven by the big circle HSS is hotter than the small circle case, particularly at low latitudes. In comparison with the Fast Bands case, the Big Circle has similar peak temperature at 1.5 AU as the

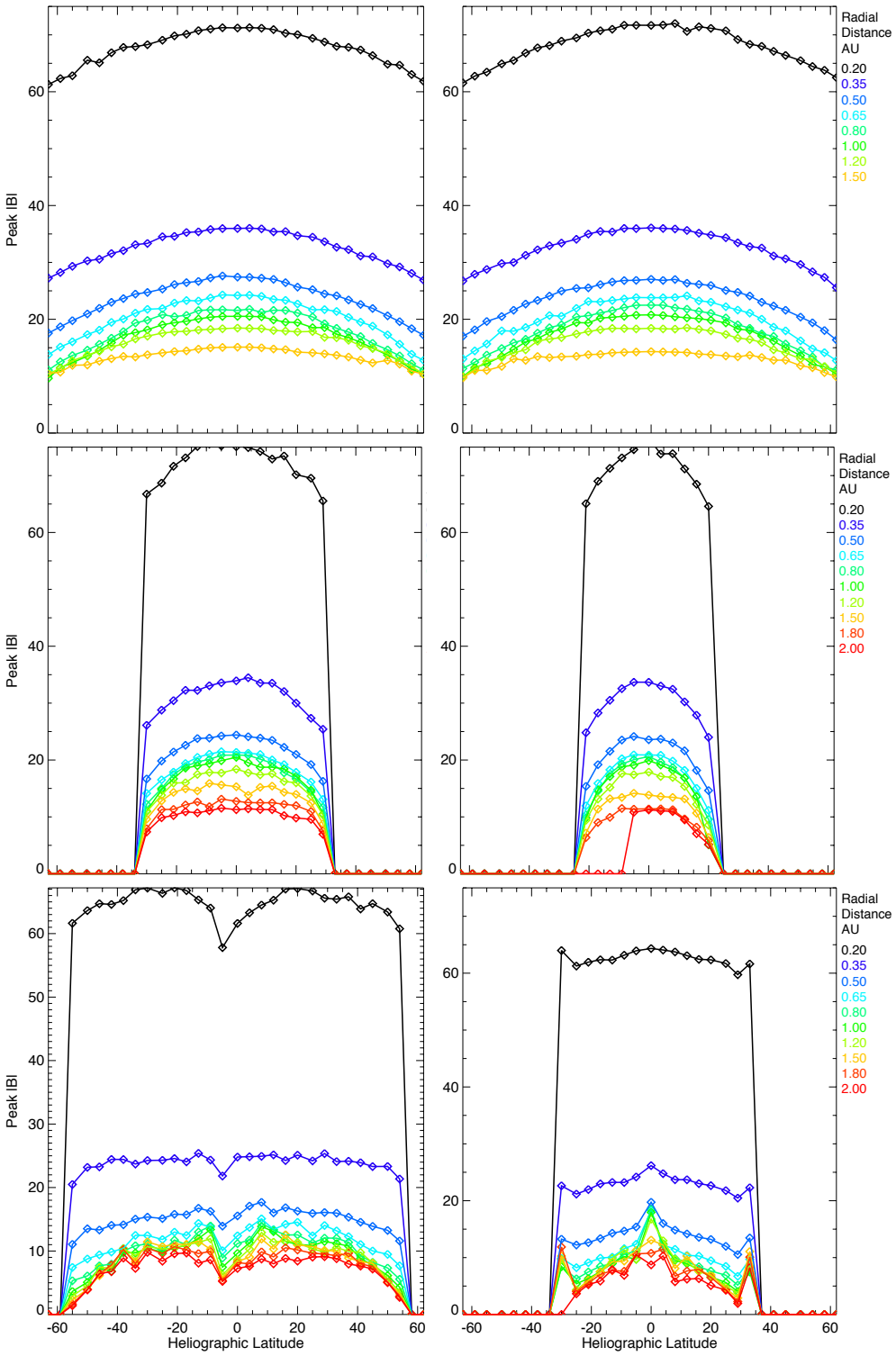

Fig. 4.26: Maximum magnetic field strength for each of the SIRs as a function of radial distance and heliographic latitude in the same format as Fig. 4.25.

Fast Bands case whereas the the Small Circles does not seem to drive quite as strong a SIR. Recall from Figure 4.9 however that the velocity profiles driving the SIRs are not the same between the Big and Small Circles.

The bottom row of Figure 4.27 shows the peak temperature for the Slow Sine case on the right and the Streamer-Pseudostreamer case on the right. Compared to the other cases, the SIR driven by the Slow Sine case reaches lower temperatures than the other cases and approximately the same temperature at all latitudes within 1.8 AU. The SIR driven by the equatorial coronal hole in the Streamer-Pseudostreamer case reaches high temperatures, close to the Fast Circles cases, in the equatorial plane and reaches cooler peak temperatures at high latitudes, with an exception at the junction of SIRs.

Thus, the peak temperatures as a function of latitudes for all four idealized cases show that, despite the same ΔV_R, and in some cases, the same V_R profile, the heating within SIRs depends on latitude and on large scale structure of the HSS. Hence, for a given SIR, the structure has latitudinal dependence. The SIR density is either similar at all latitudes, or higher at lower latitudes within 0.8 AU. The scaled temperature has similar qualitative behavior as the density with two marked differences. First, the temperature does not have as pronounced a drop at $-10°$, where the SIR-tracking switches from the northern SIR to the southern. Secondly, the plasma heating extends to higher latitudes than the high density region. Hence, the schematic view of SIRs that are strongest at the latitude to which the streamer belts extends holds well at 1.0 AU and beyond but not in the inner heliosphere, before the SIR is formed.

Figure 4.28 shows the fastest azimuthal flow deflection at several latitudes and distances for the SIRs driven by the idealized high speed configurations in the same format as Figure 4.25. The maximal flow deflections driven by the Big and Small

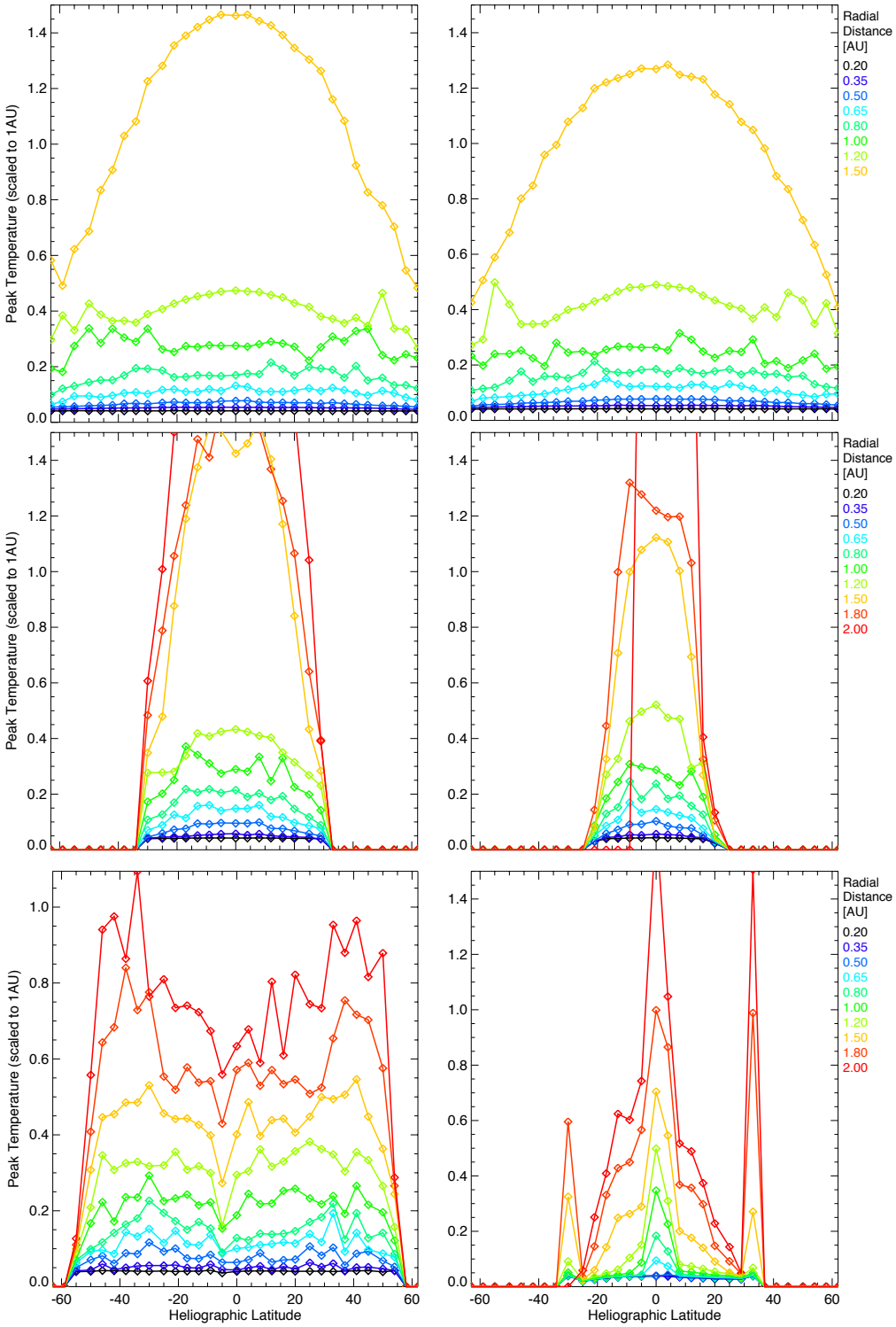

Fig. 4.27: Maximum temperature for each of the SIRs as a function of radial distance and heliographic latitude in the same format as Fig. 4.25

Fast Circles are shown on the top left and right, respectively, and those driven by the Slow Sine and Streamer-PseudoStreamer cases are shown in the bottom row. For both Fast Circles cases and the Slow Sine case, V_ϕ behaves in a similar manner: the speed of the deflected fast wind is approximately double that of the deflected slow wind. Since the factor of two corresponds to the difference in unperturbed speed, this means that the slow wind and fast wind are deflected by roughly the same amount. This supports the conceptualization of forward and reverse waves bounding the SIR as being parallel to each other. The maximum deflected speed increases with increasing distance from the Sun, up to about 1.2 AU, which is consistent with the increasing spiral angle of the SIR structure, as is the leveling off of deflected speed once the Parker spiral angle becomes greater than 45° and the pressure wave normal being more effective at slowing flow than deflecting it. Although phenomenologically the same as the Fast Circles cases, Slow Sine drives flow deflections that have only half the speed of the Fast Circles. This is due to the SIR front being more inclined with latitude, so there is a larger 'slip plane' and drives more deflection in the polar direction. Surprisingly, the flow deflection for the Streamer-Pseudostreamer case seems to deflect flow symmetrically, at the same speed, on either side of the equatorial HSS beyond 0.5 AU. This is potentially due to additional contribution of the preceding rarefaction region accelerating the flow there, as can be seen in Figure 4.23. The flow deflection follows the expected pattern at higher latitudes for the polar HSSs.

In all cases, the peak V_ϕ is latitude dependent, but the strength of the dependence is different for each of the idealized cases and also on the radial distance of the SIR. For the Fast Circles cases, within 1.2 AU, the deflection at low latitudes are faster than those closer to the latitudinal edge of the HSS. Beyond 1.5 AU, the peak deflection speeds at high latitudes increase with distance, but those at mid latitudes remain constant or decrease, flattening out the profile. The transition from increasing

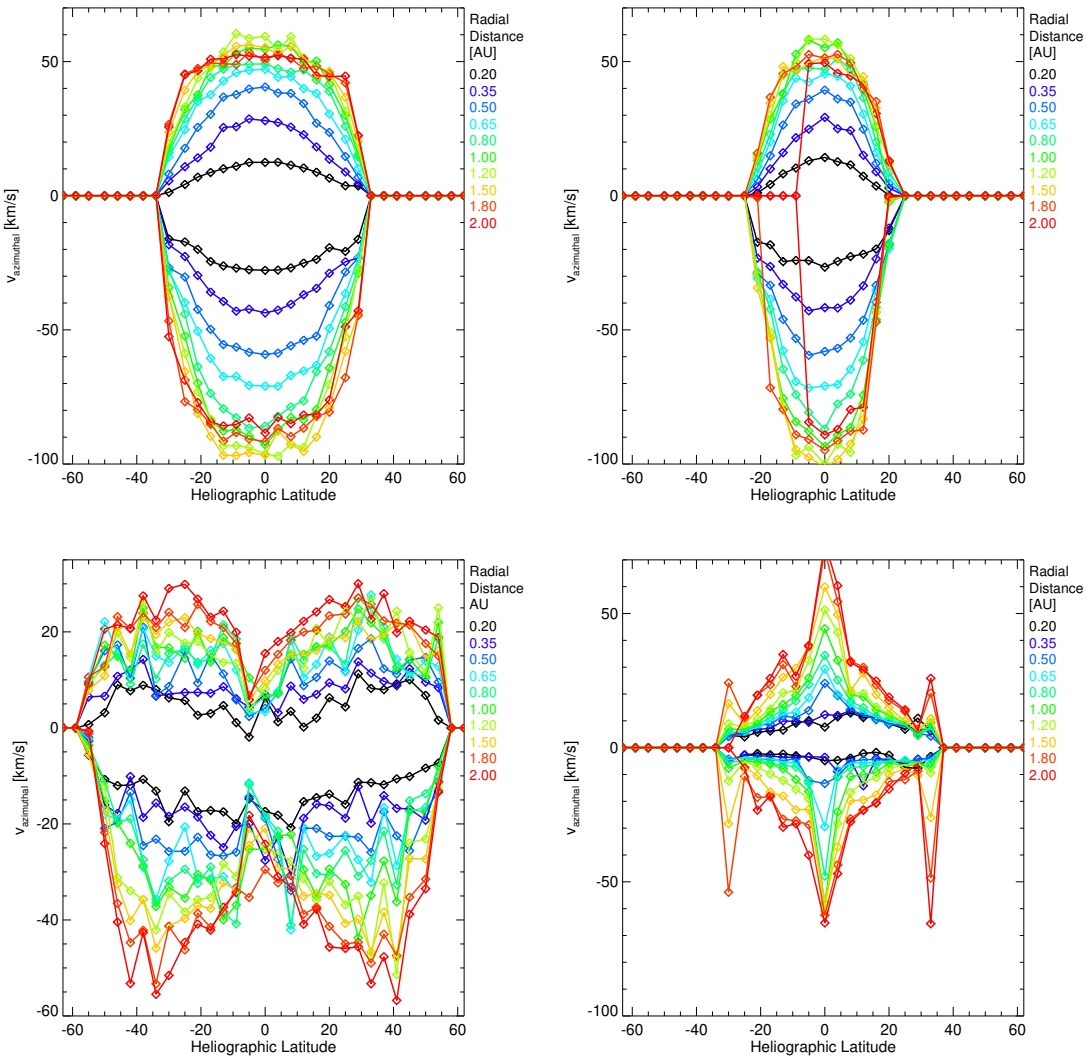

Fig. 4.28: V_ϕ as a function of latitude and distance in the same format , differentiated by color and labelled in the legend on the right of each panels. Results of the SIR driven by the big circle and small circle HSS are shown in the top left and right respectively, and for the Slow Sine and Streamer-Pseutdostreamer on the bottom left and right.

to decreasing V_ϕ magnitude occurs at smaller heliospheric distances, $1.0 - 1.2\ AU$, for the Small Circles case, implying that this SIR is more tightly wound. For both the big circle and small circle case, V_ϕ reaches a maximum between 1.2 AU and 1.5 AU in the equatorial plane and a maximum at 2.0 AU and higher latitudes. The amplitude of the maxima in V_ϕ are nearly the same for both deflected fast and slow wind in the big circles and small circles. For both the Slow Sine and the Streamer-Pseudostreamer case, the peak V_ϕ increases roughly monotonically with distance. Hence, even for the same ΔV_R for the first three cases, which we would expect to be the primary determinant for the spiral winding of SIRs and hence the angle for the azimuthal deflection, we see that the speeds attained, and even the relative angles depend on the 3D structure of SIRs.

Turning finally to the solar wind speed deflection in V_θ due to the latitudinal tilts of the HSSs, Figure 4.29 shows the peak speeds reached at each distance and latitude within the SIRs for the Fast Circles cases, in the top row, the Slow Sine case and the Streamer-Pseudostreamer case in the bottom left and right, respectively. Here again we see that the Fast Circles drive deflections in patterns that are anti-symmetric about the equator, as expected. The fast wind is deflected equatorward and the slow wind is deflected poleward in each hemisphere. In all four idealized cases, the deflected flow speeds increase with increasing distance from the Sun within 1.2 AU. The Fast Circles cases do not drive any faster flows beyond this point, whereas the Slow Sine and Streamer-Pseudostreamer cases do. The Big Fast circle drives slightly faster V_θ that the Small Fast Circle, with the fastest deflections occurring at the high latitude edge of the HSS, as expected.

The Slow Sine case drives the fastest V_θ flows of any of the cases. Furthermore, the peak values for V_θ for Slow Sine are comparable to V_ϕ within 0.65 AU but are larger beyond that point. The deflection directions are antisymmetric about the

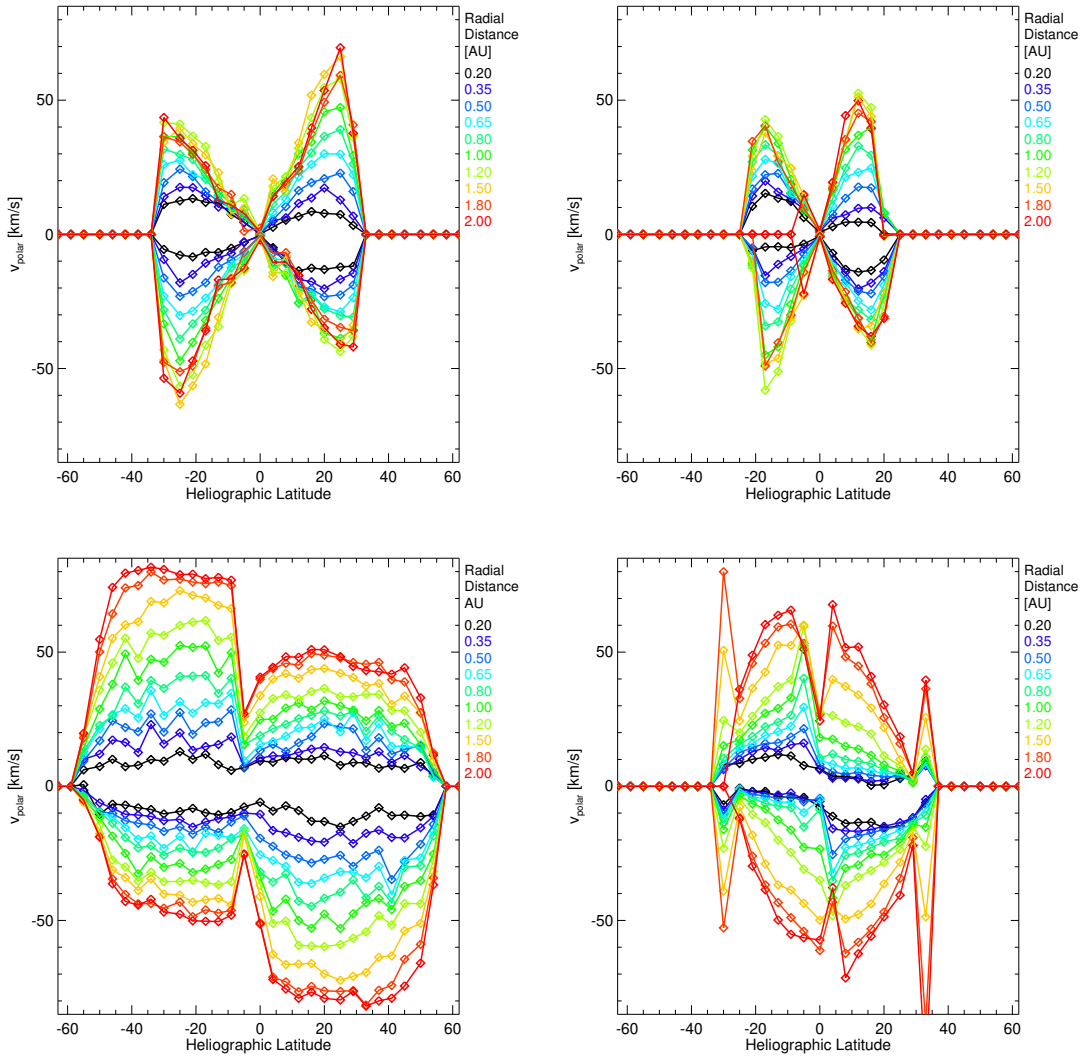

Fig. 4.29: V_θ as a function of latitude and distance in the same format , differentiated by color and labelled in the legend on the right of each panels. Results of the SIR driven by the big circle HSS are shown in the top row, and for the small circle on the bottom row.

heliographic equator, and are roughly constant with latitude, which supports the conceptualization of SIRs driven at solar minimum as roughly planar, although the tilt of this plane may change as a function of distance from the Sun, which is not a typical component of the schematic understanding of these structures.

The Streamer-Pseudostreamer case drives polar flow deflection at peak speeds more similar to those in the Fast Circles cases. The flow deflection due to the equatorial HSS is anti-symmetric about the heliographic equator as is the flow deflection due to the polar region HSSs. The latitudinal dependence of V_θ in this idealized case is complex but roughly of a consistent pattern with increasing distance. V_θ extends to latitudes of approximately 50° and at all latitudes, there is a roughly monotonic increase in maximum deflected flow peed. In this case too, the amplitude of the peak of V_θ is larger than V_ϕ beyond 0.35 AU.

Considering Figures 4.25 - 4.29, it is clear that despite identical (Fast Bands, Fast Circles, Slow Sine) or similar (Streamer-Pseudostreamer) velocity increases, as well as similar functional transitions in V_R from slow to fast wind, at the inner boundary, the resulting SIRs each have different characteristics which may be a result of the the large scale shape of the HSS that drives them. Each of the resultant SIRs also has the structural characteristics that are frequently simulated and observed in SIRs, such as a velocity transition. But the idealized configurations here each modulate the resultant SIR in slight ways, that while logical, are not frequently included in the canon of SIR features. It has been shown that the erosion of this high speed plateau begins to change the evolution of the SIR and that this occurrence can reduce the curvature of SIR fronts as a function of latitude such that the SIR will arrive earlier at higher latitudes than lower latitudes. This change in latitudinal tilt/curvature within 2.0 AU is also found for the Slow Sine case.

Keeping in mind that the relationships between solar wind speed, density, and temperature, remained the same for each of the idealized cases, any differences in the strength of the SIRs, as characterized by the peak plasma density, temperature, and magnetic field strength, will be due to the geometry of the HSS. A modulating factor here is the width and steepness of transition in V_R, which does differ from idealized case to case. The amplitude of flow deflections also depends on the shape of the HSS.

Hence, the structure of SIRs depends on latitude and the degree to which this is the case depends on the shape of the high speed stream. Furthermore, this dependence is not always consistent as the SIR flows away from the Sun. Hence, even for highly idealized inner boundary conditions and simple HSSs driving the evolution of simple SIRs, the interplay between the SIR shape and the evolution lead to latitudinal dependences and significant differences between cases in the simulated observations. Thus, the shape of the HSS should be considered when interpreting *in situ* observations.

Chapter 5

Conclusions

Having briefly given a history of the solar wind, and an overview of the typical characteristics, phenomenon, and cycles of the solar wind, the schematic structure of Stream Interaction Regions is introduced and contrasted with models and observations. The structure of SIRS as a function of distance and, to a lesser extent, latitude is discussed in context of heliospheric observations and models. The magnetohydrodynamic (MHD) description of the solar wind and embedded phenomena is described and its applicability to investigations of the large scale characteristics of SIRs is justified. The LFM-helio, a heliospheric adaptation of the 3D magnetospheric MHD model (*Lyon et al.*, 2004), is introduced and subsequently used to study the 3-D structure and evolution of stream interaction regions (SIRs) in the inner heliosphere.

The thesis begins by validating the LFM-helio model by comparing simulation results against *in situ* spacecraft observations. This technique is used often for validation of heliospheric models, as seen in WSA, ENLIL, CORHEL, SWMF, and even in the newest version of the LFM-helio; GAMERA (*Zhang et al.*, 2018). The strength of performance of a model is often quantified by quality of agreement of its results when compared to a particular spacecraft observation over select intervals. The degree of agreement is assessed by the ability of the model to reproduce several aspects of the spacecraft data such as the average magnitudes, amount of variability, and correlations of solar wind parameters such as solar wind speed, density, temperature, and magnetic field strength. As models became more complex and sophisticated, the

spatial positioning of particular structures or transitions, observationally experienced as the timing of arrival of a particular structure, has become an important benchmark for evaluating the quality of heliospheric models. In light of the importance of space weather forecasting, the magnitude of the SIR or ICME and in particular, the timing of arrival have become important parameters of comparison when evaluating the quality of a simulation.

5.1 LFM-helio Validation: Simulations vs Observations

It is these characteristics that are compared when evaluating the performance of the LFM-helio in Section 2.2. Explicitly, the simulated V_R and B_R for CR 2060 and CR 2068 are compared with data from ACE at 1 AU and with B_R data from MESSENGER during its cruise phase towards Mercury, both within the ecliptic plane and embedded in the band of variable solar wind speed. The LFM-helio simulations agree with the data within the generally accepted range of differences for V_R during both intervals. Despite having reached the community consensus for agreement, there are some large differences between model and observations, particularly in CR 2068. These are attributed to features present at the inner boundary condition, a product of a corona model, whose features are highly dependent on the magnetogram used to drive the coronal model. Different magnetograms from different heliospheric observatories, used to drive the same coronal and heliospheric models, can produce very different simulated heliospheres and therefore different synthetic observations at a spacecraft's location. It is in this context that the LFM-helio results are interpreted and validated, as a limiting factor in the ability of such a model to make predictions is dependent on the accuracy of the inner boundary. Thus the LFM-helio is validated within the bounds of what is acceptable in the field.

Another significant difference in the LFM-helio simulations as compared to *in situ* observations is the strength of the magnetic field at both MESSENGER and ACE for the Carrington Rotations considered, both occurring within solar minimum of Solar Cycle 23. Solar Cycles 23 and 24 have been unusually weak and quiet in the context of solar cycles since the beginning of the space age. The Sun's magnetic field is weaker and the dipolar component is weaker, resulting in a more quiet, and cooler heliosphere. Despite this weaker magnetic field, the LFM-helio under-represents the amplitude of the magnetic field at ACE and MESSENGER. Some of this is due to an underestimation at the inner boundary and some of this is due to the size scale of the LFM-helio grid along with the duration of its time steps being too large to include the small scale structure and turbulence, though this is the case for all intervals simulated.

Thus, the LFM-helio having been validated in the ecliptic plane is then validated, within the community consensus standards, more globally and also in a different, more typical solar cycle with the first of the Ulysses spacecraft's Fast Latitude Scans in Section 2.2.3. Here the LFM-helio reproduces the amplitude of the mean and of the variability in the high latitude fast wind as well as in the band of variable solar wind. The solar wind speed is reproduced, capturing nearly all of the high speed streams in the band of solar wind variability, though perhaps creating a band of variability that, though abrupt like the Ulysses observations, may be slightly too narrow in heliographic latitude. This could be due to the band of variability being too narrow, the shape of the fast-slow interface being misplaced, or time evolution on the Sun that is not included in the simulated coronal boundary. Further, a small shift in position can result in different synthetic observations, emphasizing that the trajectory through a structured heliosphere is position dependent. The simulated B_r and n also reproduce the observed mean values in both the fast and slow wind

and reproduce a good amount of variability in each region. The smallest scales of variability are not reproduced but the compression in plasma and field responds to increases in V_R in physically accurate ways, despite being too compressed. The LFM-helio produces temperatures that are much too cold in the fast wind, in part due to the lack of turbulent heating. The temperature of the fast solar wind has been traditionally difficult to simulate with MHD models. Despite the discrepancy in this parameter, the LFM-helio performs well in recreating the Ulysses observations during its FLS and produces a valid solution during this interval, of similar quality.

Given the number of heliospheric models, inter-comparing the models would highlight their relative strengths and potentially reveal which model made the best predictions over a particular Carrington rotation. But there are several factors to consider when determining a best simulation. In order to quantify the performance of each model, a number of metrics were developed, such as root mean square differences, skill scores of forecasts, and other methods. Ranking the reliability and performance using one of these methods emphasizes a particular component of the model and these quantitative measures often convolve amplitude and timing differences.

In running these tests, the modeling community found that the models tended to be most sensitive to their inner boundary condition, more so than the differences in the physics included or numerical schemes, that the different solar observatories that produced the magnetograms did not consistently produce similar magnetograms, that the time dependence of the solar corona might be an important factor, and that many of the solar parameters output from the coronal models were massaged before being input into the heliospheric models. For the differences between observatories for space weather applications, an enssemble modeling approach has been taken (*Owens and Riley*, 2017; *Murray*, 2018). For the time evolution of the Sun's corona over the

synodic rotation period required to construct the magnetograms used to create the coronal models, the ADAPT model addressed this issue by creating time dependent magnetograms (*Arge et al.*, 2010), and is an important step towards improving the accuracy of heliospheric models. Many heliospheric models run with time-dependent inner boundaries.

Still, despite using a static inner boundary and generating a steady state solution, the LFM-helio's simulated heliosphere during the FLS scan is comparable to other global MHD models' results in magnitude of solar wind parameters and reproduction of characteristic structures, though it perhaps propagates more small and meso-scale structure owing to its non-diffusive numerical scheme. This property makes it an ideal model for investigating meso-scale structure and regions containing sharp boundaries, such as SIRs.

Finally, since the quantitative values of the solar wind parameters are poorly constrained at 0.1 AU, it is common for heliospheric models to tweak their inner boundary conditions in order to attain agreement with *in situ* observations at 1.0 AU. The matter of adjusting solar wind parameters so as to best match observations at L1 has been justified since the solar wind conditions at the transition from sub- to super- sonic solar wind were not well known, though results from the Parker Solar Probe and the upcoming Solar Orbiter will address this. In any case, the motivation for being able to predict solar wind conditions at L1 are high. However, the effects of altering the physical relationships between solar wind parameters also changes the plasma characteristic speeds and the plasma beta, which might have an effect on the evolution of structures in the solar wind. With the intention of addressing this question as well as testing the sensitivity of the LFM-helio's results on the input parameters, a sensitivity study was performed for CR 1892 to quantify the sensitivity of the LFM-helio results to parameters input at the inner boundary.

The parameter sensitivity study for CR 1892 elucidates the effects of varying the assumptions made about the empirical relationships between solar wind parameters of v_r, n, and T. Varying the assumptions made to determine these parameters does not significantly change the LFM-helio results at the orbit of Ulysses. Varying the canonical values for temperature and magnetic field have a larger effect on the LFM-helio simulations. Increasing the average temperature at the inner boundary accelerates the wind to faster speeds throughout the heliosphere and increases the temperature at all heliospheric distances. Decreasing the adiabatic constant slows the rate of solar wind cooling as a function of heliospheric distance, leading to a hotter wind at larger distances from the Sun. Increasing the magnetic field, so that it is proportionate to V_R as is done in some models, not only increases the magnetic field strength of the fast wind at all distances in the heliosphere, but the resulting increased magnetic pressure at high latitudes compresses the band of solar wind variability and alters the global distribution of the solar wind speeds. Hence, varying the magnetic field strength at the poles has the largest effect on the global heliosphere. Therefore, an accurate measure of the magnetic field strengths at high latitudes will play an important role in the accuracy of space weather forecasts. It is also therefore possible, through judicious choice of temperature at the inner boundary and of adiabatic index, to simulate an accurate temperature along the Ulysses trajectory while maintaining good agreement with measurements of the other parameters.

Although the ability to forecast the solar wind conditions at L1 may be most strongly dependent on the accuracy of the magnetogram, the LFM-helio's reproduction of the characteristics and variability of the solar wind on the size and time scales tenable by the MHD approach and the grid resolution used, mean that it can confidently be applied to studying, at a minimum, quasi-steady-state processes and meso-scale phenomenon. Now that this has been shown, the rest of this dissertation

focusses on the evolution of SIRs between 0.1-2.0 AU, paying particular attention to the effects of the 3D shape of the high speed stream and the relations between the solar wind parameters.

5.2 SIR Evolution: Parameter Dependence and HSS shape

The evolution of a pair of SIRs within CR 1892 is studied in detail between 0.1–2.0 AU, with the pair merging b 2.0 AU. Each of the SIRs has a different minimum and maximum speed (despite having similar increases in speed on the leading edge of the SIR) , different longitudinal extent, different latitudinal shapes, flows into different upstream solar wind conditions. Each SIR evolves from the inner boundary in the classical way, by driving plasma and field compression, plasma heating, and flow deflection. The relative proportions to which each of the SIRs achieves these characteristics is different and evolves with more nuance than is generally observationally attributed to these structures.

Given this context, the interpretation of a single spacecraft's observations along a trajectory through the SIR, and further even the interpretation of observations from multiple spacecraft along different trajectories through the SIR should be equally nuanced. The pervasive conceptualization of SIRs is that of large, relatively homogenous, and planar structures that propagate and evolve uniformly is inadequate to describe what is happening. Any differences observed between nearby spacecraft are often attributed to evolution on the coronal hole boundary (*Simunac et al.*, 2009). While time evolution is a likely contributor to the discrepancies between spacecraft observation of SIRs, understanding the various contributors to local and global evolution of SIRs as a complex heliospheric structure is an important component of understanding the inner heliosphere (*Owens et al.*, 2020). Furthermore, the nuance is necessary interpreting the observed differences in SIRs between the minima of Solar

Cycle 22 and Solar cycle 23, with known differences in coronal density, temperature, field strength, and coronal hole size and placement.

The parameter sensitivity study of CR 1892 examines the sensitivity of the evolution of SIRs to variations in the plasma and field properties despite having identical velocity profiles. Though the velocity profile is often though to be the most dynamically important, we have shown that even for identical input V_R, the parameter sensitivity study shows that for different interrelations between V_R and the plasma parameters, the evolution of SIRs can vary a large amount. Since the velocity profiles are identical at the inner boundary for all of these cases, the epoch-like analysis performed here shows that any differences that arise are consequences of the plasma density, temperature, adiabatic index, magnetic field strength, or some combination.

In general, cases with higher temperatures at the inner boundary accelerate the solar wind's maximal speeds faster than the Baseline case, which leads to arrival times of up to a few days early arrival times, of import to space weather forecasts. Certain cases have the first HSS merge into the second, faster HSS by 2.0 AU whereas the runs with higher plasma pressure, made up of both thermal and magnetic pressure, are not eroded as rapidly. Although the velocity profiles differ between cases, the peak density attained in the SIRs is consistent between all cases, despite some differences in arrival times and durations. In contrast, despite the wide range of temperatures at the inner boundary, ranging by up to a factor of 4 from the Baseline case, most peak temperatures and peak densities have approximately the same range of magnitudes in up 1.2 AU and then beyond that the peak temperatures begin to differ again but only by a factor of two. The similarities in peak density and temperature, as well as thermal and magnetic pressures, suggests some moderating mechanism that regulates the steepening of SIRs.

The relative importance of HSS shape is investigated in comparison to the importance of the plasma relations for the evolution of SIRs. In order to understand the importance of HSS shape, SIRs within CR 2058 and CR 2060 with very difference characteristics were simulated; one is narrow in latitude but wide in longitude and the other has more circular aspect ratio. These realistic HSSs have different shapes and different peak speeds but flow into similar solar wind conditions, namely a thin band of slow, pseudo-streamer wind. Both drive realistic SIRs. The former SIR heats and deflects the plasma efficiently but fails to produce a significant density enhancement. The flow deflection signature does not have the typical pulse-like signature in V_ϕ, which makes the SI difficult to identify despite us having found that the $V_\phi = 0$ method was most reliable. In contrast, the SIR in CR 2060 is relatively well-ordered and exhibits the observational features typically associated with SIRs such as clear spikes in density, magnetic field strength, and temperature, although the plasma remains relatively cool. In this case, the V_{phi} signature deflected east and west as expected. The shape of the fast solar wind produces SIRs with different characteristics near the ecliptic plane.

The evolution of the SIRs as a function of distance, at a few latitudes spanning between the equatorial and ecliptic planes, are compared with each other in order to qualitatively understand the influence the shape of the HSS has on the SIR. The resulting synthetic observations of the narrow SIR show significant variation between each of the latitudinally separated spacecraft. Said differently, this comparison highlights how different SIRs can appear in a small range of latitudes depending on the shape of their HSS and the level of structure on the HSS leading edge. The latitudinal shape of the HSS strongly affects the local evolution of SIRs.

Perhaps stated more explicitly, since the local conditions of SIR evolution for a narrow HSS or a HSS that whose features vary significantly as a function of latitude,

so too do the resulting parameters of the SIR. Since the HSS that is wider in latitudinal extent is more homogeneous in solar wind properties, so too is the resulting SIR at multiple distances. While perhaps not surprising, observationally, SIRs are still described as large scale, planar structures that are largely isotropic on scales of a few degrees at 1.0AU. Therefore, significant deviations in *in situ* observations are typically attributed to time-dependent effects such as transient blobs, interactions with an ICME, or evolution of the coronal hole boundaries (*Simunac et al.*, 2009). While these phenomena are almost certainly also occurring within at least some SIR observations, we show here that it is possible to achieve a high level of variability in SIR characteristics and timing solely through the steady state latitudinal structure of the HSS. This, of course, does not detract from the importance of time-dependent effects, which are crucial in phenomena like CMEs and even the high level of variability in the slow solar wind. Rather, this argument is meant to provide an alternate solution and to say that time dependent effects are not solely responsible.

It has also been shown that small scale structure, such as irregularities along the coronal hole boundary, introduces structure in the SIR (Pizzo). There is significant small scale structure and irregularity in the LFM-helio simulations that are run with a realistic inner boundary condition, further the transition between fast and slow wind varies and do not have the same shape, and the longitudinal width of the high speed stream was not the same. In order to disentangle some of these features of HSSs, four highly idealized cases were run with the LFM-helio. The SIRs driven by the Fast Bands, Fast Circles, Slow Sine, and Streamer-Pseudo streamer were compared in the ecliptic plane and at a large range of latitudes. All idealized SIRs exhibited the canonical characteristics expected of SIRs. The cases also differed from each other, especially at varying latitudes.

For all idealized cases, the V_R profiles all begin with a smooth transition from slow wind to fast wind and all eventually develop step-like structure as the SIR develops and begins to deflect solar wind away from the radial direction. The heliospheric distance at which this occurs increases as the latitudinal tilt of the SIR increases. As long as the peak V_R is the same for the SIRs having the same tilt angle, the velocity profile on the leading edge of the SIR is identical, indicating that the evolution of the SIR does not depend on the longitudinal extent of the fast wind in the HSS. This result is not surprising for supersonic solar wind. Once the erosion of the HSS, due to the deceleration of the fast wind from both the compression and rarefaction waves, the evolution of the SIR begins to differ between the narrow and wide HSSs. Further, since the V_R profile has a latitudinal dependence, so too does the evolution of the resulting SIR, and a change in tilt of the SIR structure with heliospheric distance is shown.

The peak densities for each of the idealized cases SIRs reach similar peak values by 2.0 AU but evolved differently with heliospheric distance; the Fast Bands and Fast Circles cases have peak density increasing rapidly from 0.35 AU to 1.2 AU, then remaining roughly constant. The peak temperature for these cases, in contrast, increases slowly within 1.2 AU and then increases rapidly this point, being hottest near the equatorial plane. The Slow Streamer case has peak density and temperature increasing steadily with distance until 1.8 AU and 2.0 AU. Finally Streamer-Pseudostreamer case doesn't increase by very much until 1.0 AU, then increases more rapidly. The same is true for peak temperature. Further, all cases show a latitudinal dependence in peak density and temperature. The peak magnetic field strength in the SIRs follows a similar latitudinal dependence as the plasma compression. Hence, even for smooth, planar HSSs, the resulting SIRs have some meso-scale structure that depends on the orientation, tilt, and 'opening angle' of HSS.

The synthetic flow deflection signatures follow the same pulse patter for all cases at all heliospheric distances considered, but differ to different extents and magnitudes for each of the cases in manner that is consistent with the tilts of each of the structures. As a result, the polar component is only present in the equatorial plane for Slow Sine and Streamer-Pseudostreamer. Further the flow deflection signature is present and consistent at all latitudes of driven SIRs and is therefore a consistent and reliable marker for the stream interface. Having a reliable marker for the stream interface within 1.0 AU and very near the corona - solar wind boundary as the Solar Orbiter mission orbits at various latitudes at those heliospheric distances (*Richardson*, 2018).

5.3 Future Work

There are numerous possible extensions of this work, all with varying focusses. Most immediate perhaps is a more quantitative, statistical analysis of the SIRs produced in the idealized cases as well in the parameter sensitivity cases. Since the variability of any particular 'flight line' through the data is the result of a number of factors, which we have attempted to reduce in the idealized cases, as well as some numerical noise, a statistical approach would likely illuminate and separate the causes of the effects commented on here. Most of the SIRs discussed here focussed on the equatorial plane, which is important from an Earth-based perspective but their behavior at higher latitudes would make for a more complete picture. Furthermore, ensuring that are results are backward compatible with previous analytical and MHD models may be helpful.

A second tenable extension, which would be very interesting, would be to apply the shock analysis to the realistic inner boundary conditions for a number of Carrington Rotations in both solar cycle 22 and 23 and test whether the hypothesized reasons

for the the shock distribution holds. We have shown here that the SIRs exhibit the different characteristics thought to differentiate the two solar cycles, though perhaps not as exclusively as discussed in the literature. There are low-latitude sources of fast wind and pseudo-streamers in our inner boundary for CR 1982, though they are not as pronounced as in CR 2060, for example. Examining the differences between shock distributions and properties between the cases in the parameter sensitivity study would also highlight the role, or lack thereof, the characteristic speeds play in the development of shocks. To extend this further, the shocks identified used the magnetosonic fast speed as an identifying characteristic. This choice was made because these are the shocks most frequently observed in the inner heliosphere. It would be interesting to see which other types of discontinuities the LFM-helio can simulate accurately.

Another extension of this work would be to more carefully define the upstream and downstream regions of the shocks that are located in the LFM-helio, since they are typically quite planar though patchy, and investigate how closely the RH conditions are met in a plasma that is far from homogeneous.

The suggestions for future work thus far center on the leading edge of the SIRs, but there are open questions concerning the trailing edge of SIRs and the stream interface on the fast to slow transition of the HSSs. *Borovsky and Denton* (2016) show that the trailing edges of some SIRs have a 'v-bend' in the speed profile that they suggest is the most robust marker of the SI within the rarefaction region. One dimensional analysis suggests that this demarcates the pressure boundary between the wave moving anti-sunward from the slow, dense wind into the gap and the equivalent from the fast wind. They show that Enlil simulations of realistic Carrington Rotations recreate this feature. A superficial glance at the LFM-helio simulations show that such a v-bend is present in the realistic simulations, usually appearing

around 0.8 AU and also by 1 AU for some of the idealized simulations. This warrants more careful study and would benefit from observations of the trailing edges of SIRs within 1 AU.

Looking at more significant changes, the LFM-helio has been updated is currently more capable than ever before(GAMERA) which would allow more flexibility is studying SIRs. Furthermore, there have been significant advancements in the construction of synoptic maps. Models such as the ADAPT code allow for a time-dependent version of a synoptic map, which has already been paired with the LFM-helio. The inclusion of time-dependent effects will likely influence the evolution and characteristics of SIRs and their associated shocks. In particular, the moving boundary of a coronal hole would shift the boundaries of the slow-fast solar wind transition, which may introduce small scale structure into the leading edges of SIRs. Even an idealized case with a moving fast-slow solar wind boundary would be an interesting case study.

Finally, it would be interesting to increase resolution just along the spiral of the SIR and search for instabilities at the boundary, such as those arising from the Kelvin-Helmholtz instability. These could be sources of turbulence and their presence in SIRs is contested.

List of Journal Abbreviations

Ann. Geophys.	Annales Geophysicae
Appl. Opt.	Applied Optics
Astron. Astrophys.	Astronomy and Astrophysics
Astrophys. J.	Astrophysical Journal
Astrophys. J. Lett.	Astrophysical Journal Letters
Geophys. Monogr.	Geophysical Monograph
Geophys. Res. Lett.	Geophysical Research Letters
J. Atmos. Solar Terr. Phys.	Journal of Atmospheric and Solar-Terrestrial Physics
J. Geophys. Res.	Journal of Geophysical Research
Mon. Not. R. Astron. Soc.	Monthly Notices of the Royal Astronomical Society
Nucl. Instrum. Methods	Nuclear Instruments and Methods
Phys. Rev.	Physical Review
Rev. Geophys. Space Phys.	Reviews of Geophysics and Space Physics
Sol. Phys.	Solar Physics
Space Sci. Rev.	Space Science Reviews
Space Wea. J.	Space Weather Journal

References

Abbo, L., et al. (2016), Slow Solar Wind: Observations and Modeling, *Space Sci. Rev.*, *201*(1-4), 55–108, doi:10.1007/s11214-016-0264-1.

Abramenko, V., V. Yurchyshyn, J. Linker, Z. Mikić, J. Luhmann, and C. O. Lee (2010), Low-Latitude Coronal Holes at the Minimum of the 23rd Solar Cycle, *ApJ*, *712*, 813–818, doi:10.1088/0004-637X/712/2/813.

Acuña, M. H., K. W. Ogilvie, D. N. Baker, S. A. Curtis, D. H. Fairfield, and W. H. Mish (1995), The Global Geospace Science Program and Its Investigations, *Space Sci. Rev.*, *71*, 5–21, doi:10.1007/BF00751323.

Anderson, B. J., M. H. Acuña, D. A. Lohr, J. Scheifele, A. Raval, H. Korth, and J. A. Slavin (2007), The Magnetometer Instrument on MESSENGER, *Space Sci. Rev.*, *131*, 417–450, doi:10.1007/s11214-007-9246-7.

Angelopoulos, V. (2008), The THEMIS Mission, *Space Sci. Rev.*, *141*, 5–34, doi:10.1007/s11214-008-9336-1.

Antiochos, S. K., Z. Mikić, V. S. Titov, R. Lionello, and J. A. Linker (2011), A Model for the Sources of the Slow Solar Wind, *ApJ*, *731*(2), 112, doi:10.1088/0004-637X/731/2/112.

Arge, C. N., and V. J. Pizzo (2000), Improvement in the prediction of solar wind conditions using near-real time solar magnetic field updates, *J. Geophys. Res.*, *105*, 10,465–10,480, doi:10.1029/1999JA000262.

Arge, C. N., J. G. Luhmann, D. Odstrcil, C. J. Schrijver, and Y. Li (2004), Stream structure and coronal sources of the solar wind during the May 12th, 1997 CME, *Journal of Atmospheric and Solar-Terrestrial Physics*, *66*, 1295–1309, doi:10.1016/j.jastp.2004.03.018.

Arge, C. N., C. J. Henney, J. Koller, C. R. Compeau, S. Young, D. MacKenzie, A. Fay, and J. W. Harvey (2010), Air Force Data Assimilative Photospheric Flux Transport (ADAPT) Model, *Twelfth International Solar Wind Conference*, *1216*, 343–346, doi:10.1063/1.3395870.

Arge, C. N., C. J. Henney, J. Koller, W. A. Toussaint, J. W. Harvey, and S. Young (2011), Improving Data Drivers for Coronal and Solar Wind

Models, in *5th International Conference of Numerical Modeling of Space Plasma Flows (ASTRONUM 2010)*, *Astronomical Society of the Pacific Conference Series*, vol. 444, edited by N. V. Pogorelov, E. Audit, and G. P. Zank, p. 99.

Badruddin, A., and Z. Falak (2016), Study of the geoeffectiveness of coronal mass ejections, corotating interaction regions and their associated structures observed during Solar Cycle 23, *Ap&SS*, *361*, 253, doi:10.1007/s10509-016-2839-4.

Bale, S. D., et al. (2019), Highly structured slow solar wind emerging from an equatorial coronal hole, *Nature*, *576*(7786), 237–242, doi:10.1038/s41586-019-1818-7.

Balogh, A., T. J. Beek, R. J. Forsyth, P. C. Hedgecock, R. J. Marquedant, E. J. Smith, D. J. Southwood, and B. T. Tsurutani (1992), The magnetic field investigation on the ULYSSES mission - Instrumentation and preliminary scientific results, *A&AS*, *92*, 221–236.

Bame, S. J., D. J. McComas, B. L. Barraclough, J. L. Phillips, K. J. Sofaly, J. C. Chavez, B. E. Goldstein, and R. K. Sakurai (1992), The ULYSSES solar wind plasma experiment, *A&AS*, *92*, 237–265.

Belcher, J. W., and L. Davis Jr. (1971), Large-amplitude alfvén waves in the interplanetary medium, 2, *Journal of Geophysical Research (1896-1977)*, *76*(16), 3534–3563, doi:10.1029/JA076i016p03534.

Blanco, J. J., J. Rodríguez-Pacheco, M. A. Hidalgo, and J. Sequeiros (2006), Analysis of the heliospheric current sheet fine structure: Single or multiple current sheets, *Journal of Atmospheric and Solar-Terrestrial Physics*, *68*, 2173–2181, doi:10.1016/j.jastp.2006.08.007.

Bochsler, P., and J. Geiss (2013), *Composition of the Solar Wind*, pp. 133–141, American Geophysical Union (AGU), doi:10.1029/GM054p0133.

Borovsky, J. E. (2008), Flux tube texture of the solar wind: Strands of the magnetic carpet at 1 AU?, *Journal of Geophysical Research (Space Physics)*, *113*, A08110, doi:10.1029/2007JA012684.

Borovsky, J. E., and M. H. Denton (2010), Solar wind turbulence and shear: A superposed-epoch analysis of corotating interaction regions at 1 AU, *Journal of Geophysical Research (Space Physics)*, *115*(A14), A10101, doi:10.1029/2009JA014966.

Borovsky, J. E., and M. H. Denton (2016), The trailing edges of high-speed streams at 1au, *Journal of Geophysical Research: Space Physics*, *121*(7), 6107–6140, doi:10.1002/2016JA022863.

Burch, J. L., T. E. Moore, R. B. Torbert, and B. L. Giles (2016), Magnetospheric Multiscale Overview and Science Objectives, *Space Sci. Rev.*, *199*, 5–21, doi:10.1007/s11214-015-0164-9.

Carrington, R. C. (1859), Description of a Singular Appearance seen in the Sun on September 1, 1859, *MNRAS*, *20*, 13–15, doi:10.1093/mnras/20.1.13.

Chapman and Ferraro (1931), "A new theory of magnetic storms", *Terrestrial Magnetism and Atmospheric Electricity (Journal of Geophysical Research)*, *36*(2), 77.

Cohen, O., et al. (2007), A Semiempirical Magnetohydrodynamical Model of the Solar Wind, *Astrophys. J.*, *654*(2), L163, doi:10.1086/511154.

Crooker, N. U., and R. L. McPherron (2012), Coincidence of composition and speed boundaries of the slow solar wind, *Journal of Geophysical Research (Space Physics)*, *117*, A09104, doi:10.1029/2012JA017837.

Crooker, N. U., A. J. Lazarus, R. P. Lepping, K. W. Ogilvie, J. T. Steinberg, A. Szabo, and T. G. Onsager (1996), A two-stream, four-sector, recurrence pattern: Implications from WIND for the 22-year geomagnetic activity cycle, *Geophys. Res. Lett.*, *23*, 1275–1278, doi:10.1029/96GL00031.

Crooker, N. U., et al. (1999), CIR Morphology, Turbulence, Discontinuities, and Energetic Particles, *Space Sci. Rev.*, *89*, 179–220, doi:10.1023/A:1005253526438.

Crooker, N. U., E. M. Appleton, N. A. Schwadron, and M. J. Owens (2010), Suprathermal electron flux peaks at stream interfaces: Signature of solar wind dynamics or tracer for open magnetic flux transport on the Sun?, *Journal of Geophysical Research (Space Physics)*, *115*(A14), A11101, doi:10.1029/2010JA015496.

Crooker, N. U., S. K. Antiochos, X. Zhao, and M. Neugebauer (2012), Global network of slow solar wind, *Journal of Geophysical Research (Space Physics)*, *117*, A04104, doi:10.1029/2011JA017236.

Dai, W., and P. R. Woodward (1998), On the Divergence-free Condition and Conservation Laws in Numerical Simulations for Supersonic Magnetohydrodynamical Flows, *ApJ*, *494*, 317–335, doi:10.1086/305176.

Detman, T., Z. Smith, M. Dryer, C. D. Fry, C. N. Arge, and V. Pizzo (2006), A hybrid heliospheric modeling system: Background solar wind, *J. Geophys. Res.*, *111*(A), 7102.

Downs, C., I. I. Roussev, B. van der Holst, N. Lugaz, I. V. Sokolov, and T. I. Gombosi (2010), Toward a Realistic Thermodynamic Magnetohydrodynamic Model of the Global Solar Corona, *ApJ*, *712*, 1219–1231, doi:10.1088/0004-637X/712/2/1219.

Egeland, A., and W. J. Burke (2010), Kristian Birkeland's pioneering investigations of geomagnetic disturbances, *History of Geo- and Space Sciences*, *1*, 13–24, doi:10.5194/hgss-1-13-2010.

Einaudi, G., P. Boncinelli, R. B. Dahlburg, and J. T. Karpen (1999), Formation of the slow solar wind in a coronal streamer, *J. Geophys. Res.*, *104*(A1), 521–534, doi:10.1029/98JA02394.

Feng, X., L. Yang, C. Xiang, S. T. Wu, Y. Zhou, and D. Zhong (2010), Three-dimensional Solar WIND Modeling from the Sun to Earth by a SIP-CESE MHD Model with a Six-component Grid, *Astrophys. J.*, *723*(1), 300–319.

Foullon, C., et al. (2009), The Apparent Layered Structure of the Heliospheric Current Sheet: Multi-Spacecraft Observations, *Sol. Phys.*, *259*, 389–416, doi:10.1007/s11207-009-9452-4.

Frazin, R. A. (2000), Tomography of the Solar Corona. I. A Robust, Regularized, Positive Estimation Method, *ApJ*, *530*, 1026–1035, doi:10.1086/308412.

Frazin, R. A., and P. Janzen (2002), Tomography of the Solar Corona. II. Robust, Regularized, Positive Estimation of the Three-dimensional Electron Density Distribution from LASCO-C2 Polarized White-Light Images, *ApJ*, *570*, 408–422, doi:10.1086/339572.

Fuselier, S. A., W. S. Lewis, C. Schiff, R. Ergun, J. L. Burch, S. M. Petrinec, and K. J. Trattner (2016), Magnetospheric Multiscale Science Mission Profile and Operations, *Space Sci. Rev.*, *199*, 77–103, doi:10.1007/s11214-014-0087-x.

Gedalin, M., W. Dröge, and Y. Y. Kartavykh (2016), Dynamics of High Energy Ions at a Structured Collisionless Shock Front, *ApJ*, *825*, 149, doi:10.3847/0004-637X/825/2/149.

Goldstein, B. E., M. Neugebauer, J. L. Phillips, S. Bame, J. T. Gosling, D. McComas, Y.-M. Wang, N. R. Sheeley, and S. T. Suess (1996),

ULYSSES plasma parameters: latitudinal, radial, and temporal variations., *A&A*, *316*, 296–303.

Gosling, J. T. (1993), The solar flare myth, *J. Geophys. Res.*, *98*, 18,937–18,950, doi:10.1029/93JA01896.

Gosling, J. T., and V. J. Pizzo (1999), Formation and Evolution of Corotating Interaction Regions and their Three Dimensional Structure, *Space Sci. Rev.*, *89*, 21–52, doi:10.1023/A:1005291711900.

Gosling, J. T., A. J. Hundhausen, V. Pizzo, and J. R. Asbridge (1972), Compressions and rarefactions in the solar wind: Vela 3, *J. Geophys. Res.*, *77*, 5442, doi:10.1029/JA077i028p05442.

Gosling, J. T., J. R. Asbridge, S. J. Bame, and W. C. Feldman (1978), Solar wind stream interfaces, *J. Geophys. Res.*, *83*, 1401–1412, doi:10.1029/JA083iA04p01401.

Gosling, J. T., G. Borrini, J. R. Asbridge, S. J. Bame, W. C. Feldman, and R. T. Hansen (1981), Coronal streamers in the solar wind at 1 AU, *J. Geophys. Res.*, *86*, 5438–5448, doi:10.1029/JA086iA07p05438.

Gosling, J. T., S. J. Bame, D. J. McComas, J. L. Phillips, V. J. Pizzo, B. E. Goldstein, and M. Neugebauer (1993), Latitudinal variation of solar wind corotating stream interaction regions: ULYSSES, *Geophys. Res. Lett.*, *20*, 2789–2792, doi:10.1029/93GL03116.

Gosling, J. T., et al. (1995), The band of solar wind variability at low heliographic latitudes near solar activity minimum: Plasma results from the Ulysses rapid latitude scan, *Geophys. Res. Lett.*, *22*, 3329–3332, doi:10.1029/95GL02163.

Gosling, J. T., D. J. McComas, R. M. Skoug, and R. J. Forsyth (2001), Stream Interaction Regions at High Heliographic Latitudes During Ulysses12/22/2004 6:25PM Second Polar Orbit, *Space Sci. Rev.*, *97*, 189–192, doi:10.1023/A:1011871421324.

Guild, T. B., H. E. Spence, E. L. Kepko, V. Merkin, J. G. Lyon, M. Wiltberger, and C. C. Goodrich (2008a), Geotail and LFM comparisons of plasma sheet climatology: 1. Average values, *Journal of Geophysical Research (Space Physics)*, *113*, A04216, doi:10.1029/2007JA012611.

Guild, T. B., H. E. Spence, E. L. Kepko, V. Merkin, J. G. Lyon, M. Wiltberger, and C. C. Goodrich (2008b), Geotail and LFM comparisons of plasma sheet climatology: 2. Flow variability, *Journal of Geophysical Research (Space Physics)*, *113*, A04217, doi:10.1029/2007JA012613.

Hain, K. H. (1987), The Partial Donor Cell Method, *Journal of Computational Physics*, *73*, 131–147, doi:10.1016/0021-9991(87)90110-0.

Hayashi, K., J. T. Hoeksema, Y. Liu, M. G. Bobra, X. D. Sun, and A. A. Norton (2015), The Helioseismic and Magnetic Imager (HMI) Vector Magnetic Field Pipeline: Magnetohydrodynamics Simulation Module for the Global Solar Corona, *Sol. Phys.*, *290*, 1507–1529, doi:10.1007/s11207-015-0686-z.

Hill, F. (2000), A.l.p.o. solar section carrington rotation commencement dates from years 1853-2016 (rotation numbers -10 to 2172).

Hundhausen, A. J. (1972), Interplanetary Shock Waves and the Structure of Solar Wind Disturbances, *NASA Special Publication*, *308*, 393.

Hundhausen, A. J. (1973), Nonlinear model of high-speed solar wind streams, *J. Geophys. Res.*, *78*, 1528, doi:10.1029/JA078i010p01528.

Jackson, B. V., P. P. Hick, A. Buffington, M. M. Bisi, J. M. Clover, M. Tokumaru, M. Kojima, and K. Fujiki (2011), Three-dimensional reconstruction of heliospheric structure using iterative tomography: A review, *Journal of Atmospheric and Solar-Terrestrial Physics*, *73*, 1214–1227, doi:10.1016/j.jastp.2010.10.007.

Jian, L., C. T. Russell, J. G. Luhmann, and R. M. Skoug (2006), Properties of Stream Interactions at One AU During 1995 2004, *Sol. Phys.*, *239*, 337–392, doi:10.1007/s11207-006-0132-3.

Jian, L. K., C. T. Russell, J. G. Luhmann, P. J. MacNeice, D. Odstrcil, P. Riley, J. A. Linker, R. M. Skoug, and J. T. Steinberg (2011), Comparison of Observations at ACE and Ulysses with Enlil Model Results: Stream Interaction Regions During Carrington Rotations 2016 - 2018, *Sol. Phys.*, *273*, 179–203, doi:10.1007/s11207-011-9858-7.

Kivelson, M., and C. Russell (1995), *Introduction to Space Physics*, Cambridge atmospheric and space science series, Cambridge University Press.

Krieger, A. S., A. F. Timothy, and E. C. Roelof (1973), A coronal hole and its identification as the source of a high velocity solar wind stream, *Solar Physics*, *29*(2), 505–525, doi:10.1007/BF00150828.

Lapenta, G., and D. A. Knoll (2005), Effect of a Converging Flow at the Streamer Cusp on the Genesis of the Slow Solar Wind, *ApJ*, *624*(2), 1049–1056, doi:10.1086/429262.

Lazarus, A., J. Kasper, A. Szabo, and K. Ogilvie (2003), Solar Wind Streams and Their Interactions, in *Solar Wind Ten*, *American Institute of Physics Conference Series*, vol. 679, edited by M. Velli, R. Bruno, F. Malara, and B. Bucci, pp. 187–189, doi:10.1063/1.1618573.

Lee, C. O., J. G. Luhmann, J. T. Hoeksema, X. Sun, C. N. Arge, and I. de Pater (2011), Coronal Field Opens at Lower Height During the Solar Cycles 22 and 23 Minimum Periods: IMF Comparison Suggests the Source Surface Should Be Lowered, *Sol. Phys.*, *269*, 367–388, doi:10.1007/s11207-010-9699-9.

Lee, M. A. (2000), An analytical theory of the morphology, flows, and shock compressions at corotating interaction regions in the solar wind, *J. Geophys. Res.*, *105*, 10,491–10,500, doi:10.1029/1999JA000327.

Linker, J. A., Z. Mikic, P. Riley, R. Lionello, and V. S. Titov (2010), Magnetic Maps and Coronal/Solar Wind Modeling: Practices and Pitfalls (Invited), *AGU Fall Meeting Abstracts*, p. D3.

Linker, J. A., et al. (2017), The Open Flux Problem, *ApJ*, *848*(1), 70, doi:10.3847/1538-4357/aa8a70.

Luhmann, J. G., Y. Li, P. Riley, C. N. Arge, Y. Liu, and G. Detoma (2008), Challenges Created by Active Regions in Global Models for Space Weather Uses, in *Subsurface and Atmospheric Influences on Solar Activity*, *Astronomical Society of the Pacific Conference Series*, vol. 383, edited by R. Howe, R. W. Komm, K. S. Balasubramaniam, and G. J. D. Petrie, p. 133.

Luhmann, J. G., C. O. Lee, Y. Li, C. N. Arge, A. B. Galvin, K. Simunac, C. T. Russell, R. A. Howard, and G. Petrie (2009), Solar Wind Sources in the Late Declining Phase of Cycle 23: Effects of the Weak Solar Polar Field on High Speed Streams, *Sol. Phys.*, *256*, 285–305, doi:10.1007/s11207-009-9354-5.

Lyon, J. G., J. A. Fedder, and C. M. Mobarry (2004), The Lyon-Fedder-Mobarry (LFM) global MHD magnetospheric simulation code, *Journal of Atmospheric and Solar-Terrestrial Physics*, *66*, 1333–1350, doi:10.1016/j.jastp.2004.03.020.

McComas, D. J., J. L. Phillips, S. J. Bame, J. T. Gosling, B. E. Goldstein, and M. Neugebauer (1995), Ulysses solar wind observations to 56^{circ} south, *Space Sci. Rev.*, *72*, 93–98, doi:10.1007/BF00768760.

McComas, D. J., et al. (2000), Solar wind observations over Ulysses' first full polar orbit, *J. Geophys. Res.*, *105*, 10,419–10,434, doi:10.1029/1999JA000383.

McGregor, S. L. (2011), On tracing the origins of the solar wind, Ph.D. thesis, Boston University.

McGregor, S. L., W. J. Hughes, C. N. Arge, and M. J. Owens (2008), Analysis of the magnetic field discontinuity at the potential field source surface and Schatten Current Sheet interface in the Wang-Sheeley-Arge model, *Journal of Geophysical Research (Space Physics)*, *113*, A08112, doi:10.1029/2007JA012330.

McGregor, S. L., W. J. Hughes, C. N. Arge, D. Odstrcil, and N. A. Schwadron (2011a), The radial evolution of solar wind speeds, *Journal of Geophysical Research (Space Physics)*, *116*, A03106, doi:10.1029/2010JA016006.

McGregor, S. L., W. J. Hughes, C. N. Arge, M. J. Owens, and D. Odstrcil (2011b), The distribution of solar wind speeds during solar minimum: Calibration for numerical solar wind modeling constraints on the source of the slow solar wind, *Journal of Geophysical Research (Space Physics)*, *116*, A03101, doi:10.1029/2010JA015881.

McPherron, R. L., and J. Weygand (2006), The Solar Wind and Geomagnetic Activity as a Function of Time Relative to Corotating Interaction Regions, in *Recurrent Magnetic Storms: Corotating Solar Wind*, *Washington DC American Geophysical Union Geophysical Monograph Series*, vol. 167, edited by R. McPherron, W. Gonzalez, G. Lu, H. A. José, and S. Natchimuthukonar Gopalswamy, p. 125, doi:10.1029/167GM12.

Merkin, V. G., J. G. Lyon, S. L. McGregor, and D. M. Pahud (2011), Disruption of a heliospheric current sheet fold, *Geophys. Res. Lett.*, *38*, L14107, doi:10.1029/2011GL047822.

Merkin, V. G., J. G. Lyon, and S. G. Claudepierre (2013), Kelvin-Helmholtz instability of the magnetospheric boundary in a three-dimensional global MHD simulation during northward IMF conditions, *Journal of Geophysical Research (Space Physics)*, *118*(9), 5478–5496, doi:10.1002/jgra.50520.

Merkin, V. G., J. G. Lyon, D. Lario, C. N. Arge, and C. J. Henney (2016a), Time-dependent magnetohydrodynamic simulations of the inner heliosphere, *Journal of Geophysical Research (Space Physics)*, *121*(4), 2866–2890, doi:10.1002/2015JA022200.

Merkin, V. G., R. Lionello, J. G. Lyon, J. Linker, T. Török, and C. Downs (2016b), Coupling of Coronal and Heliospheric Magnetohydrodynamic Models: Solution Comparisons and Verification, *ApJ*, *831*(1), 23, doi:10.3847/0004-637X/831/1/23.

Mikić, Z., J. A. Linker, R. Lionello, P. Riley, and V. Titov (2007), Predicting the Structure of the Solar Corona for the Total Solar Eclipse of March 29, 2006, in *Solar and Stellar Physics Through Eclipses*, *Astronomical Society of the Pacific Conference Series*, vol. 370, edited by O. Demircan, S. O. Selam, and B. Albayrak, p. 299.

Morgan, H., L. Jeska, and D. Leonard (2013), The Expansion of Active Regions into the Extended Solar Corona, *ApJS*, *206*, 19, doi:10.1088/0067-0049/206/2/19.

Murray, S. A. (2018), The importance of ensemble techniques for operational space weather forecasting, *Space Weather*, *16*(7), 777–783, doi:10.1029/2018SW001861.

Nakamizo, A., T. Tanaka, Y. Kubo, S. Kamei, H. Shimazu, and H. Shinagawa (2009), Development of the 3-D MHD model of the solar corona-solar wind combining system, *J. Geophys. Res.*, *114*(A7).

Neugebauer, M. (2008), Heliospheric sector boundaries: Single or multiple?, *Journal of Geophysical Research: Space Physics*, *113*(A12), doi:10.1029/2008JA013453.

Neugebauer, M., and C. W. Snyder (1962), Solar Plasma Experiment, *Science*, *138*, 1095–1097, doi:10.1126/science.138.3545.1095-a.

Neugebauer, M., and C. W. Snyder (1966), Mariner 2 Observations of the Solar Wind, 1, Average Properties, *J. Geophys. Res.*, *71*, 4469.

Neugebauer, M., et al. (1998), Spatial structure of the solar wind and comparisons with solar data and models, *Journal of Geophysical Research: Space Physics*, *103*(A7), 14,587–14,599, doi:10.1029/98JA00798.

Neugebauer, M., P. C. Liewer, E. J. Smith, R. M. Skoug, and T. H. Zurbuchen (2002), Sources of the solar wind at solar activity maximum, *Journal of Geophysical Research (Space Physics)*, *107*, 1488, doi:10.1029/2001JA000306.

Odstrcil, D. (1994), Interactions of solar wind streams and related small structures, *J. Geophys. Res.*, *99*, 17, doi:10.1029/94JA01225.

Odstrcil, D., P. Riley, and X. P. Zhao (2004), Numerical simulation of the 12 May 1997 interplanetary CME event, *Journal of Geophysical Research (Space Physics)*, *109*, A02116, doi:10.1029/2003JA010135.

Oran, R., et al. (2015), A Steady-state Picture of Solar Wind Acceleration and Charge State Composition Derived from a Global Wave-driven MHD Model, *ApJ*, *806*, 55, doi:10.1088/0004-637X/806/1/55.

Owens, M. J., and P. Riley (2017), Probabilistic Solar Wind Forecasting Using Large Ensembles of Near-Sun Conditions With a Simple One-Dimensional "Upwind" Scheme, *Space Weather*, *15*, 1461–1474, doi:10.1002/2017SW001679.

Owens, M. J., H. E. Spence, S. McGregor, W. J. Hughes, J. M. Quinn, C. N. Arge, P. Riley, J. Linker, and D. Odstrcil (2008), Metrics for solar wind prediction models: Comparison of empirical, hybrid, and physics-based schemes with 8 years of L1 observations, *Space Weather*, *6*, S08001, doi:10.1029/2007SW000380.

Owens, M. J., H. E. Spence, S. McGregor, W. J. Hughes, J. M. Quinn, C. N. Arge, P. Riley, J. Linker, and D. Odstrcil (2008), Metrics for solar wind prediction models: Comparison of empirical, hybrid, and physics-based schemes with 8 years of L1 observations, *Space Weather*, *6*(8), doi:10.1029/2007SW000380.

Owens, M. J., P. Riley, and T. Horbury (2017), The role of empirical space-weather models (in a world of physics-based numerical simulations), *Proceedings of the International Astronomical Union*, *13*(S335), 254–257, doi:10.1017/S1743921317007128.

Owens, M. J. L., Riley, Pete, Lockwood, Mike, and Lawless, Amos S. (2020), Quantifying the latitudinal representivity of in situ solar wind observations, *J. Space Weather Space Clim.*, *10*, 8, doi:10.1051/swsc/2020009.

Pahud, D. M., V. G. Merkin, C. N. Arge, W. J. Hughes, and S. M. McGregor (2012), An MHD simulation of the inner heliosphere during Carrington rotations 2060 and 2068: Comparison with MESSENGER and ACE spacecraft observations, *Journal of Atmospheric and Solar-Terrestrial Physics*, *83*, 32–38, doi:10.1016/j.jastp.2012.02.012.

Parker, E. N. (1958), Dynamics of the Interplanetary Gas and Magnetic Fields., *ApJ*, *128*, 664, doi:10.1086/146579.

Phan, T. D., J. T. Gosling, and M. S. Davis (), Prevalence of extended reconnection x-lines in the solar wind at 1 au, *Geophysical Research Letters*, *36*(9), doi:10.1029/2009GL037713.

Pizzo, V. (1978), A three-dimensional model of corotating streams in the solar wind, 1. theoretical foundations, *Journal of Geophysical Research: Space Physics*, *83*(A12), 5563–5572, doi:10.1029/JA083iA12p05563.

Pizzo, V. (1980), A three-dimensional model of corotating streams in the solar wind ii. hydrodynamic streams, *Journal of Geophysical Research*.

Pizzo, V. J. (1982), A three-dimensional model of corotating streams in the solar wind. III - Magnetohydrodynamic streams, *J. Geophys. Res.*, *87*, 4374–4394, doi:10.1029/JA087iA06p04374.

Planetary
Data System (2016), Planetary plasma interactions node, https://pds-ppi.igpp.ucla.edu/search/?sc=Messenger&t=Mercury&i=MAG, aPL.

Powell, K. G., P. L. Roe, T. J. Linde, T. I. Gombosi, and D. L. De Zeeuw (1999), A Solution-Adaptive Upwind Scheme for Ideal Magnetohydrodynamics, *Journal of Computational Physics*, *154*, 284–309, doi:10.1006/jcph.1999.6299.

Provornikova, E., M. Opher, V. Izmodenov, and G. Toth (2012), Do Corotating Interaction Region Associated Shocks Survive When They Propagate into the Heliosheath?, *ApJ*, *756*, L37, doi:10.1088/2041-8205/756/2/L37.

Richardson, I. G. (2004), Energetic Particles and Corotating Interaction Regions in the Solar Wind, *Space Sci. Rev.*, *111*, 267–376, doi:10.1023/B:SPAC.0000032689.52830.3e.

Richardson, I. G. (2013), *The Formation of CIRs at Stream-Stream Interfaces and Resultant Geomagnetic Activity*, pp. 45–58, American Geophysical Union (AGU), doi:10.1029/167GM06.

Richardson, I. G. (2018), Solar wind stream interaction regions throughout the heliosphere, *Living Reviews in Solar Physics*, *15*, 1, doi:10.1007/s41116-017-0011-z.

Richter and Luttrell (1986), "Superposed epoch analysis of CIRs at 0.3 and 1.0 AU: A comparative study", *J. Geophys. Res.*, *91*(A5), 5873–5878.

Riley, P. (2007), An Alternative Interpretation of the Relationship between the Inferred Open Solar Flux and the Interplanetary Magnetic Field, *ApJ*, *667*, L97–L100, doi:10.1086/522001.

Riley, P., and J. G. Luhmann (2012), Interplanetary Signatures of Unipolar Streamers and the Origin of the Slow Solar Wind, *Sol. Phys.*, *277*, 355–373, doi:10.1007/s11207-011-9909-0.

Riley, P., J. T. Gosling, L. A. Weiss, and V. J. Pizzo (1996), The tilts of corotating interaction regions at midheliographic latitudes, *Journal of Geophysical Research: Space Physics*, *101*(A11), 24,349–24,357, doi:10.1029/96JA02447.

Riley, P., et al. (1997), ULYSSES solar wind plama observations at high latitudes, *Advances in Space Research*, *20*, 15, doi:10.1016/S0273-1177(97)00473-0.

Riley, P., J. A. Linker, and Z. Mikić (2001), An empirically-driven global MHD model of the solar corona and inner heliosphere, *J. Geophys. Res.*, *106*, 15,889–15,902, doi:10.1029/2000JA000121.

Riley, P., J. A. Linker, and Z. Mikić (2001), An empirically-driven global MHD model of the solar corona and inner heliosphere, *J. Geophys. Res.*, *106*(A), 15,889–15,902.

Riley, P., J. A. Linker, Z. Mikić, D. Odstrcil, T. H. Zurbuchen, D. Lario, and R. P. Lepping (2003), Using an MHD simulation to interpret the global context of a coronal mass ejection observed by two spacecraft, *Journal of Geophysical Research (Space Physics)*, *108*, 1272, doi:10.1029/2002JA009760.

Riley, P., J. A. Linker, Z. Mikić, R. Lionello, S. A. Ledvina, and J. G. Luhmann (2006), A Comparison between Global Solar Magnetohydrodynamic and Potential Field Source Surface Model Results, *ApJ*, *653*, 1510–1516, doi:10.1086/508565.

Riley, P., R. Lionello, J. Linker, Z. Mikic, J. Luhmann, and J. Wijaya (2011), Global mhd modeling of the solar corona and inner heliosphere for the whole heliosphere interval, *Solar Physics*.

Riley, P., et al. (2014), A Multi-Observatory Inter-Comparison of Line-of-Sight Synoptic Solar Magnetograms, *Sol. Phys.*, *289*, 769–792, doi:10.1007/s11207-013-0353-1.

Rouillard, A. P., et al. (2009), A Multispacecraft Analysis of a Small-Scale Transient Entrained by Solar Wind Streams, *Sol. Phys.*, *256*, 307–326, doi:10.1007/s11207-009-9329-6.

Roussev, I. I., T. I. Gombosi, I. V. Sokolov, M. Velli, W. I. Manchester, D. L. Dezeeuw, P. Liewer, G. Toth, and J. Luhmann (2003), A Three-dimensional Model of the Solar Wind Incorporating Solar Magnetogram Observations, *Astrophys. J.*, *595*(1), L57–L61.

Schatten, K. H. (1972), Current Sheet Magnetic Model for the Solar Corona, *NASA Special Publication*, *308*, 44.

Schwadron, N. A., and D. J. McComas (2003), Solar Wind Scaling Law, *ApJ*, *599*(2), 1395–1403, doi:10.1086/379541.

Shiota, D., R. Kataoka, Y. Miyoshi, T. Hara, C. Tao, K. Masunaga, Y. Futaana, and N. Terada (2014), Inner heliosphere MHD modeling system applicable to space weather forecasting for the other planets, *Space Weather*, *12*(4), 187–204.

Simunac, K., et al. (2009), In situ observations of solar wind stream interface evolution, *Solar Physics*.

Simunac, K. D. C., et al. (2012), The Heliospheric Plasma Sheet Observed in situ by Three Spacecraft over Four Solar Rotations, *Sol. Phys.*, *281*, 423–447, doi:10.1007/s11207-012-0156-9.

Siscoe, G., and D. Intriligator (1993), Three views of two giant streams: Aligned observations at 1 AU, 4.6 AU, and 5.9 AU, *Geophys. Res. Lett.*, *20*, 2267–2270, doi:10.1029/93GL02488.

Siscoe, G. L., B. Goldstein, and A. J. Lazarus (1969), An east-west asymmetry in the solar wind velocity, *Journal of Geophysical Research (1896-1977)*, *74*(7), 1759–1762, doi:https://doi.org/10.1029/JA074i007p01759.

Solomon, S. C., L. Qian, and A. J. Mannucci (2018), Ionospheric Electron Content During Solar Cycle 23, *Journal of Geophysical Research (Space Physics)*, *123*, 5223–5231, doi:10.1029/2018JA025464.

Spence, H. E., et al. (2013), Science Goals and Overview of the Radiation Belt Storm Probes (RBSP) Energetic Particle, Composition, and Thermal Plasma (ECT) Suite on NASA's Van Allen Probes Mission, *Space Sci. Rev.*, *179*, 311–336, doi:10.1007/s11214-013-0007-5.

Stone, E., A. Frandsen, and R. Mewaldt (1998), The Advanced Composition Explorer, *Space Sci. Rev.*, *86*, 1–22, doi:https://doi-org.uml.idm.oclc.org/10.1023/A:1005082526237.

Title, A. M., and T. D. Tarbell (1975), Measurements of solar magnetic fields by Fourier transform techniques. I - Unsaturated lines, *Sol. Phys.*, *41*, 255–269, doi:10.1007/BF00154064.

Tsurutani, B. T., G. S. Lakhina, A. Sen, P. Hellinger, K.-H. Glassmeier, and A. J. Mannucci (2018), A Review of Alfvénic Turbulence in High-Speed Solar Wind Streams: Hints From Cometary Plasma Turbulence, *Journal of Geophysical Research (Space Physics)*, *123*(4), 2458–2492, doi:10.1002/2017JA024203.

Usmanov, A. V., and M. L. Goldstein (2003), A tilted-dipole MHD model of the solar corona and solar wind, *J. Geophys. Res.*, *108*(A9).

van der Holst, B., W. B. Manchester, IV, R. A. Frazin, A. M. Vásquez, G. Tóth, and T. I. Gombosi (2010), A Data-driven, Two-temperature Solar Wind Model with Alfvén Waves, *ApJ*, *725*, 1373–1383, doi:10.1088/0004-637X/725/1/1373.

Wang, P. K., and G. L. Siscoe (1980), Ancient Chinese Observations of Physical Phenomena Attending Solar Eclipses, *Sol. Phys.*, *66*, 187–193, doi:10.1007/BF00150528.

Wang, Y.-M., and N. R. Sheeley, Jr. (1992), On potential field models of the solar corona, *ApJ*, *392*, 310–319, doi:10.1086/171430.

Wang, Y.-M., N. R. Sheeley, Jr., and N. B. Rich (2007), Coronal Pseudostreamers, *ApJ*, *658*, 1340–1348, doi:10.1086/511416.

Wiegelmann, T., J. K. Thalmann, B. Inhester, T. Tadesse, X. Sun, and J. T. Hoeksema (2012), How Should One Optimize Nonlinear Force-Free Coronal Magnetic Field Extrapolations from SDO/HMI Vector Magnetograms?, *Sol. Phys.*, *281*, 37–51, doi:10.1007/s11207-012-9966-z.

Wiengarten, T., J. Kleimann, H. Fichtner, R. Cameron, J. Jiang, R. Kissmann, and K. Scherer (2013), MHD simulation of the inner-heliospheric magnetic field, *J. Geophys. Res.*, *118*(1), 29–44.

Wimmer-Schweingruber, R. F., R. von Steiger, and R. Paerli (1997), Solar wind stream interfaces in corotating interaction regions: SWICS/Ulysses results, *J. Geophys. Res.*, *102*, 17,407–17,418, doi:10.1029/97JA00951.

Winslow, R. M., N. Lugaz, N. A. Schwadron, C. J. Farrugia, W. Yu, J. M. Raines, M. L. Mays, A. B. Galvin, and T. H. Zurbuchen (2016), Longitudinal conjunction between messenger and stereo a: Development of icme complexity through stream interactions, *Journal of Geophysical Research: Space Physics*, pp. n/a–n/a, doi:10.1002/2015JA022307, 2015JA022307.

Xu, F., and J. E. Borovsky (2015), A new four-plasma categorization scheme for the solar wind, *Journal of Geophysical Research (Space Physics)*, *120*, 70–100, doi:10.1002/2014JA020412.

Yee, K. (1966), Numerical solution of inital boundary value problems involving maxwell's equations in isotropic media, *IEEE Transactions on Antennas and Propagation*, *14*, 302–307, doi:10.1109/TAP.1966.1138693.

Yu, W., C. J. Farrugia, A. B. Galvin, N. Lugaz, J. G. Luhmann, K. D. C. Simunac, and E. Kilpua (2016), Small solar wind transients at 1 au: Stereo observations (2007–2014) and comparison with near-earth wind results (1995–2014), *Journal of Geophysical Research: Space Physics*, *121*(6), 5005–5024, doi:10.1002/2016JA022642, 2016JA022642.

Zhang, B., K. A. Sorathia, J. G. Lyon, V. G. Merkin, and M. Wiltberger (2018), A three-dimensional finite-volume MHD solver in non-orthogonal curvilinear geometry: GAMERA, a reinvention of LFM, *arXiv e-prints*.

Zhang, B., K. A. Sorathia, J. G. Lyon, V. G. Merkin, J. S. Garretson, and M. Wiltberger (2019), GAMERA: A Three-dimensional Finite-volume MHD Solver for Non-orthogonal Curvilinear Geometries, *ApJS*, *244*(1), 20, doi:10.3847/1538-4365/ab3a4c.

Zhao, L., T. H. Zurbuchen, and L. A. Fisk (2009), Global distribution of the solar wind during solar cycle 23: ACE observations, *Geophys. Res. Lett.*, *36*, L14104, doi:10.1029/2009GL039181.

CURRICULUM VITAE

DANIELLE PAHUD